Model Based Estimation of the Elastomechanical Properties of the Human Heart

Zur Erlangung des akademischen Grades einer

DOKTORIN DER INGENIEURWISSENSCHAFTEN (Dr.-Ing.)

von der KIT-Fakultät für

Elektrotechnik und Informationstechnik

des Karlsruher Instituts für Technologie (KIT)

genehmigte

DISSERTATION

von

Ekaterina Kovacheva, M.Sc.

geb. in Sofia, Bulgarien

Tag der mündlichen Prüfung:	08.07.2021
Referent:	Prof. Dr. rer. nat. Olaf Dössel
Korreferent:	Prof. Dr. Christian Wieners
Korreferent:	Dr.-Ing. Axel Loewe

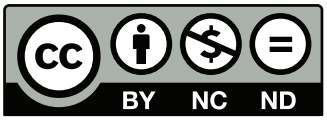

Abstract

The human heart is a complex organ involving the interaction of different phenomena. On the one hand, blood is flowing through the heart chambers and applies pressure on the inner surfaces. On the other hand, the heart is surrounded by a pericardial sac, which influences the chamber motion. Furthermore, electrical waves propagate through the heart tissue to activate a contraction force, which, added to the passive force, works against the chamber pressure and results in the deformation of the myocardium. In the last decades, advanced computational models of the heart phenomena have been created and included in simulation frameworks to study the human heart beat.

Furthermore, the rapid advancement of in vivo imaging modalities in the last years allows gaining patient-specific information, which can be transferred from individual patients to a valid cardiac model to allow conclusions about properties of the tissue.

Tissue property information can reveal new insights into the physiology and pathophysiology of the heart. They can provide novel ways to diagnose medical conditions and deliver detailed information about phenomena involved in the heartbeat, which cannot be obtained otherwise. In particular, computational models can be employed to estimate elastomechanical properties of the heart tissue: the passive force, which arises from the intrinsic elastic material properties of the tissue and the active force (tension), which leads to the contraction of the heart tissue. In this work, steps towards the estimation of the elastomechanical properties of the cardiac tissue are presented and discussed.

A whole heart model was generated based on in vivo human MRI images. The deformation of the tissue was simulated with the framework *CardioMechanics* and validated against volume curves, regional wall thickness and deformation velocity derived from motion clinical images. Further deformation measurements (regional strains, strain rates and velocities) were compared with literature values to demonstrate the validity of the developed healthy heart model.

After a valid model was created, a sensitivity study was performed to quantify the influence of the elastomechanical properties on deformation measurements. This was a prerequisite for the model based estimation of the elastomechanical properties. In a further study, the geometrical heart model was modified to simulate pathologies present in hypertrophic cardiomyopathy. It was shown which pathological mechanisms affect the ventricular deformation.

After it was shown that the elastomechanical properties of the cardiac tissue influence the deformation measurements of the left ventricle, these properties were estimated. The

parameters of the model describing the passive force were obtained based on a pressure-volume relation from the literature applying simple and robust optimization methods. In this work, it is shown that an objective function based solely on this relation could not deliver a unique parameter set and therefore, it was extended to include an additional term involving an absolute volume ratio.

Furthermore, a dynamic active force field was reconstructed from motion data of the left ventricle using an inverse solver to perform a sensitivity analysis with synthetic data. By imposing spatial regularization, the morphology of the reconstructed active force curve matched the ground truth, whereas the amplitude of the reconstructed force differed. Despite the reconstruction errors in the active force, different sized infarct areas could be identified accurately in the inverse solution. Using endocardial motion data derived from clinically measured imaging data, the method reconstructed an active force course, which is promising, but further effort is needed to apply the method directly on clinical data.

Altogether, the construction of a heart model and the validation of a simulated heart beat was presented and steps towards the estimation of the elastomechanical properties of the cardiac tissue were provided. The described results indicated directions for future improvement and in particular, showed that more input data might be needed to achieve reasonable results.

Zusammenfassung

Das menschliche Herz ist ein komplexes Organ, in dem verschiedene Phänomene zusammenwirken. Einerseits fließt das Blut durch die Herzkammern und übt Druck auf die Innenflächen aus. Andererseits ist das Herz von einem Herzbeutel umgeben, der die Bewegung der Kammern beeinflusst. Darüber hinaus breiten sich elektrische Wellen durch das Herzgewebe aus und initiieren die Kontraktion des Herzmuskels, welche, addiert zu der passiven Kraft, dem Kammerdruck entgegenwirkt und zur Deformation des Myokards führt. In den letzten Jahren wurden fortschrittliche Computermodelle des Herzens entwickelt und in Simulationsumgebungen integriert, um den menschlichen Herzschlag zu untersuchen.

Zusätzlich ermöglicht die rasante Weiterentwicklung der bildgebenden Verfahren in den letzten Jahren die Gewinnung patientenspezifischer Informationen, die auf ein valides Herzmodell übertragen werden können, um Rückschlüsse auf Eigenschaften des Gewebes zu ermöglichen.

Informationen über Gewebeeigenschaften können neue Erkenntnisse über die Physiologie und Pathophysiologie des Herzens liefern. Sie können neue Wege zur Diagnose von Krankheiten eröffnen und detaillierte Informationen über Mechanismen des Herzschlages liefern, die auf andere Weise nicht zu erhalten sind. Insbesondere können Computermodelle eingesetzt werden, um elastomechanische Eigenschaften des Herzgewebes zu bestimmen: die passive Kraft, die sich aus den intrinsischen elastischen Materialeigenschaften des Gewebes ergibt und die aktive Kraft (Spannung), die zur Kontraktion des Herzgewebes führt. In dieser Arbeit werden Schritte zur Abschätzung der elastomechanischen Eigenschaften des Herzgewebes vorgestellt und diskutiert.

Ein menschliches Ganzherzmodell wurde basierend auf in vivo MRT-Bildern erstellt. Die Deformation des Gewebes wurde mit der Simulationsumgebung *CardioMechanics* simuliert und mit Hilfe von Volumenkurven, regionalen Wanddicken und Deformationsgeschwindigkeiten aus klinischen Daten validiert. Weitere Deformationsmessungen (regionale Dehnungen, Dehnungsraten und Geschwindigkeiten) wurden mit Literaturwerten verglichen, um die Validität des entwickelten gesunden Herzmodells zu demonstrieren.

Nachdem ein gültiges Modell erstellt wurde, ist eine Sensitivitätsstudie durchgeführt worden, um den Einfluss der elastomechanischen Eigenschaften auf die Deformationsmessungen zu quantifizieren. Dies war eine Voraussetzung für die modellbasierte Schätzung der elastomechanischen Eigenschaften. In einer weiteren Studie wurde das geometrische Herzmodell modifiziert, um Pathologien zu simulieren, die bei der hypertrophen Kardiomy-

opathie auftreten. Es wurde gezeigt, welche pathologischen Mechanismen die ventrikuläre Verformung beeinflussen.

Nachdem gezeigt wurde, dass die passiven elastomechanischen Eigenschaften des Herzgewebes die Deformationsmessungen des linken Ventrikels beeinflussen, wurden diese Eigenschaften mit Hilfe eines Optimierungsverfahrens geschätzt. Die Parameter des Modells, das die passive Kraft beschreibt, wurden basierend auf einer Druck-Volumen-Relation aus der Literatur unter Anwendung einfacher und robuster Optimierungsmethoden ermittelt. In dieser Arbeit wird gezeigt, dass eine Zielfunktion, die nur auf dieser Relation basiert, keinen eindeutigen Parametersatz liefern konnte und daher wurde sie um einen zusätzlichen Term erweitert, der ein absolutes Volumenverhältnis beinhaltet.

Weiterhin wurde ein dynamisches aktives Kraftfeld aus Bewegungsdaten des linken Ventrikels mit Hilfe eines inversen Lösers rekonstruiert, um eine Sensitivitätsanalyse mit synthetischen Daten durchzuführen. Mit Hilfe einer zusätzlichen räumlichen Regularisierung stimmte die Morphologie der rekonstruierten aktiven Kraftkurve mit der Grundwahrheit überein, während die Amplitude der rekonstruierten Kraft unterschiedlich war. Trotz der Rekonstruktionsfehler in der aktiven Kraft konnten unterschiedlich große Infarktgebiete in der inversen Lösung genau identifiziert werden. Unter Verwendung von endokardialen Bewegungsdaten, die aus klinisch gemessenen Bildern abgeleitet wurden, rekonstruierte die Methode einen aktiven Kraftverlauf. Allerdings sind weitere Untersuchungen erforderlich, um die Methode direkt auf klinische Daten anzuwenden.

Insgesamt wurde die Konstruktion eines Herzmodells und die Validierung eines simulierten Herzschlags vorgestellt und Schritte zur Abschätzung der elastomechanischen Eigenschaften des Herzgewebes geliefert. Die beschriebenen Ergebnisse weisen Richtungen für zukünftige Verbesserungen auf und zeigen insbesondere, dass mehr Eingabedaten benötigt werden, um realistische Ergebnisse zu erzielen.

Acknowledgments

I would like to express my sincere gratitude to all the people, who made this work possible.

First, I would like to thank Prof. Dr. Olaf Dössel for providing me the opportunity to join the IBT team and do research work in the cardiac modelling group. Furthermore, I would like to thank him, Prof. Dr. Christian Wieners and Dr.-Ing. Axel Loewe for being my examiners. Second, I would like to extend my gratitude to Dr.-Ing. Axel Loewe for supervising and supporting me throughout the last years.

Additionally, I would like to thank all my colleagues for making the IBT feel like a second home for the last three years. We shared not only successful and content moments but also frustration and failure. In particular, I am very thankful to Lukas Baron, who introduced me to the field of cardiac mechanics; to Steffen Schuler, who always gave expert advice and novel suggestions for improvements; to Tobias Gerach, whom I spent countless hours of exciting discussions with and who supported me tremendously during my work.

Finally, I would like to thank the people in my private surrounding: my family, Lora, Alexandrina and Milena, my partner, Korbinian and my friends. I am thankful for their continuous support, belief and positive attitude throughout the last years.

Contents

Abbreviations

AHA	American Heart Association
AV	atrioventricular
BC	boundary condition
CT	computed tomography
DT-MRI	diffusion tensor magnetic resonance imaging
ED	end-diastole
EF	ejection fraction
ES	end-systole
EW	external work
FA	fractional anisotropy
FO	fiber orientation
HCM	hypertrophic cardiomyopathy
LA	left atrium
LGE	late gadolinium enhancement
LV	left ventricle
MI	myocardial infarction
MRI	magnetic resonance imaging
MRTE	mean relative tension error
MTE	mean tension error
PTT	peak tension time
PV	pressure-volume
RA	right atrium
RMSD	root mean squared deviation
RMSE	root mean square error
ROC	receiver operating characteristic
RV	right ventricle
SV	stroke volume
US	ultrasound
WT	wall thickness

Chapter 1

Introduction

The human heart is a complex organ, involving the interaction of different phenomena. On the one hand, blood is flowing through the heart chambers and applies pressure on the chambers inner surfaces. On the other hand, the heart is surrounded by a pericardial sac, which influences the chamber motion. Furthermore, electrical waves propagate through the myocardium to activate a contraction force, which – added to the passive force – works against the chamber pressure and results in the deformation of the myocardium. The development of active and passive forces depends on the elastomechanical properties of the heart tissue.

In the last decades, advanced computational models of these phenomena have been developed and included in frameworks for numerical simulations of the human heart beat. A review of computational models in cardiology is provided in Niederer et al. [1]. The rapid advancement of in vivo imaging modalities in the last years allowed to gain patient-specific information, which can be incorporated in biomechanical heart models. Magnetic resonance imaging (MRI) or computed tomography (CT) show the morphology of the heart and can be used as a starting point for a geometrical model generation. Diffusion tensor magnetic resonance imaging (DT-MRI) provides information over the orientation of the alignment of the cardiac cells. The heart function can be captured by ultrasound (US), CT and MRI, which reveal the myocardial wall mechanics: regional myocardial wall motion, strain, twist and rotation.

Measures obtained from imaging modalities can be compared to the same measures extracted from a simulated heart beat to validate the numerical result and the heart model. Furthermore, imaging data can be transferred from individual patients to a valid cardiac model to allow conclusions about elastomechanical properties of the tissue. Such information can reveal new insights into the physiology and pathophysiology of the heart. They can provide novel ways to diagnose medical conditions and deliver detailed information about phenomena involved in the heart beat, which cannot be obtained otherwise.

In particular, the passive forces which arise from the intrinsic material properties of the tissue, cannot be measured in vivo. US elastography can measure tissue stiffness, which determines the development of the passive forces. It is not yet clinically applicable on humans, but only in open-chested animals [2]. Furthermore, it was demonstrated that MRI

elastography can be used to diagnose different cardiac diseases but further advances have to be made in order to be established as a clinical tool [2]. However, myocardial stiffness is a major determinant of cardiac function, with large changes in stiffness associated with heart failure. Furthermore, it is known that the stiffness is increased in many diseases, including ischemic insult, hypertension and hypertrophic cardiomyopathy (HCM).

Death of cardiac cells following an ischemic insult results in the loss of myocardial viability, which is related with reduced development of active contraction forces in the tissue. In clinical routine, US is employed to detect wall motion abnormalities and therefore, to determine the regions of reduced myocardial viability. This is less precise than identifying the tissue composition and extracellular fibrosis by employing cardiac MRI with contrast agents. However, contrast agents are known to deposit in brain tissue with potentially detrimental long-term effects [3].

Computational models can be employed to estimate elastomechanical properties of the heart tissue in order to avoid difficulties related to measuring such properties directly in clinical routine. Steps towards this goal are presented and discussed in this work.

Based on a computational model, methods are described to estimate contractility and passive properties of the myocardium from image data. Prior to the model based estimation, a whole heart model was generated based on static MRI images. Tissue surrounding the heart was added, a local system was calculated to represent the myocyte orientation and a pressure-free state was estimated. This heart model is the starting point of a numerical simulation, which calculates the deformation of the tissue. In this work, the in-house numerical solver *CardioMechanics* was used. An evaluation framework was created to compare the simulated result against volume curves, regional wall thickness and deformation velocity derived from dynamic clinical images of the same heart. Further measures (regional strains, strain rates and velocities) were compared to literature values to demonstrate the validity of the healthy heart model. Additionally, a sensitivity study was performed to quantify the influence of the elastomechanical properties on deformation measures: this was a prerequisite for the model based estimation of these properties. Furthermore, the geometrical heart model and the myocyte orientations were modified to create pathologies present in HCM. The passive properties were estimated based on a pressure-volume relation described in the literature applying simple and robust optimization methods. A dynamic active force field was reconstructed from motion data of the left ventricle (LV) using an inverse solver, which was initially proposed and developed by Thomas Fritz [4] and adapted for this work. Ischemic regions were identified based on the reconstructed active force in a model of the LV.

Structure of the Thesis

This thesis is structured as follows:

- **Chapter 1** introduces the topic and provides a state of the art.
- **Chapter 2** delivers medical fundamentals.
- **Chapter 3** delivers mathematical fundamentals.

- **Chapter 4** provides a way to create a computational heart model based on imaging data, which is suitable for a finite element simulation.
- **Chapter 5** describes a framework for the evaluation of the heart deformation, which is used to validate the heart model.
- **Chapter 6** provides a sensitivity analysis to quantify the influence of model components on the deformation measures and introduces model modifications for a virtual HCM heart.
- **Chapter 7** describes an estimation method for identifying material properties based on a pressure-volume relation.
- **Chapter 8** provides a quantification of the influence of noise in the input data on a reconstructed dynamic active force field and delivers a method to localize ischemic regions.
- **Chapter 9** provides an outlook and conclusions.

State of the Art

Model generation workflow A model generation workflow provides the steps necessary to create a model suitable for in-silico simulations of the heart beat. The first step is the creation of a geometrical model. It can represent an idealized ventricle, e.g. a truncated ellipsoid [5]. The geometry can be derived from a cardiac atlas [6–8], a bi-ventricular [9] and bi-atrial statistical shape model [10], which are created based on human CT and MRI datasets. To obtain a personalized geometry, which accurately represents the heart anatomy, imaging modalities are employed (MRI, CT or US). These reveal the shape, size and location of the heart. The images are processed to obtain a finite element volumetric mesh. The creation of a patient-specific four chamber geometry was described in [11–17] and reviewed in [18]. Strocchi et al. [15] created 24 four-chamber models semi-automatically and made them publicly available[1] [15]. Neic et al. [16] and Fedele et al. [17] presented ways to speed-up the mesh generation process by offering automatable, high performance mesh manipulation tools. Jafari et al. [19] used a cubic-Hermite mesh for a four chamber model, which needed fewer elements compared to linear tetrahedral meshes. However, cubic-Hermite meshes cannot accurately capture the anatomical structures [12]. To avoid the burden of mesh generation, meshless models of the heart have been developed [20, 21]. However, they are not commonly used in cardiac mechanics yet due to the lack of techniques to correct instabilities near the boundary conditions [21].

The myocytes tend to align along their long axis to form bundles that are represented by fibers in the geometrical model. In a computational model, the fiber orientation determines the deformation of the tissue [22, 23] and strongly influences the stroke volume and the atrio-ventricular plane displacement [24].

[1] Available at `https://doi.org/10.5281/zenodo.3890034`

An ex vivo DT-MRI modality can acquire the orientation of the fibers [25, 26] to build an atlas and derive angles which approximate the fiber orinetation [2]. Recently, an in vivo DT-MRI on human hearts was performed [27]. However, it is too time consuming to be applied in a clinical routine and therefore, rule-based algorithms were developed to prescribe the fiber orientation in the ventricles [28–30] and in the atria [31–33]. The algorithm of Bayer et al. [28] was adapted by Steffen Schuler to eliminate a discontinuity of fibers in the free walls and to yield a fiber rotation that is approximately linear across the wall[2]. Nagler et al. [34, 35] developed an estimation method for the fiber orientation using sparsely acquired clinical DT-MRI images. To personalize the fiber orientation in the atria, Grandits et al. [36] used a neural network to estimate the fiber orientation from electroanatomical maps and Fastl et al. [37] estimated these by interpolating solutions of Laplace's equations.

The fiber angles in the ventricles are changing transmurally from the endocardium to the epicardium and different angles have been described: 60° and -60° [38], respectively; 80° and $-70°$ [30], respectively. Extreme values of the angles were measured as 90° on the endocardium to $-90°$ on the epicardium [38]. These angles are used to parametrize rule-based algorithms.

To constrain the motion of the heart and mimic the conditions under which the heart is embedded in the human body, boundary conditions are imposed on the geometrical model. Fritz et al. [39] imposed a Robin boundary condition on the whole heart model: they modelled the effect of the pericardium and the surrounding tissue on the myocardium by introducing a frictionless contact problem. Others [40–42] modelled the pericardial influence as a spring acting in normal direction to the epicardium. Strocchi et al. [43] varied the stiffness of the springs spatially that act on the ventricles to yield a more physiological behaviour of the ventricles. Furthermore, they imposed a spring condition on the right pulmonary veins and at the superior vena cava.

Additionally, Neumann boundary conditions have been applied on the endocardial surfaces of the chambers by including pressure acting in normal direction (to the triangles on the surfaces). The time course of the pressure can be either prescribed by a predefined curve [5] or calculated during the numerical simulation by a circulatory model coupled to the mechanical model [43–52].

To directly constrain the displacement of tissue, Dirichlet boundary conditions can be imposed on the nodes. In an idealized model of the LV, the base was fixated in all directions [5, 23]. In a bi-ventricular model, Peirlinck et al. [53] described the influence of the fixation of the base on the global functional behaviour of the ventricles. In a whole heart model, the terminal ring of the major vessels and the apex were fixed [39]. Alternatively, a Dirichlet boundary condition was enforced on the free ends of the mesh representing the pulmonary veins and vena cava, and at the bottom of the soft material attached to the apex [12, 13].

[2]Code available at `https://github.com/KIT-IBT/LDRB_Fibers`

During in vivo image acquisition, the blood pressure is not zero and therefore, the heart walls are stressed even in end-diastolic state. Since it is impossible to measure the stress in the heart walls, a stress-free state needs to be estimated to obtain the initial state for a numerical simulation. It is assumed that the stress-free state is the pressure-free state of the geometry, also called reference state or unloaded state. Iterative methods for the estimation of the reference state have been proposed [54–56] and further developed to improve their convergence [52, 57]. The methods compute the geometry configuration such that, when inflated with the predefined end-diastolic pressure, it equals the image based input geometry. Mostly, the value of the ventricular end-diastolic pressure for a particular heart is not available (an invasive measurement) and therefore, to perform the unloading procedure, population-based values are used: e.g. 8 mmHg [57], 9 mmHg [58] or 12 mmHg [59]. To avoid the application of the unloading method, Nasopoulou et al. [60] used a geometry created from MRI images corresponding to the minimum pressure in the heart cycle as an approximation of the pressure-free state.

Model validation and calibration Clinical data can be either applied to calibrate input parameters of cardiac heart models or as a measurable observation to compare and quantify the output of the model. Niederer et al. [18] provided a review on the creation and validation of a whole heart model on the way to a transition to industrial and clinical applications. Ways to incorporate clinical data into computation models to build 'the digital twin' of the patient are presented in [61]. Genet et al. [58] validated the computational model by calculating strain differences between MR imaging and the FE model. Pfaller et al. [40] compared the volume curves and the atrio-ventricular plane displacements from the numerical model and the one derived from motion MRI images. Pagani et al. [62] presented a data-model integration pipeline using clinical data. Recorded pressure values from the LV and the aorta have been applied to identify circulatory model parameters in a cohort of 17 left ventricular models [50]. Additionally, using MRI and an electrocardiogram, the anatomy and electrophysiological, mechanical and circulatory model components were personalized [63]. Baillargeon et al. [64] showed that the simulated pressure-volume relationship of four-chamber human heart models matched clinical observations. Lluch et al. [21] personalized a fully coupled model of cardiac electromechanics using minimally invasive in vivo pressure measurements and MRI data of the LV. They estimated the parameters of the electromechanics and hemodynamics models by fitting the simulated volumetric and displacement data to those obtained from MRI.

Sensitivity analysis Campos et al. [65] performed a sensitivity analysis considering uncertainties in wall thickness, in the material properties and fiber orientation based on a 17 American Heart Association (AHA) segments diagram [66]. In [67], they additionally incorporated uncertainties in active stress and the circulatory model to quantify their impact on the model prediction. Osnes et al. [68] studied the effect of uncertainties in material input parameters on cavity volume, the elongation and radius of the ventricle, wall thickness and the rotation. Niederer et al. [23] demonstrated the importance of model parameters and boundary conditions in a whole heart model. Pfaller et al. [40] compared different boundary

conditions regarding their influence on pumping of the heart. Additionally, they investigated the influence of pericardial stiffness on the deformation. Augustin et al. [69] quantified the impact of wall thickness and curvature on wall stress in patient-specific electromechanical models of the left atrium. The influence of the fiber orientation on stroke volume in the human LV was shown by Baron et al. [24].

Hypertrophic cardiomyopathy HCM is a relatively common inherited disorder, with a prevalence of 1:500, which develops in the absence of an identifiable cause [70, 71]. There are several phenotypes of HCM, depending on the localization and distribution of hypertrophy in the heart - asymmetric, symmetric/concentric, apical or mid-ventricular obstruction [72]. Despite normal LV ejection fraction, reduced myocardial function has been reported in HCM [73]. HCM results in an increased ratio of wall to lumen volume [70]. Besides this morphological modification, further abnormalities are underlying the HCM phenotype: fibrosis and myocardial cell disarray [70, 74, 75], increased passive stiffness [75] and decreased development of active force [76]. These abnormalities lead to an altered function of the heart, which can be assessed by US or MRI measurements (strain, strain rate and myocardial velocities) [70, 73, 77, 78]

Usyk et al. [79] developed a computational model of HCM mouse heart by incorporating fiber disarray in the model. The model showed similar septal systolic strains as the experimental measurements.

Estimation techniques Estimation techniques allow to identify quantities, which cannot be measured directly but can be determined based on measurable observations. In the literature, two classes of techniques for cardiac biomechanics are described. Methods of the first class estimate the input parameters of a specific model based on measurable observations to obtain a personalized model. The second class directly reconstructs the values of the quantity of interest based on the measurable observations, omitting the use of a model during the purely data-driven estimation process.

The reconstruction of the passive properties of the myocardium is performed by techniques from the first class, e.g. [60, 80–83]. A comparison of the parameters of the model proposed by Guccione et al. [84] was provided for fifteen studies [59] and shows the necessity of personalizing those parameters.

The active force developed in the myocardium can be reconstructed using techniques of both classes. Among others, Balaban et al. [80], Finsberg et al. [85] and Dabiri et al. [86] applied techniques of the first class. Otani et al. [87] reconstructed the active tension with techniques of the second class. Theoretically, the first class provides better comparability of the estimated parameters in case the same underlying model is used. Practically, each group applies a different active tension model, e.g. derived from calcium dynamics [86] or based on the degree of muscle fiber shortening [80]. When the active tension is estimated by a technique of the second class, it represents a direct measure of the myocardial function and is directly proportional to the contractile mechanical work [88].

Estimation of passive properties The passive behaviour of the tissue is modelled by a constitutive law and plays an important role in the deformation of the heart. There are several constitutive laws, which are broadly applied for the in-silico modelling of the cardiac function. However, finding values for the parameters of these models, which yield a realistic heart deformation, is an active field of research.
To characterize the passive behaviour of myocardial slabs, biaxial material tests have been employed [89, 90] and experimental strain measurements in biological tissue were conducted [91]. Martinova et al. [92] applied mechanical testing to characterise the passive properties in healthy and infarcted rat myocardium. However, these experimental techniques have the drawback of sectioning the tissue samples and destroying the tissue micro-structure [93]. Augenstein et al. [93] conducted isolated pig heart inflation experiments, measured the tissue kinetics with MRI tagging and determined the fiber orientation by ex vivo DT-MRI. These information were used to calibrate the passive behaviour of a finite element (FE) model and to identify the parameters of the constitutive law. A similar approach was developed by Walker et al. [94]: they used tagged MRI strain measurements and ex vivo fiber orientation measurements to estimate passive mechanical properties. Wang et al. [83] included invasive pressure recordings to calibrate a heart model. These studies were performed on animal hearts and therefore, the fiber orientation could be measured ex vivo. Today, this can be avoided by using a rule-based algorithm to generate the fiber orientation in the FE model [28]. However, further studies employed invasive pressure measurements to estimate the passive behaviour of the heart tissue. Lluch et al. [21] used minimally invasive in vivo pressure measurements and in vivo MRI data of the LV to estimate the passive parameters based on diastolic data of a canine heart. Balaban et al. [80, 95] used regional LV strains (US and MRI) and in vivo pressures measured during atrial systole to estimate heterogeneous passive properties in a model of human cardiac mechanic including myocardial infarction. Finsberg et al. [96] used pressure, volume and regional strains measured in patients with pulmonary arterial hypertension to calculate regional passive stiffness in a computational framework of the ventricles. Nasopoulou et al. [60] used diastolic pressure measurements in the LV to yield a unique identification of material parameters by a suitable choice of the cost function based on deformation and energetics analysis. Since invasive measurements are not applicable to obtain information for healthy human volunteers, estimation methods based on non-invasive measurements have been developed.
Finsberg et al. [97] fitted the material parameters of the ventricles to match the measured end-diastolic volume after the loading of the pressure-free geometry. They obtained distinct passive properties in the left and the right ventricle. Tagged MRI data which describes the tissue displacement information in three dimensions (3D) has been employed in estimation methods [81, 98, 99]. Passive properties of the tissue were estimated based on an empirical end-diastolic pressure-volume relation [58, 86], derived by Klotz et al. [100]. Palit et al. [101] identified ranges of material paramters by minimizing the distance between a simulated Klotz curve and the one proposed in [100]. Marx et al. [50] fitted one material parameter of the constitutive law applied in the LV, again based on the empirical Klotz relation [100]. Augustin et al. [63] and Marx et al. [57] also calibrated the parameters

based on the Klotz relation. However, they used one recorded pressure value to estimate a pressure-free configuration of the LV.

The parameters of the constitutive laws were coupled to reduce the dimension of the optimization process [57, 58, 81, 97, 99, 101].

Estimation of active force Finsberg et al. [85] and Balaban et al. [80] described an adjoint gradient-based method to estimate the active force field, which was applied to a cohort of heart failure patients [85].

Different levels of spatial resolution of the active tension have been estimated. Asner et al. [81] and Hu et al. [98] estimated one active tension value for the entire ventricle per time step. Dabiri et al. [86] estimated the maximal active tension for every ventricle segment out of 16 segments. Asner et al. [81] and Otani et al. [87] investigated the accuracy of their methods by adding noise with Gauss distribution of zero mean to the displacement data and to the fiber distribution in the tissue.

Different measures of deformation of the heart have been used as an input data: strain measurements in the AHA segments obtained by echocardiographic speckle tracking [80, 85], data from tagged MRI [81, 86, 98]. Such input data contains information about the twist and rotation of the heart muscle contrary to displacement data of the endocardial surface. Linte et al. [88] and Otani et al. [87] used a 3D displacement field of the myocardial volume.

PART I

FUNDAMENTALS

Chapter 2

Medical Fundamentals

This section is based on Hall et al. [102].

The human heart is a hollow organ which primary function is to pump blood through the body. It plays a crucial part in maintaining the blood flow in the cardiovascular system, as it simultaneously powers two different blood circulations. The blood flow in the smaller circulation is maintained by the right half of the heart and transports oxygen-depleted blood from the main circulatory system to the lungs. The oxygenated blood is then pumped back by the left heart to the rest of the body (the systemic circulation).

The heart consists of four chambers: two ventricles and two atria (Figure 2.1). The left part of the heart incorporates a left atrium (LA) and a left ventricle (LV), as it pumps blood in the vast systemic circulation, providing sufficient blood flow to all organs. The right half of the heart consists of right atrium (RA) and a right ventricle (RV), as the right heart pumps blood through the minor, pulmonary circulation. Longitudinally, the two heart compartments are separated by an interatrial and an interventricular septum. Within a compartment, the atria and ventricles are separated by fibrous valves. As the blood flows from an atrium to a ventricle or from a ventricle to an artery, it is pushed through a valve, which function is to ensure correct unidirectional blood flow through the heart. Thus, after the oxygen has been taken up by the organs, the blood returns to the right heart through the hollow veins, passes the tricuspid valve into the RV, where it is further propelled through the pulmonary valve into the pulmonary arteries. In the lungs, gases are exchanged and oxygenated blood is returned to the left atrium via the pulmonary veins. From the left atrium the blood is pressed through the mitral valve and enters the LV, where it is further pumped through the aortic valve into the systemic circulation.

Microscopically, the heart consists of multiple layers: inner endocardium, myocardium, outward epicardium and on top a pericardium layer. The endocardium is a very thin, single-cell coating of the heart inner surface and valves. The myocardium is a thick, muscular layer, which is accountable for the heart contraction and pump efficiency. The myocardium is constructed from a complex three-dimensional organisation of cardiomyocytes (heart muscle cells) layers in spiral/helical arrangement. The heart perfuses its own myocardium via the coronary arteries, occlusion of which leads to heart attack (myocardial infarction) with cardiac muscle scaring and heart failure. The epicardium is the most outward layer of

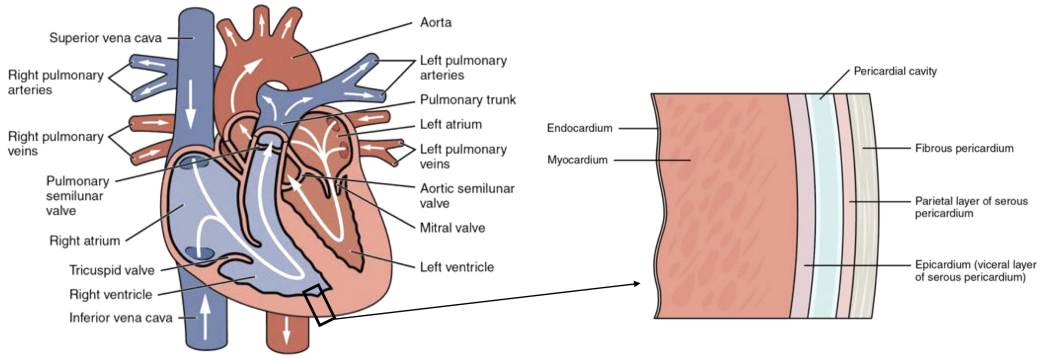

Figure 2.1: Anatomy of the heart and the direction of blood flow. The heart consists of several layers (endocardium, myocardium and pericardium). Adapted from [103], Figure 19-4 and 19-5, published under the Creative Commons Attribution 4.0 International (CC BY 4.0) License.

the heart and together with a fibrous external layer it builds the pericard. In the pericardial space (between the epicardium and parietal part of the pericard) a small amount of pericardial fluid is hold to minimize friction during a heart beat. Furthermore, the pericard protects the heart and holds it in place.

The continuous contractions of the heart muscle (cardiac rhythmicity) is ensured by a self-excitation pacemaking system. Electrical impulses are regularly generated in the sinus node, placed in the RA. These changes in voltage across the cell membrane are also called action potentials. Every electrical signal is rapidly and coordinately conducted through the tissue, to initiate a synchronous contraction of the heart. The heart conductive system is organised in such a way that the current propagation is delayed at the atrioventricular (AV) node, which is the only electrical connection between the atria and the ventricles. This delay of around 130 ms allows the atria to contract first and sufficiently empty their blood volume in the ventricles, before the ventricular contraction begins. The electrical impulse propagates further through a fast conducting system in the ventricles (bundle of His and the Purkinje fibres), spreads in the entire ventricular muscle mass (in about 60 ms) and reaches every cardiomyocyte in the myocardium, where an action potential is transformed into a muscle contraction. This translation is also called electromechanical coupling. Consequently, a single depolarization wave causes a full heart beat with two consecutive components – initial atrial contraction followed by the ventricular contraction.

Each cardiomyocyte contains myofilament bundles, or myofibrils, which are the fundamental contracting units. Myofibrils are further organized by repeating components, i.e. sarcomere. A sarcomere is a complex structure with multiple myosin- and actin-filaments, which can glide upon each other and thus, shorten the sarcomere. This sarcomere shrinkage is an active process, occurring only under the presence of high Ca^{2+}-concentration and with consumption of energetic molecules (ATP). Each sarcomere has a length of approximately $2\,\mu$m at rest and can contract up to $1.6\,\mu$m, which is 80 % of its initial length. Another substantial organelle within a cardiomyocyte is the sarcoplasmatic reticulum (SR). It forms a complex network of tubes around the myofibrils and is an important reservoir for Ca^{2+}-ions.

When an action potential depolarizes a cardiomyocyte, an immense amount of Ca^{2+}-ions enter inside the cell and induces further Ca^{2+}-release from the SR – so called calcium-induced calcium release. Intracellular Ca^{2+}-concentration increases dramatically, about 100 fold, and now the conditions are met for the initiation of an actin-myosin filament interaction and thus, induce mechanical contraction of the cardiomyocytes. Next, Ca^{2+}-ions are actively (under ATP consumption) pumped back into the SR and the interaction between the myosin and actin is ceased. When the myofibrils contract, a force (tension) is developed, which leads to reduction of ventricular volume and thus, blood is pumped out.

Particularly interesting is the contraction in the LV, as it has to maintain strong blood flow within the extensive systemic circulation. The cardiomyocytes align along their longitudinal direction and form fiber layers that are usually described as helical. In the LV specially, the epicardial layer spirals in a leftward direction, and the endocardial layer spirals in the opposite direction. The shortening of the cardiomyocytes occurs along the fiber direction and causes the LV to contract in a twisting motion: the apex of the heart rotates in clockwise direction and the base of the LV rotates in counter-clockwise direction. Thus, this strong wriggling of the LV provides a substantial force to propel the ventricular blood volume through the aortic valve into the systemic circulation.

The cardiac cycle can be divided into two phases. On the one hand, systole, in which blood is pumped out of the ventricles into the circulatory system, and on the other hand, diastole, in which the heart fills with blood. Systole and diastole are each subdivided into two further phases, resulting in a total of four phases of heart action (two phases during a systole and two phases during a diastole). In the first phase (tension phase), while valves are closed, the ventricle contracts, but its volume remains constant – isovolumetric contraction. Thus, the pressure rises abruptly, causing the aortic and pulmonary valves to open. In brief, in this initial phase, the cardiac muscle tension increases, but no shortening in the fibers occurs. Only after sufficient pressure (about 80 mmHg in the LV and 8 mmHg in the RV) is reached, the aortic and pulmonary valves open, and the second phase of the systole begins: the ejection of blood into the arteries – ejection phase. Further contraction of the myocardium (starting at the distal septum and the apex of the heart) thickens the ventricles walls. Thus, the internal diameter of the ventricles is reduced, while the pressure in the ventricles increases (reaching up to 120 mmHg), resulting in ejection of substantial blood volume (about 70 ml) out of the ventricle. Subsequently, the pressure in the ventricles slowly drops below the pressure in the aorta or the pulmonary artery, which causes the closure of the corresponding aortic and pulmonary valve. Now, the first relaxation phase of the diastole can begin – the isovolumetric relaxation. All valves are closed and the myocard relaxes, causing the pressure to rapidly decrease (to about 10 mmHg in the LV), while the volume remains unchanged. The ventricular pressure falls below the pressure in the atria, and thus, AV valves open to begin the second phase of the diastole – the filling phase. The blood flows rapidly into the ventricles, from the veins through the atria. During the last third of the diastole, the atria contract briefly (atrial kick) to provide additional inflow of blood into the ventricles (about 20 % of end diastolic ventricular volume). The pressure in the ventricles exceeds again the

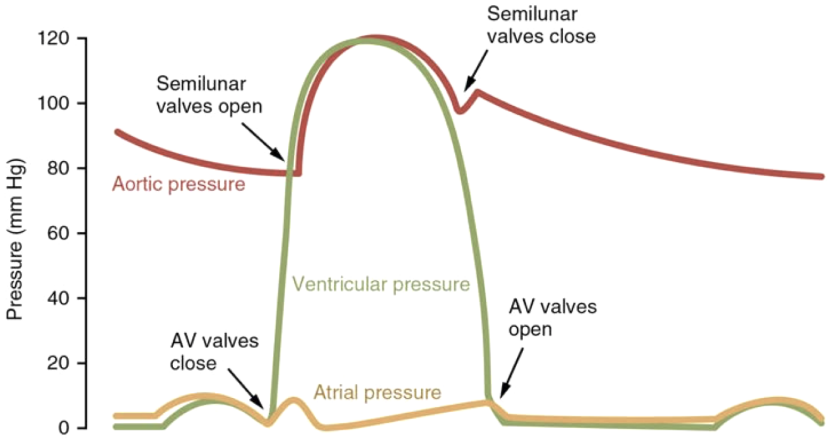

Figure 2.2: Events of the cardiac cycle for LV function: LA pressure, LV pressure, aortic pressure, ventricular volume. Adapted from [103], Figure 19-29, published under the Creative Commons Attribution 4.0 International (CC BY 4.0) License.

pressure in the atria, closing the AV valves and allowing the tension phase of the systole to begin again.

Figure 2.2 shows the events during the cardiac cycle for the LV. The relation between the pressure and the volume of the LV is called PV loop (see [102], Figure 9-11). The stroke volume (SV) is the volume difference between the end-diastole (ED) and end-systole (ES). The external work (EW) of the LV is the shaded area of the PV loop. EW becomes higher when the heart pumps larger quantities of blood or produces larger aortic pressure.

Although the heart can generate excitation independently thanks to its pacemaker cells, it must adapt its pump power constantly to the changing requirements during daily life activities. A short-term intrinsic regulation of the heart pumping is achieved by the Frank-Starling mechanism. Its purpose is the SV of both ventricles to remain constant, despite pressure and volume fluctuations between heart beats. Preload can be defined as the initial stretching of the myocytes and it is related to the sarcomere length. Because sarcomere length cannot be determined in the intact heart, other indices of preload are used such as ventricular ED volume or pressure are used. Whereas the mean blood pressure in the aorta or pulmonary artery and the associated ejection resistance of the left and right ventricles, respectively, are characterised as afterload. Employing the Frank-Starling mechanism, the heart adapts to increasing preload (higher volumes of inflow blood): the more the heart muscle is stretched during a filling, the greater is the quantity of blood ejected into the aorta. This prior stretching causes the sarcomeres to contract with increased force, since an optimal degree of overlap between actin and myosin filaments is reached. Thus, the SV is increased for a single heart cycle. In the event of an afterload rise, the initial SV will be decreased due to the elevated pressure. During the next heart cycle the SV will be increased, leading to a high preload situation. In the subsequent heart cycle, the SV and the pressure will normalize again. In both cases (preload and afterload increase), the Frank-Starling-mechanism will lead to short-term enhancement of cardiac work. Possible causes of the Frank-Starling mechanism

are improved overlap of actin and myosin filaments, as well as increased sensitivity of the contractile apparatus to calcium.

2.1 Cardiac Disorders

From the countless cardiac disorders, in this work, two were modeled and included in numerical simulations: myocardial infarction (MI) and hypertrophic cardiomyopathy (HCM).

Ischemic heart disease is the primary cause of death worldwide. It manifests as MI and ischemic cardiomyopathy. MI results from a coronary artery blockage, typically by thrombus formation from a disrupted atherosclerotic plaque in a heart artery. The corresponding muscle area has then restricted blood flow and thus, cannot receive sufficient oxygen and nutrients to sustain the muscle function, leading to tissue degeneration. This process is named infarction. Post-infarction consequences are cardiogenic shock, decreased cardiac output (i.e. heart failure), heart arrhythmia, congestion in the pulmonary vessels and occasionally, rupture of the heart (due to wall thinning), which leads to death.

In the infarction area some cardiomyocytes are not functioning and others contract with less force than prior to the infarction. Therefore, the EW of an infarcted heart is significantly reduced. Additionally, the contraction force is partly dissipated, since the area of non-functional cardiac muscle is bulging outwards during the systole. This causes further stretch in the infarcted area and leads to thinning of the wall in this area, i.e. ventricular aneurysm. When the area of infarction is large, the cells in the middle of the area die and over time are replaced by immobile fibrous tissue. The surrounding tissue may gradually hypertrophy, to insufficiently account for the stiff fibrous tissue. Consequently, due to the scaring tissue dilatation, the ES ventricular volume may increase, but the total EW is reduced, resulting in a significantly decreased SV and enhanced cardiac tension.

One method the access the severity of the infarction is with cardiac imaging. Cardiac magnetic resonance is considered as the gold standard for myocardial viability assessment, since it can demonstrate changes in regional function as well as myocardial perfusion, tissue composition and cellular death. It is mainly achieved by utilizing a late gadolinium enhancement (LGE) method. A contrast agent containing gadolinium is moving in and out of the imaged tissue and thus, can unveil to what extend the region of interest is perfused. Consequently, this method allows an accurate measurement of infarct size and location.

HCM is one of the most common inheritable heart disorders, with an prevalence of more than 1 in 500 people [2], and it is usually based on sarcomere protein gene defects. The most frequent symptoms of HCM include exercise intolerance, angina, dyspnea, dizziness, syncope, but it can also present as heart failure or even sudden cardiac death (leading cause of death in adolescents and young athletes). One of the most common secondary causes of LV hypertrophy is afterload increase, a pressure overload due to obstruction of the aortic valve, aortic stenosis, or chronic hypertension.

Myocardial hypertrophy describes the process of continuous ventricular wall thickening through enlargement of the myocytes, which leads to restriction of ventricular blood volume.

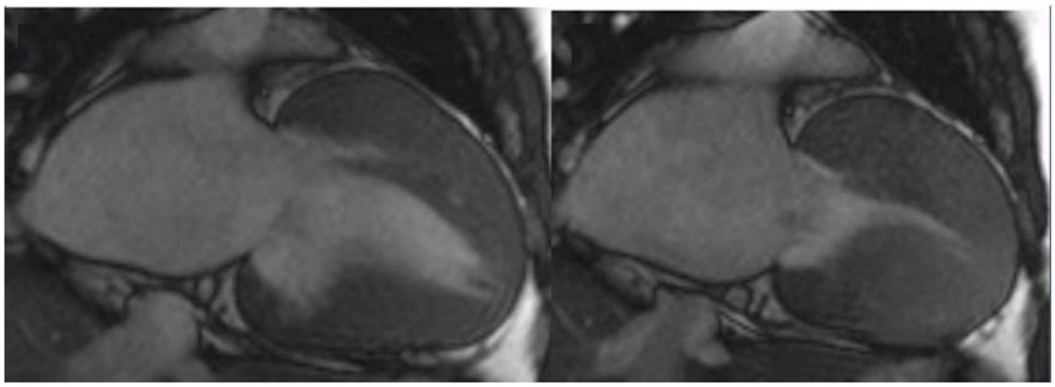

Figure 2.3: Symmetric HCM: hypertrophy of the LV in a long axis view at diastole (left) and systole (right). Adapted from [72], Figure 3, published under the Creative Commons Attribution License.

There are several classes of HCM, depending on the localization and distribution of hypertrophy in the heart: asymmetric, symmetric/concentric, apical or mid-ventricular obstruction in the LV, as well as RV hypertrophy. In Figure 2.3, a long axis view of a symmetric HCM is shown. Besides morphological modification, further abnormalities are underlying the HCM phenotype.

The HCM heart undergoes maladaptive processes, which lead to myocardial fibrosis and cell disarray. The pathological myocardial reformation might have evolved years before the onset of symptoms and therefore, HCM has a long asymptomatic period. Gradually the ventricular walls thicken and reduce the ES ventricular volume, thus, significantly diminishing the SV. As a compensation, the heart rate speeds up, further promoting hypertrophy and potentially inducing symptoms. Additionally, HCM causes dysfunctional diastolic relaxation, also known as diastolic stiffness. Here the intracellular calcium increase and the interstitial fibrosis play a crucial role. Ultimately, in the HCM heart, the myocardial stiffness is considerably increased and the maximal active force developed in HCM myocytes is markedly lower compared to healthy myocytes.

In the last decade, the ability to diagnose HCM has improved eminently [70]. Diagnosis is often made using echocardiographic assessment of LV hypertrophy, systolic and diastolic function, and parameters derived from tissue imaging: tissue Doppler, strain, strain rate. MRI also has a diagnostic role by determining the extent and location of LV hypertrophy. MRI quantifies the heart motion and function by cine imaging, allowing for calculating the LV wall thickness and wall thickening during systole. Furthermore, tissue phase mapping and feature tracking provide LV radial, circumferential and long-axis myocardial velocity time courses, as well as global and segmental systolic and diastolic peak velocities [73]. LGE is sensitive to find fibrotic tissue and can be useful to asses the severity of the HCM. With diffusion tensor magnetic resonance imaging (DT-MRI), the cell disarray is measured to quantify the directionality of diffusion of water along cardiac muscle fibers [74]. Imaging modalities allow the precise assessment of cardiac structure and function of the HCM heart.

Chapter 3

Mathematical Fundamentals

3.1 Continuum Mechanics

Continuum mechanics is a field of mechanics and deals with the mechanical behaviour of materials modeled as a continuous mass rather than as discrete particles (e.g. molecular or crystal structures). Fundamental physical laws such as the conservation laws are applied to continuous models to obtain differential equations describing their behaviour. In the following, some basic concepts are briefly described based on the book of Belytschko et al. [104] and the thesis of Fritz [4].

Deformation and motion A body is in an initial (undeformed) state at time point $t = 0$ as shown in Figure 3.1 and denoted by Ω_0 and its boundary by Γ_0. The domain of the current configuration of the body at time t is denoted by Ω and its boundary by Γ.

The position vector of a material point in the the reference configuration is given by $\mathbf{X}$, where $\mathbf{X} = X_i \mathbf{e_i}$ and $\mathbf{e_i}$ are the unit base vectors of a rectangular Cartesian coordinate system. The variable $\mathbf{X}$ does not change with time and is called *Lagrangian coordinates*. The spatial

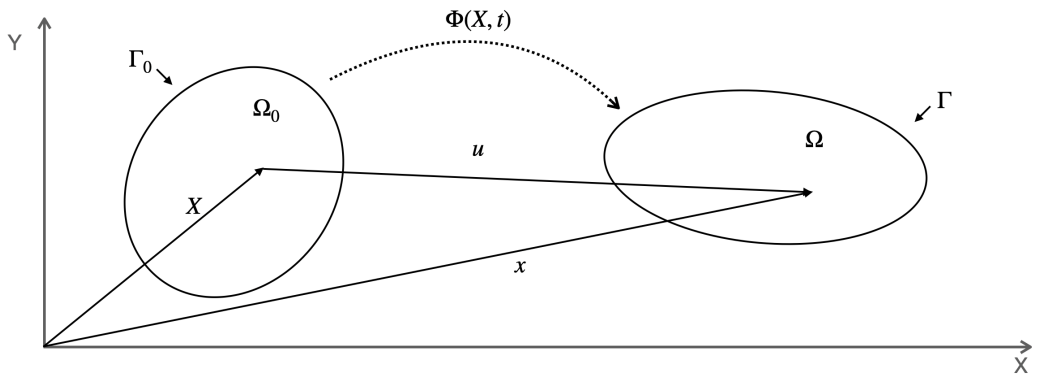

Figure 3.1: Undeformed (initial) state and deformed (current) configuration of a body.

position of a point in the current configuration is given by $\mathbf{x} = x_i \mathbf{e_i}$, which is called *Eulerian coordinates*.

The motion of the body is described by $\mathbf{x} = \phi(\mathbf{X},t)$. The function $\phi(\mathbf{X},t)$ maps the reference configuration into the current configuration. The displacement of a material point is the difference between its current position and its original position $\mathbf{u}(\mathbf{X},t) = \phi(\mathbf{X},t) - \mathbf{X}$. The velocity is the rate of change of the position vector

$$\dot{\mathbf{u}} = \mathbf{v}(\mathbf{X},t) = \frac{d\phi(\mathbf{X},t)}{dt}. \tag{3.1}$$

The acceleration is the rate of change of the velocity and its denoted by $\mathbf{a}(\mathbf{X},t)$. The deformation gradient is the Jacobian matrix of the motion and its defined by

$$\mathbf{F} = \frac{d\phi(\mathbf{X},t)}{d\mathbf{X}} = \frac{dx}{d\mathbf{X}}. \tag{3.2}$$

The Jacobian determinant is $J = \det(\mathbf{F})$ and it can be used to relate integrals in the current and undeformed configuration. Furthermore, it measures the volume change and can be incorporated into incompressibility penalty terms.

The polar decomposition theorem states that every deformation gradient tensor $\mathbf{F}$ can be multiplicatively decomposed into a product of an orthogonal matrix $\mathbf{R}$ (rotation matrix) and a symmetric tensor $\mathbf{U}$ (right stretch tensor): $\mathbf{F} = \mathbf{RU}$. The Cauchy-Green tensor $\mathbf{C}$ is given by

$$\mathbf{C} = \mathbf{F}^T\mathbf{F} = \mathbf{U}^T\mathbf{R}^T\mathbf{RU} = \mathbf{U}^T\mathbf{U} \tag{3.3}$$

and therefore, it does not change under simple rotation (rotational invariant). Applied to the elastomechanics of the heart, the deformation gradient $\mathbf{F}$ can be used to calculate the change in the fiber length. If f_0 is the fiber orientation and $\|f_0\| = 1$ in the initial configuration, the fiber in the current configuration is given by $f_t = \mathbf{F}f_0$ and its relative change in length (stretch) λ_f is

$$\lambda_f = \frac{\|f_t\|_2}{\|f_0\|_2} = (\mathbf{F}f)^T(\mathbf{F}f) = f^T\mathbf{C}f. \tag{3.4}$$

For λ_f values higher then one, the fiber is stretched and for values lower then one, it is compressed.

Strain measure A strain measure must vanish for any rigid body motion (rotation and translation) and should increase as the deformation increases. There are several different measures of strain, one of which is the Green-Strain tensor $\mathbf{E}$ and it is defined by

$$\mathbf{E} = \frac{1}{2}(\mathbf{F}^T\mathbf{F} - \mathbf{I}) = \frac{1}{2}(\mathbf{C} - \mathbf{I}), \tag{3.5}$$

where $\mathbf{I}$ is the identity matrix. The Green-Strain tensor $\mathbf{E}$ measures the difference of the square of the length of an infinitesimal segment in the deformed configuration.

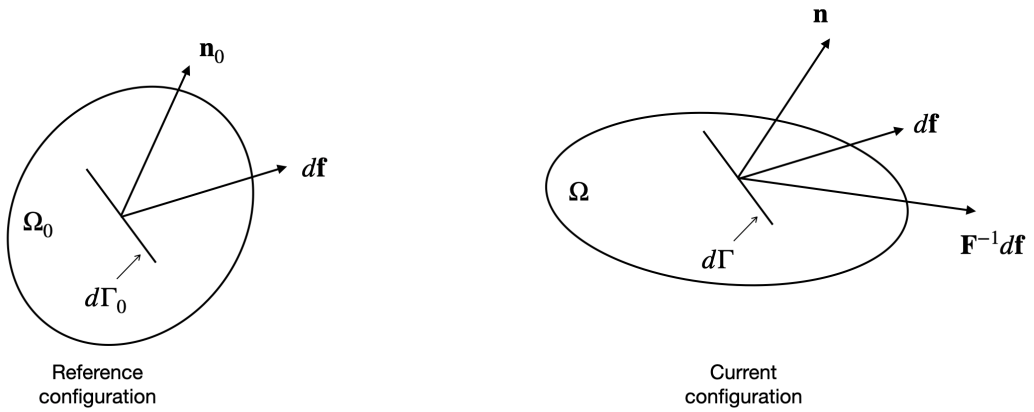

Figure 3.2: Definition of stress measures.

Stress measures While strain is a measure of deformation, stress describes the internal forces acting in infinitesimal volume of the body. The definition of stress involves the traction $\mathbf{t}$ (force per unit area) and the normal of a tangential surface in either the initial (denoted by $\mathbf{n}_0$) or the current configuration (denoted by $\mathbf{n}$) (Figure 3.2).

The Cauchy stress tensor σ (physical/true stress) is defined by Cauchy's law:

$$\mathbf{n} \cdot \sigma d\Gamma = \mathbf{t} d\Gamma. \tag{3.6}$$

The first Piola-Kirchhoff (1PK) stress tensor (nominal stress) $\mathbf{P}$ is the counterpart of Cauchy's law in the initial configuration:

$$\mathbf{n}_0 \cdot \mathbf{P} d\Gamma = \mathbf{t}_0 d\Gamma_0. \tag{3.7}$$

The second Piola-Kirchhoff (2PK) stress tensor $\mathbf{S}$ is defined by

$$\mathbf{n}_0 \cdot \mathbf{S} d\Gamma = \mathbf{F}^{-1} \mathbf{t}_0 d\Gamma_0. \tag{3.8}$$

The Cauchy stress tensor and the 2PK stress tensor are symmetric tensors. The different stress tensors are interrelated and can be transformed to each other [104], p. 103.

Conservation equations The conservation equations, also known as the balance laws, are one group of fundamental equations of continuum mechanics: e.g. conservation of mass, linear momentum, energy and angular momentum. These equations must be satisfied by physical systems. In the numerical solver used in this work, the *linear momentum conservation* was employed, which is equivalent to Newton's second law of motion:

$$\hat{\mathbf{F}} = m\mathbf{a}, \tag{3.9}$$

where the total force $\hat{\mathbf{F}}$ is the sum of all forces acting on the body with mass m and acceleration $\mathbf{a}(t)$. For an arbitrary subdomain of the body with mass density ρ, Newton's second law can be rewritten to

$$\int_\Omega \rho \mathbf{a}(\mathbf{x},t) d\Omega = \int_\Gamma \mathbf{t}(\mathbf{x},t) d\Gamma + \int_\Omega \rho \mathbf{b}(\mathbf{x},t) d\Omega, \tag{3.10}$$

where Γ is the boundary of the domain Ω, $\mathbf{t}$ is the surface traction, $\mathbf{b}$ is the body force per unit mass.

If loads are applied slowly, the inertial forces are very small and can be neglected. In this case, the acceleration in Equation 3.10 disappears and the *equilibrium equation* is obtained.

3.2 Numerical Discretization

In solid mechanics, Lagrangian meshes are mostly used, since they can handle boundary conditions easier than the Eulerian meshes. They follow material points, so that history-dependent materials can be treated easily. In the *total Lagrangian formulation*, the derivatives and integrals are taken with respect to the Lagrangian (material) coordinates $\mathbf{X}$. All formulations (updated Lagrangian, total Lagrangian and Eulerian) can be transformed to each other.

Spatial discretization On the integral relation described in Equation 3.10, the Gauss theorem is applied, which relates a volume integral to a surface integral. The balance of linear momentum is obtained as a differential equation in the total Lagrangian formulation [104] p.196:

$$\rho_0 \ddot{u}_i - \frac{\partial P_{ji}}{\partial X_j} - \rho_0 b_i = 0, \tag{3.11}$$

where $\ddot{\mathbf{u}} = \mathbf{a}$, $\mathbf{P}$ is the nominal stress and the Einstein summation notation is used. The aim is to solve this equation to find the value of the displacement $\mathbf{u}$.

The weak form is developed from the strong form Equation 3.11 by the principle of virtual work [104], p. 196. Equation 3.11 is multiplied by trial (test) functions and integrated over the initial domain Ω_0, the derivative product rule and the Gauss theorem are applied to obtain the weak form of this equation ([104] p. 197).

For the spatial discretization, the Finite Element Method (FEM) is applied. The computational domain is divided in a finite number of elements, which are described by nodes and their connectivity. There are many types of elements, in this work, tetrahedra/triangles were used. On each element, a shape function is defined, which interpolates quantities from the nodes into the inside of the elements. In this work, linear volume elements (T4), quadratic volume elements (T10) and linear surface elements (T3) were used. With a shape function N_I (linear/quadratic), the semidiscretization of the weak form in matrix notation is obtained:

$$\mathbf{M}\ddot{\mathbf{u}} + \mathbf{C}\dot{\mathbf{u}} + \mathbf{f}^{\text{int}}(\mathbf{u},t) + \mathbf{f}^{\text{ext}}(\mathbf{u},t) = 0, \tag{3.12}$$

where $\mathbf{M}$ is the mass matrix with

$$M_{IJ} = \int_{\Omega_0} \rho_0 N_I N_J d\Omega_0, \tag{3.13}$$

$\mathbf{f}^{\text{int}}$ are the internal forces

$$f_{iI}^{\text{int}} = \int_{\Omega_0} \frac{\partial N_I}{\partial X_j} P_{ji} d\Omega_0, \tag{3.14}$$

and $\mathbf{f}^{\text{ext}}$ are the external forces

$$f_{iI}^{\text{ext}} = -\int_{\Omega_0} N_I \rho_0 b_i d\Omega_0 - \int_{\Gamma_{t_i}^0} N_I t_i^0 d\Gamma_0. \tag{3.15}$$

The damping term $\mathbf{C}\dot{\mathbf{u}}$ was added to the linear momentum equation. In the numerical framework, the Rayleigh damping term was available

$$\mathbf{C} = \alpha_1 \mathbf{M} + \alpha_2 \nabla \mathbf{f}^{\text{int}}, \tag{3.16}$$

where $\nabla \mathbf{f}^{\text{int}}$ is called the tangent stiffness matrix (Jacobian matrix of the internal nodal forces).
For the equilibrium equation, Equation 3.12 simplifies to

$$\mathbf{f}^{\text{int}}(\mathbf{u},t) + \mathbf{f}^{\text{ext}}(\mathbf{u},t) = 0. \tag{3.17}$$

Equation 3.17 can be directly solved by the Newton method. However, for solving Equation 3.12, a time integration scheme is required to resolve the time derivatives.

Temporal discretization The simulation framework uses the implicit Newmark-Beta scheme. The initial value of the displacement is $\mathbf{u}^0 = \mathbf{u}(t = t^0)$, of the velocity $\mathbf{v}^0 = \mathbf{v}(t = t^0)$ and the acceleration $\mathbf{a}^0 = \mathbf{a}(t = t^0)$. For each time step t^{n+1} and time step size Δt, the update of the acceleration is given by

$$\mathbf{a}^{\mathbf{n+1}} = \frac{1}{\beta \Delta t^2}(\mathbf{u}^{\mathbf{n+1}} - \mathbf{u}^{\mathbf{n}} + \Delta t \mathbf{v}^{\mathbf{n}} + 0.5\Delta t^2(1-2\beta)\mathbf{a}^{\mathbf{n}}). \tag{3.18}$$

And the update of the acceleration is given by

$$\mathbf{v}^{\mathbf{n+1}} = \mathbf{v}^{\mathbf{n}} + (1-\gamma)\Delta t \mathbf{a}^{\mathbf{n}} + \gamma \Delta t \mathbf{a}^{\mathbf{n+1}}. \tag{3.19}$$

The parameters β and γ can be chosen to yield an unconditionally stable time integration. The latter two relations are inserted in Equation 3.12 to obtain a set of non-linear algebraic equations, which are iteratively solved by the Newton method to obtain the displacement $\mathbf{u}^{\mathbf{n+1}}$

$$\mathbf{M}\mathbf{a}^{\mathbf{n+1}} + \mathbf{C}\mathbf{v}^{\mathbf{n+1}} + \mathbf{f}^{\text{int}}(\mathbf{u}^{\mathbf{n+1}}, t^{n+1}) + \mathbf{f}^{\text{ext}}(\mathbf{u}^{\mathbf{n+1}}, t^{n+1}) = 0. \tag{3.20}$$

The Jacobian matrix $\mathbf{A}$ was provided by

$$\mathbf{A} = \frac{1}{\beta \Delta t^2}\mathbf{M} + \frac{\gamma}{\beta \Delta t}\mathbf{C} + \mathbf{K}, \tag{3.21}$$

where the stiffness matrix $\mathbf{K}$ is equal to the sum of the tangent stiffness matrix and the load stiffness matrix (Jacobian matrix of the external nodal forces) and $\mathbf{C}$ is the Rayleigh damping matrix.

3.3 The Mechanical Solver

To calculate cardiac deformation, the mechanical solver *CardioMechanics* [4] was employed. It has been developed in C++ and makes use of the PETSc library for parallel matrix vector operations and for solving the systems of equations [4]. Two solvers were available: the static solver, which determines the deformation by solving the equilibrium equation for every time step and the dynamic solver, which uses the Newmark-Beta time integration and takes into account mass inertia and damping. Additionally to the displacement, it computes velocity and acceleration vector fields [4]. A schematic description of the mechanical solver is provided in the thesis of Fritz [4], Figure 9.1.

CardioMechanics was previously verified in a benchmark using three examples including an uniaxial stress test, a pressure application and an active stress application on an ellipsoid geometry [4, 5]. The balance of linear momentum equation ensures that all forces are in balance at all times during the heart beat. External forces arise outside the myocardium, internal forces arise inside the myocardium. To calculate the external forces, a circulatory model and a pericardial model was included. The internal forces are calculated by the combination of passive and active force models. All together, the interplay of those forces delivers a deformation field, one three dimensional displacement vector for each node of the computational mesh for each time step of the simulation.

Force Models

Passive force models The passive internal forces arise from the constitutive law, which relates the stress and the strain of the tissue. Due to the microstructure of the heart tissue, it has an anisotropic behaviour, i.e. the stress depends on the direction of deformation. The heart tissue is modelled by an incompressible hyperelastic material law. In this case, the stress depends only on the current state of deformation and has no history. It can be derived from a potential describing the deformation energy, called a strain energy function $W(\mathbf{E})$

$$\mathbf{S} = \frac{dW}{d\mathbf{E}}, \tag{3.22}$$

where $\mathbf{E}$ is the Green-Strain tensor.

In this work, two constitutive models were used: the model of Guccione et al. [105] was applied for the contractile tissue and the Mooney-Rivlin model [106] was applied for the non-contractile tissue, except the pericardium and the adipose tissue. The Mooney-Rivlin model is a hyperelastic model developed for a large deformation for rubber. It is incompressible and initially isotropic. Its strain energy function is

$$W = C_1(I_1 - 3) + C_2(I_2 - 3), \tag{3.23}$$

where C_1 and C_2 are the model parameters and I_1 and I_2 are the first and second invariant of the Green-Strain tensor.

The model of Guccione et al. [105] describes a hyperelastic transversely isotropic material by the following strain energy function

$$\begin{aligned} W &= \frac{C}{2}\left(e^{Q}-1\right)+\frac{K}{2}\left(\det(\mathbf{F})-1\right)^{2}, \\ Q &= b_f E_{11}^2 + b_t\left(E_{22}^2+E_{33}^2+E_{23}^2+E_{32}^2\right)+b_{ft}\left(E_{12}^2+E_{21}^2+E_{13}^2+E_{31}^2\right), \end{aligned} \tag{3.24}$$

where C, b_f, b_t and b_{ft} are the parameters of the Guccione model, E_{ij} $(i,j \in [1,2,3])$ are elements of the Green-Strain tensor, $\det(\mathbf{F})$ is the determinant of the deformation tensor and K scales the incompressibility term, which penalizes volume change of the tissue.

Active force model The active force (tension/stress) model delivers the force acting along the fiber direction, which leads to fiber shortening and therefore, to the contraction of the tissue. In this work, the active force was described by a predefined curve, called *double-Hill* (DH), as described by Stergiopulos et al. [107]

$$e(t) = \frac{1}{k}\underbrace{\left(\frac{g_c}{1+g_c}\right)}_{H1}\underbrace{\left(\frac{1}{1+g_r}\right)}_{H2}, \tag{3.25}$$

with $g_c = \left(\frac{f'}{\tau_c}\right)^{m_c}$ and $g_r = \left(\frac{f'}{\tau_r}\right)^{m_r}$, $t' = \mathrm{mod}(t-t_0, T)$ and $k = \max(ke(t))$. The construction of the DH curve is shown in Figure 4.26 in [108]. The parameters τ_c, τ_r, m_c, m_r, the onset time t_0 and the period duration T were set as in Table 4.9, [108] and were used for the atria and the ventricles. The normalized curve was scaled by a parameter $T_{\max}$ which determines the maximal active force to obtain the active force driver function

$$T_k(t) = T_{\max} e(t). \tag{3.26}$$

The ventricles were simultaneously activated at 150 ms and the atria were also simultaneously activated at 0 ms.

Circulatory model The circulatory model provides a pressure-volume relation in the heart and delivers the pressure values, which are acting on the endocardial surfaces of the four chambers [46]. A lumped element model of the closed loop human circulatory system was used in this work. Systemic and pulmonary circulations were each represented by a three-element Windkessel model and the model was strongly coupled to the finite element model. Further information can be found in Schuler et al. [46, 108].

Pericardial model The pericardial model represents the pericardial sac, in which the heart is embedded, and the surrounding tissue. The interaction between the pericardial model and the heart is modeled as a frictionless contact problem [39]. The inner surface of the pericardium and the outer surface of the heart are in permanent contact and can slide along each other. The distance between these surfaces results in a contact force acting on the nodes on both surfaces. The pericardial model limits the motion of the heart by reducing the myocardial radial contraction and increasing the atrioventricular plane displacement. Further information can be found in Fritz et al. [4, 39].

PART II

PROJECTS

Chapter 4

Model Creation Workflow for Cardiac Simulations

A workflow for the creation of a human heart model is presented based on magnetic resonance imaging (MRI) data acquired on the whole heart. The workflow creates:

1. volumetric tetrahedral elements, representing myocardial tissue, valves, adipose tissue, inflow (veins) and outflow (aorta and pulmonary artery) vessels, pericardial tissue;
2. surface triangular elements, representing the boundaries of the volume: endocardial and epicardial surface, inner pericardial surface, a surface enclosing both the myocardial and adipose tissue;
3. subdivision of the elements in material classes for which elastomechanical properties can be assigned;
4. local coordinate system (one for each quadrature point in the volume mesh), which represents the fiber, sheet and sheet-normal orientation as a 3×3 matrix;
5. Dirichlet boundary condition: the nodes on the outer surface of the pericardium and the free ends of the vessels are fixated in all directions;
6. a pressure-free and pressure-loaded configuration.

Figure 4.1 provides an overview of the workflow. The steps visualized in the green and blue squares (Figure 4.1) are necessary for cardiac simulations with CardioMechanics with activated plug-ins. In particular, the pericardium and the adipose tissue (green square in Figure 4.1) are necessary for the sliding boundary condition in a four chamber simulation. The pressure-free and pressure-loaded state (blue square in Figure 4.1) are necessary for a simulation, which includes the circulatory model.

The presented workflow is mostly based on open source and in-house (IBT) tools. To present the workflow, the steps were executed for one particular heart, called in the following *geo20*. This workflow is based on preliminary works executed by Lukas Baron and presented in [109].

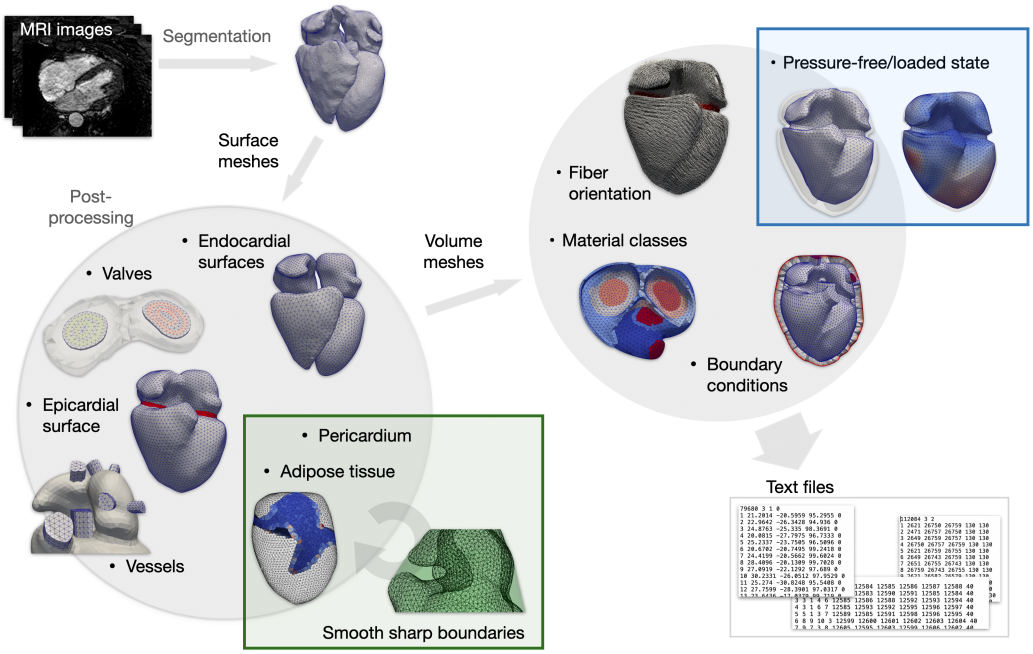

Figure 4.1: A schematic representation of the workflow for the creation of a heart model from imaging data.

4.1 Methods

4.1.1 From MRI Images to a Volumetric Mesh

MRI data set The heart morphology is captured by a 3D whole heart MR study. The MR images (grey-scale DICOM format) were taken from a healthy volunteer with a 1.5 Tesla MR tomography system (Ingenia CX, Philips Medical Systems) at the University Hospital in Heidelberg (Figure 4.2). The voxel spacing was $0.62 \times 0.62 \times 0.8$ mm, the image dimension was $560 \times 560 \times 160$ voxels and the trigger time was 560 ms. The images were taken during the diastasis (middle stage of diastole). The mean heart rate of the volunteer was 77 bpm. The volunteer gave informed consent and the study was approved by the institutional review board.

Surface segmentation The endocardial surface of the four chambers, the epicardial surface of the left ventricle (LV) and the vessels were automatically segmented with the Philips IntelliSpace Portal (Figure 4.3) and exported as .stl files. It was the only tool used in this workflow, which is neither open source nor an in-house tool, but purchased from the University Hospital in Heidelberg.

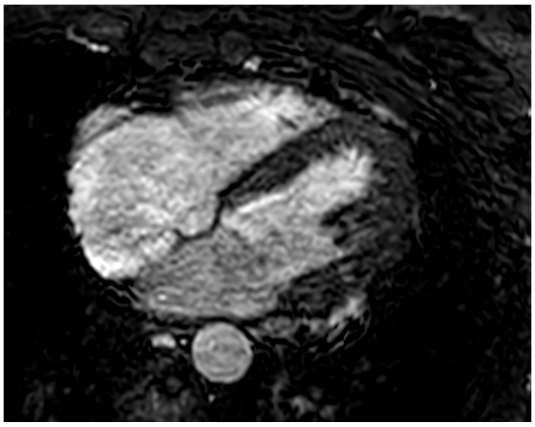

Figure 4.2: One MR image of the data set, in which the four chambers are visible.

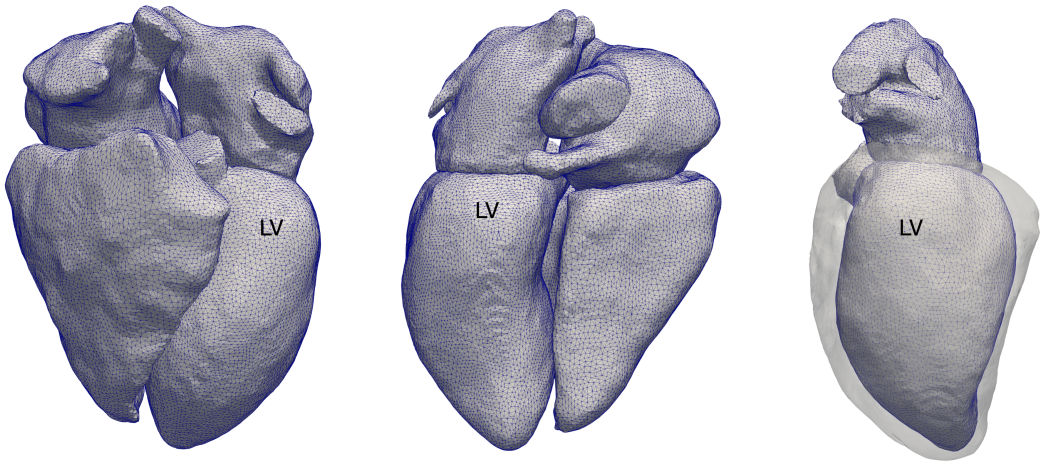

Figure 4.3: Automatically segmented surfaces of the four chambers and the vessels. Left: endocardial surfaces in anterior view. Middle: endocardial surfaces in posterior view. Right: the epicardial surface of the LV in a semi-transparent gray colour, overlaid on the endocardial surface in lateral view.

Endocardial surfaces The four automatically segmented endocardial surfaces were smoothed. In the atria, the automatically segmented veins were deleted in order to close the endocardial surface. The segmented coronary sinus, visible in Figure 4.3, in the middle, underneath the inferior vena cava, was also removed. The endocardial surfaces were remeshed in Instant Meshes[1] [110] to obtain around 2000 triangles in each atria and around 2500 triangles in each ventricle (Figure 4.4).

Valves Openings were created in the endocardial surfaces of the LA and LV for the mitral valve and of right atrium (RA) and right ventricle (RV) for the tricuspid valve. In the openings, meshes were inserted, which are flat and consist of five rings (Figure 4.5). The

[1]Available at `https://github.com/wjakob/instant-meshes`

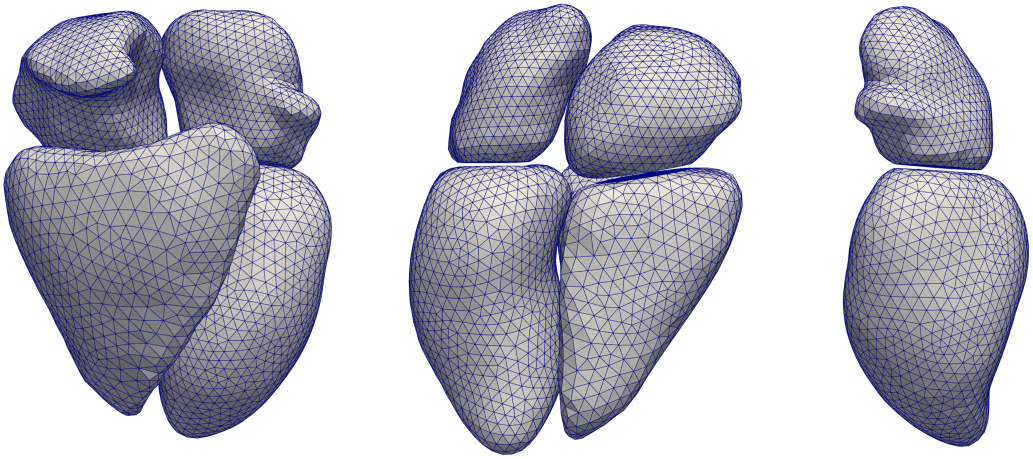

Figure 4.4: Smoothed endocardial surfaces of the four chambers. Left: anterior view. Middle: posterior view. Right: surfaces of LV and LA in lateral view.

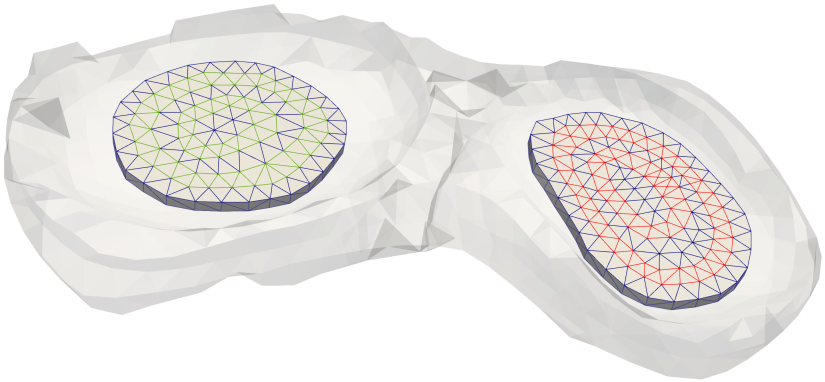

Figure 4.5: The tricuspid and the mitral valve with surrounding tissue (semi-transparent grey colour). The five rings in each valve are colour-coded: green/blue in the tricuspid valve and red/blue in the mitral valve.

mesh of the rings is created consecutively, from the outer to the inner ring, as follows: an opening is created, the border of the opening is smoothed and then closed. The rings are only relevant for the use of this geometry for a fluid dynamic solver, where a step wise opening of the valves is implemented [111]. Between the segmented surfaces of the ventricles and the atria no space was available to place volumetric valves (Figure 4.3). Therefore, a small volume of the atria and the ventricles was removed to place the valves with a thickness of 1.5 mm (Figure 4.5).

Epicardial surface The automatically segmented epicardial surface of the LV was smoothed. The other three epicardial surfaces were obtained by enlarging the endocardial surfaces. Although it is known that the atria have a non-homogeneous wall thickness [112], the atria

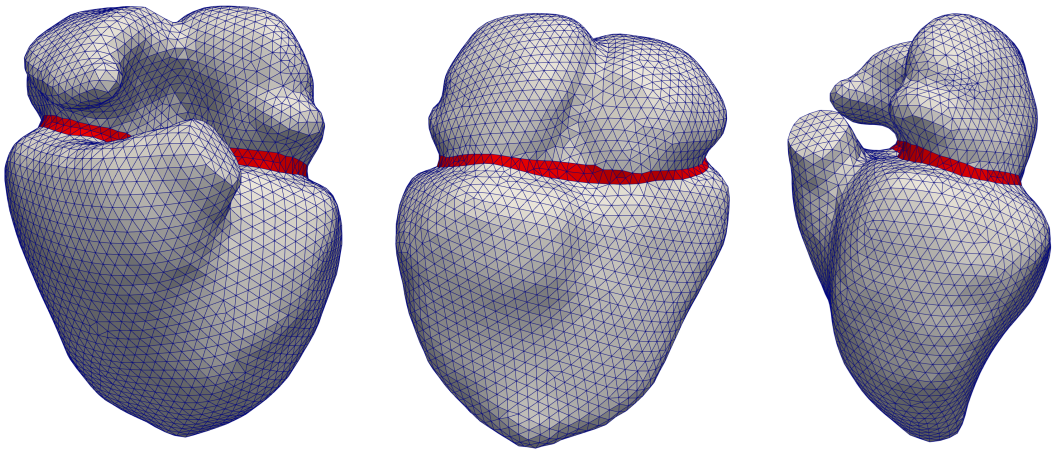

Figure 4.6: Smoothed epicardial surface and the AV plane ring (red). Left: anterior view. Middle: posterior view. Right: lateral view.

endocardial surfaces were enlarged with a constant offset of 2 mm, which corresponded to atria wall thickness ranges [112]. The epicardial surface of the RV was obtained with an offset of 3.3 mm (control RV wall thickness 2–5 mm[113]). In each of the four epicardial surfaces, the triangles in the septal regions and around the tricuspid and mitral valves were removed. The remaining triangles were joined together to form one epicardial surface (Figure 4.6). The surface around the atrioventricular (AV) plane was remeshed to obtain a smooth ring (shown in red in Figure 4.6) which separates the atria from the ventricle surface. To obtain the smooth border of the ring, an opening is created in the mesh, the border of the opening is smoothed and then closed.

Vessels The vessels are modeled by non-hollow trunks which are connected to the epicardial surface. The connecting regions of the epicardial surface and the surrounding surface triangles are remeshed to obtain connecting regions with approximately the diameter of the corresponding vessel. Each of these connecting regions are used to obtain the free ends of the vessels by a translation along the normal direction of the region and the free ends are flattened (Figure 4.7). A flat free end is relevant for the use of this geometry for a fluid dynamic solver, where a pressure boundary condition is defined on the free ends of the vessels [111]. All vessels are 10 mm long, except the aorta which is 20 mm.

Adipose tissue A further component of the geometrical model is epicardial adipose tissue. It is placed around the AV plane and between both atria and the pulmonary artery. This space is between the epicardial surface and its convex hull, calculated in MATLAB. In Figure 4.8, sharp edges of volume between the convex hull and the epicardial surface are indicated by red circles. A part of the surface mesh of the convex hull is joined with a part of the epicardial surface to form a closed surface mesh of the adipose tissue. Then, a volumetric mesh was

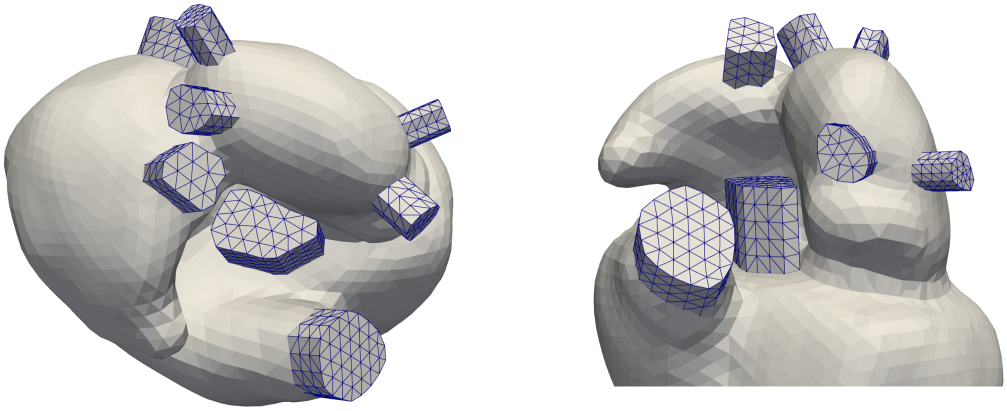

Figure 4.7: Vessels in the geometrical model. Left: top view. Right: lateral view, the ventricles are not entirely visible.

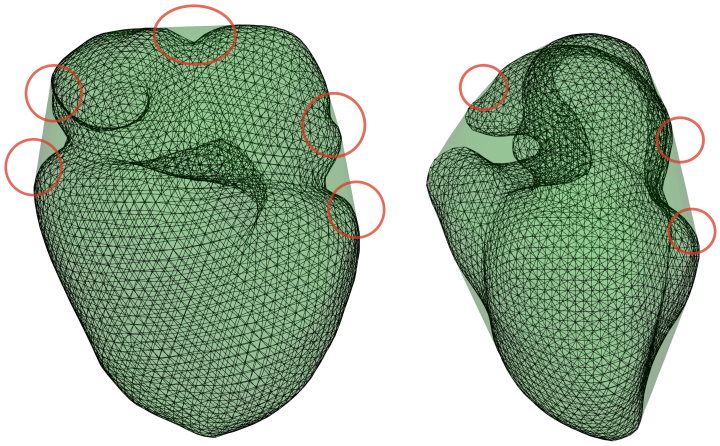

Figure 4.8: The epicardial surface (black wireframe) and its convex hull (semi-transparent green colour). The red circles indicate sharp boundaries between both surfaces. Left: anterior view. Right: lateral view.

created with Gmsh[2] [114], which had a poor element quality due to the sharp edges (zero angle edges) of the volume. Therefore, a simulation with this mesh was not possible, since large deformations are expected in the adipose tissue due to the AV plane displacement.

For this problem (Figure 4.8), there were two solutions: 1) to create a finer mesh in the problematic regions of the adipose tissue or 2) to smooth the sharp boundaries of the volume. A benefit of the first solution is that it preserves the epicardial shape and a drawback is that it leads to more elements in the adipose tissue and in the myocardium and therefore, longer computational time of the mechanical simulation. The second solution reduces the number of elements in the adipose tissue, but modifies the shape of the epicardial surface. For this geometry, the second solution was used.

[2]Available at `www.gmsh.info`

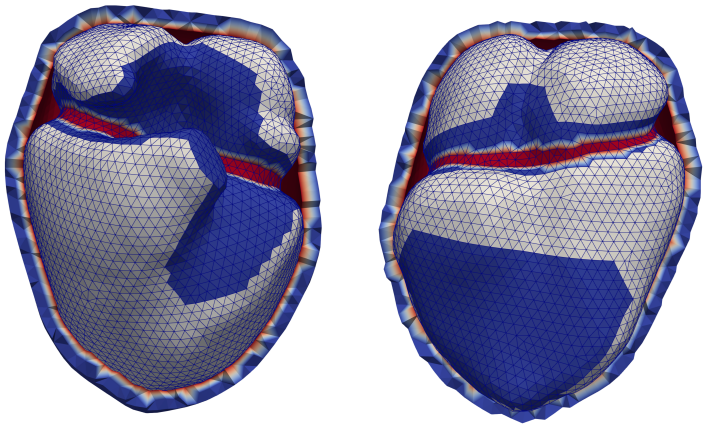

Figure 4.9: The volumetric mesh used for the contact problem: fixated nodes (inner convex hull and AV plane nodes) are shown in red, one contact surface (part of the epicardial surface) is shown in grey. The second contact surface is the inner convex hull (all nodes are red). Left: anterior view. Right: posterior view.

To smooth the sharp boundaries of the volume, the epicardial surface was modified by solving a contact problem [39] between a part of the epicardial surface and the non-deformable (fixated) convex hull. The part of the epicardial surface used as a contact surface is shown in grey colour in Figure 4.9. The inferior epicardial wall of the LV and RV is not entirely included in the contact surface, in order to preserve the shape of the LV (Figure 4.6, right). The contact problem is part of CardioMechanics and therefore, volumetric meshes were required. The surface of the convex hull was enlarged and together with the convex hull, defined the volumetric mesh (Figure 4.9). The thickness of the volumetric hull is irrelevant, since the inner surface was fixated. A volumetric mesh of the myocardium was also created and the AV plane ring was fixated (only for one simulation aiming at smoothing the sharp boundaries of the volume). The parameters of the contact problem were: MaxDistance=0.01, MaxAngle=120° and Alpha=5e+6. The contact problem simulation was run for 6.5 s, which is long enough to ensure that the contact part of the epicardial surface (grey surface in Figure 4.9) fits to the inner surface of the convex hull.

The fitted epicardial surface is joined with a part of the convex hull to form a closed surface mesh of the adipose tissue. The modification of the shape of the epicardial surface is shown in Figure 4.10, second row. Therefore, it deviated from the initially segmented surface (Figure 4.10, first row). Furthermore, the endocardial surfaces were also modified as a consequence of the contact problem and needed to be remeshed.

Pericardium The pericardium represented the tissue surrounding the heart [39]. The inner surface of the pericardium was obtained by extracting the outer surface of the merged modified epicardial surface and the one of the adipose tissue. Therefore, the inner surface of the pericardium differs from the convex hull in the mid and apical regions of the inferior epicardial wall of the LV and RV. In contrast to the previous workflow [109], the characteristic concave curvature of the LV is preserved (visible in the lateral view of the LV, e.g. Figure 4.6,

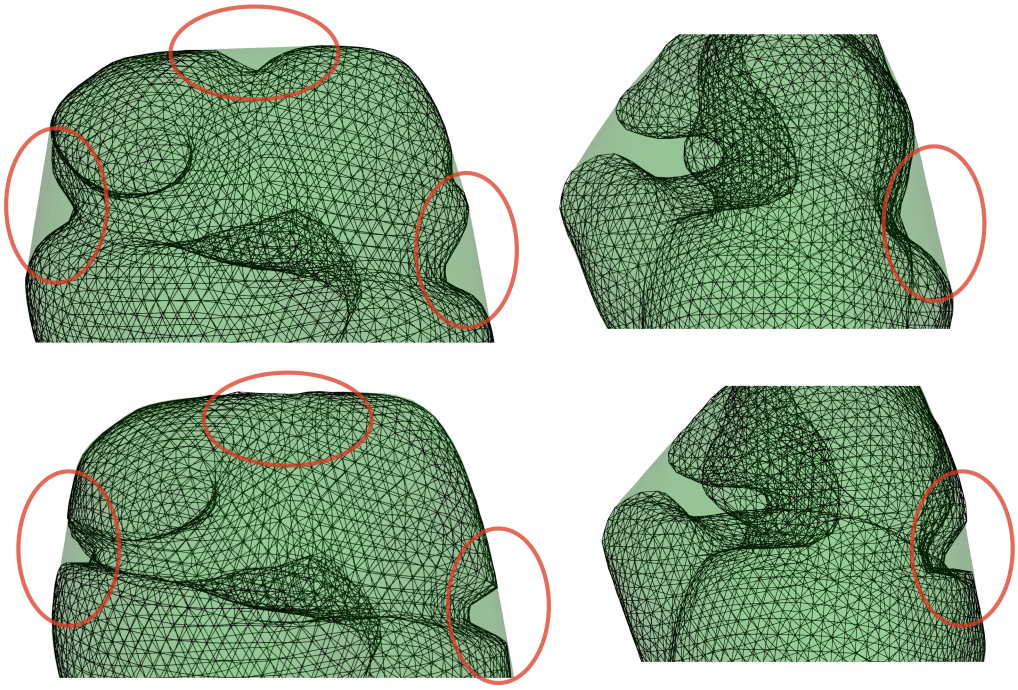

Figure 4.10: The epicardial surface (black wireframe) and its convex hull (semi-transparent green colour), the ventricles are not entirely visible. The epicardial surface is shown before (first row) and after (second row) it was fitted to the convex hull, in anterior (left) and lateral view (right). The red circles indicate sharp boundaries between both surfaces (first row) and their transformation to flat boundaries (second row).

right) and thus, the inner pericardial surface is not convex. The latter surface was remeshed to a coarser mesh (Instant Meshes, around 6000 elements). To obtain the outer surface of the pericardium, the surface of the inner pericardium was enlarged with an offset of 10 mm.

Volume mesh Four volumetric meshes were created in Gmsh: 1) pericardium (bounded by its inner and outer surface), 2) adipose tissue, 3) vessels (Figure 4.7) and 4) epi-endo tissue (bounded by the modified epicardial and the four endocardial surfaces). The epi-endo tissue includes the four chamber tissue, the mitral and the tricuspid valve, rings, surrounding the valves (Figure 4.5) and the vessel bases, which are the connecting regions between the vessels and the myocardial tissue.

Material regions The Laplace equation was solved multiple times with an appropriate boundary condition (BC) on the volumetric mesh of the epi-endo tissue. The BC was defined by at least two surfaces: one (or more) surfaces as source and one (or more) surfaces as a sink. For the BC, the following surfaces were extracted from the epicardial and endocardial meshes: the septal region and the free wall region of the RA and RV endocardial surfaces; the mitral and tricuspid valve surfaces; the ring of the epicardial surface; epicardial and endocardial vessel bases. Combinations of these surfaces are used as a BC to obtain Laplace solutions.

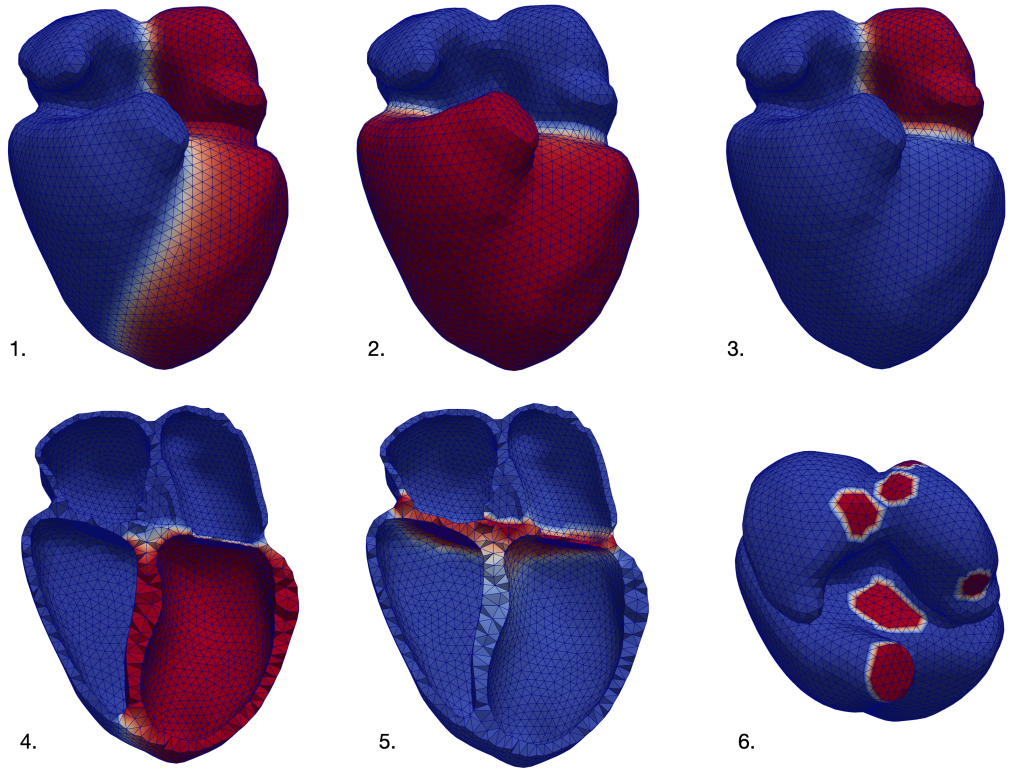

Figure 4.11: Laplace solutions used to separate (1) the left (LV, LA) from the right (RV, RA) heart, (2) the ventricles from the atria, (3) LA, (4) LV, (5) AV plane and (6) vessel bases from the rest of the tissue.

Some of the solutions are shown in Figure 4.11 and they had the following BC: (1) source: left heart endocardial surfaces and sink: right heart endocardial surfaces; (2) source: ventricular endocardial surfaces and sink: atrial endocardial surfaces; (3) source: LA endocardial surface and sink: the other three endocardial surfaces; (4) source: LV endocardial surface and the septal region of RV and sink: free wall region of the RV, and LA and RA endocardial surfaces; (5) source: mitral and the tricuspid valve and the ring of the epicardial surface and sink: the epicardial surface; (6) source: epicardial and endocardial vessel bases and sink: epicardial surface.

Thresholds were applied on the Laplace solutions to separate the epi-endo tissue in material regions. The values of the threshold were chosen manually in order to obtain smooth borders between the regions. Each of these regions is labeled by a unique material number (Figure 4.12), which can be used to assign the elastomechanical properties of the finite elements in this region. For the vessels the material index 39 was assigned, for the adipose tissue 40 and for the pericardium 60. The material indexes were chosen as the one of the already existing geometry. After all materials were assigned, the volume mesh of the epi-endo tissue was appended to the one of the adipose tissue and the vessels. The double nodes and elements in the connecting regions were removed. The resulting volume mesh was appended to the one of the pericardium to obtain the final volume mesh.

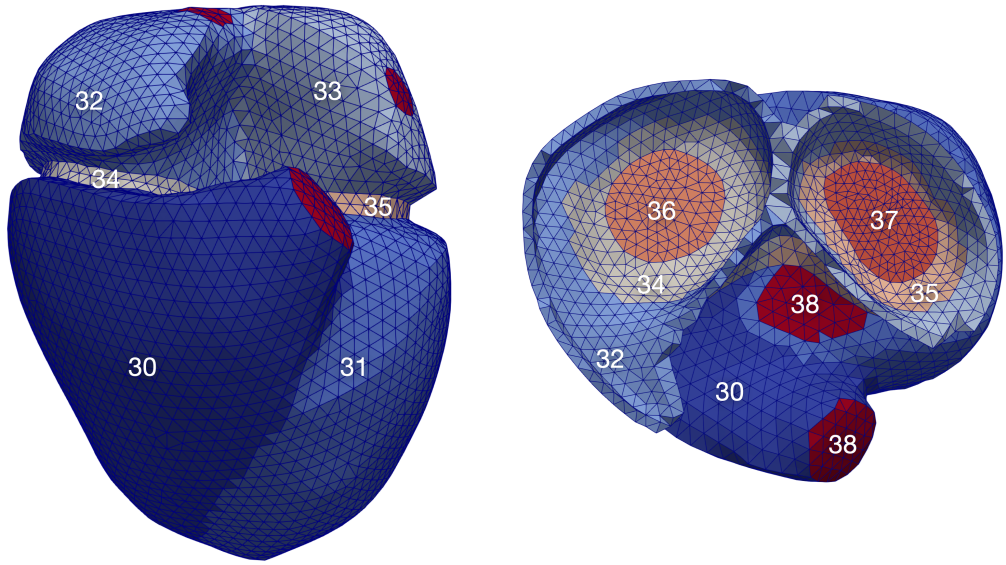

Figure 4.12: Material regions (30–38) of the heart tissue. Left: anterior view. Right: a view from the top on the AV plane.

Fiber, sheet and sheet-normal orientation The fiber, sheet and sheet-normal orientation in the heart build a local coordinate system. In this workflow, the tools created one coordinate system per volume element. In a second order Finite Element Method, four quadrature points per element are required for the calculations and thus, four distinct coordinate systems (one per quadrature point) can be provided. Therefore, the initial volume mesh of the heart was subdivided three times to obtain a fine mesh used as input for the tools. The coordinate systems created on the fine mesh are transferred (nearest neighbour interpolation) to the quadrature point of the initial mesh.

In the atria, the rule-based algorithm of Wachter et al. [32] was applied to obtain the fiber orientation. In Table A.1 (Appendix A), the input seed points and the applied options in the tool are provided. The required material classes in the atria are separated based on a Laplace solution. Additionally, the sheet and sheet-normal orientation were calculated. The sheets on the epicardial surface were aligned with the outward normal direction of the corresponding triangle. A nearest neighbour mapping between the surface and the volume mesh was applied to obtain the sheets in the volume elements. The sheet-normals were the result of the cross products between the vectors pointing in the sheet and the fiber direction.

In the ventricles, the local coordinate system was created by the adapted version of the rule-based algorithm based on Bayer et al. [28][3]. The fiber orientation angles were changing transmurally from 60° on the endocardium to -60° on the epicardium and $\beta = 0^\circ$ [38].

The fiber orientations of the ring around the valves (red-coloured fibers in Figure 4.13) were created with the algorithm for the atrial fiber generation. Nevertheless, in the numerical simulation, the ring was considered to be part of the ventricular tissue, since it had the same

[3]Code available at `https://github.com/KIT-IBT/LDRB_Fibers`

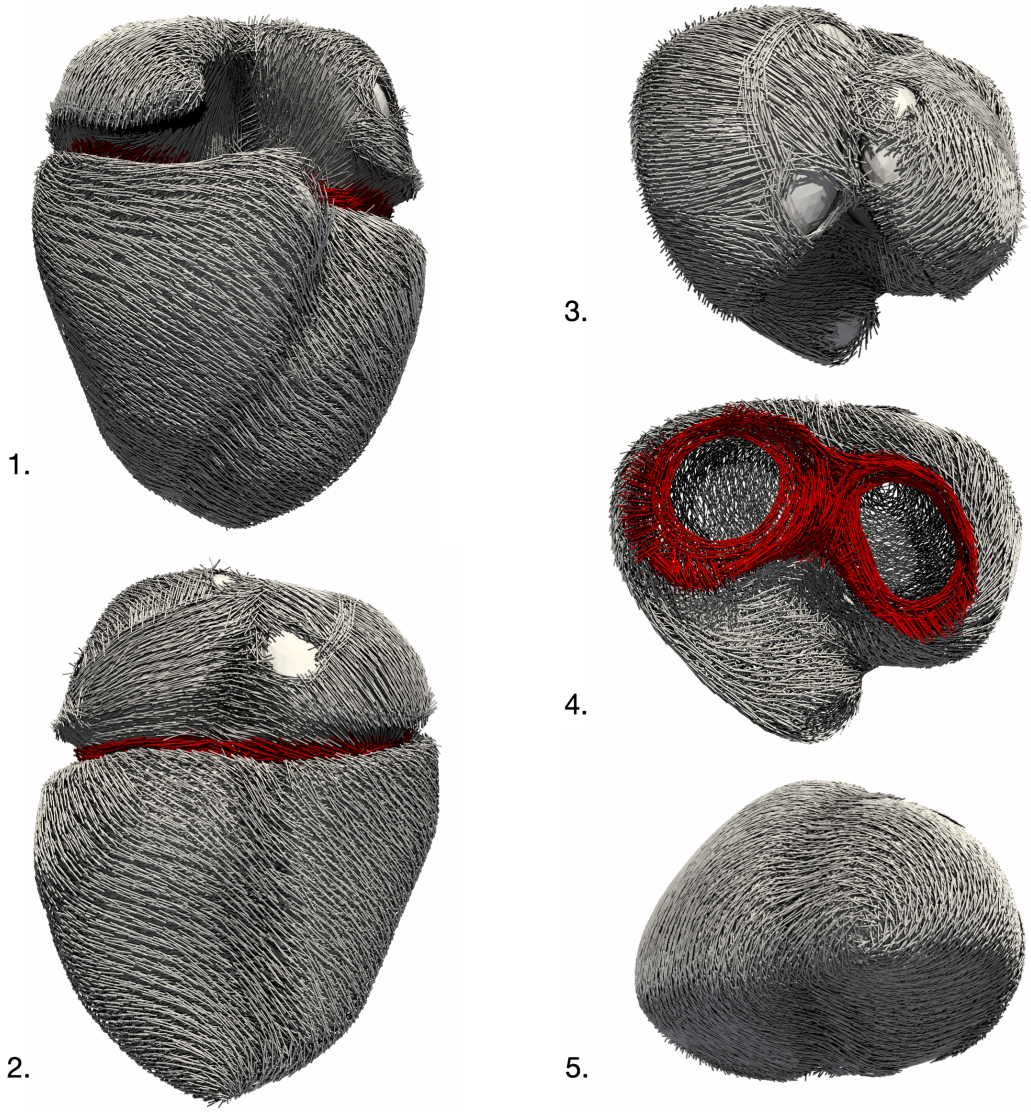

Figure 4.13: Fiber orientation in anterior view (1), posterior view (2), top view (3), top view, without atria (4) and bottom view (5). The fiber orientation in the rings around the mitral and the tricuspid valve are shown in red.

elastomechanical properties as the ventricles. In case only one or bi-ventricular geometry is created, the circular course of the fibers around the valves is not available.

Boundary conditions The motion of the nodes on the outer surface of the pericardium and the nodes on the free ends of the veins was restricted in all directions (*Dirichlet boundary condition*). For solving the contact problem, two surfaces (slave and master) were needed: 1) the inner pericardium and 2) the outer surface of the merged epi-endo volume mesh with one of the adipose tissue. These two surfaces had a different mean edge length, but were overlapping since they describe the same physical domain. Furthermore, the four endocardial

surfaces were extracted, which are used to apply pressure, which acts in normal direction on the chamber's surfaces (*Neumann boundary condition*). The nodes of these surfaces are a subset of the nodes of the volumetric mesh.

Geometry in text files The nodes coordinates (mm) and their fixation were provided in a .node file. The connectivity for each volume element and its material class is provided in a .ele file. The connectivity for each surface element and a surface identifier is provided in .sur file. The fiber, sheet and sheet-normal orientation is provided for each quadrature point of each volume element as a 3×3 matrix, in a .bases file.

4.1.2 Pressure-Free and Pressure-Loaded States

For a simulation of the heart beat in which the circulatory model is included, a pressure-free state of the geometry has to be provided. The difference between the node positions of the pressure free state and an initial heart geometry (pressure-loaded state) was needed to calculate deformation tensors. These were used to evaluate the constitutive laws in each material class and obtain an initial stress in the tissue. This initial stress opposed the initial pressure provided as starting values in the circulatory model to obtain an equilibrium of the forces at the beginning of the numerical simulation. Therefore, it was necessary to obtain a pressure-free state of the geometry by 1) using the same pressure values as the starting values in the circulatory model and 2) using the same parameters of the constitutive laws and incompressibility terms as in the numerical simulation of the deformation. From the deformation tensors the stretch of the fibers can be calculated and used as an input for a length dependent active force model.

Unloading procedure A pressure-free state of the heart state cannot be captured in vivo and therefore, it was estimated by an iterative method proposed by Bols et al. [56] (*unloading* procedure). In the left heart (LV and LA), a pressure of 7.5 mmHg was used in the procedure and in the right heart (RV and RA) 4 mmHg. The pressure-free state of the second iteration (out of four) was chosen for further calculations (Figure 4.14, first row), since it delivered the lowest maximal residual norm 0.004 m (further explanation can be found in Chapter 4.3). Additionally, the LV volume of the pressure-free state (74 ml) was almost half the one of the geometry created from the imaging data (146 ml) [100]. During the unloading procedure, the fiber, sheet and sheet-normals were rotated according to the deformation in the pressure-free state (*unloaded fiber system*).

Loading procedure A pressure-loaded state was needed: it corresponds to a geometry configuration in which the pressure during the diastasis is acting on the chambers. In theory, it is exactly the geometry created from the imaging data, since the images were acquired during the diastasis. In reality, the state was obtained by inflating the pressure-free state combined with the unloaded fiber system (*loading* procedure). The loaded state differed from the geometry created from the imaging data: the LV volume was 126 ml and the maximal

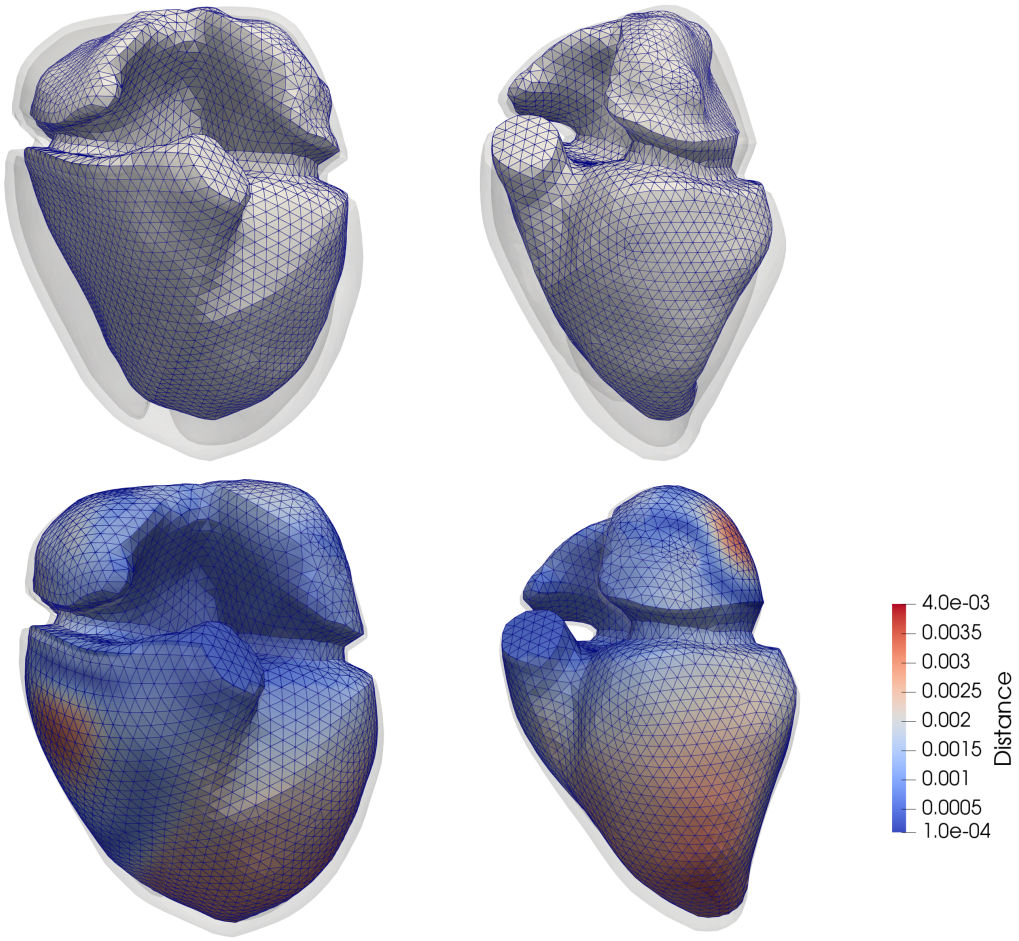

Figure 4.14: First row: the pressure-free state. Second row: the pressure-loaded state. Left: anterior view. Right: lateral view. The second row is colour-coded depicting the point distance (in meter) between the pressure-loaded state and the geometry created from the imaging data. The latter geometry is superimposed in semi-transparent grey colour in all views.

node distance between both geometries was 4 mm (Figure 4.14, second row). The loading procedure was executed with the initial pressure values used in the circulatory system (left heart: 7.5 mmHg and right heart: 4 mmHg).

Fitting the pericardial mesh The loading and unloading procedures were executed on the geometry without any influence from the pericardial tissue, since the pericardial mesh is disconnected from the rest of the volumetric mesh and the contact boundary condition was not applied. Otherwise, the pericardial tissue would restrict the deformation during loading and unloading.

The pressure-loaded state differed from the initially created geometry (Figure 4.14, second row) and therefore, the pericardial mesh had to be fitted to the pressure-loaded state. In theory, the pericardial mesh could be actually created (as described in paragraphs *Pericardium* and *Volume mesh*) after the loading and unloading procedures are completed, to

avoid the pericardial fitting. However, the experience showed that the loading and unloading procedures had to be executed several times with different pressure values or material parameters. Therefore, fitting of the pericardium is included in the workflow.

The nodes on the pericardium are unfixed and the nodes on the outer surface of the merged myocardial and adipose tissue are fixed. The contact problem between these surfaces is solved (MaxDistance=0.01, MaxAngle=90°, Alpha=5e+5, Beta=1) and the fitted pericardium is used instead of the previous one.

4.1.3 Evaluation of the Quality of the Whole Heart Geometry

During and after the creation process of the geometry, the quality of the computational mesh was evaluated. The resulting geometry should fulfill the following requirements:

1. it is a topologically valid geometry (no self intersecting elements),
2. it is suitable for large deformation simulation (sufficient mesh quality),
3. the mean deviation of the geometry boundaries from the initially segmented surfaces is in the range of 1) the inter-observer variability obtained for whole heart segmentation and 2) the precision of algorithms applied for whole heart segmentation.

The first criterion was easily tested: a numerical simulation was initiated with the geometry and if it does not break immediately after the start, then the mesh is topologically valid. However, if it breaks it might be due to other problems. For the second and third criteria, metrics are needed to measure the quality of the geometry. On the one hand, the quality of the geometry quantifies characteristics of the computational mesh that permit an efficient and accurate solution of the problem described by underlying physics [115]. On the other hand, the quality of the geometry quantifies the difference between the discrete domain and the physical domain. In particular, it measures how well the created geometry fits the initially segmented imaging data.

Element quality of the computational mesh One quality measure is the coarseness of the mesh. In general, an optimum of element number exists – enough to obtain a valid result, but not too high so that the efficiency of the solving method is maintained [115]. To obtain such an optimum, a sensitivity analysis can be made [115]. In this work, this was not the case since the implemented direct solvers in CardioMechanics restrict the maximal number of finite elements in the mesh.

Alternatively, the quality of the mesh can be assessed by evaluating metrics based on element geometry [115]. In particular, for one element, the *edge ratio* (a ratio between the longest and the shortest edge of the element) and the *element Jacobian* (element volume) were evaluated. The edge ratio is calculated with the Mesh Quality Filter in Paraview[4] [116] and the element Jacobian is an output of CardioMechanics.

[4]Available at `www.paraview.org`

Distances between discrete and physical domain Distance vectors between the epicardial and endocardial surfaces of the geometry in different steps of the presented workflow were calculated. The distance vector d between two surfaces was calculated by two methods:

1. node distance (ND): the entry d_i is the distance of the node n_i between the first and the second mesh. This calculation requires the same mesh topology and the same numbering of the nodes.
2. nearest neighbour (NNB) based distance calculation: for every node (n_i) in the first mesh, the shortest distance to any node in the second mesh is calculated. This is the distance d_i. This calculation can be applied on meshes with different topologies, but it is not symmetric (regarding order of the input meshes) and depends on the mesh resolution. Therefore, it is applied only when ND could not be applied.

In case both surface meshes describe very similar physical domains, both methods deliver the same result.

4.1.4 Further Geometries

Previously Available Geometries

Previous to this work there were two geometries available at IBT: an idealized LV geometry and a whole heart geometry.

Idealized LV geometry An idealized LV geometry was represented by a hollow, truncated ellipsoid as described in Land et al. [5]. In the following, this geometry will be referred to as *elli15*. The volume mesh consists of 4237 nodes and 2074 cells. The endocardial surface consists of 544 triangles and 285 nodes. The long axis of the ellipsoid measured 25 mm and the diameter of the base plane was 20 mm. The mean edge length of the surface elements was 1.9 mm and the wall thickness was 3 mm. All nodes on the open end of the truncated ellipsoid were fixed in all three directions as a boundary condition. The fixed nodes are marked by red colour in Figure 4.15. The fiber orientation was determined by the algorithm of Bayer et al. [28] and was transmurally changing from 90° on the endocardium to -90° on the epicardium [38].

A whole heart geometry The workflow for the creation of a whole heart geometry was briefly described by Baron et al. [109] (an abstract). In the following this geometry will be referred to as *geo17*.

Similarly to geo20, geo17 was based on MRI data of the whole heart, acquired from a healthy volunteer at University Hospital Heidelberg with a 1.5 T MR tomograph (Philips Medical Systems). Voxel spacing was $0.7\times0.7\times1.8$ mm. The geometry had the same components as geo20: four chambers, valves, valve rings, trunks (to approximate vessels), adipose tissue and a pericardium (Figure 4.16). The boundary condition slightly differed

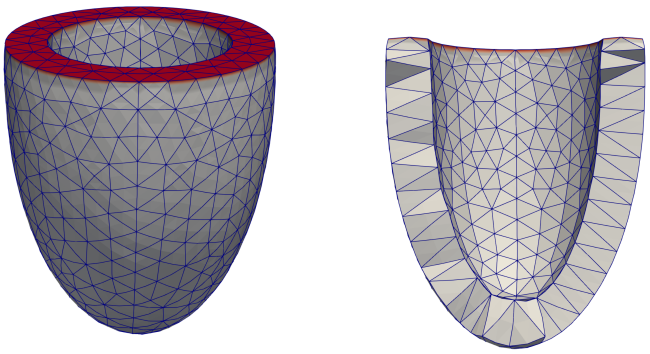

Figure 4.15: The idealized LV geometry (elli15): the fixated nodes are shown in red colour. Left: anterior view. Right: clipped geometry.

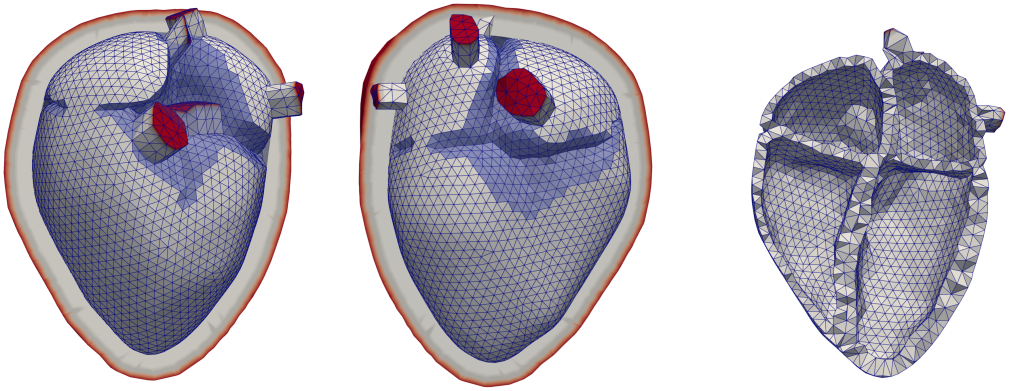

Figure 4.16: The whole heart geometry (geo17): the fixated nodes (the outer surface of the pericardium and on the free ends of the vessels) are shown red colour and the adipose tissue is superimposed in blue semi-transparent colour. Left: anterior view. Middle: posterior view. Right: clipped geometry.

from the one of geo20: the nodes on the free ends of all trunks in geo17 and the outer surface of the pericardium were fixated in all three directions, while in geo20, the free ends of the aorta and pulmonary artery were not fixated.

Geometries Created for This Work

Additionally to geo20, further geometries were created for this work: two whole heart geometries (modified from geo17) with hypertrophic LV walls and two patient-specific LV geometries. These geometries were created by the techniques described previously. In the following, additionally executed steps are described.

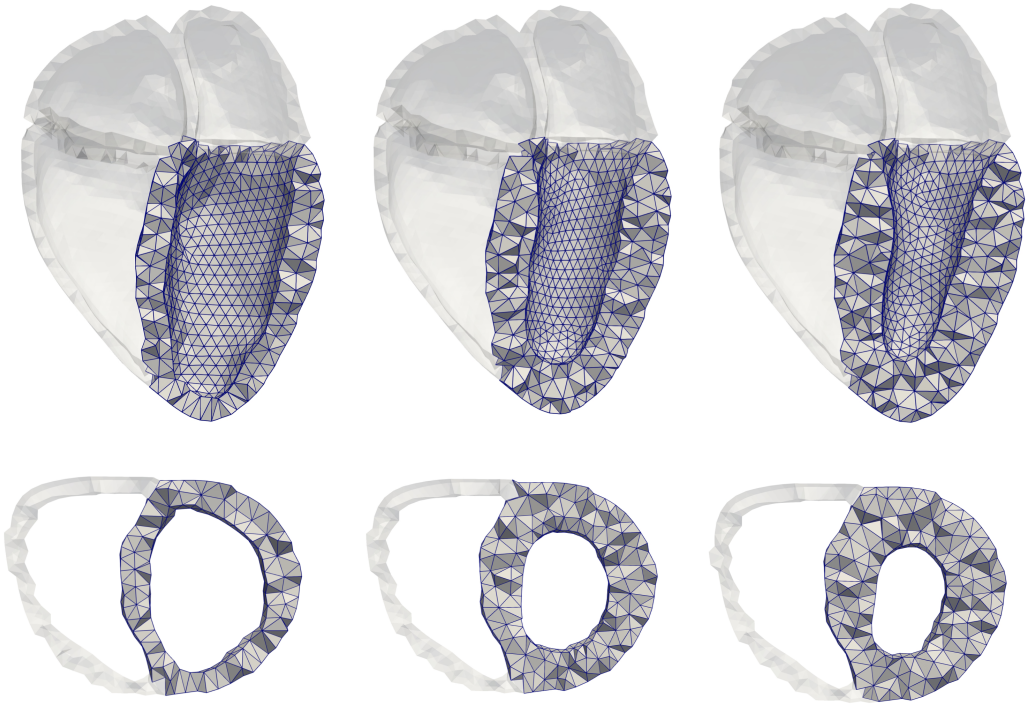

Figure 4.17: The whole heart geometries: clipped through their long axis (first row) and a short axis slice through both ventricles (second row). Left: geo17 (mean WT 10 mm). Middle hypertrophic geometry (geo17HCM1, mean WT 15 mm). Right: hypertrophic geometry (geo17HCM2, mean WT 17 mm). Modified from the preprint [117], published under the Creative Commons Attribution 4.0 International (CC BY 4.0) License.

Hypertrophic LV walls of a whole heart geometry (geo17) In order to conduct a study on the influence of the wall thickness on the deformation of the heart (described in [117] and Chapter 6), two modifications of geo17 were created to obtain hypertrophic LV walls.

The wall thickness (WT) (mean $\pm$ std) of the LV of geo17 was 10 ± 2.3 mm and its cavity volume was 193 ml. Tissue was added on the LV endocardial surface to increase the WT to 1) 15 ± 3.3 mm (*geo17HCM1*) and 2) 17 ± 4.1 mm (*geo17HCM2*) with a concomitant decrease of the LV volume to 118 ml and 94 ml, respectively. In both cases, the added tissue was distributed concentrically (Figure 4.17). To obtain the thickened wall, the LV endocardial surface of geo17 was shrunk and remeshed in Instant Meshes. The epicardial surface mesh was identical in all three cases (geo17, geo17HCM1 and geo17HCM2), while the myocardial volume was remeshed for both hypertrophic geometries to keep the element quality and preserve the mean edge length of the LV (6.4 ± 1.5 mm). Further geometrical characteristics of the mesh are provided in Table 4.1. Figure 4.17 shows the LV of three geometries with distinct WT. The RV and both atria were not modified compared to geo17.

Patient-specific LV geometries In order to provide a proof-of-concept for an inverse problem of cardiac mechanics based on MRI imaging data, two patient-specific LV geome-

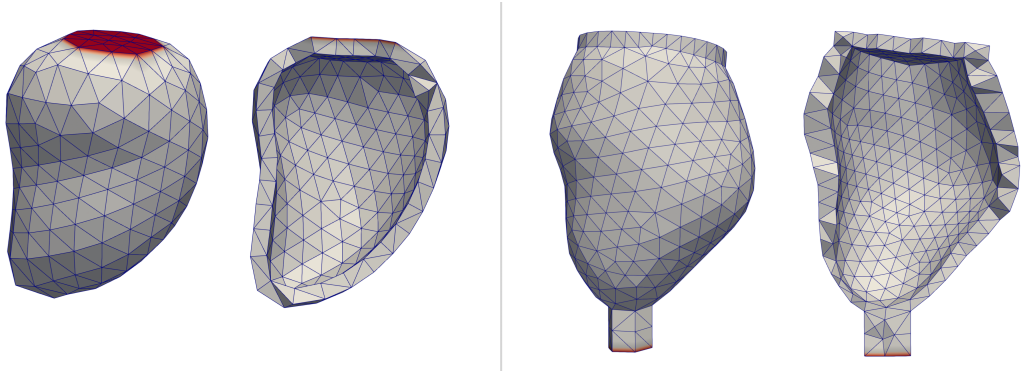

Figure 4.18: The patient-specific LV geometries and the fixated nodes are shown red colour. Left part: anterior and clipped view of geo20LV. Right part: anterior and clipped view of geoCardAtl.

tries were created: 1) the LV of geo20 and 2) a LV geometry from an MRI image data, as described in the following.

The endocardial surface of the LV of geo20 was based on the MRI images described previously. The epicardial surface was modeled as an inflated version of the endocardial surface with an offset of 6 mm. In the following, this geometry will be referred to as *geo20LV* (Figure 4.18, left part). The geometrical parameters are provided in Table 4.1. All nodes on the base were fixed in all three directions as a boundary condition.

The second patient-specific geometry of the LV is created based on SCD0003801 image data provided in Sunnybrook Cardiac Data[5] (2009 Cardiac MR Left Ventricle Segmentation Challenge), published under Public Domain (CC0 1.0 Universal) [118]. In the following, this geometry will be referred to as *geoCardAtl* (Figure 4.18, right part). The epicardial and endocardial surfaces were provided in the data set, but they were remeshed to improve the surface element quality around the apex region (from 3.1 to 1.02). Geometrical characteristics of the mesh are provided in Table 4.1. Tissue was added around the apex, which was fixated at the free end to serve as a boundary condition (red colour in Figure 4.18, right part).

The fiber direction for both patient-specific LV geometries was determined by the algorithm of Bayer et al. [28] with angles 80° on the endocardium to -70° on the epicardium as suggested by Wong et al. [30].

4.1.5 Overview of the Geometries

Table 4.1 provides an overview for all geometries use in this work. The number of nodes is provided for the T10 meshes, which are mostly used in this work.

[5] `https://www.cardiacatlas.org/studies/sunnybrook-cardiac-data/`

Table 4.1: Overview on the geometrical properties of the meshes, their BC and the fiber orientation (FO). N: numbers of nodes of the T10 mesh; M: number of volumetric elements in the entire mesh; l_e: mean edge length of volume elements in the myocardial tissue (in mm); V: volume of LV (in ml); WT: mean wall thickness of LV (in mm); the BC was peri (sliding pericarium BC) +t (fixated trunks) or +v (fixated veins), base (fixated base plane) or apex (fixated tissue close to the apex). g-HCM1 is geo17HCM1 and g-HCM2 is geo17HCM2.

	Whole heart geometries				**LV geometries**		
	geo20	geo17	g-HCM1	g-HCM2	elli15	geo20LV	geoCardAtl
N	79680	48780	51246	50935	4522	2160	6147
M	156129	90801	92476	91401	3162	2816	4421
l_e	4.1	5.9	6.0	6.0	1.9	4.3	6.7
V	126	193	118	94	24.4	133	122
WT	6.8 ± 1.7	10 ± 2.3	15 ± 3.3	17 ± 4.1	157	6	57
BC	peri+v	peri+t	peri+t	peri+t	base	base	apex
FO	60°/-60°	60°/-60°	60°/-60°	60°/-60°	90°/-90°	80°/-70°	80°/-70°

4.2 Results

4.2.1 Element quality of the computational mesh

The evaluated edge ratios and the element Jacobians of the myocardial tissue and the valves (material 30–38) of the geometrical mesh geo20 are provided in Table 4.2. Different stages were evaluated: prior and after the unloading/loading procedures and during the numerical simulation: at the time point of end-diastole (0.16 s) and end-systole (0.5 s) in the first beat after the simulation was started.

For geo20, prior the unloading, after the loading and at the end-diastole, more than 99 % of the volume elements had an edge ratio below 3 (Table 4.2). At the end-systole, the percentage of elements with an edge ratio above 3 increased to 17 % of the elements (from 1 % at end-diastole). Their distribution is visualized in Figure 4.19, first row.

Furthermore, all element Jacobians were greater than 0.2. The distribution of the elements with Jacobian below 0.7 is visualized in Figure 4.19, second row. The Jacobians prior to the unloading and after the loading procedure were not evaluated.

Quality of the adipose tissue The edge ratio of the initially created elements in the adipose tissue was bad: up to 570. After the epicardial surface was modified, as described previously, the edge ratios of the volumetric mesh were smaller than 10 (Figure 4.20, second row). Furthermore, the number of elements in the adipose tissue was almost halved (from around 14000 to around 7000). Nevertheless, the shape of the epicardial surface was modified (Figure 4.10, second row) and deviated from the initially segmented surface (Figure 4.10, first row).

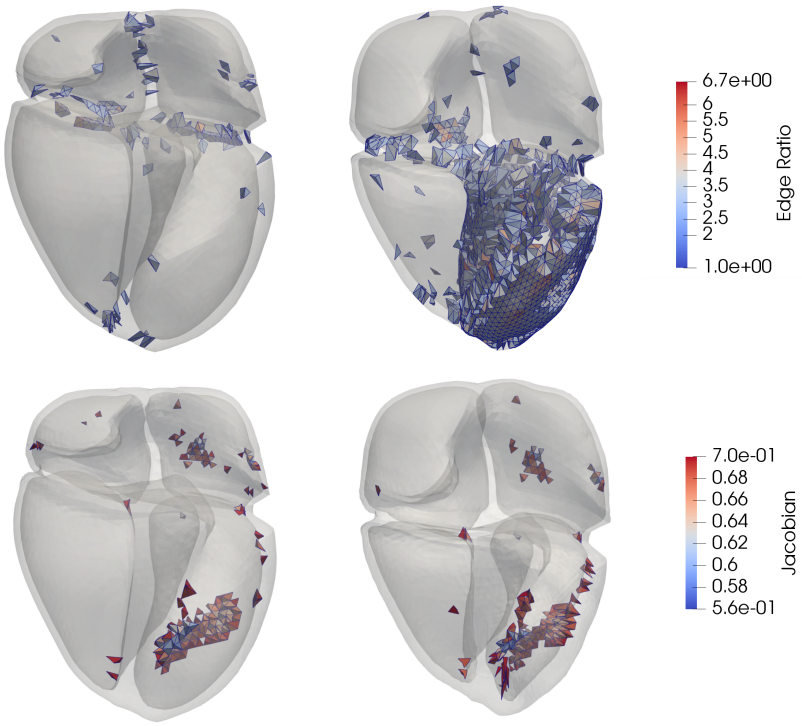

Figure 4.19: Mesh quality measures: the elements with edge ratio above 3 are colour-coded (first row) and the elements with Jacobians below 0.7 are colour-coded (second row). Left: geometry at end-diastole. Right: geometry at end-systole.

Table 4.2: The characteristics of the geometrical mesh in different stages: prior and after the unloading/loading procedures and during the numerical simulation – at the time point of end-diastole (0.16 s) and end-systole (0.50 s). The ranges of the edge ratios ε_R and the elements Jacobian (J) for all cells are provided. The percentage of cells which fulfill the requirements of ε_R>3 and J<0.7 is provided.

	range of ε_R	$\lvert \varepsilon_R>3 \rvert$	range of J	| J<0.7 |
prior unloading	[1.05, 5.43]	0.5 %	-	-
after loading	[1.04, 5.57]	0.3 %	-	-
at end-diastole	[1.03, 4.81]	1.0 %	[0.57, 1.06]	0.7 %
at end-systole	[1.07, 6.71]	17.2 %	[0.56, 1.10]	0.7 %

4.2.2 Distances between discrete and physical domain

A further aim of the workflow was to create a geometry with a mean distance of its boundaries to the initially segmented surfaces (mean(d)) of less than a threshold **T**=3 mm.

Three geometries were used to calculate distances. The first one was obtained by smoothing the endocardial surfaces, which were automatically segmented from the MRI images and the corresponding epicardial surface. The endocardial surface (*endoInit*) is

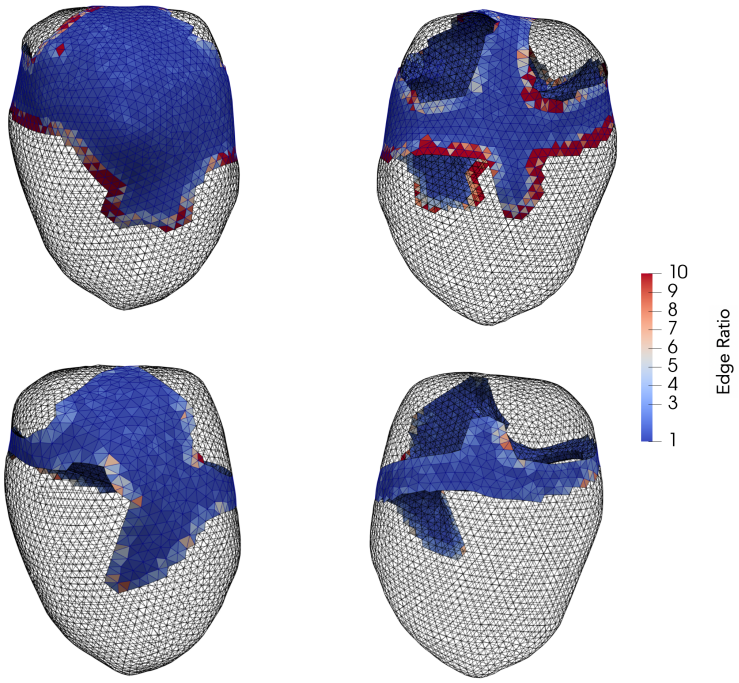

Figure 4.20: The volumetric elements of the adipose tissue are colour-coded corresponding to their edge ratios. The adipose tissue is shown before (first row) and after (second row) the epicardial mesh was fitted to the convex hull in anterior (left) and posterior view (right).

visible in Figure 4.4 and the epicardial surface (*epiInit*) is visible in Figure 4.6. The second geometry is obtained after it has been modified due to the inclusion of adipose tissue in the model. The endocardial surface is referred to as *endoMod*. The epicardial surface (*epiMod*) is visible in Figure 4.12. The third geometry is obtained after the unloading and loading procedures were executed and its epicardium (*epiLoad*) is visible in Figure 4.14. The endocardial surface is referred to as *endoLoad*.

The distance between the epicardial surfaces and the endocardial surfaces was calculated for the following combinations of geometries: 1) endo/epiInit vs. endo/epiMod, 2) endo/epiMod vs. endo/epiLoaded, 3) endo/epiLoaded vs. endo/epiInit. The maximum, minimum, mean and standard deviation (std) of the distance (d) between the surfaces in these combinations are provided in Table 4.3. The mean distance is smaller than the threshold of 3 mm in all combinations.

The distribution of the distances on the epicardial surfaces is shown in Figure 4.21 and on the endocardial surfaces is visualized in Figure 4.22.

The mean distances between the endo/epiInit and endo/epiMod were 1.3–1.4 mm ($< \mathbf{T}$). The errors occurred in the area around the AV plane and the myocardial tissue close to the adipose tissue (first column in Figures 4.22 and 4.21). The mean distances between the endo/epiMod and endo/epiLoaded were 2.3–2.4 mm ($< \mathbf{T}$). The errors, close to the apex region, mainly contributed to the value of the mean distance (second column in Figures 4.21 and 4.22). The mean distances between the endo/epiLoaded vs. endo/epiInit were 2.0–

Table 4.3: The maximal, minimal, mean and the standard deviation of the distance (in mm) between the epicardial and the endocardial surfaces of combinations of geometries. ND: node distance, NNB: nearest neighbor.

Combination	Method	max(d)	min(d)	**mean(d)**	std(d)
endoInit vs. endoMod	NNB	7.2	0.6	1.3	1.0
endoMod vs. endoLoaded	ND	5.3	0.7	2.3	1.2
endoLoaded vs. endoInit	NNB	7.0	0.9	2.0	1.0
epiInit vs. epiMod	ND	7.9	0.4	1.4	1.1
epiMod vs. epiLoaded	ND	5.3	0.9	2.4	1.2
epiLoaded vs. epiInit	ND	8.7	0.8	2.9	1.3

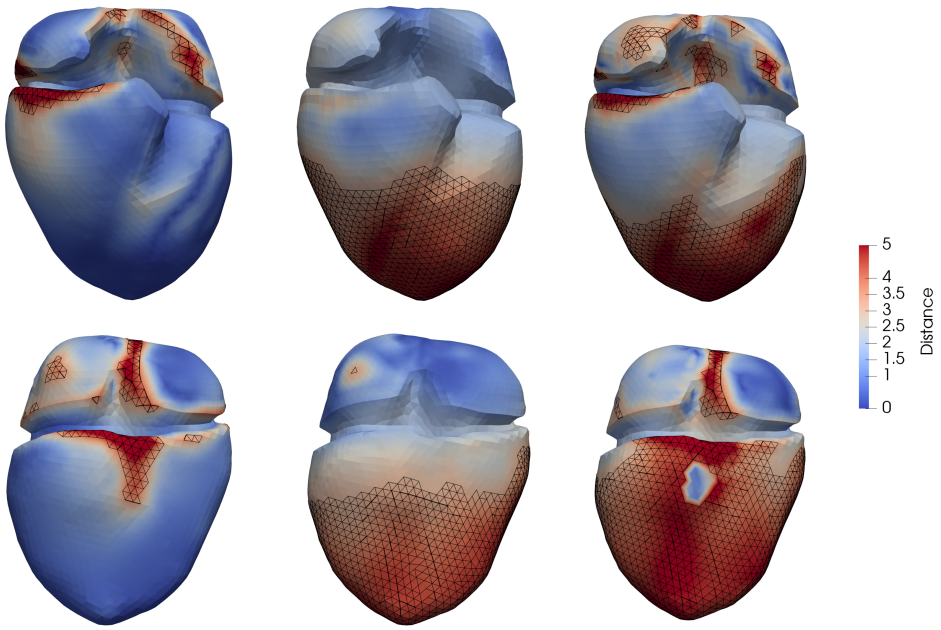

Figure 4.21: The distribution of the distance between epicardial surfaces is colour-coded (0–5 mm). The nodes with distance larger than 3 mm are superimposed in black wireframe. First column: epiInit vs. epiMod. Second column: epiMod vs. epiLoaded. Third column: epiLoaded vs. epiInit.

2.9 mm ($< \mathbf{T}$). The errors were present in the area around the AV plane and in the area close to the apex (third column in Figures 4.21 and 4.22).

Ground truth segmentation The surface endoInit approximates the automatically segmented surfaces from the MRI images very well (Figure 4.23). Therefore, it was assumed to be the ground truth of the endocardial surface in the heart. A distance calculation is not provided. It would be incorrect since endoInit is a closed surface and the automatically segmented surfaces have openings for the vessels (Figure 4.23). The epicardial surface epiInit was assumed to be the ground truth of the epicardial surface of the heart.

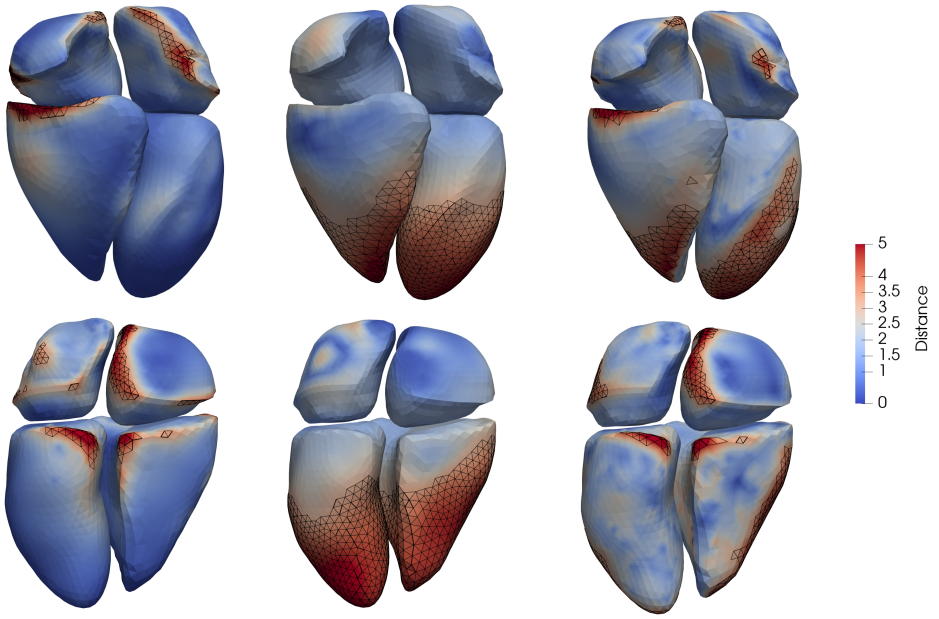

Figure 4.22: The distribution of the distance between endocardial surfaces is colour-coded (0–5 mm). The nodes with distance larger than 3 mm are superimposed in black wireframe. First column: endoInit vs. endoMod. Second column: endoMod vs. endoLoaded. Third column: endoLoaded vs. endoInit.

4.3 Discussion

Reproducibility of the workflow Reproducibility of the presented workflow is provided if starting with the same image data set, the same final heart model is achieved independently of the tools employed [119]. However, there might be further interpretations of the definition of *reproducibility*, since in the literature there is no clear consensus on the definition [119].

In the presented workflow, evaluation of intermediate steps is provided to facilitate reproducibility: by measuring the deviation introduced in intermediate workflow steps (Subsection 4.2.2), one could produce a comparable result by aiming at the same deviation, distributed the same way (Figure 4.21 and 4.22). Furthermore, ways to evaluate the element quality were included in the workflow.

However, in the presented workflow, manual post-processing of the data (surface smoothing) was performed, which is against *rules* ensuring the reproducibility in a workflow [120]. In future, it could be avoided by implementing these procedures in deterministic algorithms, as part of an automated workflow: e.g. Neic et al. [16] and Fedele et al. [17] presented concepts towards this goal and Prassl et al. [11] proposed ways to semi-automatically generate a volumetric mesh.

Distances between discrete and physical domain The threshold **T**=3 mm was chosen to be in the range of the inter-observer variability obtained for a whole heart segmentation: the mean surface distance between manual contouring ranged from 2 mm to 3 mm for the

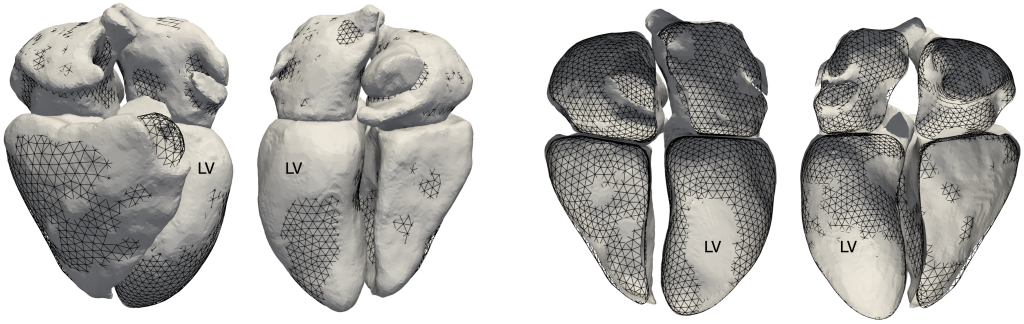

Figure 4.23: The automatically segmented endocardial surfaces in grey colour. The smoothed endocardial surfaces are superimposed in black wireframe. From left to right: anterior view, posterior view, clipped surfaces in anterior view and posterior view. The left ventricle is marked by LV.

chamber segmentation and up to 4 mm for arteries segmentation [121]. Furthermore, the threshold is in the range of the precision of algorithms applied for whole heart segmentation: the surface to surface distance between the manually segmented whole heart surface and the one obtained by algorithms ranged from 1.6 mm to 9.7 mm and the mean($\pm$std) was 2.9($\pm$3.3) mm [122].

The mean distances between the endo/epiInit and endo/epiMod are the smallest among the observed meshes. The modification of the geometry was necessary due to the inclusion of adipose tissue in the model. Therefore, the distances were the highest in the area around the AV plane and the myocardial tissue close to the adipose tissue (first column in Figures 4.22 and 4.21).

The mean distances between the endo/epiMod and endo/epiLoaded occurred close to the apex region (second rows in Figures 4.22 and 4.21). The loading procedure inflated the pressure-free state. Additionally, the boundary condition was a fixation on the free ends of the veins. This led to a strong deformation of the nodes in the ventricles, close to the apex region.

The mean distances between the endo/epiLoaded vs. endo/epiInit were the highest among the observed meshes. These distances comprise the errors introduced during the entire workflow: creating the modified surfaces (endo/epiMod) was an intermediate step. The distances on the endocardial surface are underestimated (compared to the epicardial distances) due to the NNB method, which was necessary to apply since the compared meshes had different topology.

Element quality of the computational mesh To optimize the computational accuracy and the condition of the problem, moderate edge ratios ε_R are required: $1<\varepsilon_R<3$ are acceptable; $3<\varepsilon_R<10$ should be treated with caution; $\varepsilon_R>10$ should be avoided [115]. Furthermore, the total number of elements with an edge ratio higher than three ($\varepsilon_R>3$) and their locations are also important for assessing the mesh quality: it is recommended that the percentage of these elements remain below 5 % [115]. This recommendation is fulfilled for the myocardial tissue of geo20 at the end-diastole since more than 99 % of the volume elements had an

acceptable quality (Table 4.2). However, at end-systole, the percentage of elements with edge ratio above the recommended one increased to 17 % of the elements. They are located mainly in the LV (Figure 4.19, first row) since there the largest deformation occurred at end-systole. Still, the worst element edge ratio in the myocardium during the whole cycle was below 6.7, which is in the *better* half of the range of [3,10].

In the adipose tissue, the edge ratio was sufficient for a simulation (less than 10) (Figure 4.20, second row).

Furthermore, the element Jacobians should be greater than 0.2 and less than 5 % of all Jacobians should fall below a magnitude of 0.7 [115]. For geo20, both criteria were fulfilled (Table 4.2). The distribution of the elements with Jacobian below 0.7 is visualized in Figure 4.19, second row. Again, they are located in the LV.

Adipose tissue creation In the presented workflow, adipose tissue is created and included in the computational mesh as suggested by Baron et al. [109]. It has three purposes: the first is the trivial purpose of modelling the adipose/fat tissue which is actually present around the in vivo heart. The second purpose is to fill the volumetric gap between the epicardial surfaces of the atria and ventricles and therefore, connect these two additionally to the connection via the AV plane. The third purpose is to close the surface, which is needed for the sliding boundary condition: the outer surface of the merged epi-endo volume mesh with the one of the adipose tissue. This surface needs to be closed since otherwise discontinuity in the sliding forces occur.

In this work, all simulations of the whole heart were performed with the model which includes the adipose tissue. Therefore, no evaluation of its influence on the deformation was performed. However, the influence of the adipose tissue creation on the geometrical model generation was evaluated (Table 4.3, Figure 4.21 and 4.22). The shape of the epicardial surface was modified and deviated from the initially segmented surface.

The highest errors occurred around the AV plane and were up to 7.9 mm, which is higher than the maximal error introduced by the loading and unloading procedures (5.3 mm).

The presented creation of the adipose tissue including modifications of the surfaces was necessary to obtain an element quality which is sufficient for a simulation. Furthermore, it lead to less volumetric elements (almost halved compared to initially created tissue), which is relevant for the computational time.

Unloading and loading procedures In theory, the unloading procedure iterates either until convergence of the summed squared distances between the nodes of the inflated pressure-free state and the geometry created from the imaging data is reached or the maximal node distance between these geometries is under a predefined threshold. For the presented geometry, the procedure terminated before it could converge, since too high values of the acceleration (second derivative of the displacement) in one node (1e+13) appeared. The unloading procedure was executed additionally with a method prosed by Marx et al. [57], which improves convergence and robustness. However, the result did not differ from the one obtained with the method of Bols et al. [56].

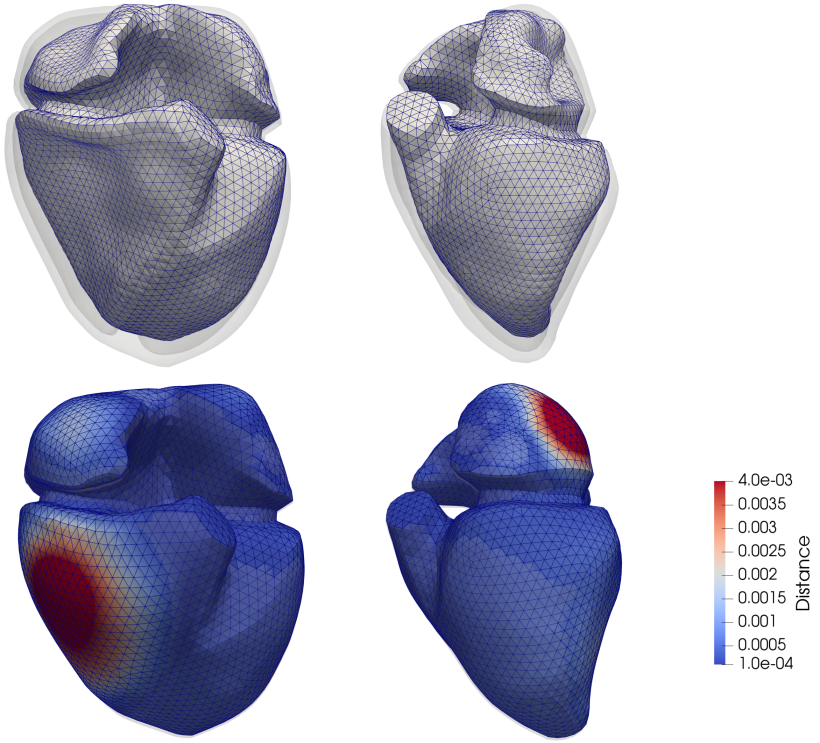

Figure 4.24: First row: the pressure-free state from the last iteration of the unloading procedure. Second row: the corresponding pressure-loaded state. Left: anterior view. Right: lateral view. The second row is colour-coded corresponding the point distance (in meter) between the this pressure-loaded state and the geometry created from the imaging data. The latter geometry is superimposed in semi-transparent grey colour in all views.

In the current chapter, the unloaded state from the second iteration was chosen for the evaluation: it had the lowest maximal residual norm (0.004 m) but the highest summed residual norm (0.53 m) (Table 4.4). The inflated volume was 126 ml which deviates from the volume of the initially segmented LV (146 ml).

In contrast, the unloaded state from the fourth iteration (Figure 4.24, first row) had the lowest summed residual norm (0.26 m) but the highest maximal residual norm (0.006 m) (Table 4.4). These maximal distances appeared in the posterior wall of the LA and in the anterior wall of the RV. Nevertheless, the LV of the pressure-loaded state matched very well with the geometry created from the imaging data (Figure 4.24, second row). The inflated volume was 145 ml which matches the volume of the initially segmented LV (146 ml). Thus, the unloaded state from the fourth iteration could be used to obtain a better initial match between the MRI imaging data and the geometry used for the simulation (compared to the second iteration).

The unloaded state also depends on the choice of the parameters of the constitutive laws defined in the material regions (see Chapter 7). Marx et al. [57] used this dependency to simultaneously determine these parameters and the unloaded configuration. In this work, the

Table 4.4: The volumes of the chambers in the initial geometry (second row) and during the iterations of the unloading procedure (iteration 2, 3 and 4). The distance vector d contains the node distance between the inflated pressure-free state from the corresponding iteration and the initial geometry. The distance is in meter and the volume (Vol) of each chamber of the pressure-free state is in ml.

Iteration	max(d)	$\|\|d\|\|_2$	Vol(RV)	Vol(LV)	Vol(RA)	Vol(LA)
initial	0	0	157	146	79	57
2	0.0040	0.53	76	73	50	29
3	0.0051	0.28	75	88	52	28
4	0.0063	0.26	60	83	51	24

parameters of the constitutive laws were identified first (as described in Chapter 7) and then, the unloading and loading procedures were executed.

Kallhovd et al. [59] unloaded geometries with 21 different material parameters and could achieve a maximum residual norm of 0.1 mm between the unloaded and the initial geometry. However, they used only LV geometries, while the errors presented in this work are evaluated on the whole heart and therefore, the problematic areas in the RV and LA are included in the error calculation.

Fiber angles The fiber angles of the whole heart geometries were chosen to transmurally rotate from 60° on the endocardium to -60° on the epicardium [38], while the fiber angles of the LV geometries were chosen to have a wider range: for the ellipsoid geometry, 90° on the endocardium to -90° on the epicardium, which are the extremes of the angles [38] and which were also applied in the benchmark of Land et al. [5]. For the patient-specific geometries, 80° on the endocardium to -70° on the epicardium was used [30]. It was observed that for a simulation only of the LV, a wider range (than $60^\circ/-60^\circ$) is needed to obtain a longitudinal shortening due to the coarse mesh (one transmural element). In a whole heart simulation, the sliding boundary condition supports the AV plane displacement and the tissue shortening in longitudinal direction as it restricts the radial contraction [39].

Additionally, all geometrical models consist of a rather coarse mesh: geo17 and geo20 have up to two element transmurally and all LV geometries, have only one transmural element. Therefore, only two distinct fiber directions are assigned to the quadrature points (4 per element) across the wall. Since unstructured meshes were created, more than two values were obtained across the wall. A histogram of the fiber orientation of a LV geometry (geo20LV) is provided in Figure 4.25 for $60^\circ/-60^\circ$ and $90^\circ/-90^\circ$ angles on the endocardial/epicardial surface. The fibers pointing in circumferential direction (around 0°) are strongly underrepresented compared to the fiber distribution described by Streeter et al. [38]. Furthermore, the most frequent fiber orientations for the input configuration $90^\circ/-90^\circ$ are around $65^\circ/-65^\circ$ (Figure 4.25, right), which is actually closer to the input configuration $60^\circ/-60^\circ$ compared to $90^\circ/-90^\circ$.

Obtaining more fiber orientated circumferentially can be improved by increasing the number of finite elements in transmural direction. This leads to a smoother transition between

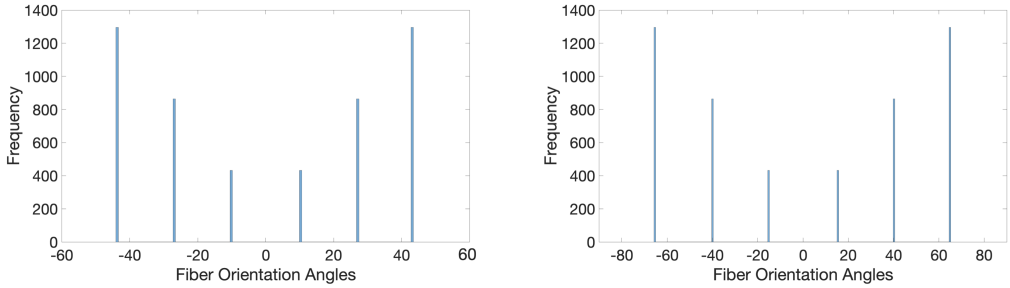

Figure 4.25: A histogram of the fiber orientation assigned to the quadrature points in the finite elements of a LV geometry with fiber angles $60°/-60°$ (left) and $90°/-90°$ (right). On the x-axis, the angles are in degree. Modified from [123], published under the Creative Commons Attribution 4.0 International (CC BY 4.0) License.

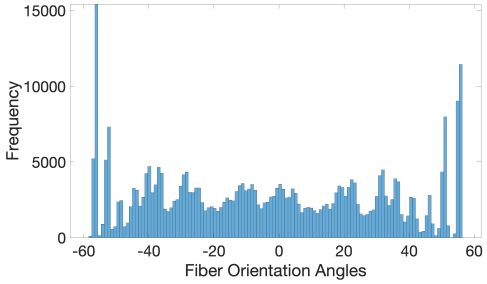

Figure 4.26: A histogram of the fiber orientation assigned to the quadrature points in the finite elements of a LV geometry with fiber angles $60°/-60°$. The geometry had four elements in the transmural direction and 82944 elements in total. On the x-axis, the angles are in degree.

the fiber orientation defined on the endocardial and epicardial surfaces and more continuous transmural rotation of the fibers: e.g. in Figure 4.26, the histogram of the fiber orientation is shown of the LV geometry with four elements in the transmural direction.

Boundary conditions of a whole heart model In the previous work of Fritz et al. [39], no representation of the vessels existed and therefore, nodes, which are part of atrial tissue were fixated in all directions. In this workflow, a representation of the vessels was added to restrict the nodes on the free ends. In geo17, the nodes on all vessels are fixated, while in geo20, only the nodes on the veins are fixated. Augustin et al. [13] also fixated only the veins in a four chamber model. In this work, it was observed that the fixation of the free ends of the arteries restricted the longitudinal contraction of the ventricles. This might be amplified by their short extent: pulmonary artery 10 mm and aorta 20 mm.

Furthermore, in contrast to Fritz et al. [39], in this workflow, the apex was not fixated. The deformation of the apex region was constrained by the sliding boundary condition [39]. In [39] and this work, the influence of the thickness of the pericardium was not investigated and might be included in future studies.

Boundary conditions of a LV model For the LV models, no sliding boundary condition was imposed, but only fixations: at the base (elli15 and geo20LV) and on the free end of a soft tissue added around the apex (geoCardAtl). The latter condition was enforced in a whole heart model as described by Augustin et al. [13].

For the geoCardAtl, this condition was necessary to achieve a mitral valve displacement which matches the one from segmented cine data: the base moves toward the apex. While in geo20LV, the apex moves towards the base, since the base is fixated (as described in [5]).

Conclusion

In this Chapter, a workflow for creating a whole heart model was presented. The geometry was personalized based on static MRI data acquired during the mid diastole. A local coordinate system was generated to approximate the orientation of the myocytes in the myocardium. The tissue surrounding the heart was represented by a pericardial tissue. A pressure-free configuration was estimated. The latter two introduced an error in the geometrical model compared to the segmented surfaces: the mean error was below 3 mm, which is in the range of errors obtained for whole heart segmentation methods. The errors, which occurred in the area around the AV plane, could be reduced by excluding the adipose tissue from the heart model (not tested in this work). The errors, which occurred in the area close to the apex region, can be reduced by using the pressure-free configuration obtained in the fourth iteration. However, the latter configuration leads to higher maximal errors in the RV and LA between the pressure-free and loaded configuration.

Therefore, for this geometrical model, it was decided that having a lower mean error is the preferable scenario (than a higher maximal error): the pressure-free configuration obtained in the second iteration was used in Chapter 5.

The workflow was demonstrated on one geometry with a coarse computational mesh. However, this is not a limitation of the workflow but of the solver CardioMechanics used to perform the numerical experiments. The coarse mesh led to deviations in the angles of the fiber orientation in the model from the angles used as input. This can be improved by estimating the input angles depending on the coarseness of the geometry. Furthermore, the limitation of the solver hinders from preforming a sensitivity analysis by reducing the element size. However, the results obtained with this geometry can be valid since all criteria for element quality at end-diastole (ED) were fulfilled and at end-systole (ES), almost all of them.

Chapter 5

Deformation Evaluation

The motion of the heart tissue is a result of the complex interaction of phenomena, which can be reproduced by mathematical models. These are integrated in a mechanical solver to calculate the tissue deformation. Once a heart model is created (e.g., as described in Chapter 4), a simulation is initiated to calculate the tissue deformation: for each time step of the simulation period, the position of each node in the geometry is obtained.

In this chapter, evaluation metrics are defined to quantify the simulated deformation. These metrics correspond to measures obtained from imaging modalities and allow:

1. quantifying the differences between the deformation of a virtual heart and the deformation measured with imaging modalities or described in the literature,
2. quantifying the influence of variations in model components on the deformation of the virtual heart.

The first point is presented in the current chapter and the second in Chapter 6. Deformation measures obtained for the heart model geo20 (described in Chapter 4) with CardioMechanics are compared to measures derived from magnetic resonance imaging (MRI) imaging data and values, found in the literature for healthy volunteers. A good agreement between the observed and the simulated deformation can prove the fidelity of the numerical experiment and the plausibility of the interaction of the mathematical models used to compute the deformation.

5.1 Methods

5.1.1 Simulation of the Deformation

The deformation of the heart model geo20 was obtained by a simulation initiated with CardioMechanics. The DH active force model (see Chapter 3.3) was applied for the contractile tissue (see Chapter 3.3) with $T_{max} = 160\,\text{kPa}$ in both ventricles and $T_{max} = 40\,\text{kPa}$ in both atria. The passive force model of Guccione [124] with $C = 313\,\text{Pa}$, $b_f = 17.8$, $b_t = 7.1$ and

$b_{ft} = 12.4$ was defined on the entire myocardium. The free ends of the veins in the model were fixated (as described in Chapter 4) and a sliding boundary condition was imposed. The circulatory model was used with initial values as defined in [108]. The result of the second iteration of the unloading algorithm was selected (as described in Chapter 4) as starting configuration for the simulation. The simulation was run 9.6 s, corresponding to 12 heart beats with a cycle length 0.8 s. The entire setting file of the simulation is provided in B. The final beat was evaluated.

The definitions of the evaluation metrics in the following are based on Kovacheva et al. [117].

5.1.2 Evaluation Metrics

Metrics to evaluate the deformation of the left ventricle (LV) and one metric for the left atrium (LA) were introduced based on features, which are commonly evaluated in imaging modalities [125, 126].
The following measures were calculated: *strain*, *strain rate*, *velocity* and *wall thickening* in radial, longitudinal and circumferential directions [125]. To obtain these directions, a local coordinate was defined [125].

Local coordinate system The strain, strain rate and velocities were calculated in a local orthonormal heart coordinate system (R-Lo-C), spanned by radial (R), longitudinal (Lo) and circumferential (C) directions [125]. The radial axis is perpendicular to the epicardium; the longitudinal axis is perpendicular to the radial axis (tangent to the epicardium); the circumferential axis is perpendicular to both the radial and longitudinal axis. The axes were obtained by the algorithm used for creating the fiber orientation [28] with angles 0° on both epicardial and endocardial surface. Figure 5.1 shows the orientation of the R-Lo-C axis for geo17 (for geo20, it looks comparable). For every finite element in the LV geometry, the R-Lo-C axes were calculated at the initial time point of the simulation and preserved over the heart beat.

The measures were evaluated *globally* – one value for the entire ventricle per time point – and *regionally* – one value per one of the 17 American Heart Association (AHA) segments [66] per time point. Regional measures were derived as the mean over all elements in the respective regions.

Spatial separation of the LV in 17 AHA segments To separate the LV in segments, the origin and orientation of the long axis and the coordinates of one point were required. The point was manually selected (from the nodes in the LV tissue) on the anterior junction between the right ventricle (RV) and LV and should be chosen to be in the plane, which is perpendicular to the long axis and contains the origin of the long axis. Based on these inputs, a rotational coordinate for all nodes of the LV is calculated ranging from 0° to 360°. The basal and mid-cavity regions are separated in 6 segments, respectively (1–6 and 7–12), each

Figure 5.1: Local coordinate system spanned by longitudinal (blue, left) circumferential (red, middle) and radial (yellow, right) directions. Adapted from [117] (Creative Commons Attribution 4.0 International (CC BY 4.0) License).

of which contains 60° of the rotational coordinate and the apical-cavity region is separated in 4 segments (13–16), each of which contains 90° of the rotational coordinate. To obtain the separation in basal, mid-cavity, apical-cavity and apex region, an apico-basal coordinate was calculated ranging from 0 (base) to 1 (apex). Thresholds were applied: 0.47 to separate the basal from the mid-cavity region; 0.76 to separate the mid-cavity from the apical-cavity region and 0.96 to separate the apical-cavity from the apex region.

The separation in 17 AHA segments was done for all whole heart geometries in this work. The latter thresholds were used for the healthy geometries (geo20 and geo17). For the hypertrophied one, different values were used: 0.45, 0.7 and 0.88 for geo17HCM1 and 0.44, 0.67 and 0.86 for geo17HCM2, since the endocardial apex should be included in the 17-th segment and in the hypertrophied geometries, the apex region is thickened. The separation of the LV in 17 AHA segments of geo20 is visualized in Figure 5.2, for geo17 and geo17HCM2 in Figure 14 [117].

The regional measures are visualized in bull's-eye displays [66]. Figure 5.3 shows an example of such a display: the septal regions are 2,3,8,9,14 and the free-wall (lateral) regions are 5,6,11,12, 16.

Temporal separation of the heart cycle The measures were calculated during the systolic and during the diastolic period, and at end-systole (ES) and end-diastole (ED). The ES and ED were determined based on the pressure-volume relation. In particular, the ED was at 160 ms and the ES at 500 ms after the start of the last beat (in a multi-beat simulation).

Strain In a one dimensional object, the strain ε (%) describes the change in length relative to the initial length. Positive strain values correspond to lengthening and negative to shortening [125].

In the numerical simulation, the deformation of the heart in each finite element is described by a *deformation gradient tensor* F calculated for each time step of the heart beat. It relates the current shape and displacement of the element to its initial shape and

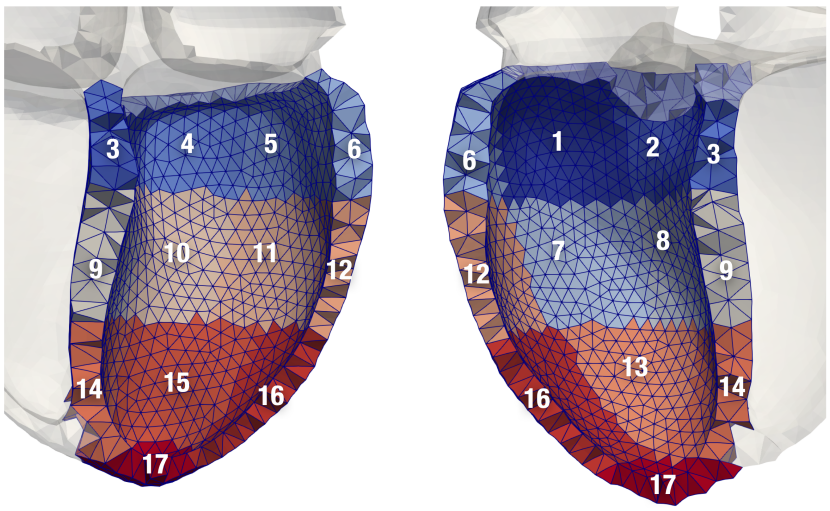

Figure 5.2: The division of the LV of geo20 in 17 AHA segments. Each segment is numbered in both the anterior (left) and posterior (right) views. The apex segment (17) includes the endocardial apex.

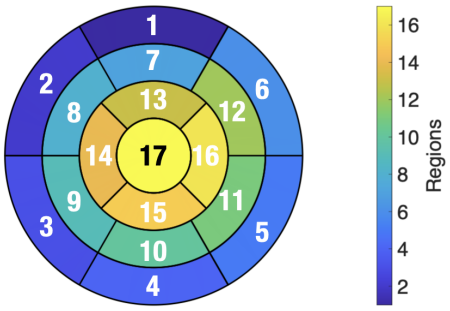

Figure 5.3: A bull's-eye display: the value in each segment is the number of the segment.

displacement. The fiber, sheet, and sheet-normal direction in each element are the one dimensional objects used to calculate the strain in the tissue. The fiber orientation (FO) f_d in the deformed element is $F f_{init}$, where f_{init} is the initial FO (Figure 5.4).

The stretch of the deformed fiber is $\lambda(f_d) = \sqrt{f_{init}^T F^T F f_{init}}$. The strain is calculated from the stretch as $\varepsilon(f_d) = \lambda(f_d) - 1$. The strain of deformed sheet $\varepsilon(s_d)$ and sheet-normal $\varepsilon(sn_d)$ directions is obtained likewise.

In each time step, for each finite element, the strain in the fiber, sheet and sheet-normal directions is calculated in the mechanical solver. The strain in the R-Lo-C system is then calculated by a coordinate transformation

$$\varepsilon_{RLoC} = |T(f_d/\|f_d\|_2)|\,\varepsilon(f_d) + |T(s_d/\|s_d\|_2)|\,\varepsilon(s_d) + |T(sn_d/\|sn_d\|_2)|\,\varepsilon(sn_d). \tag{5.1}$$

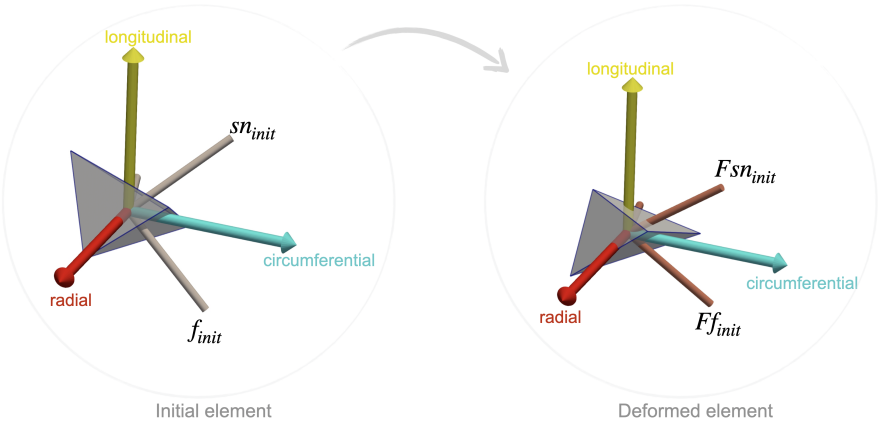

Figure 5.4: An initial state of one finite element (left) and its deformed state (right). The R-Lo-C system is indicated by the red, yellow and cyan coloured arrows. The fiber and sheet-normal orientations and lengths have changed from the initial (f_{init} and sn_{init}) to the deformed state (Ff_{init} and Fsn_{init}).

The matrix T transforms the Cartesian coordinates (with respect to the standard basis of $\mathbb{R}^3$) into the local R-Lo-C coordinates. The rows of T are the vectors of the radial, longitudinal and circumferential axis of the R-Lo-C system in the current element. The strain in radial direction is the first entry of the transformed strain: $\varepsilon_{RLoC}(1)$, the strain in longitudinal direction is $\varepsilon_{RLoC}(2)$ and the strain in circumferential direction is $\varepsilon_{RLoC}(3)$.

Strain rate Strain rate $\dot{\varepsilon}_t$ (%/s) is the speed at which the strain changes [125]. It was calculated at time t with $\Delta t = 0.01$ s

$$\dot{\varepsilon}_t = (\varepsilon_t - \varepsilon_{t-\Delta t})/\Delta t, \tag{5.2}$$

where ε_t is the strain at time t.

Velocity Velocity (m/s) is the temporal change of the displacement. By solving the governing equation of the heart mechanics, the displacement was obtained and thus, the velocity for every node and each time step [104].

The velocity of each finite element was calculated as the mean of the velocity over its four nodes. It was done for each of the three directions in the Cartesian coordinate system: $v = (v_x, v_y, v_z)$. To convert the Cartesian velocity into the local R-Lo-C system, the coordinate transformation with the matrix T was conducted analogous to the transformation of the strain: $v_{RLoC} = Tv^T$. Then, for the observed finite element at the current time point, the absolute value of the velocity in radial direction is $|v_{RLoC}(1)|$, in longitudinal direction $|v_{RLoC}(2)|$ and in circumferential direction $|v_{RLoC}(3)|$. In the following, the absolute value of the velocity will be referred to as *velocity*.

Wall thickening The wall thickness (WT) ω (in mm) of the LV was calculated as proposed by Yezzi et al. [127]: the thickness is the "length of trajectories, which run from one tissue

boundary to the other, and which follow a smooth vector field constructed in the region between the boundaries". For every time step of the heart beat and each surface node, one WT was calculated. The wall thickening (in percent) for time t was then: $(\omega^t - \omega^0)/\omega^0$, where the upper index corresponds to the time with 0 denoting the initial WT.

Mitral valve displacement Due to the sliding boundary condition imposed on the whole heart models, only minor displacement of the apex are available along the global longitudinal axis (mean of all local longitudinal axes). Therefore, the mitral valve displacement is equal to the global LV longitudinal shortening and elongation along the global longitudinal axis. For every time point, all nodes of the LV were orthogonally projected on the global longitudinal axis. With the maximal euclidean distance d^t_{MV} between any two projected points, the valve displacement for time t is then: $(d^t_{\mathrm{MV}} - d^0_{\mathrm{MV}})/d^0_{\mathrm{MV}}$, where the upper index 0 corresponds to the initial geometry configuration at time 0.

Tricuspid valve displacement For the RV, the global longitudinal axis was not calculated to obtain the valve displacement. Instead, two nodes were manually chosen on the endocardial surface of the RV: one on the intersection of the septal wall and the valve ring and the second, the other on the intersection of the free wall and the valve ring. The displacement of the point in the middle of the connecting line of these two points approximated the tricuspid valve displacement.

LV volume The volume of the LV cavity was calculated as well as the normalized volume: for every time point, the current volume was divided by the maximal volume over all time steps (after the atrial kick).

Mechanics of the left atrium The longitudinal strain of LA was evaluated. The main longitudinal axis of the LA was calculated as the mean of the local longitudinal directions over all elements in the LV. For every time point t, all nodes of the LA were orthogonally projected onto the main axis. With the maximal euclidean distance l^t_{LA} between any two projected points, the longitudinal strain for time t is then: $(l^t_{LA} - l^0_{LA})/l^0_{LA}$, where the upper index 0 corresponds to the reference configuration at time 0.

5.1.3 Clinical Data

The clinical data were acquired at the University Hospital in Heidelberg on a 1.5 Tesla MR tomography system (Ingenia CX, Philips Medical Systems). The volunteer gave informed consent and the study was approved by the institutional review board. The data used for validation and for model generation (of geo20) were acquired on the same heart and the same day.

Motion data Long axis and short axis Cine MRI data were acquired to capture the motion of the ventricles. The voxel spacing was $0.77\times0.77\times0.8$ mm (short axis) and

$0.91 \times 0.91 \times 0.8$ mm (long axis), the image dimension was $560 \times 560 \times 160$ voxels, the trigger time was approximately every 20 ms and the mean heart rate of the volunteer was 82 bpm during the acquisition. This resulted in 35 images describing the motion in each slice (12 short axis and 1 long axis).

The data was evaluated by Tobias Gerach using the freely available software Segment (version 3.2 R8531, [128]). The evaluation included LV and RV volume over time, atrioventricular (AV) plane displacement over time, ED and ES wall thickness (for 1–16 AHA segments of LV), contraction and expansion velocities (for 1–16 AHA segments of LV) and segmented short axis slices at ED and ES. The time point for the evaluation of the contraction and expansion velocities was the maximal change in LV volume during contraction and relaxation, respectively.

Strain data Strain-encoded magnetic resonance images (SENC) were acquired to measure the deformation of the LV [129]. A tool (MyoStrain[1], Myocardial Solutions, Morrisville, NC, USA) available at the University Hospital in Heidelberg was used to evaluate the longitudinal strain of the LV at mid-systole and at ES.

End-systolic state The heart morphology at ES was captured by a 3D whole heart MRI scan. The voxel spacing was $0.62 \times 0.62 \times 0.8$ mm, the image dimension was $560 \times 560 \times 160$ voxels and the mean heart rate of the volunteer was 78 bpm during the acquisition. As described in Chapter 4.1.1, the images were automatically segmented to obtain the endocardial surfaces. While the segmentation of the 3D whole heart images acquired at diastasis were used to create the geometry of the heart (Chapter 4.1.1), these segmentations were used to compare the end-systolic state of the simulated deformation of the created model.

The peripheral blood pressure of the volunteer was 135/90 mmHg, obtained by a cuff measurement one hour after all images were acquired.

5.2 Results

5.2.1 Comparison between Simulated and Clinically Measured Deformation

Motion data

Volume Figure 5.5 shows the absolute (first row) and the normalized volume (second row) of the LV (red curves) and RV (blue curves) and the volume obtained from the segmented short axis Cine MRI data (black dotted curves). The LV volume obtained from the long axis and the short axis Cine images differed by only 0.5 ml.

[1] Available at `https://www.myocardialsolutions.com`

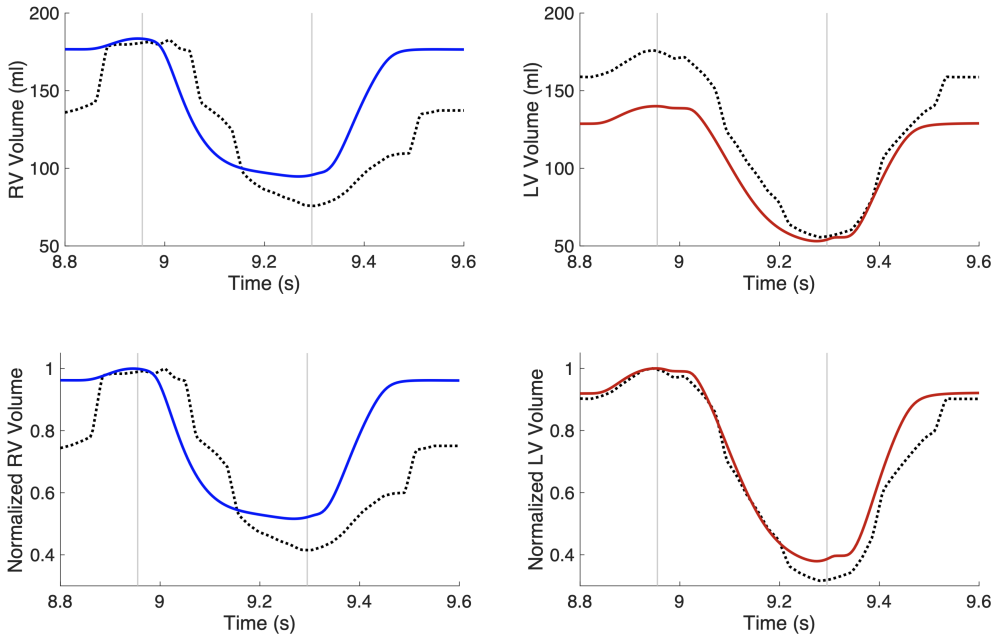

Figure 5.5: A comparison between the LV and RV volumes obtained in the simulation (red and blue curves, respectively) and from the MRI data (black dotted curves). First row: the absolute volumes. Second row: the normalized volumes. In each plot, the first vertical line (at 8.96 s) indicates ED and the second line (at 9.3 s) ES.

The initial LV volume of the virtual heart is underestimated compared to the clinically measured volume: 128 ml and 158 ml, respectively. The left atrial kick contributes 12 ml and 17 ml to the simulated and clinically measured LV volume, which is 9.3 % and 10.7 % of the ED volume, respectively. At ES, the LV volumes were matching well: 54 ml (simulated) and 55 ml (clinical data). Furthermore, the morphologies of the LV volume curves matched: the ES and ED occurred at the same time point and thus, the time extent of the contraction was equal: from 8.96 s to ES (9.3 s). The expansion of the LV in the MRI data was slightly longer (40 ms) than in the simulation. The ejection fraction (EF) of the virtual LV was 63 % and the stroke volume (SV) was 88 ml, while those obtained from the clinical data were 68 % and 120 ml.

The initial RV volume of the virtual heart is overestimated compared to the clinically measured volume: 176 ml and 136 ml, respectively. The right atrial kick contributes 7 ml and 45 ml to the simulated and clinically measured RV volume, which is 4 % and 33 % of the ED volume, respectively. This difference is apparent in the plot of the normalized volumes (Figure 5.5, second row, left). At ES, the RV volumes were differing: 95 ml (simulated) and 75 ml (clinical data). Additionally, the contraction of the virtual RV was initiated about 40 ms earlier compared to one observed in the clinical data. Similar to the LV, the expansion of the RV in the MRI data was slightly longer (50 ms) than in the simulation. The ejection fraction (EF) of the virtual RV was 51 % and the SV 88 ml (same as the one of the LV), while those obtained from the clinical data were 58 % and 106 ml.

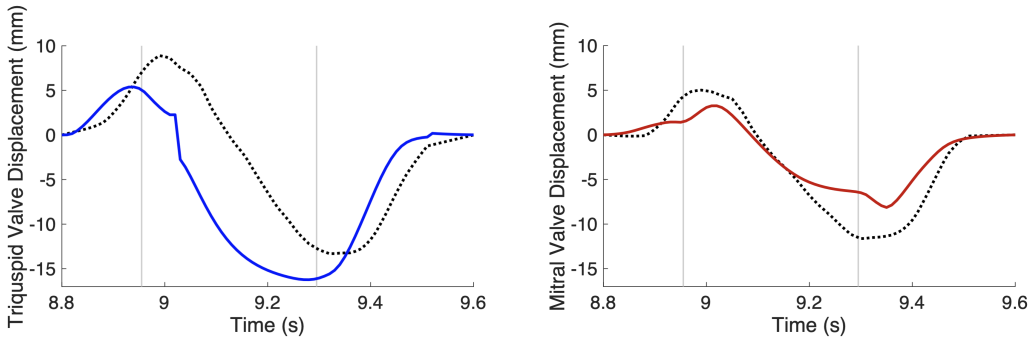

Figure 5.6: A comparison between the mitral and tricuspid valve displacement obtained in the simulation (red and blue curves, respectively) and from the MRI data (black dotted curves). In each plot, the first vertical line (at 8.96 s) indicates ED and the second line (at 9.3 s) ES.

AV displacement Figure 5.6 shows the displacement of the tricuspid (blue curve) and mitral valve (red curve) compared to these displacements obtained from the segmented long axis Cine MRI data (black dotted curves).

While the mitral valve displacement of the virtual heart is underestimated compared to MRI data during the entire cycle, the tricuspid valve displacement is underestimated only during the atrial systole. During the ventricular systole, it is slightly overestimated. However, the extent of the displacement values for both virtual tricuspid valve and clinically measured one were 22 mm. The extent of the displacement values for the virtual LV valve was 11 mm, while the mitral valve in the MRI data displaced by 17 mm, in total.

Wall thickness The first row of Figure 5.7 shows the ED (left) and ES (right) wall thickness measured in 16 AHA segments (apex is excluded) of the virtual LV (red circles) and in the short axis Cine MRI data (black circles). The second row of Figure 5.7 shows the wall thickening. While the ED WT is slightly overestimated in most of the segments of the virtual LV, the ES WT appears in a similar range as the thickness obtained from the MRI data. Therefore, the wall thickening of the virtual LV is lower than the one from the MRI data.

Contraction and expansion velocity Figure 5.8 shows the contraction (left) and expansion (right) velocities measured in 16 AHA segments (apex is excluded) of the virtual LV (red circles) and in the short axis Cine MRI data (black circles). Since the short axis is used as a base for the calculation of the clinical data, for the simulated data, the radial velocities were provided. They were evaluated at the time point of maximal change in the simulated volume.

The velocities in all segments were indicating slower motion in the virtual LV compared to the MRI data since they are closer to zero during both contraction and expansion. However, the distribution among the segments is comparable: the basal segments (1–6) deformed faster than the mid-cavity segments (7–12). The apical segments (13-16) were the slowest. During

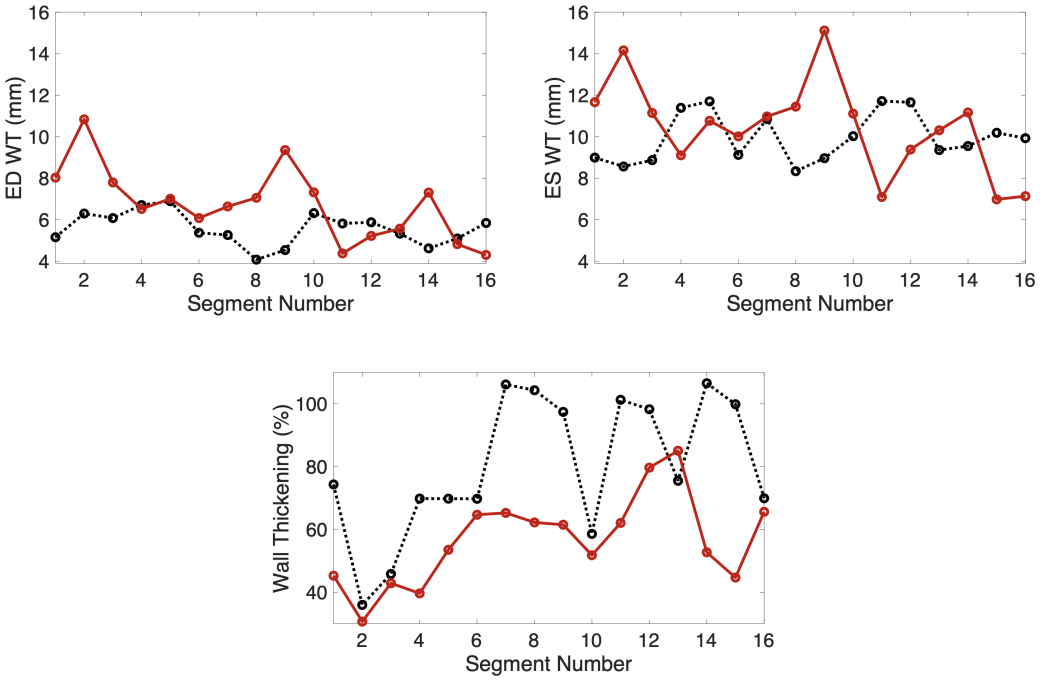

Figure 5.7: First row: A comparison between the end-diastolic (left) and end-systolic (right) wall thickness of the LV obtained in the simulation (red circles) and from the MRI data (black circles). Second row: A comparison between the wall thickening obtained in the simulation (red curve) and from the MRI data (black dotted curve). The x-axis provides the number of the AHA segment, as shown in Figure 5.3. ED: end-diastolic, ES: end-systolic, WT: wall thickness.

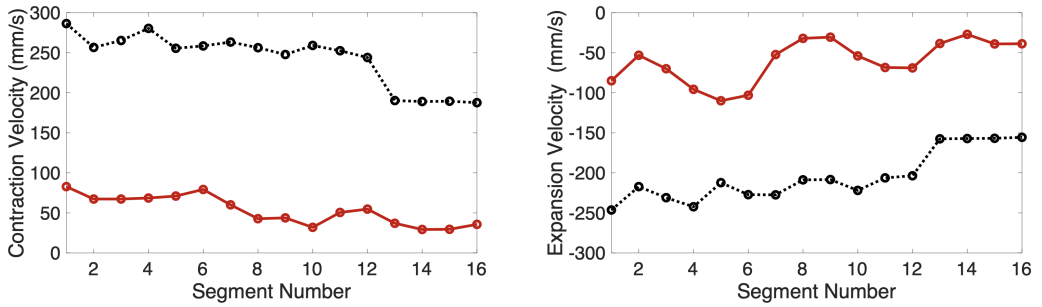

Figure 5.8: A comparison between the contraction (left) and expansion (right) velocities of the LV obtained in the simulation (red circles) and from the MRI data (black circles)

contraction, this spatial difference was more prominent in the MRI data compared to the virtual LV.

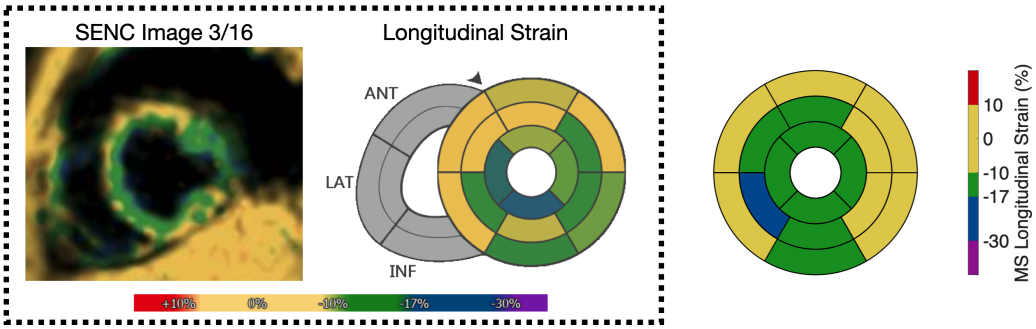

Figure 5.9: A comparison between the longitudinal strain at mid-systole (MS) of the LV obtained in the simulation (bull's eye plot on the right) and from the MRI data (framed by the black dotted lines, on the left): the MRI data contains the bull's eye plot, the strain values and the SENC colour-coded image (evaluated in MyoStrain).

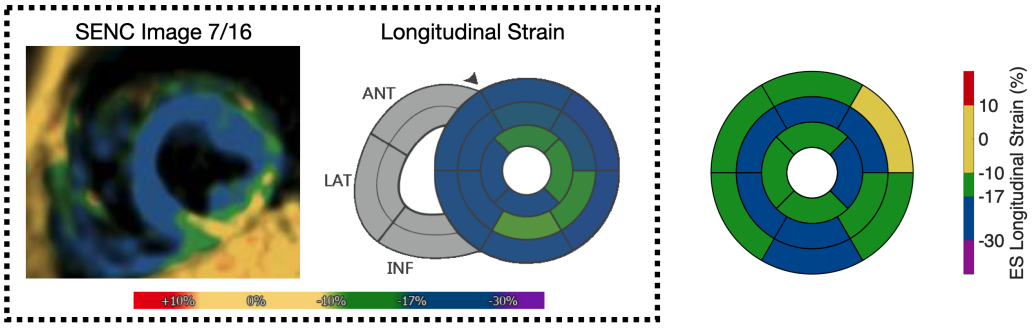

Figure 5.10: A comparison between the longitudinal strain at end-systole (ES) of the LV obtained in the simulation (bull's eye plot on the right) and from the MRI data (framed by the black dotted lines, on the left): the MRI data contains the bull's eye plot, the strain values and the SENC colour-coded image (evaluated in MyoStrain).

Strain data

Figure 5.9 and Figure 5.10 show a comparison between the longitudinal strain of the simulated LV and the one obtained via clinical evaluation of SENC data at mid-systole (MS) and ES, respectively. The strain of the simulated LV is shown in the same colour map as the clinically evaluated data. At MS, the basal segments (1–6) of the simulated LV indicated longitudinal shortening in the same range as in the MRI data, while the other segments differ slightly. At ES, the mid-cavity segments (7–12) of the simulated LV indicated longitudinal shortening in the same range as in the MRI data, while the basal segments were indicating less shortening in the simulation result.

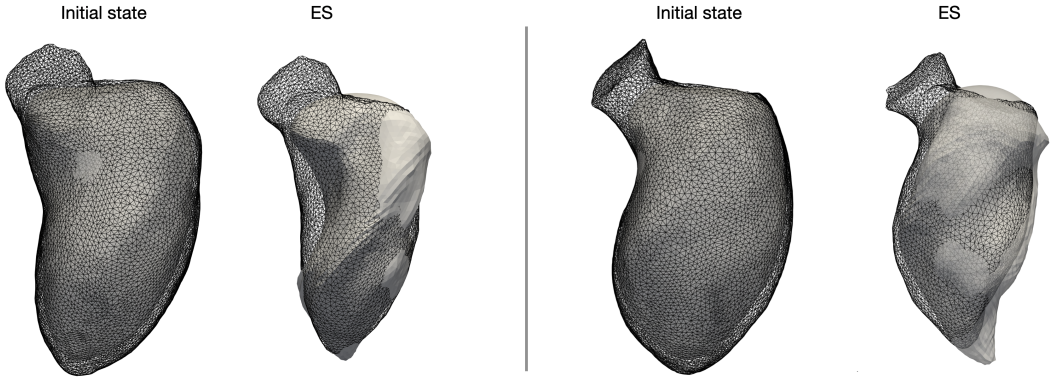

Figure 5.11: A superposition of the end-diastolic (ED) and end-systolic (ES) state of the LV endocardial surfaces obtained in the simulation (grey surface) and segmented from the 3D whole heart MRI data (black wireframe). Left to the vertical line: anterior view. Right to the vertical line: lateral view.

End-systolic state

LV comparison Figure 5.11 shows the simulated result (gray surface) superimposed on the automatically segmented LV endocardial surface. The initial and ES states are shown in anterior and lateral views. Since the endocardial surface of the heart model is created based on the segmented surface at diastasis (as described in Chapter 4), the surfaces match except for the apex region, where an error due to the unloading/loading procedures is introduced. The ES states differ slightly: in the anterior view, a deviation in the septal region is visible and in the lateral view, an apex region is deformed differently.

Whole heart comparison Figure 5.12 shows the simulated heart (grey wireframe) and the automatically segmented endocardial surfaces of the four chambers (black wireframe) at ES. The simulated displacement of the AV plane is comparable to the one obtained from the segmented surfaces of the static whole heart MRI images. Therefore, the elongation in the atria due to the ventricular contraction was comparable to the one visible in the clinical data. The RV had smaller volume in the segmented data compared to the simulated result, especially visible around the AV plane.

Pressure-volume loops The pressure volume loops of the four chambers for the last beat are provided in Figure 5.13. The maximal LV and aortic pressure was 134 mmHg and the minimum aortic pressure was 80 mmHg (not visible in Figure 5.13). The volunteer had a measured peripheral blood pressure of 135/90 mmHg, which upper limit is slightly higher than the pressure value in the heart for healthy volunteer [102]. No other pressures were measured but the RV ES pressure of 36 mmHg is above the healthy ranges (15-25 mmHg).

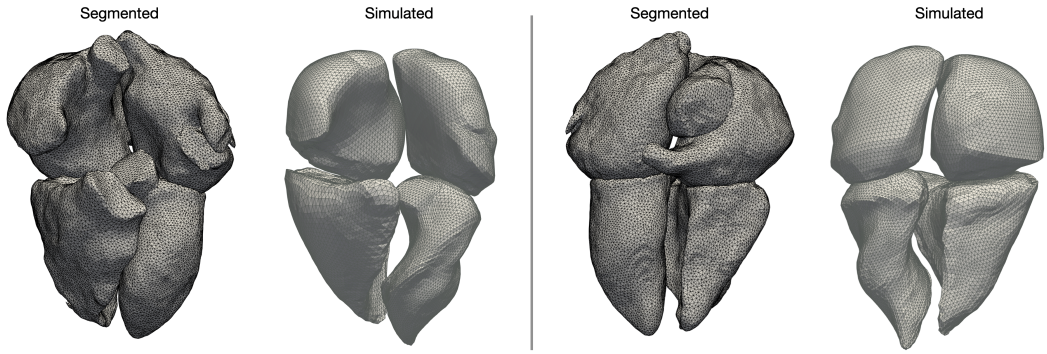

Figure 5.12: A comparison between the end-systolic state of the endocardial surfaces of the whole heart obtained in the simulation (grey wireframe+grey surface) and segmented from the 3D whole heart MRI data (black wireframe+grey surface). Left to the vertical line: anterior view. Right to the vertical line: posterior view.

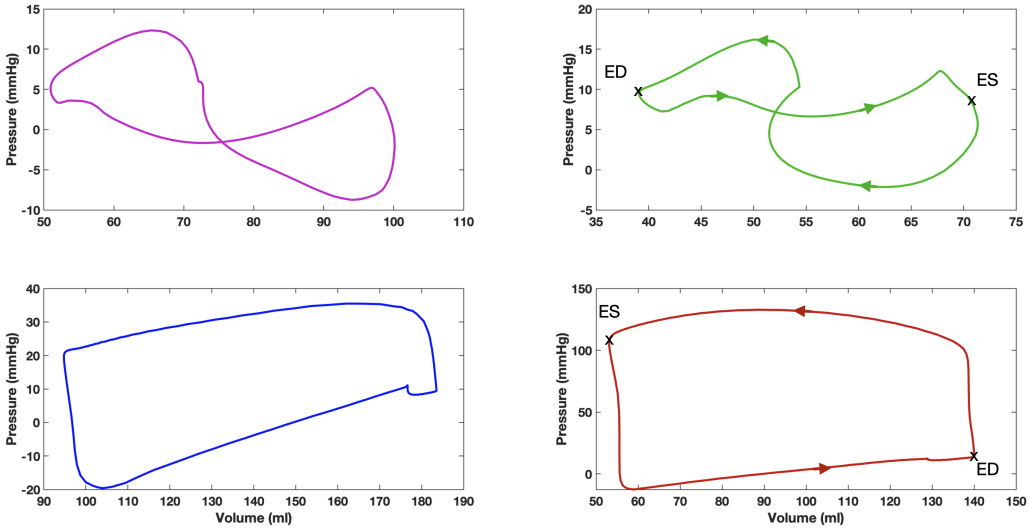

Figure 5.13: The pressure-volume loops of the four chambers during the last beat: RA magenta, RV blue, LA green and LV red curves. ES indicates the end-systole of the LV and ED indicates the end-diastole of the LV.

5.2.2 A Comparison between Simulated Deformation and Literature Values

For the strain curves, the circumferential and radial strain at ES, the strain rates and velocities, no clinical data were available and therefore, they were compared with literature values for healthy volunteers.

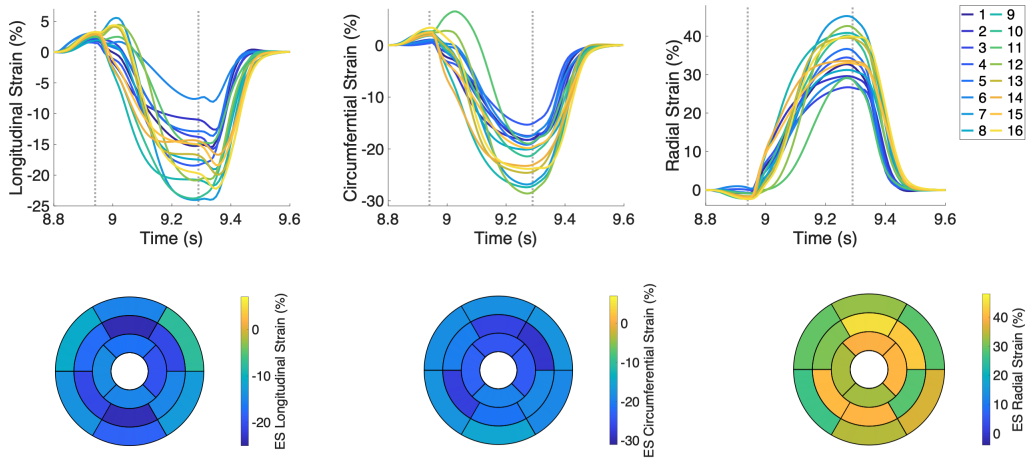

Figure 5.14: The strain over time (first row) and strain at ES (second row) for the simulated result for 16 AHA segments (the apex was excluded). Left: longitudinal strain; Middle: circumferential; Right: radial direction. In each plot, the first vertical line (at 8.96 s) indicates ED and the second line (at 9.3 s) ES.

Strain Figure 5.14 shows the strain curves for 16 segments and their strain distribution at ES for the virtual heart. During the atrial contraction (left to the first vertical line at 8.96 s in each plot), the longitudinal and circumferential strain increased for all segments. This is also visible in the strain curves provided in Figure 2 in [130]. In both the simulated and the measured curves, the increase of the strain in the longitudinal direction at ED was more prominent compared to the one in circumferential direction.

The longitudinal strain at ES matched literature values for the mid-cavity segments (they also matched the measured strains of this particular heart, as described previously). The longitudinal strain in the other segments was too low: it was ranging up to -5 %, while reference ranges were from -24 % to -13 %, Table 4 in [131] (absolute strain values were converted to %).

The circumferential strain at ES matched literature values for most of the segments: in the virtual heart, it was ranging from -28 % to -12 %, while reference ranges were from -26 % to -17 %, Table 4 in [131]. The radial strain at ES was overestimated (25 % to 45 %) compared to reference values ranging from 12 % to 35 %, Table 4 in [131]. However, in Figure 2 in Nabeshima et al. [130] radial strain values between 40 % and 80 % were shown.

Strain rate and velocity Figure 5.15 shows the strain rates and velocities for the 16 segments. The maximal systolic strain rates in longitudinal and circumferential direction were around -220 %/s, while the minimal values were -70 %/s. Augustine et al. [131] measured values between -70 %/s and 160 %/s. In the simulated result, the radial strain rates were higher, up to 400 %/s, compared to the measured rates, up to 170 %/s. Since the strain rate reflects the change in the strain values, the latter mismatch is a direct result of the higher ES radial strain compared to the measured one, described previously.

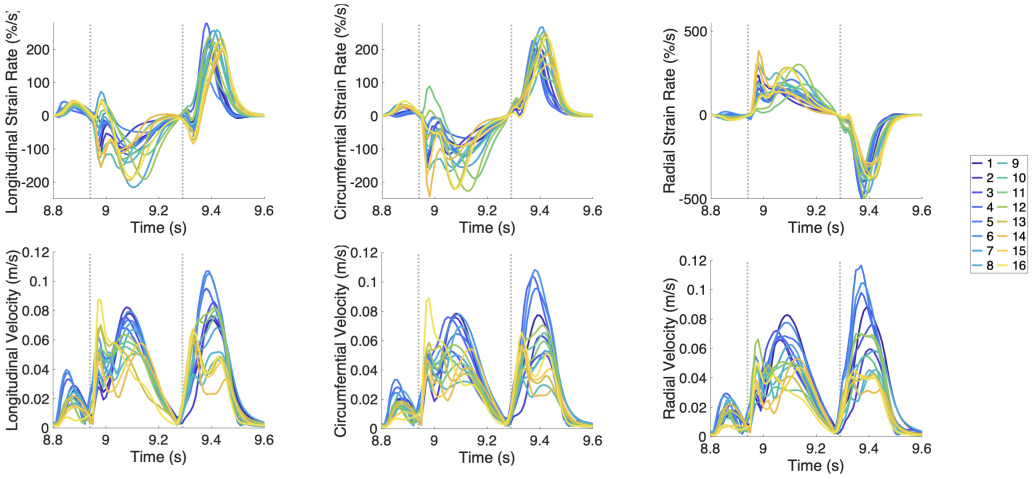

Figure 5.15: The strain rate (first row) and velocity (second row) over time for the simulated result for 16 AHA segments (the apex was excluded). Left: longitudinal strain; Middle: circumferential; Right: radial direction. In each plot, the first vertical line (at 8.96 s) indicates ED and the second line (at 9.3 s) ES.

If the sign of the rates are ignored for a moment, the measured strain rates in all directions have approximately the same range [131]. For the simulated result, this was observed for the velocities in all directions (and not for the strain rates) during the entire heart cycle. Measured longitudinal systolic velocities were between 0.017 m/s and 0.034 m/s and the velocity decreased from base to apex (Table 3 in [131]). Similar gradual decrease between velocities from basal (segment 1–6) to apical (segment 13–16) segments was present also in the simulated results at MS. However, the maximal velocities in the virtual heart (up to 0.08 m/s) were more than double of the measured values. Furthermore, a gradual decrease of the velocities from basal to apical segments was present also during the diastolic period and for the other two directions, especially visible during the relaxation in radial direction. In contrast, measured systolic velocities in radial direction were rather homogeneous, between 0.022 m/s and 0.028 m/s [131].

Li et al. [132] measured significant differences in velocity, strain and strain rate between lateral (segment 5, 6, 11, 12 and 16) and septal areas (segment 2, 3, 8, 9 and 14) of the LV, which were not present in the virtual heart.

Global measures Figure 5.16 shows global measures evaluated for the LA and LV. The peak LA longitudinal strain was 20 %, which is lower than clinically measured values: around 27 % [133]. The global peak systolic longitudinal strain was -17 %, which is slightly underestimated compared to -19 % [131], but in the range provided by Truong et al. [134] (-15.8 % to -23.4 %). The global peak systolic circumferential strain was -21 %, which is exactly the value provided in [130, 131]. The global peak systolic radial strain was 36 %, which is higher than 25 % [131] but also lower than 60 % [130] and inside the range 19.8 % to 86.6 %, provided in [134].

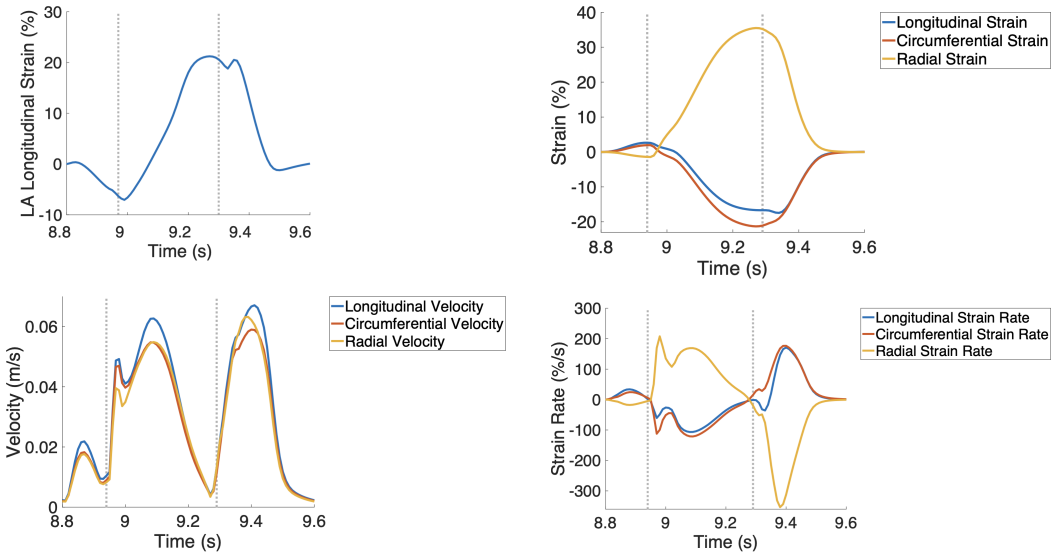

Figure 5.16: Global measures of deformation: LA longitudinal strain (top left); strain (top right), velocity (bottom left) and strain rate (bottom left) of the LV, averaged over 16 AHA segments. In each plot, the first vertical line (at 8.96 s) indicates ED and the second line (at 9.3 s) ES.

All global velocities were overestimated in the simulation result compared to [131]. The global peak systolic longitudinal strain rate was comparable to measured values, which were -108 %±24 %/s, while the strain rate in radial direction was higher in the virtual heart compared to measured values (-125 %/s±40 %/s) [131].

5.3 Discussion

A framework for evaluation of the simulated heart deformation was presented. The evaluated measures were compared to clinical data and values obtained from the literature. The comparison showed good agreement for some of the measures: normalized volume curves, tricuspid valve displacement, ES WT and strain values.

Clinically measured deformation The initial volume of the LV was too low compared to the clinical data (see Figure 5.5 and the visual comparison to static MRI (Figure 5.11)). This is partly due to the choice of unloading state from the second iteration, which led to an inflated volume of 126 ml. The inflated volume of the unloading state from the fourth iteration led to an inflated volume of 145 ml, which matches the initially segmented LV (146 ml) from the static MRI images. While the LV fitted very well, the absolute error in the RV and LA was higher (see Chapter 4.3). Furthermore, a strong bending of the posterior wall in the unloaded LV led to not plausible stretch values and therefore, wrong strain evaluation in the LV. Note that the initial volume of 126 ml (inflated state) slightly shifted to 128 ml in the final beat due to adaptations made by the circulatory model.

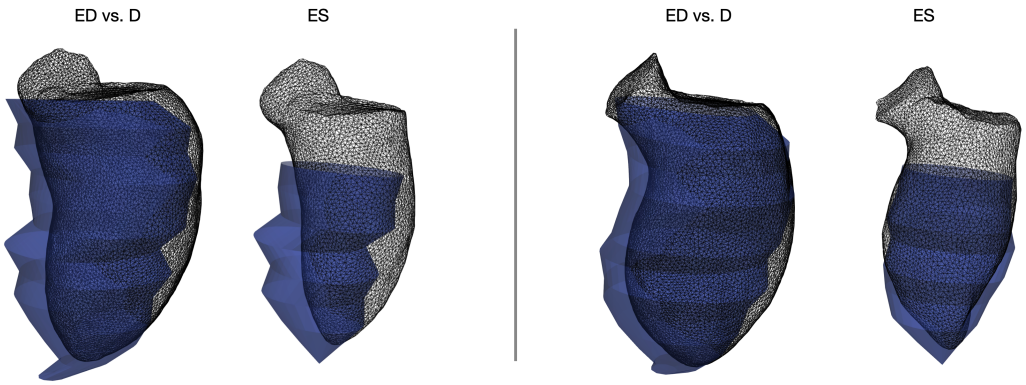

Figure 5.17: A superposition of the segmentation of the LV endocardial surface obtained from short axis Cine MRI (blue surface) and the 3D whole heart MRI data (black wireframe). Left to the vertical line: anterior view. Right to the vertical line: lateral view.

Additionally, there was a disagreement between the volume calculated from the Cine MRI (158 ml) and the one from static MRI (146 ml). Figure 5.17 shows a comparison between the short axis segmentation of the Cine MRI exported from the tool Segment (blue surface) and the LV segmentation of the static MRI exported from the Philips IntelliSpace Portal (black wireframe). The ED state from the Cine MRI is superimposed on the state acquired during diastasis (D), just before the atrial kick. The difference at ES is apparent and it seems that the segmentation of the Cine data did not include the regions close to the mitral valve. However, values derived from the segmented short axis Cine slices were used to compare to the simulation output.

While the onset of decrease of volume matches between simulated and measured results for the LV, for the RV, a time shift is present (second row in Figure 5.5). In the simulation, all elements in the ventricles were activated simultaneously, which might contribute to this time shift. A more physiological activation might improve this mismatch, e.g. providing the local activation time of each cell according to a prior simulation of the electrical activation of the tissue. Additionally, the isovolumetric contraction of the LV lasted slightly longer than the one of the RV.

The circulatory model included in the simulation yields equal SV between the LV and RV (88 ml). However, in the clinical data, this was not the case: the LV SV was 120 ml and the RV SV was 106 ml. This indicates an error in the segmentation since the SV of both ventricles in a healthy heart is equal.

During the acquisition of the data, the volunteer had different heart rates. Therefore, the volumes and valve displacement time courses were extended by values which linearly interpolate the last and the first value in the time series to obtain a time extent of 0.8 s.

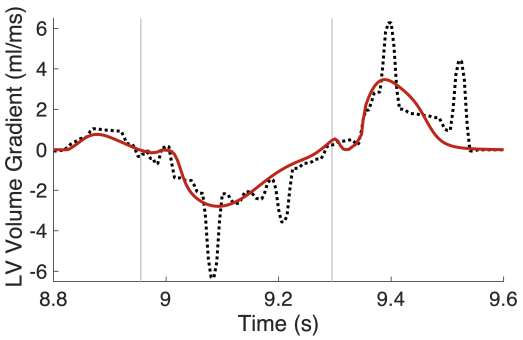

Figure 5.18: The gradient of the LV volume for the simulated (red curve) and measured volume in the MRI images (black dotted curve). The first vertical line (at 8.96 s) indicates ED and the second line (at 9.3 s) ES.

The maximal contraction and expansion velocities were strongly underestimated in the simulated heart compared to the clinically measured. The time points to determine these velocities is the time of maximal change in the LV volume in the simulated and clinically measured curves, respectively. Figure 5.18 shows the gradient of the LV volume for the simulated and measured volume in MRI images. Generally, both follow the same course, which is expected since the absolute volume curves matched well. However, in the MRI volume gradient, there are outliers which coincide with the maximal gradient values of the simulated volume. The change in the volume is directly related to the change in the position of the short slices which determines also the velocity. Therefore, it was assumed that the high maximal contraction and expansion velocities in the clinical data are related to this too rapid changes in the volume and therefore, might be wrongly overestimated. The segmentation of the slices in one time frame might include the papillary muscles and in the next frame, they might be excluded and therefore, the volume changes are higher than in reality.

Deformation values reported in the literature Imaging techniques are promising clinical tools for assessment of myocardial performance and for the calculation of strain, strain rates and velocities in the tissue. However, different modalities in combination with different vendors provide often wide value ranges [134]. Therefore, there are no normal values provided by current guidelines and no true “gold standard” for 3D myocardial mechanics [130, 135]. Recent effort in standardization of strain led to a markedly reduction of inter-vendor variability in the longitudinal strain calculations [135].

The ranges used for a comparison between the simulated deformation and the one measured in clinical studies were derived from feature tracking MRI, which showed reasonable agreement with tagging MRI and acceptable inter-observer reproducibility [131]. Furthermore, values derived from echocardiography speckle tracking analysis [130] were compared to the simulated result.

The zero reference point of the strain curves in [130] were at ED, while zero reference point for the evaluation of the simulation was set prior the atrial kick. This difference was

not regarded during the comparison. However, it might be minor compared to the general differences among the literature values.

For the RV, no strain, strain rate or velocity was calculated. Also, the subdivision in standard segments for the RV cannot be achieved as described for the LV, since it requires an ellipsoid-like geometry to obtain the rotational coordinate. However, this could be avoided by developing a separation based on bi-ventricular coordinate system, e.g. Cobiveco [136].

Conclusion

A framework was presented, which allows evaluating the deformation of a virtual heart via measures commonly used in clinical practice. The deformation obtained in the simulation was validated against clinically measured MRI data and general value ranges provided in the literature for healthy hearts. The morphology of the LV volume matched the one obtained from Cine MRI very well. The strain in all directions was in ranges also found in the literature.

However, already for one heart, differences were present between measures extracted from the static whole heart acquisition and the Cine MRI. Furthermore, more information could be extracted from the available clinical data. The values found in the literature could not uniquely provide correct values but were rather value ranges indicating directions. Therefore, it is important to obtain a large data set for an extensive analysis of one heart. In future, the data set can be separated to 1) generate the heart model 2) calibrate the model and its parameters and 3) validate the model.

Chapter 6

Sensitivity Analysis and Application in Hypertrophic Cardiomyopathy

Here, a sensitivity analysis is presented. The variation in the model components is based on literature values applicable for hypertrophic cardiomyopathy (HCM).

HCM results in an increased ratio of wall to lumen volume, which can be diagnosed by echocardiographic or magnetic resonance assessment of left ventricular anatomy [70]. Besides this morphological modification, further abnormalities are underlying the HCM phenotype.

In HCM hearts, fibrosis and myocardial cell disarray can be present and might have evolved for years before the onset of symptoms [70]. The disarray of the cells can be quantified by fractional anisotropy (FA) – a measure obtained by diffusion tensor magnetic resonance imaging (DT-MRI) or shear wave imaging (SWI). Ariga et al. [74] reported reduced FA in HCM patients compared to control subjects, measured by DT-MRI. Villemain et al. [75] reported similar findings in pediatric HCM patients using SWI.

Further structural abnormalities in HCM were detected by SWI on an organ level: passive ventricular stiffness was significantly higher in HCM compared to the control group [75]. In HCM, increased stiffness on the organ level could not be explained by an alteration in the viscoelastic properties of the cardiac myocytes, since the passive stiffness of prepared HCM cardiac myocytes was measured to be the same as healthy donor myocytes [76]. The stiffer tissue behaviour might be due to further factors such as cell disarray or tissue fibrosis. Furthermore, the maximal active force was markedly lower in HCM myocytes than in donor myocytes [76]. In clinical routine, it is not possible to measure active force development of the myocytes in vivo. Furthermore, the application of SWI for stiffness measurement is limited to the entire ventricle and might be not applicable for all patients [137]. A

reconstruction of the myocardial cell orientation with DT-MRI is very time consuming and delivers limited anatomical coverage of the ventricle [138].

These limitations of the available imaging modalities make it impossible or at least cumbersome to identify abnormalities underlying the HCM phenotype in clinical routine. Nevertheless, the consequences of these structural changes can be measured and quantified to provide a basis to diagnose HCM. This diagnosis is often based on echocardiographic assessment of the systolic and diastolic function of the left ventricle (LV) [70] and parameters derived from tissue imaging (strain and strain rate) [77]. Furthermore, MRI can quantify heart motion and function by cine imaging, which enables LV wall thickness calculation. Tissue phase mapping and feature tracking provide LV radial, circumferential and longitudinal myocardial velocity time courses, as well as global and segmental systolic and diastolic peak velocities [73]. The left atrial longitudinal strain is measured as well to inform HCM diagnosis [78]. Such precise assessment of the cardiac function enables the quantification of altered mechanics in HCM patients compared to healthy volunteers.

In this chapter, in-silico experiments were conducted to identify potential underlying causes of altered ventricular mechanics observed in HCM patients. Models capturing different pathological mechanisms were defined in a virtual heart and different combinations of these were explored to analyse their effect on ventricular mechanics.

The identification of distinct underlying abnormalities leading to the altered mechanical behaviour of HCM hearts complementary to imaging could be valuable information for clinicians on the way to clearer and faster diagnoses. It can provide directions to differentiate HCM from other cardiac conditions in which thickened walls are present. Moreover, it could help to separate healthy hearts from HCM genotype-positive but phenotype-negative hearts.

This sensitivity study aims at 1) establishing cause-effect relationships between pathological mechanisms in HCM hearts and their effect on ventricular mechanics and 2) comparison of the mechanical behaviour of the virtual hearts to literature reports of clinical measurements.

6.1 Methods

6.1.1 Sensitivity analysis

The internal forces (passive and active) were varied, geometries with increased wall thickness (WT) of the LV were applied and the fiber orientation (FO) in the LV was distorted. For all cases, the external forces were defined using the same parametrization of circulatory and pericardial models. Furthermore, an identical unloaded and loaded state for each geometry was used to initiate the simulations. All simulations were run for 2.4 s and the third (last) beat was evaluated with the framework presented in Chapter 5.

Passive forces The input parameters of the passive force model (described in Chapter 3.3), which determines the tissue stiffness was varied. The parameters of the passive force model

for the control case were identified as described in Chapter 7: $C = 309$ Pa, $b_f = 17.8$, $b_t = 7.1$ and $b_{ft} = 12.4$ was used for for the Guccione model [124]. Villemain et al. [75] measured a five fold increase of the stiffness in HCM patients compared to controls. Thus, the parameter C which determines the global stiffness was increased to 1545 Pa for the entire myocardium (all four chambers) to capture increased tissue stiffness.

Active forces The input parameters of the DH active force model (described in Chapter 3.3) were varied. For the control case, the scaling parameter of the active force, T_{max}, was set to 100 kPa in both ventricles and 35 kPa in both atria. These values were chosen to obtain a control systolic LV pressure of 120 mmHg in the control geometry. Hoskins et al. [76] measured a 40 % decrease of the active force in HCM donor cells compared to controls. Therefore, the maximal active force was reduced to $T_{max} = 60$ kPa in both ventricles and to 21 kPa in both atria. Furthermore, for the control geometry, the maximal active force was increased by 40 % to $T_{max} = 140$ kPa in both ventricles, since the heart might try to compensate changes in the stiffness by increasing the active force.

Wall thickness The WT of the LV of the control geometrical model (geo17) was modified as described in Section 4.1.4. Two geometries with hypertrophic LV walls were applied in this study: geo17HCM1 with WT (mean $\pm$ std) 15 $\pm$ 3.3 mm and geo17HCM2 with WT 17 $\pm$ 4.1 mm. The control and the hypertrophic geometries are visualized in Figure 4.17.

Fiber orientation Two configurations of FO in the LV of the hypertrophic geometries: one control case and one representing fiber disarray. The control FO was determined by the adapted rule-based algorithm based on Bayer et al. [28] (described in Section 4.1.4).

Ariga et al. [74] measured fiber disarray in HCM hearts. The adapted rule-based algorithm was modified to yield disarrayed FO in the mid-wall ring of the LV (described in Section 6.1.2). On the epicardium and endocardium, the same angles were used as in the control case. The disarray was quantified by calculating the FA in the mid-wall ring, which was 0.95$\pm$0.11 for control and 0.81$\pm$0.25 for the disarrayed FO (Figure 6.1). The minimum FA (0.3) for the control fiber was at the junction of LV and RV.

Overview Table 6.1 provides an overview of the cases covered in the sensitivity analysis. Each case is defined by a combination of the four model variants described above. Case 3.1 and Case 4.1 are additional to the cases described in Kovacheva et al. [117].

6.1.2 Modeling of Fiber Disarray

Fractional anisotropy Ariga et al. [74] visualized the myocardial microstructure of HCM hearts with DT-MRI. DT-MRI allows quantifying the direction of diffusion of water molecules, which can be translated to FA. A diffusion-weighted signal intensity is measured to construct the diffusion tensor [139]. The DT is a 3$\times$3 matrix obtained for each voxel and can be transformed to a diagonal matrix with its eigenvalues λ_1, λ_2 and λ_3 as diagonal

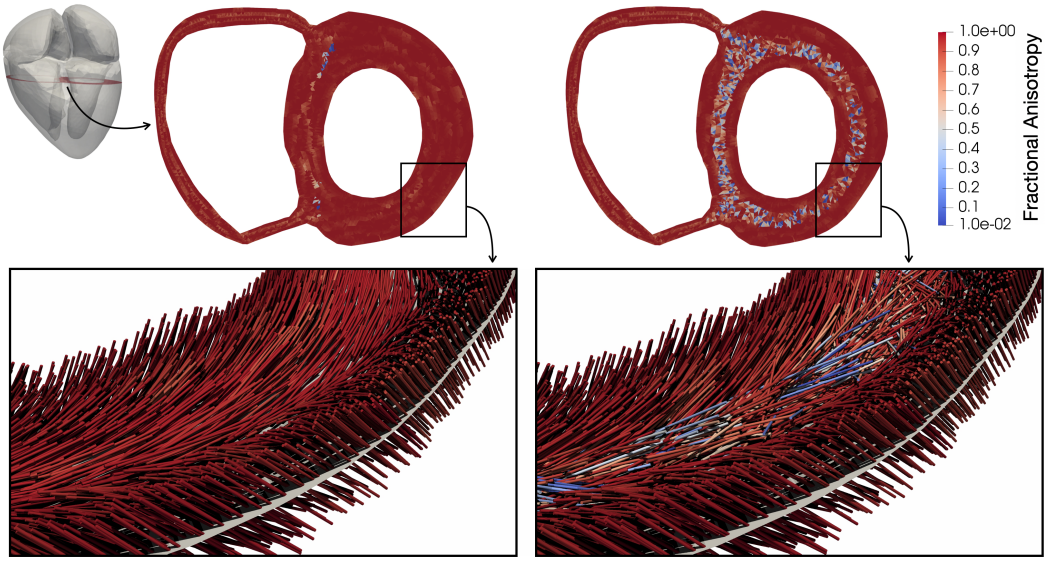

Figure 6.1: Fractional anisotropy (FA) and fiber orientation in a slice of the LV wall of geo17HCM2. FA is colour-coded in short-axis slices. Bottom: close-up of fiber orientation in a part of the LV free wall. Left: control fiber orientation. Right: fiber disarray. Adapted from [117], published under the Creative Commons Attribution 4.0 International (CC BY 4.0) License.

elements [139]. The eigenvector belonging to λ_1 indicates the orientation of the long axis of the myocytes and λ_1 the magnitude of the diffusion in this direction. The other two eigenvectors are orthogonal to the primary one and define a transverse orthogonal plane. FA is calculated from the eigenvalues of the DT as follows [139]:

$$FA = \sqrt{\frac{3}{2}}\sqrt{\frac{(\lambda_1 - D_{av})^2 + (\lambda_2 - D_{av})^2 + (\lambda_3 - D_{av})^2}{\lambda_1^2 + \lambda_2^2 + \lambda_3^2}}, \tag{6.1}$$

where D_{av} is the mean diffusivity, $D_{av} = (\lambda_1 + \lambda_2 + \lambda_3)/3$. A FA value close to 0 corresponds to isotropic diffusion and therefore indicates tissue with variable FO. A FA value close to 1 corresponds to anisotropic diffusion and therefore indicates coherently aligned tissue [74].

Ariga et al. [74] measured reduced FA in the mid-wall ring (circumferentially aligned fibers) in the hearts of HCM patients compared to controls. A *virtual* DT was constructed to measure the FA in the computational heart model.

Virtual diffusion tensor In the geometrical model, the FO is known for each element. Therefore, the diffusivity of the fibers λ_1 in finite element regions was estimated to construct the virtual DT. The LV was subdivided in N regions (v_i, $i = 1,\ldots,N$, N = 1500) of similar size (around $6 \times 20 \times 20$ mm) and in each region the mean FO f_i^{mean} was calculated. For each element in the region (e_i^k, $k = 1,\ldots,M$ with M the number of elements in the current region), the length of the projection of the fiber on the mean FO (l_i^k) was calculated. Then,

Table 6.1: Overview of the cases of the sensitivity analysis and the corresponding variations of model components. The gray color of the text indicates unaltered model component compared to the control case.

Case	Geometry	Passive Behaviour	Active Force	Fiber Orientation
Case 1	control	control	control	control
Case 2	control	stiffened	control	control
Case 3	control	control	decreased	control
Case 3.1	control	control	increased	control
Case 4	control	stiffened	decreased	control
Case 4.1	control	stiffened	increased	control
Case 5	HCM 1	control	control	control
Case 6	HCM 2	control	control	control
Case 7	HCM 2	stiffened	control	control
Case 8	HCM 2	control	decreased	control
Case 9	HCM 2	stiffened	decreased	control
Case 10	HCM 2	control	control	disarray
Case 11	HCM 2	stiffened	control	disarray
Case 12	HCM 2	control	decreased	disarray
Case 13	HCM 2	stiffened	decreased	disarray

λ_1 of the region v_i equals the mean of these lengths across all elements in the region:

$$\lambda_1(v_i) = \frac{1}{M}\sum_{k=1}^{M} l_i^k. \tag{6.2}$$

The diffusivity in the other two directions are $\lambda_{2,3}(v_i) = 0.5(1-\lambda_1(v_i))$. Finally, the values obtained for λ_1, λ_2 and λ_3 were used in Equation 6.1 to obtain FA for the provided fiber configuration. Here again, for a coherent fiber arrangement in a specific region, $\lambda_1 = 1$, $\lambda_{2,3} = 0$ and therefore FA $= 1$. In a region of strongly disarrayed FO, $\lambda_{1,2,3} = 1/3$ is obtained and therefore, FA $= 0$.

Disarrayed fiber orientation The fiber assignment algorithm was adapted to generate disarrayed FO in the mid-wall ring of the LV (Figure 6.1). The mid-wall ring was defined to enclose all elements with transmural coordinates between 0.34 and 0.66. The transmural coordinate ranged from 1 on the endocardial surface to 0 on the epicardial surface and was obtained by solving the Laplace's equation in the volume. In this ring, the gradient value in each element was multiplied by a random number from a uniform distribution on the interval $[0,1]$ to obtain the distorted FO in this element. The sheet and sheet-normal directions were calculated to yield an orthonormal system together with the distorted fiber. Outside the mid-wall ring, the FO was assigned as in the control case. The FO were generated on a fine mesh (around one million elements). A nearest neighbour interpolation transferred the FO to the coarse geometry used for the simulations.

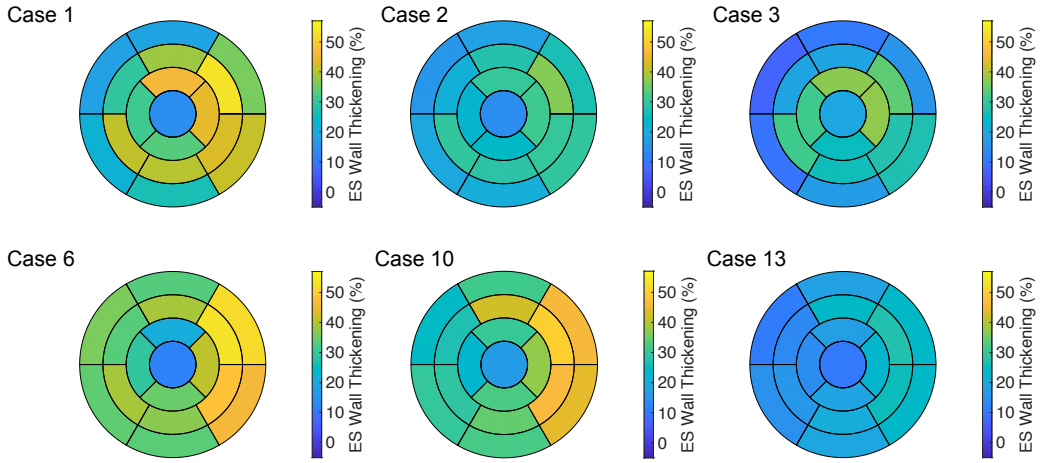

Figure 6.2: Bull's-eye displays for Case 1, 2, 3, 6, 10 and 13 showing the wall thickening at ES. Case 1: control case; Case 2: increased stiffness; Case 3: decreased active force; Case 6: hypertrophic geometry (17 mm); Case 10: hypertrophic geometry, fiber disarray; Case 13: virtual HCM case (all pathologies included). Adapted from [117], published under the Creative Commons Attribution 4.0 International (CC BY 4.0) License.

6.2 Results

For each global measure (defined in Chapter 5), the root mean squared deviation (RMSD) between each pair-wise combination of cases (Table 6.1, except Case 3.1 and 4.1) was calculated during the systolic and diastolic period (Figure C.1 and C.2 in Appendix C).

6.2.1 Altered Mechanics Due to the Stiffness of LV

Isolated changes in the passive force were quantified by comparing the deformation of the simulation with control stiffness (Case 1) to the one with increased stiffness (Case 2), both with the control geometry.

Wall thickening At the ED, the regional wall thickening was comparable between Case 1 and Case 2. At the ES, it differed – the extent of the thickening values was reduced (Case 1: 18.7 %–50.0 % and Case 2: 16.9 %–35.8 %), since the maximum decreased more than the minimum did, when the stiffness of the tissue was increased. In particular, the wall thickening of the segments in the free wall of the LV (5, 6, 11 and 12) were diminished compared to the one in the septal segments (2, 3, 8 and 9). This led to a more homogeneous distribution of the wall thickening among all segments, when the stiffness of the tissue was increased (Figure 6.2, Case 1 vs. Case 2).

Strain Similar to the wall thickening, the regional strain in all directions (longitudinal, circumferential and radial) at the ES had reduced extent of the values when the stiffness was increased. Therefore, a more homogeneous distribution of the strain among the all segments at ES was present for Case 2 compared to Case 1 (Figure 6.3).

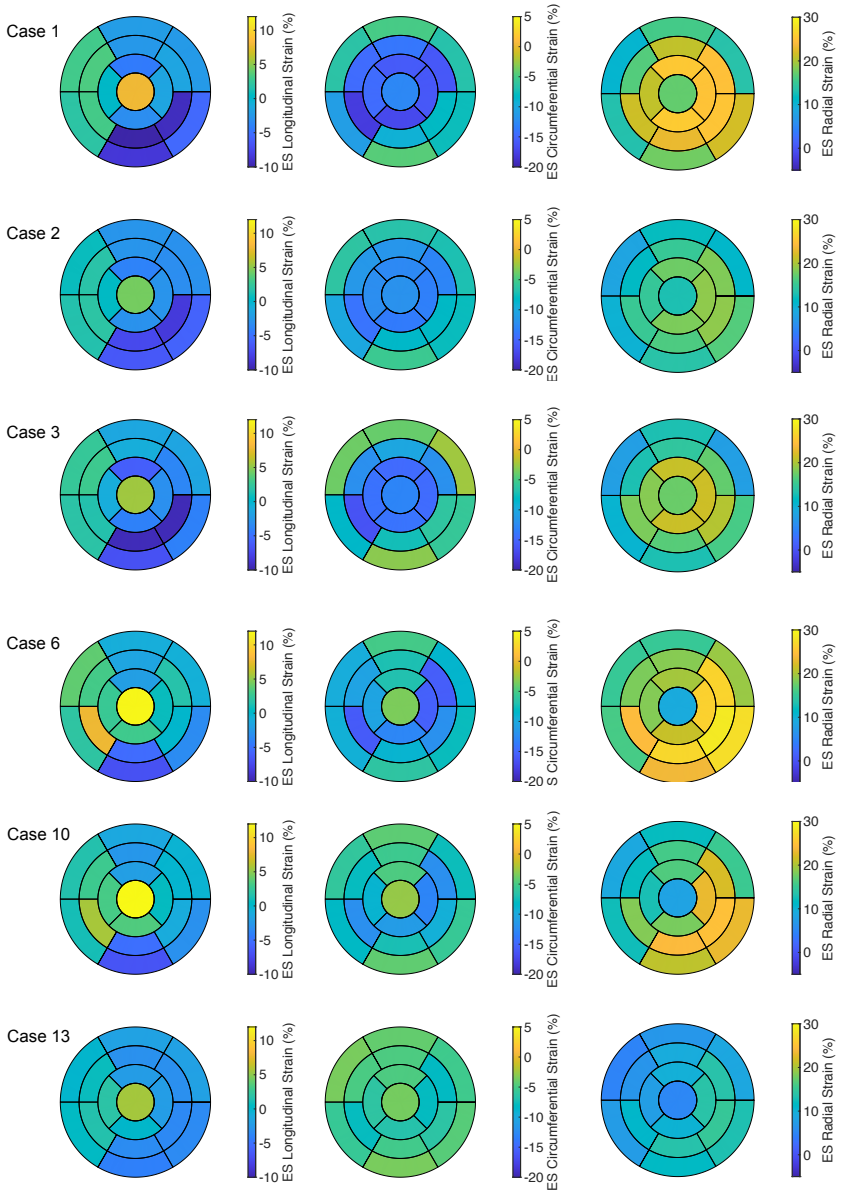

Figure 6.3: Bull's-eye displays for Case 1, 2, 3, 6, 10 and 13 showing the longitudinal, circumferential and radial strain at ES (first, second and third column, respectively). Each row corresponds to one case. Case 1: control case; Case 2: increased stiffness; Case 3: decreased active force; Case 6: hypertrophic geometry (17 mm); Case 10: hypertrophic geometry, fiber disarray; Case 13: virtual HCM case (all pathologies included). Adapted from [117], published under the Creative Commons Attribution 4.0 International (CC BY 4.0) License.

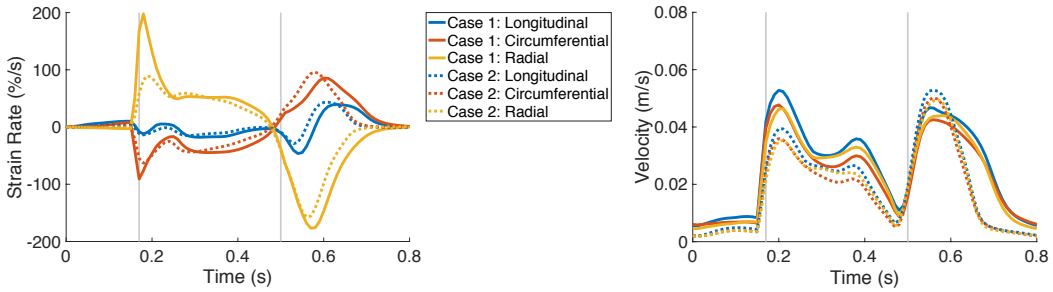

Figure 6.4: The time courses of the global strain rates (longitudinal, circumferential and radial) are on the left and the global velocities (longitudinal, circumferential and radial) are on the right, for Case 1 (solid lines) and Case 2 (dotted lines). In each plot, the first vertical line (at 0.17 s) indicates ED and the second line (at 0.5 s) ES. Case 1: control case; Case 2: increased stiffness. Adapted from [117], published under the Creative Commons Attribution 4.0 International (CC BY 4.0) License.

Strain rate and velocity The global radial strain rate at the beginning of the systolic period was halved when the stiffness was increased (Figure 6.4, left).

During the entire systolic period, the global velocities in all directions reduced when the stiffness was increased. During the diastolic period, the maximal velocities in all local directions slightly increased as the stiffness increased (Figure 6.4, right). Furthermore, the velocities decreased quicker as the stiffness was increased. While for the control case (Case 1) the maximal velocities during the diastole are similar compared to the velocities during the systole, increased tissue stiffness (Case 2) led to higher velocities during the diastole compared to the velocities during the systole.

LA shortening The longitudinal strain of the left atrium (LA) strongly decreased for the case of increased stiffness: 20 % for Case 1 to 10 % for Case 2.

A comparison the deformation of the simulation with control stiffness (Case 6) and the one with increased stiffness (Case 7), both with the hypertrophic geometry (geo17HCM2), confirmed these results.

Pressure-volume loops Figure 6.5 shows pressure-volume (PV) loops of the differently stiff LV for cases with control active force (left) and increased active force by 40 % (right) for the third beat of a multi-beat simulation of the deformation.

An increase in the stiffness (dotted line in Figure 6.5) led to a decrease in the LV pressure by 20 mmHg and 25 mmHg for the case with control and increased active force, respectively. Additionally, the stroke volume (SV) decreased by ≈ 20 ml when the stiffness was increased.

Stiffer tissue led to a more steep increase of the pressure between the end of the isovolumetric passive filling phase and the ED. Furthermore, it resulted in 3 mmHg higher ED pressure compared to control stiffness.

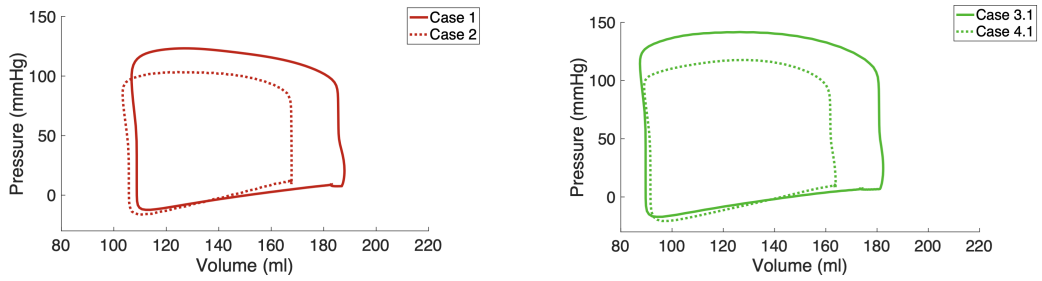

Figure 6.5: Pressure-volume loops for cases with control active force (left) and increased active force (right). In each plot, the difference between the loops is due to variations in the stiffness: control (solid line) and increased (dotted line). Left: Case 1: control case; Case 2: increased stiffness; Right: Case 3.1: control stiffness + increased active force; Case 4.1: increased stiffness + increased active force.

Summary An increased stiffness of the tissue of the LV led to more homogeneous wall thickening among the American Heart Association (AHA) segments and it equalized the strains at the ES. The strain rates and velocities were reduced during the systole, especially visible at the beginning of the systole. In contrast, the maximal velocities during the diastole increased when the stiffness was increased and reduced quicker in the stiffer tissue. The longitudinal strain of the LA was halved when the stiffness of the tissue was increased. Furthermore, increased stiffness led to reduced SV and ES pressure but increased ED pressure in the LV. An increased active force could compensate for that.

6.2.2 Altered Mechanics Due to the Active Force Development of LV

Isolated changes in the maximal active force developed in the tissue were quantified by comparing the deformation of the simulation with control active force (Case 1) to the one with decreased active force (Case 3), both with the control geometry.

Wall thickening At the ED, the regional wall thickening was comparable between Case 1 and Case 3. At ES, the regional wall thickening differed – the extent of the thickening values remained similar, while the maximum decreased when the force was decreased. At the same time, the distribution of the thickening values among the AHA segments was retained when the active force was decreased (Figure 6.2).

Strain The regional circumferential and radial strain at the ES had similar extent of the values ($\approx$13.5 %) for Case 1 and Case 3. The ranges at ES were shifted – the circumferential strain indicated less shorting of the tissue (values are higher, since they are negative) and the radial strain indicated less elongation of the tissue (values are lower, since they are positive) (Figure 6.3).

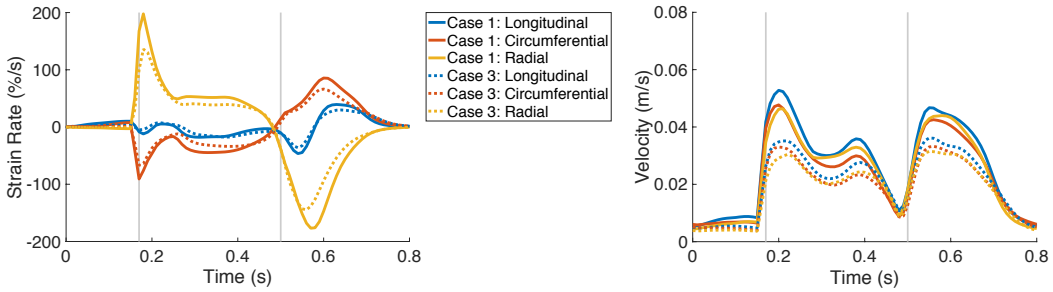

Figure 6.6: The time courses of the global strain rates (longitudinal, circumferential and radial) are on the left and the global velocities (longitudinal, circumferential and radial) are on the right, for Case 1 (solid lines) and Case 3 (dotted lines). In each plot, the first vertical line (at 0.17 s) indicates ED and the second line (at 0.5 s) ES. Case 1: control case; Case 3: decreased active force. Modified from [117], published under the Creative Commons Attribution 4.0 International (CC BY 4.0) License.

Strain rate and velocity The maximal global circumferential and radial strain rates differed between Case 1 and Case 3. The circumferential strain rate indicated slower decrease of the strain, while the radial strain rate indicated slower increase of the strain when the active force was reduced (Figure 6.6, left).

The velocities in all directions (longitudinal, circumferential and radial) were reduced during the entire heart cycle when the active force was reduced (Figure 6.6, right).

LA shortening The longitudinal strain of the LA was lower for the case of reduced active force – 20 % for Case 1 and 12 % for Case 3.

A comparison of the deformation of the simulation with control active force (Case 6) and the one with decreased active force (Case 8), both with the hypertrophic geometry (geo17HCM2), confirmed these results.

Pressure-volume loops Figure 6.7 shows the PV loops of the LV for cases with control stiffness (left) and increased stiffness (right) for the third beat of a multi-beat simulation of the deformation.

An increase in the active force (green lines) led to an increase in the LV pressure by 20 mmHg and 10 mmHg for the control and increased stiffness, respectively. Additionally, the SV increased by ≈ 20 ml (Case 1 vs. Case 3.1 and Case 2 vs. Case 2.1 in Figure 6.7).

A decrease in the active force (blue lines) led to a decrease in the LV pressure by 26 mmHg and 20 mmHg for the control and increased stiffness, respectively. Additionally, the SV decreased by 23 ml (Case 1 vs. Case 3) and 17 ml (Case 2 vs. Case 2).

Summary A reduced maximal active force development in the tissue of the LV results in reduced wall thickening as well as reduced circumferential and radial strain at the ES in all AHA segments. It also results in reduced strain rates and velocities in the entire heart cycle.

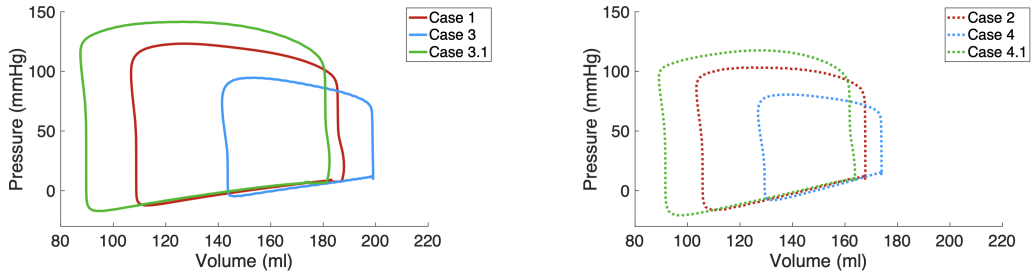

Figure 6.7: Pressure-volume loops for cases with control stiffness (left) and increased stiffness (right). In each plot, the difference between the loops is due to variations in the maximal active force: control (red curve), increased (green curve) and decreased (blue curve). Left: Case 1: control case; Case 3: decreased active force; Case 3.1: increased active force; Right: Case 2: increased stiffness; Case 4: increased stiffness + decreased active force; Case 4.1: increased stiffness + increased active force.

Furthermore, the ES pressure and the SV of the VL reduces. In total, less deformation is available in the entire LV.

6.2.3 Altered Mechanics Due to the Wall Thickness of LV

Isolated changes of the LV WT were quantified by comparing the deformation for different geometries – control geometry geo17 (Case 1), geo17HCM1 (Case 5) and geo17HCM2 (Case 6).

Wall thickening During the diastolic period, the RMSD of the global wall thickening between each two out of the three cases was less than 1.3 %. During the systolic period, the RMSD of the global wall thickening between Case 1 and both hypertrophic cases was higher than 10.8 % and the RMSD between Case 5 and Case 6 was 2.6 % (Figure C.1 and C.2).

The increase of the regional WT for the hypertrophic geometries (Case 5 and Case 6) during systole for all 17 segments, was faster compared to the one of the control geometry (Case 1). Between Case 5 and Case 6, no marked difference was observed (Figure 6.8). Wall thickening at end-systole (ES) was in the same range in all three cases (Case 1: between 18.1 % and 50.0 %, Case 5: between 18.4 % and 48.1 %, and Case 6: between 18.1 % and 51.3 %). Nevertheless, the distribution among the segments changed – the thickening of the basal segments (1–6) increased as the initial WT increased. Figure 6.2 shows the ES distribution of the wall thickening.

Strain and strain rate The circumferential and radial strains and strain rates (both global and segmental) for the control geometry differed from those of the hypertrophic geometries. During the systole, the RMSD of the global strain between Case 1 and each of the cases of hypertrophic geometries was between 1.4 % and 3.6 %. An increase of radial strains and a decrease of circumferential strains for Case 1 was observed during the entire systole, while

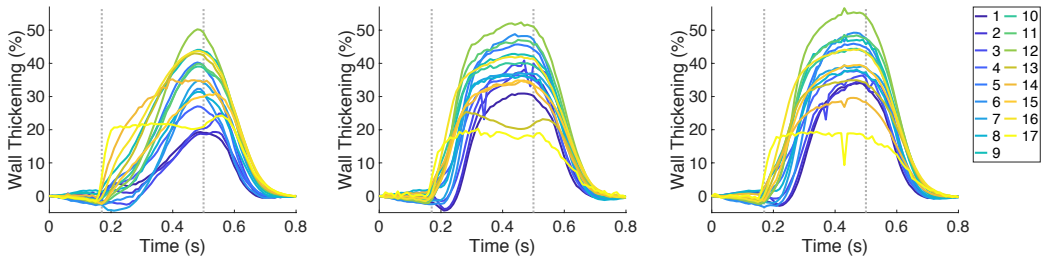

Figure 6.8: The time courses of the regional wall thickening for Case 1, 5 and 6 (left, middle, right, respectively). In each plot, the first vertical line (at 0.17 s) indicates ED and the second line (at 0.5 s) ES. Case 1: control case (initial WT = 10 mm); Case 5: hypertrophic geometry (15 mm); Case 6: hypertrophic geometry (17 mm). Adapted from [117], published under the Creative Commons Attribution 4.0 International (CC BY 4.0) License.

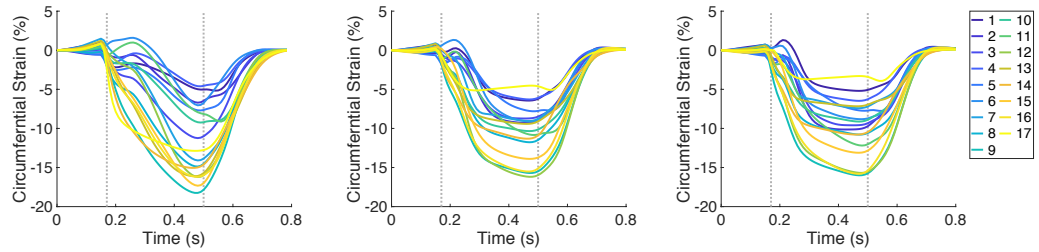

Figure 6.9: The time courses of the regional circumferential strain for Case 1, 5 and 6 (left, middle, right, respectively). In each plot, the first vertical line (at 0.17 s) indicates ED and the second line (at 0.5 s) ES. Case 1: control case (initial WT = 10 mm); Case 5: hypertrophic geometry (15 mm); Case 6: hypertrophic geometry (17 mm). Adapted from [117], published under the Creative Commons Attribution 4.0 International (CC BY 4.0) License.

those for the hypertrophic geometries occurred during the first half of the systolic period (Figure 6.9 and Figure 6.10).

This can be derived also from the strain rate – they are higher for the radial direction and lower for the circumferential direction in the mid systole for the hypertrophic geometries compared to those in the control case. An initially similar strain rate is available for all three cases during the systole, with amplitude 200 %/s for the radial strain rate and around 90 %/s for the circumferential strain rate (Figure 6.11, left). The end-diastolic (ED) regional strains in all three directions were comparable in all three cases.

The ES longitudinal strain indicated less shortening of the tissue since its minimum over the segments became higher as the WT increased – from -11.0 % for Case 1 to around -6.5 % for Case 5 and Case 6. Furthermore, the circumferential and radial strain at ES indicated slightly less shortening of the tissue (Figure 6.9 and Figure 6.10). In Figure 6.3 the distribution of the strains at ES are visualized for each local direction (longitudinal, circumferential and radial).

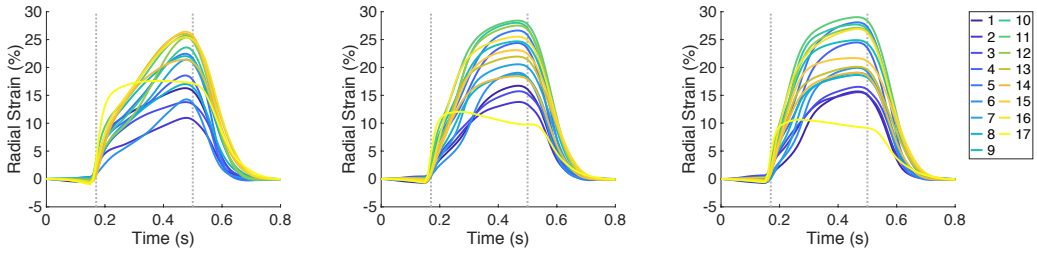

Figure 6.10: The time courses of the regional radial strain for Case 1, 5 and 6 (left, middle, right, respectively). In each plot, the first vertical line (at 0.17 s) indicates ED and the second line (at 0.5 s) ES. Case 1: control case (initial WT = 10 mm); Case 5: hypertrophic geometry (15 mm); Case 6: hypertrophic geometry (17 mm). Adapted from [117], published under the Creative Commons Attribution 4.0 International (CC BY 4.0) License.

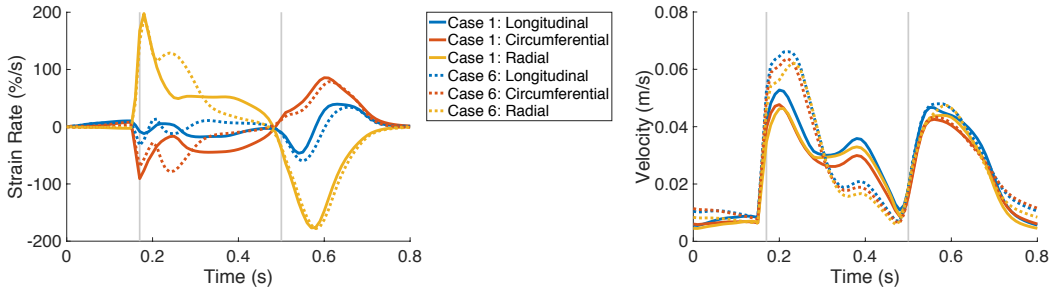

Figure 6.11: The time courses of the global strain rates (longitudinal, circumferential and radial) are on the left and the global velocities (longitudinal, circumferential and radial) are on the right, for Case 1 (solid lines) and Case 6 (dotted lines). In each plot, the first vertical line (at 0.17 s) indicates ED and the second line (at 0.5 s) ES. Case 1: control case (initial WT = 10 mm); Case 6: hypertrophic geometry (17 mm). Adapted from [117], published under the Creative Commons Attribution 4.0 International (CC BY 4.0) License.

Velocity The velocities in all local directions for the control case were differing from those of the hypertrophic geometries during the entire systole (RMSD ranged from 0.01 m/s to 0.013 m/s). The velocities for the control case were between 0.04 m/s and 0.05 m/s during the beginning and the middle of the systole, while the velocities for the hypertrophic geometries were high at the beginning of the systole (around 0.06 m/s) and decreased quickly to 0.02 m/s until the middle of the systole. The ES velocities were comparable in all three cases. During the diastolic period, the RMSD between the control case and each of the cases of the hypertrophic geometries ranged from 0.002 m/s to 0.003 m/s. The time course of the velocities in all three local directions for Case 1 and Case 6 are visualized in Figure 6.11, right. The visualization of Case 5 was omitted, since it was comparable to Case 6.

LA shortening The longitudinal strain of the LA increased slower during the systolic period for Case 1 compared to Case 5 and Case 6. The maximal longitudinal strain of the LA occurred at ES and it was 20 % for all three cases.

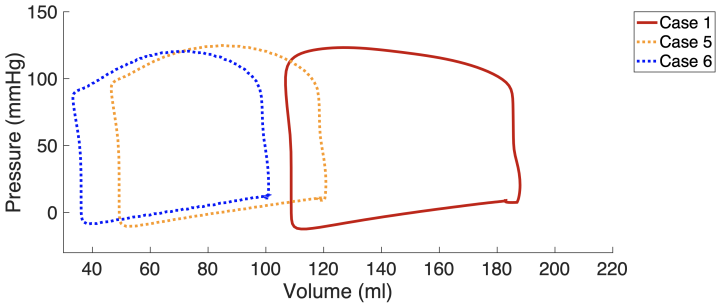

Figure 6.12: Pressure-volume loops for cases with control (red curve) and hypertrophic (yellow and blue curves) geometries (geo17HCM1 and geo17HCM2, respectively). Case 1: control case; Case 5: hypertrophic geometry (15 mm); Case 6: hypertrophic geometry (17 mm).

Pressure-volume loops Figure 6.12 shows the PV loops of the LV for the control case and both hypertrophic geometries for the third beat of a multi-beat simulation of the deformation.

An increase in the WT of the LV (dotted lines in Figure 6.12) led to a reduction in the SV: from 92 ml (control case) to 74 ml and 68 ml (Case 5 and Case 6, respectively). The pressure at ES reduced as the WT increased: 109 mmHg (control case) and 87 mmHg (Case 6). The pressure at ED increased as the WT increased: 7.5 mmHg (control case) and 13 mmHg (Case 6). However, the three cases had comparable maximal pressure in the LV (123 mmHg, 124 mmHg and 120 mmHg for Case 1, 5 and 6, respectively), which occurred later after the ED for the control case compared to the case with increased WT (Case 6) (250 ms and 120 ms after the ED, respectively). Therefore, different morphology of the PV loops for control case and the case of increased WT of the LV is visible in Figure 6.12.

Summary During the systolic period, the time course of the wall thickening and strain is altered between the control geometry and the hypertrophic geometries in all AHA segments. At ES, the circumferential and radial strain had only minor differences between the control geometry and the hypertrophic geometries, while the longitudinal strain indicated less shortening as the WT increased. The myocardial velocities for both hypertrophic geometries are increased during the systolic period compared to the control case. While the maximal pressure in LV was comparable among the cases, it appeared at distinct time points. The pressures at ES and ED changed and the SV reduced for the hypertrophied LV.

Only minor differences in the measures between both hypertrophic geometries were observed and therefore, the less hypertrophic geometry (geo17HCM1) was omitted for further comparisons.

6.2.4 Altered Mechanics Due to Fiber Disarray of LV

Isolated changes in the FO of the LV were quantified by comparing the deformation of the simulation with control FO (Case 6) to the one with disarrayed FO (Case 10).

Wall thickening The RMSD of the global wall thickening was less than 3.2 % for the entire heart cycle (Case 6 vs. Case 10: 1.1 % (ED) and 3.2 % (ES)).

Similarly, the regional wall thickening showed minor differences. At the ES, the range of the values for Case 6 was 18.1 %–51.3 % and for Case 10 it was 19.7 %–49.4 %, while differences occurred mainly in the basal segments (1–6).

Strain The regional longitudinal strain at the ES was not influenced by the disarrayed FO. The regional circumferential and radial strain at the ES had smaller extend of the values for the case with disarrayed FO. The difference was more pronounced for the circumferential strain – the range of the values for Case 6 was -15.5 %– -3.4 % and for Case 10, it was -12.9 %– -2.7 %. Therefore, the circumferential strain indicated less shorting of the tissue (values are higher, since they are negative) and the radial strain indicated slightly less elongation of the tissue (values are lower, since they are positive) (Figure 6.3).

Strain rate and velocity The regional circumferential and radial strain rates indicated a slower change in the strains at the beginning of the systolic period. The values of the longitudinal strain rate were similar – the systolic RMSD was 2.2 %.

The velocities in all three directions were comparable – the RMSD was 0.003 m/s during the systole and 0.001 m/s during the diastole.

LA shortening The longitudinal strain of the left atria slightly decreased when the FO was disarrayed – from 20 % to around 18 %.

A comparison the deformation of the simulation with control FO (Case 7) to the one with disarrayed FO (Case 11), both cases with increased stiffness, confirmed these results.

Summary Disarrayed FO in the mid-wall of the LV led to less deformation in circumferential direction – the strain indicated less circumferential shortening of the tissue. Furthermore, it led to slightly less deformation in radial direction. The strain rates, the velocities and the PV loops were not considerably changed.

6.2.5 Altered Mechanics Due to Combination of Pathological Model Components

The deformation of the control case (Case 1) was compared to the virtual HCM heart (Case 13), which was the combination of hypertrophic geometry, stiffened passive behaviour, decreased active force development and disarrayed FO.

Wall thickening The RMSD of the global wall thickening was 7.6 % for the systole and 7.7 % for the diastole.

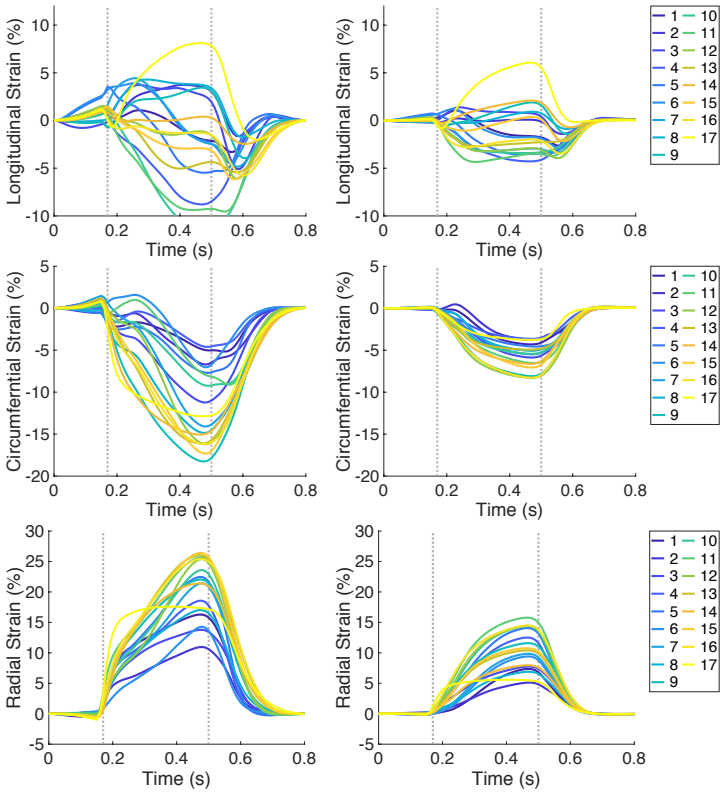

Figure 6.13: The time courses of the regional strains for Case 1 and Case 13 on the left and right, respectively. The longitudinal, circumferential and radial strain are in shown in the first, second and third row, respectively. In each plot, the first vertical line (at 0.17 s) indicates ED and the second line (at 0.5 s) ES. Case 1: control case; Case 13: virtual HCM case (all pathologies included). Adapted from [117], published under the Creative Commons Attribution 4.0 International (CC BY 4.0) License.

The maximum of the regional wall thickening decreased – from 50.0 % for the control case to 27.7 % for virtual HCM heart. As previously described, a decrease in the maximum was observed when the active force was decreased (e.g. Case 1 vs. Case 3). Furthermore, the extent of the wall thickening values reduced since the maximum decreased more than the minimum (at ES, the wall thickening ranged from 18.7 % to 50.0 % for Case 1 and from 10.4 % to 27.7 % for Case 13). As previously described, a decrease in the range of the wall thickening, which led to a more homogeneous distribution of the wall thickening, was observed when the stiffness of the tissue was increased (e.g. Case 1 vs. Case 2).

Strain Similar to the wall thickening, the regional strain values in all directions (longitudinal, circumferential and radial) were closer to zero for the virtual HCM case compared to control case (Figure 6.13). The extent of the strain values reduced as well – the ES longitudinal strain was between -11.0 % and 7.8 % for Case 1 and between -3.5 % and 5.5 % for Case 13. At ES, the circumferential strain for Case 1 ranged from -17.8 % to -4.5 %

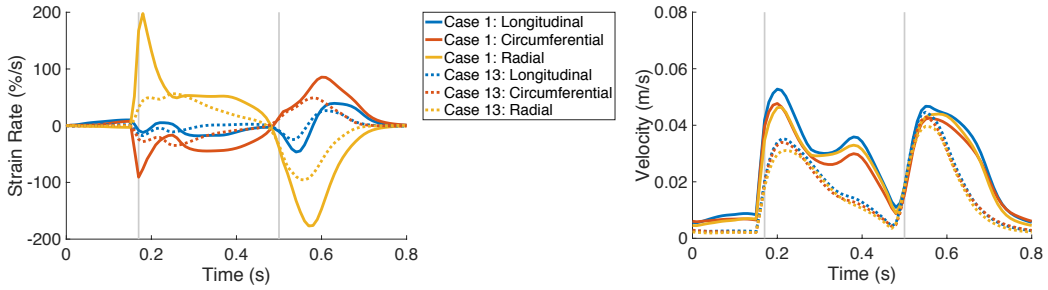

Figure 6.14: The time courses of the global strain rates (longitudinal, circumferential and radial) are on the left and the global velocities (longitudinal, circumferential and radial) are on the right, for Case 1 (solid lines) and Case 13 (dotted lines). In each plot, the first vertical line (at 0.17 s) indicates ED and the second line (at 0.5 s) ES. Case 1: control case; Case 13: virtual HCM case (all pathologies included). Adapted from [117], published under the Creative Commons Attribution 4.0 International (CC BY 4.0) License.

and for Case 13: from -8.0 % to -3.5 %. The radial strain for Case 1 ranged from 10.6 % to 25.7 % and for Case 13: from 4.8 % to 14.8 % (Figure 6.3).

Strain rate and velocity The global strain rates reduced for the HCM heart compared to control case for the entire heart cycle (Figure 6.14, left).

For each direction, the RMSD of the strain rates were similar for the diastolic and systolic period – around 12 % in longitudinal direction, 23 % in circumferential direction and 41 % in radial direction. During the systolic period, the major difference was observed during the first half of the systole. The global velocity in all three directions differed as well during the systolic and diastolic period – the RMSD was between 9.0 % and 10.5 % during the diastole and between 11.3 % and 14.4 % during the systole (Figure 6.14, right).

LA shortening The longitudinal strain of the left atria strongly decreased – from 20 % for Case 1 to 8 % for Case 13.

Pressure-volume loops Figure 6.15 shows the PV loops of the LV for the control case and the virtual HCM heart.

The virtual HCM heart had a decreased ES pressure of (68 mmHg) and an increased ED pressure (88 mmHg) compared to the control case. The SV was less then the half of SV of the control case (38 ml vs. 92 ml, respectively). The ejection fraction (EF) of the control case was 44 % and EF of the HCM heart was higher, 49 %, since the ED volume of the HCM heart was much lower than the one of the control case (89 ml vs. 189 ml, respectively).

Summary For the combined HCM heart, a decreased and more homogeneous wall thickening was observed at ES compared to the control case. Furthermore, the strain in all three directions indicated less deformation for HCM case compared to the control case. The strain rate revealed slower shortening and elongation of the tissue during the entire heart beat, but especially visible during the beginning of the systole. The longitudinal strain of the LA was

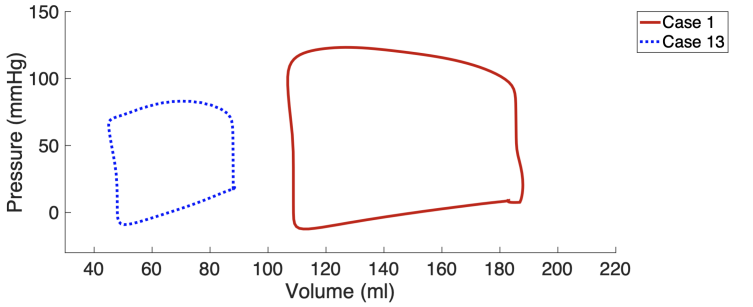

Figure 6.15: Pressure-volume loops for the control case (red curve) and the virtual HCM heart (blue dotted curve). Case 1: control case; Case 13: virtual HCM case (all pathologies included).

more than halved for HCM case compared to control case. The SV was strongly decreased in the virtual HCM case. In total, the deformation and its rate of the LV was diminished for the virtual HCM heart compared to the control case.

6.2.6 Overview of Results

Table 6.2 provides an overview of the results. Note, that the measures, which are negative, indicate less or slower deformation as they increase, e.g. an increase in the diastolic radial strain rate indicates slower relaxation.

6.3 Discussion

Altered Mechanics in HCM Patients Reported in the Literature

In HCM patients, global strains and strain rates are reported to be significantly lower [70, 78, 140], while Ito et al. [77] measured preserved (or even increased) circumferential shortening. Furthermore, altered myocardial velocities are detected in HCM patients compared to controls – global and segmental diastolic velocities are decreased and systolic longitudinal velocities were reduced in HCM [73]. In the LA, a higher minimum volume and a lower peak atrial longitudinal strain was measured in HCM compared to controls [78].

Causes of Altered Mechanics in HCM Patients Reported in the Literature

Previous studies have examined potential origins of altered cardiac mechanics in HCM patients in clinical studies. In a cohort of fifty-nine HCM patients, Urbano-Moral et al. [71]

Table 6.2: Effect of model changes reflecting different pathological mechanisms (columns) on phenotypic mechanical markers (rows). WT = wall thickness, FA = fractional anisotropy, Comb. = combination

Metrics	Time period	WT ↑	Passive force ↑	Active force ↓	FA ↑	Comb.
Wall thickening	systolic (ES)	↑ (≈)	↓ (↓)	↓ (↓)	≈ (≈)	↓ (↓)
	diastolic (ED)	≈ (≈)	≈ (≈)	≈ (≈)	≈ (≈)	≈ (≈)
Strain (L)	systolic (ES)	↑ (↑)	↑ (↑)	≈ (≈)	≈ (≈)	↓ (↓)
	diastolic (ED)	≈ (≈)	≈ (≈)	≈ (≈)	≈ (≈)	≈ (≈)
Strain (C)	systolic (ES)	↑ (≈)	↑ (↑)	↑ (↑)	↑ (≈)	↑ (↑)
	diastolic (ED)	≈ (≈)	≈ (≈)	≈ (≈)	≈ (≈)	≈ (≈)
Strain (R)	systolic (ES)	↑ (≈)	↓ (↓)	↓ (↓)	↓ (≈)	↓ (↓)
	diastolic (ED)	≈ (≈)	≈ (≈)	≈ (≈)	≈ (≈)	≈ (≈)
Strain rate (L)	systolic (ES)	≈ (≈)	≈ (≈)	≈ (≈)	≈ (≈)	≈ (≈)
	diastolic (ED)	≈ (≈)	≈ (≈)	≈ (≈)	≈ (≈)	↓ (≈)
Strain rate (C)	systolic (ES)	↓ (≈)	↑ (≈)	↑ (≈)	≈ (≈)	↑ (≈)
	diastolic (ED)	≈ (≈)	↑ (↑)	↓ (↑)	≈ (≈)	↓ (↓)
Strain rate (R)	systolic (ES)	↑ (≈)	↓ (≈)	↓ (≈)	≈ (≈)	↓ (≈)
	diastolic (ED)	≈ (≈)	↑ (↓)	↑ (↓)	≈ (≈)	↑ (↓)
Velocity (L,C,R)	systolic (ES)	↑ (≈)	↓ (≈)	↓ (↓)	≈ (≈)	↓ (≈)
	diastolic (ED)	≈ (↑)	↑ (↓)	↓ (≈)	≈ (≈)	↓ (↓)
LA strain (L)	ES	≈	↓	↓	≈	↓

demonstrated the relation of a reduction in longitudinal shortening of the LV and the extent of hypertrophy. Furthermore, the reduction of the global strain and strain rate was correlated with the mean WT [141]. In a clinical study, Villemain et al. [75] suggested that altered LV relaxation might result from increased myocardial stiffness. Hoskins et al. [76] hypothesized that reduced active force might contribute to systolic dysfunction in HCM patients.

In a HCM patients' heart, distinct underlying phenomena are present simultaneously, but are differently pronounced. Thus, the effects of these phenomena can not be clearly separated from measurements obtained in clinical studies. In contrast, the presented numerical study could relate the observed alterations of mechanics to their underlying causes.

Identification of Underlying Pathophysiology

An alteration of the wall thickening and the strain time course during the systole can be related to hypertrophic LV walls. Longitudinal strain, which indicates less shortening is as well related to hypertrophic LV walls. Reduced ES wall thickening and strain values (circumferential and radial) in all segments can be related to less active force development in the LV. A homogeneous distribution of the ES wall thickening and strains among all AHA segments can be related to stiffer tissue. A reduction of the circumferential strain can be attributed to the fiber disarray in the mid-wall of the LV, but also to less active force development or increased stiffness of the tissue.

Strain rates that are reduced during the entire systole and strongly reduced during the beginning of the systole can be traced back to increased tissue stiffness. Strain rates that are reduced during the entire heart cycle are caused by reduced active tension developed in the tissue.

An increase in the myocardial velocities in all directions during the systolic period can be related to hypertrophic walls of the LV. In contrast, these velocities decreased during the systolic period when the stiffness of the tissue was increased. Additionally, an increase in the velocities during the diastolic period combined with a rapid decay of the velocities can be as well related to an increased stiffness of LV tissue. A reduction of the active tension development did not affect the velocities during the diastolic period.

A reduced longitudinal strain of the left atria at ES was present in case of increased stiffness of the tissue or reduced active tension development.

Comparison between Simulated and Clinically Measured Deformation

Wall thickening A segmentation of the endocardial and epicardial surfaces of the LV for the entire heart cycle is time consuming and user dependent. Therefore, in clinical routine, the wall thickening is not commonly evaluated, but instead, the radial strain is used. On the virtual hearts, two distinct methods were applied to calculate the radial strain and the wall thickening. For both measures, comparable time course morphology and ES distribution for each case were obtained, but different maximal values were present (compare for Case 1 the wall thickening (max 50 %) in Figure 6.8, left and the radial strain (max 26 %) in Figure 6.13, left).

Kato et al. [142] showed that the radial thickening of the tissue arises due to the circumferential fiber shortening. This implies that fiber disarray in the mid-wall (fiber oriented in circumferential direction) will change the radial thickening and strain. In contrast, it was observed a reduction of the deformation in circumferential direction, which was more pronounced than the reduction of the deformation in radial direction.

Strain and strain rate The strain values obtained for the virtual control case (Case 1) indicated less shortening compared to healthy volunteers in all three directions [131]. Nevertheless, the regional values of the circumferential and radial strain of the virtual control heart are inside the ranges (mean$\pm$SD) provided in Table 4 in [131] but deviate from the mean values (e.g. the mean values of the regional circumferential strain were between -26 % and -17 % and the mean values of the regional radial strain were between 12 % and 39 %in [131]). Additionally, heterogeneous distributions among the AHA segments are obtained and heterogeneous values were as well measured, e.g. radial strain was 39$\pm$21 % in the anterior basal segment and it was 12$\pm$8 % in the septum basal segment [131]. The heterogeneity in the circumferential strain was significant ($p < 0.05$) [143]. The regional longitudinal strain in the virtual control heart strongly deviated from the ranges provided

for the healthy volunteers (from -24±11 % to -13±7 % [131]). For the virtual HCM heart, the longitudinal strain also deviated from literature values, which were around -11 % for HCM hearts [78]. For each virtual heart, the values in the free wall were negative as well, but closer to zero (Figure 6.3), while the positive values of the longitudinal strain were mainly in the septal segments. The torsion of the ventricle, which is pronounced in the apical region, leads to an elongation of the septal segments – the apex pulls the septal segments as it rotates. At the same time, the free wall shortened.

For the virtual HCM heart, the strain values indicated less (and slower) shortening in the circumferential direction and less (and slower) thickening in the radial direction of the tissue compared to the virtual control case, in agreement with [70, 78, 140]. In contrast to Ito et al. [77], the circumferential strain of the virtual HCM heart indicated clearly reduced shortening.

Two articles state that the stiff heart syndrome (cardiac amyloidosis) can be identified by the longitudinal strain, which shows a strong gradient between the apex and base regions (apical sparing) [144, 145]. In the stiffened virtual hearts (e.g. Case 2 and Case 7), an opposite effect appeared when the stiffness was increased, the strain became more homogeneous.

Velocity Li et al. [73] measured reduced global and segmental diastolic radial and longitudinal peak velocities in patients with HCM vs. controls. In contrast, a reduction of any peak velocity during the diastolic period in the virtual HCM heart was not present compared to the control heart. Nevertheless, a decrease in these velocities was observed when the active force was reduced (Case 3) and an increase when the stiffness was increased (Case 2). Therefore, it was shown that the effect of these two pathologies cancel out in the virtual HCM heart to obtain the same peak diastolic velocity as in the control case (Figure 6.14, right). If either the active force in the LV would be further reduced or tissue stiffness deviates less from the control stiffness (or both), reduced diastolic velocities in line with [73] can be obtained.

When the stiffness of the tissue was increased, the amplitude of the diastolic velocity increased and also the morphology of the diastolic velocity course changed compared to the control case. Therefore,the suggestion of Villemain et al. [75] was confirmed that modified LV relaxation might result from increased myocardial stiffness.

Furthermore, Li et al. [73] measured reduced peak velocities during the systole in patients with HCM in the longitudinal direction (radial peak velocities were comparable). A reduction of the velocities during the systolic period was observed as well but for all directions (longitudinal, circumferential and radial). The absolute values of velocities was not compared, since different imaging modalities provide different values for the velocities – feature tracking peak velocities are lower than directly measured tissue phase mapping velocities [73]. Hoskins et al. [76] hypothesized that reduced active force might contribute to systolic dysfunction in HCM patients. In agreement with [76], reduced systolic function was observed when the force was decreased – the velocities during the systole were decreased and the strain at ES was diminished.

In a cohort of healthy volunteers, similar global longitudinal and radial velocities during the systole were measured (longitudinal was 2.6±0.55 cm/s and radial 2.5±0.36 cm/s) [131].

Likewise, similar global longitudinal and radial velocities were obtained. Nevertheless, the circumferential velocity was also in the same range, while Lin et al. [146] measured negative circumferential velocities since they considered the direction of deformation along the circumference . In this study, the absolute values of these velocities were calculated which equal the speed of deformation in the circumferential direction. However, the direction of the deformation can be deduced from the strain values.

Left atria strain The LV of the virtual HCM heart deformed less compared to the control case, which led to reduced maximal longitudinal strain of the LA. Similar behaviour was reported by Aly et al. [78]. Additionally, they discovered that LA dysfunction is present in HCM patients before global LV dysfunction can be measured. This behaviour could not be reproduced in the numerical model – in each case, in which LA longitudinal strain was reduced, the deformation of the LV was as well reduced. This reported statement demonstrates the importance of using a whole heart model, in which the deformation of all chambers is related.

Limitations

Geometrical model The creation of the hypertrophic geometries (geo17HCM1 and geo17HCM2) was not based on imaging data, which provide the exact distribution and the extent of the initial WT. Instead, the endocardial surface of the control image-based geometry was modified to obtain a smaller LV volume and a concentric hypertrophy of the wall (described in Chapter 4)).

For the control geometry, the finite element mesh of the ventricle was coarse – up to two elements in the transmural direction. The linear course of the FO is represented by two or three fibers in the transmural direction. Thus, a combination of control geometry and disarrayed FO could not be created.

Furthermore, the linearity of the solution to Laplace's equation depends on the width of the domain between the boundaries [136]. Therefore, the course of the transmural coordinates used to define the LV mid-wall region close to the apex is not linear. A linear course can be obtained by solving a trajectory distance equation in the LV [136].

Fiber disarray The measure of FA was calculated on a fine geometry (also used to create the FO, Figure 6.1) and delivered values close to one (0.95 ± 0.11) in the mid-wall ring of the control FO and 0.81 ± 0.25 for the disarrayed FO. Ariga et al. [74] measured for a control case a FA of 0.52 ± 0.03 and for HCM patients 0.49 ± 0.05, which are considerably lower values compared to the values in the virtual hearts. This is the result of a rule based algorithm, since it creates idealized FO. Nevertheless, the difference between the mean FA of the control and the one of the disarrayed FO in the virtual heart is 0.14, which is much higher compared to this difference measured by Ariga et al. [74] (0.03). Therefore, the cases with disarrayed FO were considered to be representative for severely disarrayed FO.

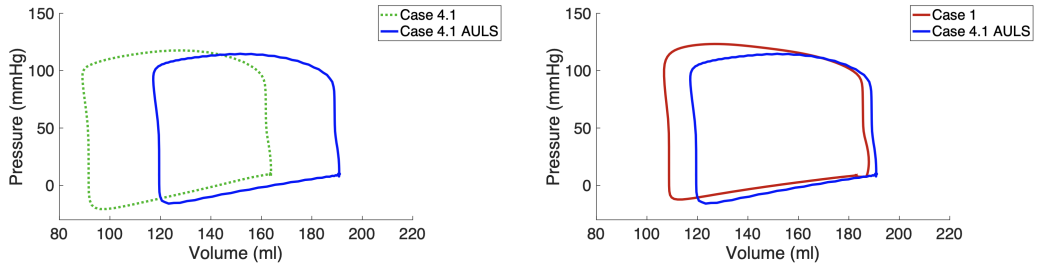

Figure 6.16: Pressure-volume loops for cases with the control geometry. Left: Case 4.1: increased stiffness + increased active force; Case 4.1 AULS: increased stiffness + increased active force + adapted unloaded and loaded states; Right: Case 1: control case; Case 4.1: increased stiffness + increased active force.

Unloaded state and circulatory model The stiffness of the tissue influences the unloaded and loaded state of the heart (Chapter 7). However, for the sensitivity analysis, only one parameter was changed at a time, in order to exclude influences which are due to several simultaneous changes in the model. Therefore, as the tissue stiffness was increased, the unloaded and loaded state were not adapted, but the ones calculated with the control stiffness were used. For the cases with increased stiffness, this led to 1) a decrease in the initial LV volume: from 183 ml (control case, Case 1) to 166 ml (increased stiffness of geo17, Case 2), since the initial pressure in the LV was not enough to oppose the increased passive stress in the tissue and 2) the atrial kick did not lead to an increase in the volume of the LV with stiffened tissue, since the pressure in the left atria was lower than the pressure in the LV. Therefore, the PV loops of the cases with increased stiffness were shifted to the left (in the x-axis) compared to the one of the cases with control stiffness (Figure 6.5).

The left plot in Figure 6.16 shows a comparison between the PV loops of the third beat of the simulation between Case 4.1 and the same case but with adapted unloaded and loaded states (AULS): both states were obtained with the stiffness applied in the simulation. The shift along the x-axis is clearly visible and the SV was the same in both cases($\approx$ 74 ml).

The right plot in Figure 6.16 shows a comparison between the PV loops of the third beat of the simulation between the control case and Case 4.1 with AULS. Both cases have initially the same LV volume, but the atrial kick leads to a slightly different ED volume. It is visible that the increase of the stiffness can be compensated by an increase in the active force, which together lead to a similar SV as in the control case. However, a higher increase in the active force is needed (then +40 %) to obtain exactly the same SV.

Circulatory model parameters For all numerical simulations, an identical input parameter set for the circulatory model was applied. It led to healthy systolic pressure (120 mmHg) for the virtual control heart, but to lower systolic pressures in the virtual HCM heart (68 mmHg). The pressure, applied on the endocardial surface, influences the deformation and therefore, the evaluated measures. In both control and HCM cases, the EF

was lower compared to literature values – 44 % vs. 72 % [147]. A diminished deformation results in a reduced EF and therefore in reduced strains, as discussed previously.

Active force model The active force model provided the force based on a predefined curve (force over time) and a maximum value of the force (T_{max}). A more complex model will adjust the intervals of the increase and the decrease of the force based on the velocities (e.g. Land et al. [148]) and therefore, the duration of the contraction and relaxation of the LV. Ito et al. [77] reported that regional LV filling for HCM hearts was prolonged compared to control hearts and that the impairment of the diastolic relaxation is a major sign of HCM. In this study, the major changes in the measures occurred during the systole rather than diastole with exception of the strain rates – the RMSD are higher during the systole for the strains, velocities and wall thickening Additionally, the diastolic relaxation time extent was not evaluated.

Strain calculation In general, the values of the metrics in the apex segment might be misleading, since the local longitudinal directions in the apex strongly deviate from the global longitudinal direction (Figure 5.1). This is a result of the algorithm which creates the local directions. Instead the global longitudinal direction could be used (as a local one), but then the three local directions (longitudinal, circumferential and radial) will not build an orthogonal system in each volume element and could not provide linearly independent information. In this work, the strain was calculated based on the deformation tensor $\mathbf{F}$. Werys et al. [149] used the Green-Lagrangian strain tensor $\mathbf{E} = 0.5(\mathbf{F}^T\mathbf{F} - \mathbf{I})$ to derive the strain directly from the motion of the myocardium from cine MRI images. Santiago et al. [41] projected the components of the Green-Lagrangian strain tensor on a global longitudinal direction to obtain the strain. There is no agreement in the literature how to apply the deformation tensor to obtain the strain and therefore, depending on the definition of strain, different strain values will be obtained.

Open loop heart The human heart is adjusted by the needs by several control loops. These control loops are interrupted on purpose in the simulated case in order to observe the influence of each individual component. Therefore, the comparison with in vivo data must be handles with care.

Conclusion

An in-silico study on virtual human whole hearts was conducted to identify causes of altered mechanics in HCM hearts. The deformation resulting from combinations of physiological and pathological models was simulated and the mechanical behaviour was evaluated by local and global measures (wall thickening, strain, strain rate and deformation velocities).

The presented study shows which pathological mechanisms are required to be present in the LV to obtain altered mechanics and how they affect the deformation measures. An increased wall thickness leads to deformation alteration during the systole, while the ES

values are comparable to control case. Stiffer tissue equalizes the strains at ES, while reduced active force development reduces the deformation of LV. Disarrayed FO in the mid wall did not influence the deformation of the LV. An inversion of these arguments allows to identify present pathological mechanisms in the tissue which cause an altered mechanical behaviour.

In the clinical routine, it is cumbersome to directly measure underlying pathological mechanisms and therefore, those, derived from a numerical simulation, might be a valuable information for clinicians and can contribute to a more accurate diagnosis in HCM patients.

Chapter 7

Model Based Estimation of Passive Force

The intrinsic material properties of the heart tissue are described by constitutive laws which provide a relation between strain and stress in the tissue. Several laws have been proposed in the literature. In this work, the constitutive law of Guccione et al. [105] was applied. The values of the input parameters for the equations have to be set prior to the simulation. However, a wide range of values can be found in the literature, e.g. between 189 Pa and 3000 Pa for the parameter, which scales the global stiffness and between 8 and 67 for the parameter which scales the stiffness in fiber direction [59].

In Chapter 6, it was shown that the value of global stiffness influences the deformation of the left ventricle (LV): an increased global stiffness led to more homogeneous wall thickening among the American Heart Association (AHA) segments, the strain rates and velocities were reduced during the systole. Furthermore, the longitudinal strain of the left atria was halved when the stiffness of the tissue was increased and the stroke volume and end-systolic pressure were reduced. Therefore, it is important to use stiffness values for modeling of the heart tissue which lead to physiological deformation in a numerical simulation of the contraction.

In this chapter, ways are provided to identify the parameters of the constitutive equations for a certain heart geometry. The parameter which scales the global stiffness (C), the stiffness in fiber direction b_{f} and two further parameters b_{t} and b_{ft} (see 3.3) were estimated. The estimation techniques are based on measured end-diastolic pressure-volume relations (EDPVR) as described in Klotz et al. [100], which are characterized by the passive behaviour of the tissue. Furthermore, a target ratio of pressure-free and pressure-loaded LV volume is included in the estimation.

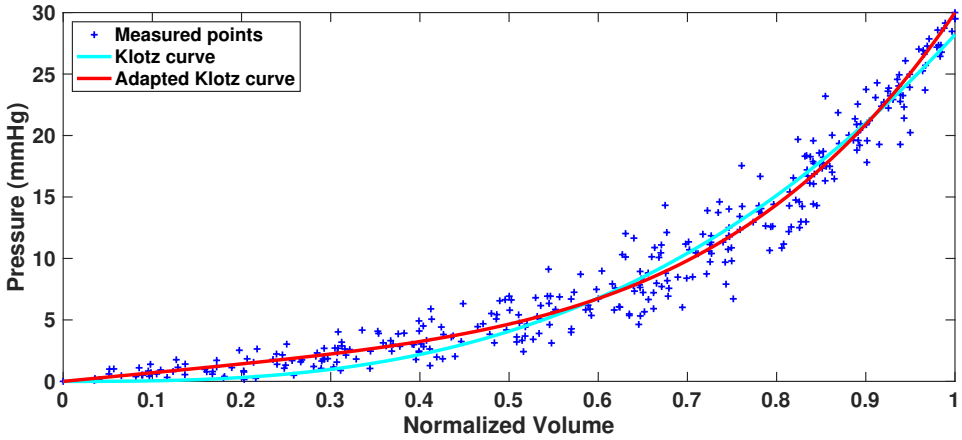

Figure 7.1: The experimentally measured points (blue crosses) and the original Klotz curve (cyan colour) [100]. The adapted curve is shown in red colour. Modified from [150], published under the Creative Commons Attribution 4.0 International (CC BY 4.0) License.

7.1 Methods

Two frameworks are presented: a sweep in a predefined parameter space and a gradient-free optimization method. Both aim at identifying optimized parameters of a constitutive law for a given patient-specific geometry. In particular, in this chapter the parameters were identified for geo17.

7.1.1 Adaptation of the Klotz curve

Klotz et al. [100] measured the end-diastolic pressure volume relation (EDPVR) in 80 ex vivo human hearts of different etiologies by applying pressure between 0 and 30 mmHg in the LV and simultaneously measuring the volume of the cavity. For every ventricle, they normalized the volume to range between 0 and 1 and provided one exponential curve approximating all measurements with a single equation: $P = 28.2\bar{V}^{2.79}$ mmHg, where $\bar{V}$ is the normalized volume and P is the corresponding ventricular pressure. Figure 7.1 shows the original Klotz curve (cyan colour) and the measurements (blue crosses).

The original curve described by an exponential expression was adapted by adding a linear term in order to allow a non-zero derivative at the start point (0; 0). Furthermore, a regression condition was imposed for both start and end points of the curve (0; 0) and (1; 30), since a simulated curve will certainly pass through these points due to the definition of volume normalization. The following expression was obtained for the *adapted Klotz curve* (Figure 7.1, red curve)

$$P^{\mathrm{ad}} = 7.015\bar{V} + 22.985\bar{V}^{4.322}\,\mathrm{mmHg}\,. \tag{7.1}$$

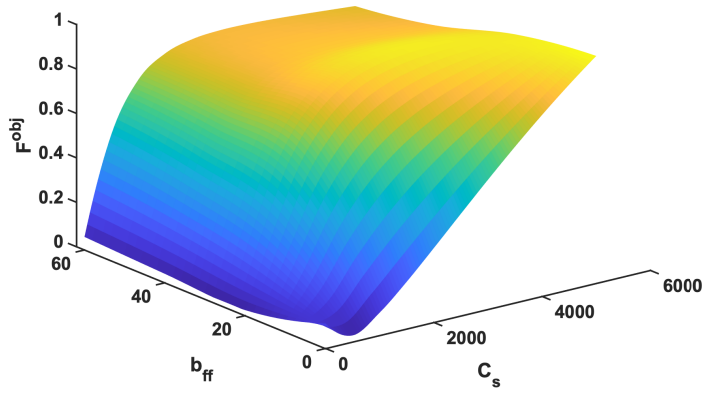

Figure 7.2: The normalized values of the objective function F^{obj}.

7.1.2 Parameter Sweep

For the parameter sweep optimization method, a series of simulations were run with different combinations of parameters of the constitutive law. The LV was passively inflated starting with pressure of 0 mmHg. It was linearly increased until 30 mmHg over 10 s simulation time. The initial state of the geometry was the one directly obtained from imaging data (no unloading and loading was used). The aim was to identify the parameter combination which delivers a simulated Klotz curve as close as possible to the adapted one.

Coarse sampling A coarse parameter sweep was executed in two dimensional parameter space: $C_{\text{s}} \in [150, 5150]$ Pa and the fiber stiffness b_{ff} was in the range $[2, 62]$. The parameter $C_{\text{s}} = 0.5C$, where C is the the global stiffness in Equation (13) in [105]. The transverse stiffness (b_{xx}) was defined as 40 % of fiber stiffness and the shear stiffness (b_{ff}) was the average between normal and transverse stiffness: $b_{\text{xx}} = 0.4b_{\text{ff}}$, $b_{\text{fx}} = 0.7b_{\text{ff}}$, as suggested by Genet at al. [58]. The parameter space was sampled with a step size of 500 Pa for the C_{s}-direction and 20 for b_{ff}-direction.

The cost function was

$$F^{\text{objAbs}}(C_{\text{s}}, b_{\text{ff}}) = \sum_{i=1}^{I} (P_i^{\text{sim}}(C_{\text{s}}, b_{\text{ff}}) - P_i^{\text{ad}})^2, \tag{7.2}$$

where $P^{\text{sim}}(C_{\text{s}}, b_{\text{ff}})$ is the pressure applied in the simulation of inflation with material parameter $(C_{\text{s}}, b_{\text{ff}})$ in the LV and RV, the index i samples equidistantly the range of the volume values, $I = 100$. F^{objAbs} was normalized by dividing the function values by its maximal value to obtain F^{obj}, shown in Figure 7.2.

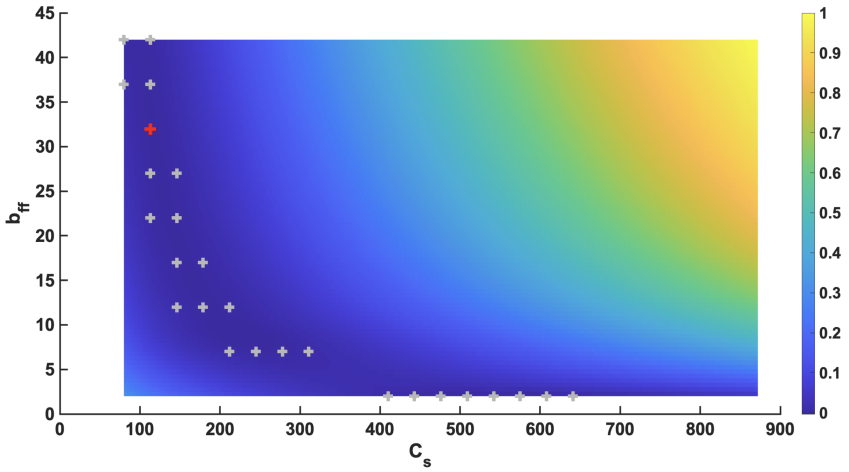

Figure 7.3: The normalized values of the objective function F^{obj} are colour-coded for the parameter sweep with fine sampling. The red cross symbol (+) indicates the optimal parameter combination and the grey crosses deliver a function value close to the minimal value (Equation 7.3).

Fine sampling Based on the minimal values of the cost function F^{obj} (dark blue colour in Figure 7.2), a new range of interest for the parameters was identified: $C_s \in [80, 872]$ Pa and $b_{ff} \in [2, 42]$. The new space was sampled with step size 33 Pa for the C_s-direction and 5 for b_{ff}-direction. This resulted in 225 parameter combinations. The landscape of the cost function is shown in Figure 7.3. The optimal parameter combination is marked by the red plus symbol. The grey plus symbols mark 25 further parameter combinations (C_s^n, b_{ff}^n), which were close to the minimum, $\varepsilon = 0.01$

$$\|F^{\text{obj}}(C_s^*, b_{ff}^*) - F^{\text{obj}}(C_s^n, b_{ff}^n)\| < \varepsilon. \tag{7.3}$$

Extension of the cost function The fine sampling could deliver a unique minimum. However, there were further parameter combinations, which yielded similar cost function values. Therefore, the distance to the adapted Klotz curve could not be used as a sole criteria to identify the parameters of the constitutive law.

Therefore, the cost function was extended to include a target volume ratio as follows

$$F_\beta^{\text{obj}}(C_s, b_{ff}) = (1 + F^{\text{obj}}(C_s, b_{ff})) \cdot (1 + V(C_s, b_{ff}, \beta)), \tag{7.4}$$

$$V(C_s, b_{ff}, \beta) = \frac{\left|V_0/V_{30} - \beta\right|}{\max_{(C_s, b_{ff})}(\left|V_0/V_{30} - \beta\right|)}, \tag{7.5}$$

where $F^{\text{obj}}(C_s, b_{ff})$ was the normalized objective function from Equation 7.2, $V_p = V_p(C_s, b_{ff})$ is the LV volume at pressure p for $p = 0$ mmHg and 30 mmHg. The target volume ratio β was set to 0.42 and was obtained from Equation (8) in [100]: $V_0 = V_m(0.6 - 0.006P_m)\,\text{mmHg}^{-1}$ with $P_m = 30$ mmHg and $V_m = V_{30}$. The extended objective function $F_\beta^{\text{obj}}(C_s, b_{ff})$ was again normalized and its values are shown in Figure 7.4.

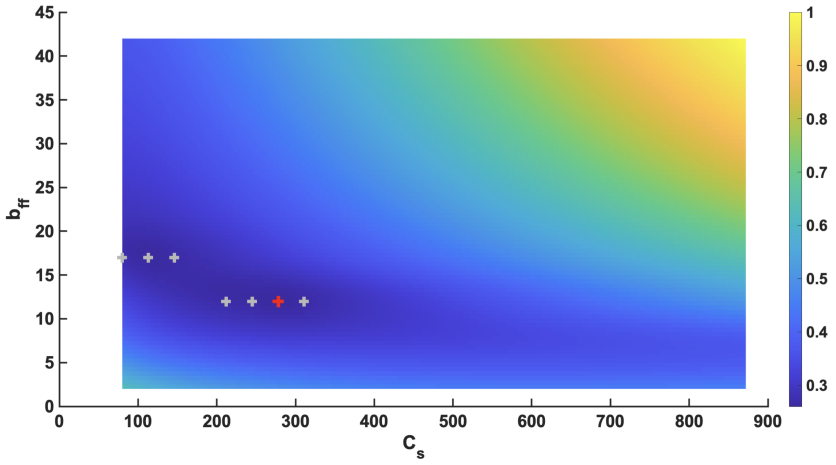

Figure 7.4: The normalized values of the objective function F_β^{obj}, $\beta = 0.42$ are colour-coded for the parameter sweep with fine sampling. The red cross symbol (+) indicates the optimal parameter combination and the grey crosses deliver a function value close to the minimal value (Equation 7.3).

7.1.3 Minimization Method

This method was described in Kovacheva and Baron et al. [150], published under the Creative Commons Attribution 4.0 International (CC BY 4.0) License.

A series of simulations were run with different parameter combinations, which were chosen by the minimization method. Similarly to the parameter sweep, the simulations were passive inflation of the LV with pressure from 0 mmHg to 30 mmHg. The initial state of the geometry was the unloaded state obtained by the unloading algorithm proposed by Bols et al. [56] (with parameter set $C = 324$ Pa, $b_{\text{f}} = 8$, $b_{\text{t}} = 3.2$ and $b_{ft} = 5.6$). The Nelder-Mead algorithm was applied to minimize the objective function [151]. It is a gradient-free direct search method and is suited for non-linear unconstrained optimization problems. To approximate an optimal point, the method iteratively generates a sequence of simplexes: geometric figure in n dimensions that is the convex hull of $n+1$ vertices [151]. The implementation of the Nelder-Mead algorithm in SciPy[1] [152] was employed. The tolerance was set to 1e-3 for both the function value and the parameters, which are optimized. If the change in these in the current iteration is less than the tolerance value compared to the previous iteration, then the algorithm terminates.

The objective function was defined based on F^{objAbs}. Additionally, a weight term was added, which considers the deviation from a target volume ratio

$$F_\lambda^{obj} = F^{\text{objAbs}} + \lambda \left| \frac{V_{30}}{V_0} - 2.38 \right|, \tag{7.6}$$

where the weight λ is set to 100 and $V_p = V_p(C_{\text{s}}, b_{\text{ff}})$ is the LV volume at pressure p for $p = 0$ mmHg and 30 mmHg.

[1] Available at `https://www.scipy.org`

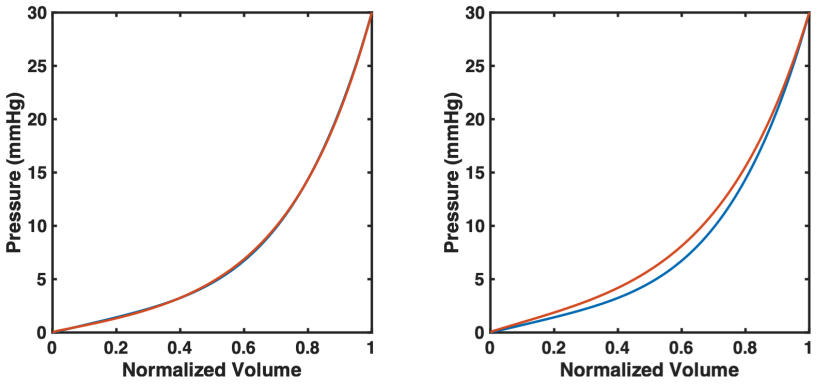

Figure 7.5: The adapted (blue) Klotz curve and the simulated (red) curve obtained from inflation simulation with the optimal parameters from the parameter sweep method with F^{obj} (left) and F_β^{obj}, with $\beta = 0.42$ (right). Left: $C_s^* = 150\,\text{Pa}$ and $b_{\text{ff}}^* = 22$; Right: $C_s^* = 278\,\text{Pa}$ and $b_{\text{ff}}^* = 12$.

7.2 Results

Adapted Klotz curve The adapted Klotz curve yields a better fit for the measured data for pressures smaller than 10 mmHg (the squared distance is 18.02 mmHg) compared to the original Klotz curve (the squared distance is 22.43 mmHg). Pressures smaller than 10 mmHg are particularly relevant for the description of the passive mechanical function during diastole.

Optimal parameter combination The optimal parameter combination resulting from the parameter sweep without the extended objective function was $C_s^* = 150\,\text{Pa}$ and $b_{\text{ff}}^* = 22$, and the minimal function value was $F^{\text{obj}}(C_s^*, b_{\text{ff}}^*) = 2.4\text{e}-4$ (red plus symbol in Figure 7.3). After the extension of the objective function and for $\beta = 0.42$, the optimal parameter combination was $C_s^* = 278\,\text{Pa}$ and $b_{\text{ff}}^* = 12$ and delivered $F_\beta^{\text{obj}}(C_s^*, b_{\text{ff}}^*) = 0.26$ (red plus symbol in Figure 7.4).

Note that the values of the objective functions are not comparable: while F^{obj} can reach zero values, the minimal values of F_β^{obj} is 0.25 due to its definition. The simulated Klotz curves obtained with the optimal parameter combination of each objective function (F^{obj} and F_β^{obj}) are visualized in Figure 7.5. The optimal parameter combination obtained with F^{obj} yields a very good match between the simulated and the adapted Klotz curve, while the parameters obtained with F_β^{obj} result in a deviation between these curves.

The optimization with Nelder-Mead algorithm provided $C_s^* = 156.56\,\text{Pa}$, $b_{\text{ff}}^* = 17.77$ ($b_{\text{xx}} = 7.11$ and $b_{\text{fx}} = 12.44$).

The starting state for inflation For the parameter sweep, the starting state of the geometry for the inflation simulation was the initial state of the geometry, which is not unloaded. It is the geometry, which is created from the imaging data. In contrast, for the Nelder-Mead

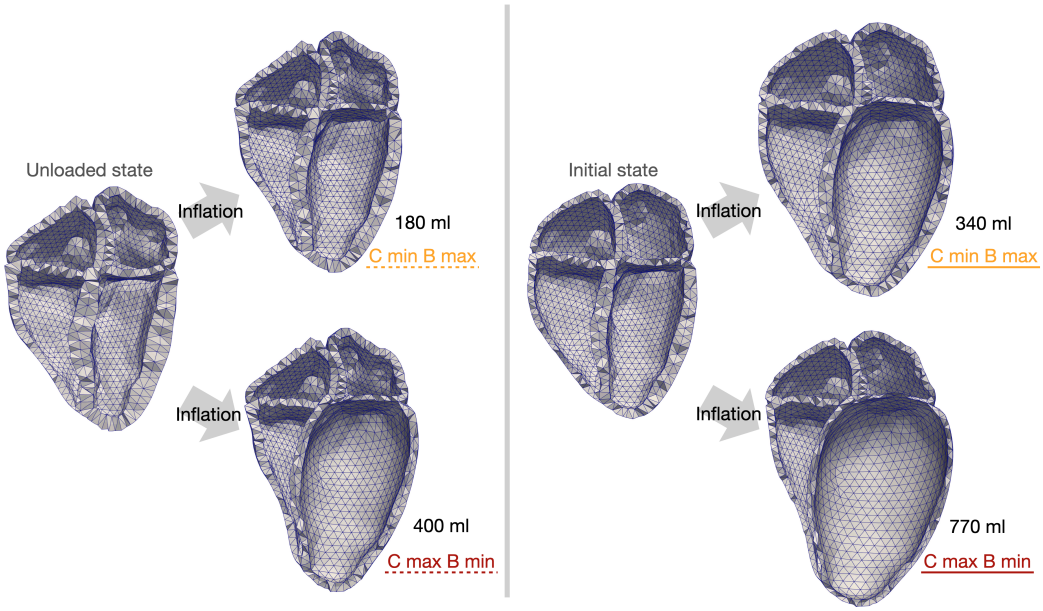

Figure 7.6: The result of the inflation simulation executed with different starting states: unloaded state (left part) and initial state (right part). Two parameter combinations were tested: $C_s^{min} = 110$ Pa and $b_{ff}^{max} = 42$ (inflated hearts in the upper part) and $C_s^{max} = 509$ Pa and $b_{ff}^{min} = 4$ (inflated hearts in the lower part).

optimization, this geometry was unloaded for a fixed parameter combination. Figure 7.6 visualizes the differences in the result of the inflation with different starting states (unloaded and initial) and two parameter combinations, both are close to the grey crosses in Figure 7.3. The first combination $(C_s^{min}, b_{ff}^{max})$ (indicated with yellow letters in the figure) is in the lower right part of the landscape of F^{obj}. The second combination $(C_s^{max}, b_{ff}^{min})$ (indicated with red letters in the figure) is in the upper left part of the landscape of F^{obj}. Both combinations yielded a value of F^{obj}, close to the minimal value. However, the absolute values of the volume of the LV was different: 180 ml vs. 400 ml (starting from unloaded state) and 340 ml vs. 770 ml (starting from initial state) for $(C_s^{min}, b_{ff}^{max})$ vs. $(C_s^{max}, b_{ff}^{min})$, respectively. A thinning of the myocardial wall is evident.

The left part of Figure 7.7 shows pressure-volume loops during the inflation procedure for four cases: both parameter combinations and both starting states. The simulation was extended to close the loop: after the pressure has reached 30 mmHg, it dropped immediately to 0 mmHg and the simulation was run until the starting LV volume was obtained. Again, the difference in the inflated volumes is apparent. However, the simulated Klotz curves for the experiment started with the initial geometry and the unloaded geometry (yellow curves in Figure 7.7, right) appear both close to the adapted Klotz curve (in blue colour).

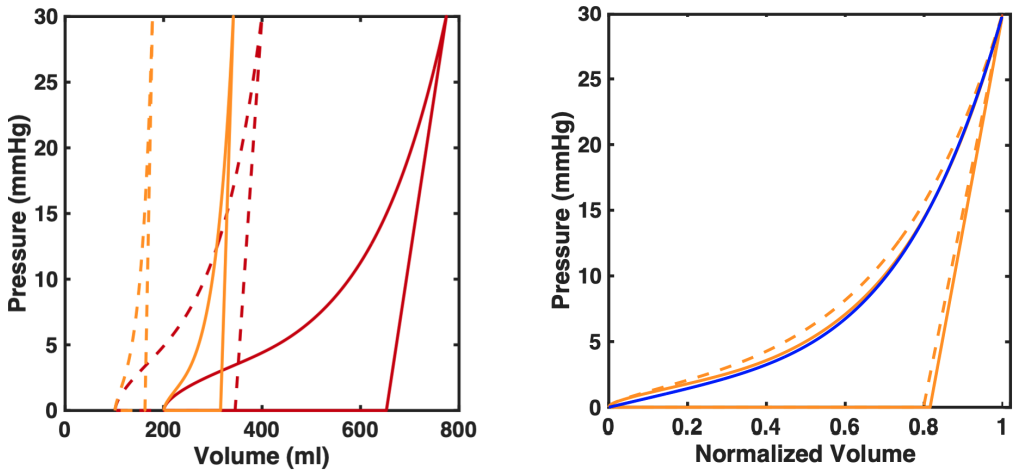

Figure 7.7: Left: pressure-volume loops during the inflation simulation executed with different starting states: unloaded state (dotted curves) and initial state (solid curves). Two parameter combinations were tested: $C_s^{min} = 110$ Pa and $b_{ff}^{max} = 42$ (yellow curves) and $C_s^{max} = 509$ Pa and $b_{ff}^{min} = 4$ (red curves). Right: The simulated curves simulated with unloaded state (dotted yellow curves) and initial state (solid yellow curves) and the adapted Klotz curve (blue).

7.3 Discussion

Two ways were described to identify parameters of a constitutive law determining the passive behaviour of the myocardium. Both methods are based on global data: EDPVR and volume ratio during a simulated inflation process. Parameter sets were identified for a whole heart model and the values are within the ranges found in literature [59].

Optimization methods The parameter sweep method has the advantage to deliver the pressure volume relation for all predefined parameter combinations. Therefore, several objective functions can be evaluated after the execution of the inflation simulations. This is not the case for the Nelder-Mead minimization method, which requires the optimization function to be defined prior to the start of the optimization. However, the parameter sweep method can be time consuming depending on the time needed for the inflation simulation. The parameter sweep method has a further advantage compared to Nelder-Mead: it can detect local and global minima and can be applied for flat functions (which have regions with very similar values). In the latter case, the result from the Nelder-Mead method depends on the choice of the tolerances [151]. The parameter sweep method can deliver the optimal values with accuracy up to the sampling step width (33 Pa for C_s and 5 for b_{ff}).

Volume ratio It was shown that a sole comparison to the adapted Klotz curve can deliver an optimal parameter set. However, within a certain tolerance, it is not unique (Figure 7.3). Therefore, the objective function was extended to include a volume ratio β, which was 0.42

at pressure 30 mmHg. However, the value of the target ratio, derived from the linear relation (Equation (8) in [100]) was established based on measurements, which appear to lie within a circular region rather than on a line. For small variations in the volume ratio, e.g. $\beta = 0.45$, the optimal values of the parameter set changed: $C_s = 179\,\text{Pa}$ and $b_{ff} = 17$. Furthermore, the volume ratio can be evaluated for different pressure values, e.g. for $P_m = 8\,\text{mmHg}$, the ratio between V_8 and V_0 is 0.55. This ratio set in the objective function leads to $C_s = 80\,\text{Pa}$ and $b_{ff} = 32$. Therefore, the problem of not obtaining a unique optimized parameter set was shifted to choosing an appropriate objective function.

The same holds for the choice of the weight factor λ in the objective function of the Nelder-Mead method: it is crucial as it determines the balance of two objectives.

Unloaded vs. initial state The optimization methods were applied on a whole heart geometry, determined from MRI images acquired during diastasis, where the pressure in the LV is about 8 mmHg. For the Nelder-Mead optimization, an unloaded state, which corresponds to the geometry at pressure zero was used. Figure 7.7, right showed the simulated Klotz curve from inflation starting with unloaded state and with initial state: there was only a small difference. However, the absolute volumes of the inflated LV differed strongly. The parameter sweep method was run with the same objective function as the Nelder-Mead optimization, but used the initial state of the geometry to start the inflation. This led to a parameter set, which is close to the one obtained starting with the unloaded state: $C_s = 146\,\text{Pa}$ and $b_{ff} = 17$ vs. $C_s = 156\,\text{Pa}$ and $b_{ff} = 17$, respectively. Therefore, it was assumed, that the starting state (unloaded or initial) does not influence the optimal parameter set strongly. However, it was not investigated how the unloaded state calculated individually for each parameter set will influence the optimization result.

The proposed frameworks can be applied to further constitutive laws, as far as they are implemented in the numerical framework which simulates the inflation. Also, it can be applied to any geometry with a closed cavity. The proposed workflows regard only global passive behaviour and does not compare to any local measurements such as strain and stretch of the tissue.

Currently, there is no way to validate the obtained parameters for a patient-specific geometry. Therefore, in future, developing an alternative method to estimate material properties and compare them to the proposed parameters in this work might be necessary. This might include patient specific clinical measurements, such as cine magnetic resonance imaging (MRI) or tagged MRI together with intraventricular pressure measurements.

Conclusion

The presented optimization methods can identify parameters for the constitutive law underlying numerical simulations of the heart's biomechanics. The commonly used normalized EDPVR derived from experiments was adapted to yield a better fit to the experimental data. The objective function based solely on this relation delivered several potential parameter sets.

Extension terms of the objective function were proposed, which yield unique identification of constitutive parameters. For future simulation, the parameter set $C_s = 156.5\,\text{Pa}$, $b_{ff} = 17.7$, $b_{xx} = 7.1$ and $b_{fx} = 12.4$ will be considered. Furthermore, it was shown that the starting state of the geometry (initial state or unloaded) had only minor influence on the optimal parameters. Avoiding the calculation of the unloaded state simplifies the procedure and saves calculation time. In future, these frameworks could be extended to include patient specific clinical measurements.

Chapter 8

Model Based Estimation of Active Tension and Location of Infarcts

In a numerical simulation, which delivers the deformation of the tissue, a dynamic active tension field is part of the input data and needs to be specified prior to the start of the simulation. Despite progress in the field of cardiovascular imaging in the last years, there is no clinical modality that measures the active tension field. Still, the resulting deformation can be observed in various imaging techniques: echocardiography, computed tomography (CT) or magnetic resonance imaging (MRI). In Chapter 5, the clinically measured deformation of the left ventricle (LV) was compared to the simulated deformation and therefore, used to validate the model. In this Chapter, the dynamic active tension field is estimated, so that the resulting deformation of the LV matches clinically measured deformation. Therefore, the deformation is part of the input data of the estimation method. In particular, the deformation of the endocardial surface of the LV is used as an input. This corresponds to a general definition of an inverse problem, which calculates the causal factors that produce the input set of observations. In the following, it is called an inverse problem of cardiac biomechanics.

Since when using clinical data, there is no ground truth available to ensure the result is correct, first, the accuracy of the reconstruction of active tension and its sensitivity to variation of model parameters using synthetic data must be determined. In particular, the influence of the fiber orientation on the reconstruction is studied since changes in fiber orientation affect the distribution of the active tension in the heart [153]. Furthermore, the effect of variability in the endocardial deformation is explored, considering the potential inter-and intra-observer variability in MRI segmentation [154]. A relation between the error in the reconstruction of the active tension field and the error in the input data is provided and different regularization parameters are investigated.

Additionally, it was assumed that the myocardial regions which do not develop active tension are related to infarct scars. Therefore, by reconstructing the dynamic active tension distribution, it is possible to detect the size and the location of infarct regions. Furthermore,

the active tension distribution and dynamics could be complementary information. In clinical routine, scar tissue can be identified by abnormal regional wall motion using echocardiography or by injecting gadolinium to the patient in a late gadolinium enhancement (LGE) MRI study. However, in both techniques, passive material properties and active tension in and around the scar cannot be depicted. Additionally, it has been shown that LGE has adverse side effects and should be employed with caution [155]. Additionally, areas not showing hyper-enhancement might still have undergone remodelling and developed more, less or dynamically different active tension. In the sensitivity analysis, defined sizes of infarct areas were defined. Finally, a proof of concept using only clinical data for the reconstruction is provided.

Prior to this work, a solution method for this inverse problem has been proposed by Fritz et al. [4, 156] and implemented in the framework CardioMechanics. In the Methods section, the differences between this implementation and the current version are described.

8.1 Methods

8.1.1 Method for Solving the Inverse Problem to Estimate Active Tension

The deformation of the endocardial surface, which is input data for the inverse problem to estimate active tension, is referred to as *target* surface. The aim of solving this inverse problem is to reconstruct the active tension distribution over time which leads to the provided target deformation. In particular, for each volumetric finite element $e_l \in \mathscr{E}$ ($l = 1,\dots,M$, $M = |\mathscr{E}|$, where $\mathscr{E}$ is the set of volume elements) for each time step t_i ($i = 1,\dots,T$, where $T = T_{CL}/\Delta t$, $\Delta t = 10\,\text{ms}$ and $T_{CL} = 800\,\text{ms}$ is the heart cycle duration) a distinct value for the active tension s_i^l is estimated. The distance between the target surface and the endocardial surface of the inverse model, called the *reconstructed* surface, is calculated and minimized.

Distance calculation The distance vector (*gap*) is denoted by $g \in \mathbb{R}^N$. For every triangle on the reconstructed surface, each node is matched with the closest triangle on the target surface. The distance in x-, y- and z-direction is calculated between the reconstructed node and a point $p_j^T \in \mathbb{R}^3$ on the target triangle. This point p_j^T is the intersection point of the reconstructed triangle normal (starting at the reconstructed node) and the matched target triangle. Then, the component-wise distance g_i from the j-th reconstructed node to the target surface is obtained as the mean over the distance (belonging to the j-th node) of the set of reconstructed triangles including this node ($\mathscr{K}_j$):

$$g_i = \frac{1}{|\mathscr{K}_j|} \sum_{k \in \mathscr{K}_j} |p_{k,r}^T - n_{j,r}^R|, \tag{8.1}$$

where $\mathscr{K}_j = \left\{ k \in \left[1, |\mathscr{T}^R|\right] \text{ with } \iota_k^R \in \mathscr{T}^R \text{ and } n_j^R \in \iota_k^R \right\}$.

In Equation (8.1), $i = 3(j-1)+r$, where $r = 0,1$ or 2 for the x-, y- and z-component, respectively and j is the index of the reconstructed node observed ($j = 1,\dots,\hat{N}$), $\hat{N}$ is the number of nodes on the reconstructed surface, $N = 3\hat{N}$ and $\iota_k^R \in \mathscr{T}^R$ is a triangle on the reconstructed surface with nodes n_j^R ($j = 1,2,3$). The index $k = 1,\dots,|\mathscr{T}^R|$, where $\mathscr{T}^R$ is the set of reconstructed triangles.

The target surfaces are available every 20 ms, but the distance is calculated for every simulation time step t_i. Therefore, the coordinates of the nodes of the target triangles are interpolated linearly over time.

Distance minimization In order to obtain the change of the active tension contributing to the overall tension, for every time step t_i, the distance g_i is minimized iteratively using a Newton scheme. The change of the active tension in the n-th iteration is denoted by $\tau_{i,n} \in \mathbb{R}^M$ and the gap by $g_{i,n}$ (the index i corresponds to the i-th time step). The overall active tension vector s_i at the i-th time step adds up to $s_i = s_{i-1} + \tau_i$, where $\tau_i = \sum_{k=1}^{n} \tau_{i,k}$. Here, the number of Newton iterations is denoted by n and determined by the following stop criteria:

$$g_{i,n} < \varepsilon_a \vee |g_{i,n} - g_{i,n-1}| < \varepsilon_r \vee n > \bar{N}_{max}. \tag{8.2}$$

Both the absolute tolerance ε_a and the relative tolerance ε_r are set to 10^{-5} and the maximal number of iteration $\bar{N}_{max}$ is 5 [4]. In every Newton step, the gap $g_{i,n}$ is recalculated to regard the deformation of the reconstructed surface caused by the estimated active tension of the previous iteration. To calculate the deformation, the forward problem is solved for one time step to assert the balance of all forces. In particular, the active tension is balanced with the passive force and the pressure applied on the surface. After the forward solver is executed, the distance between the target and reconstructed triangles is once again calculated.

In every Newton iteration step, the change of active tension is estimated. For this purpose, the relation of the gap $g_{i,n}$ and $\tau_{i,n}$ is linearly approximated by the matrix A as follows:

$$A\tau_{i,n} = g_{i,n}. \tag{8.3}$$

The matrix $A \in \mathbb{R}^{N\times M}$ is the product of the inverse tangential stiffness matrix $K_d^{-1} \in \mathbb{R}^{N\times S}$ and a matrix $K_T \in \mathbb{R}^{S\times M}$, where S is the number of nodes of all volume elements. In general, the stiffness matrix describes the linearised relation of a small change of the nodal displacement Δd and the resulting change of the nodal forces Δf. In order to reduce the dimension of the stiffness matrix, only the rows related to the reconstructed nodes are used for the matrix K_d. In particular, the reconstructed nodes are displaced in a positive and negative direction and the resulting nodal forces in the entire volume are computed. A further dimension reduction is possible by removing some reconstructed nodes prior to the simulation. The latter reduction is only necessary for a large number of endocardial nodes, which was not the case in the presented experiments. The second matrix K_T describes the change of all nodal forces Δf due to the change of the active tension Δs in all volume elements. Both matrices K_d and K_T are calculated using central finite differences with $\varepsilon_d = 10^{-12}$ m and $\varepsilon_t = 1$ kPa, respectively. Altogether, the matrix A is the following:

$$A = K_d^{-1}K_T = \left(\frac{\Delta f}{\Delta d}\right)^{-1}\frac{\Delta f}{\Delta s}. \tag{8.4}$$

Regularization techniques Due to the construction of the matrix A, the active tension $\tau_{i,n}$ in each volume element is mapped to the displacement of the endocardial surface. Computing $\tau_{i,n}$ from equation (8.3) is an underdetermined, ill-posed problem since there is no unique solution, as the matrix A is not symmetric ($N < M$). Furthermore, this matrix has a high condition number (for the geometry elli15, it was 10^9). Thus, it requires regularization and a second order Tikhonov approach with spatial and temporal regularization was employed. Therefore, equation (8.3) was extended by a regularization term yielding the following minimization problem:

$$\arg\min\left(||A\tau_{i,n} - g_{i,n}||^2 + \lambda_1 \frac{1}{\Delta t^2}||s_{i,n} - 2s_{i-1,n} + s_{i-2,n} + \tau_{i,n}||^2 + \lambda_2||\Delta_c(s_{i,n} + \tau_{i,n})||^2\right). \quad (8.5)$$

The solution is obtained by solving the regularized normal equations:

$$(A^T A + \frac{\lambda_1}{\Delta t^2} I + \lambda_2 \Delta_c)\tau_{i,n} = A^T g_{i,n} - \lambda_1 \frac{1}{\Delta t^2}(s_{i,n} - 2s_{i-1,n} + s_{i-2,n}) - \lambda_2 \Delta_c s_{i,n}. \quad (8.6)$$

Here, I is the identity matrix and Δ_c is the discrete Laplace operator, which contains the connectivity information of the volume elements. Equation (8.6) is solved in every iteration using LU decomposition to provide the change of the active tension $\tau_{i,n}$ of the current iteration.

Regularization parameters The parameter λ_1 controls the temporal regularization and λ_2 the spatial one. From Equation (8.5), each regularization parameter can be expressed as a ratio between the squared residual norm and the corresponding squared norm of the regularization term. The residual norm depends on the element discretization of the computational domain, as the volume of each element is involved in the construction of the matrix A. Thus, the choice of regularization parameters depends on the spatial discretization of the computational domain and will be discussed for each geometry.

In Figure 8.1, the method for solving the inverse problem to estimate active tension is graphically represented.

8.1.2 Adaptions of the inverse solver

The inverse solver was adapted to the current structure of CardioMechanics since it differed from the one developed by Thomas Fritz. Figure 9.1 in [4] shows a schematic description of CardioMechanics. The active tension was part of the data container in the geometrical model class. It was represented in one object describing the tension values in all elements for one time point. In the current version, the active tension is part of the element class: each finite element has one instance of the object describing the active tension. Therefore, the calculation of the matrix K_T was adapted to these changes: the central finite differences were executed by evaluating the object describing the active tension for the current element.

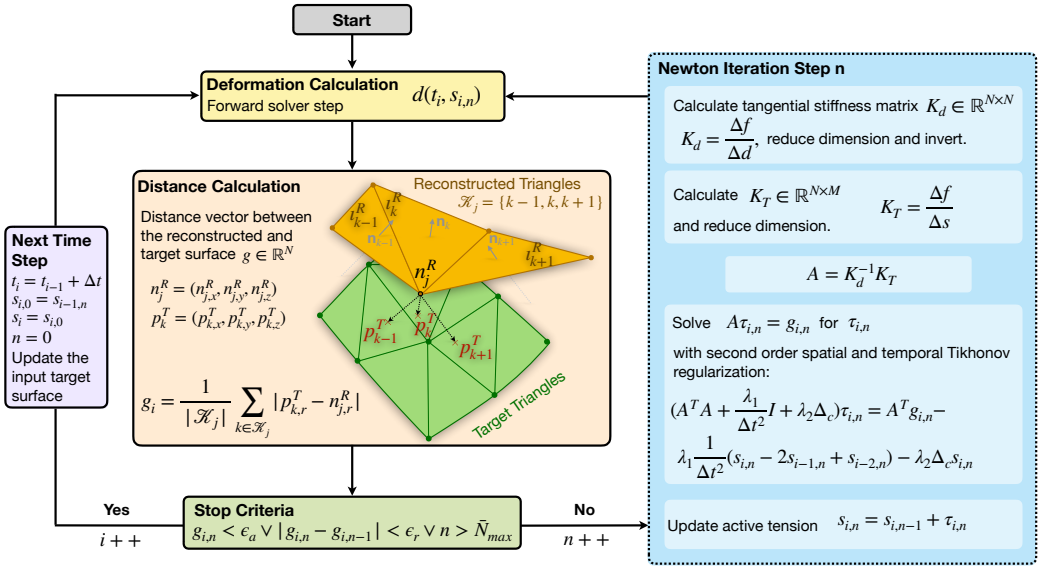

Figure 8.1: A graphical representation of the method for solving the inverse problem to estimate active tension. Adapted from [123], published under the Creative Commons Attribution 4.0 International (CC BY 4.0) License.

8.1.3 Sensitivity analysis using synthetic data

To explore the sensitivity of the inverse method regarding the uncertainty of input parameters, the parameters were systematically varied and the reconstructed active tension was evaluated. In particular, the fiber orientation and displacement of the target surfaces were varied. Furthermore, infarct areas of different size were defined and reconstructed.

Each experiment (case) consists of two simulations, one forward and one inverse. For both simulations, a set of parameters are defined: related to the geometry (the fiber direction, the number of nodes and elements); related to the solution method: time step size, tolerances, length of one heart beat (cycle length); related to the different models: passive parameters, active tension curve and its maximum. The forward simulation is executed with the ground truth of the active tension and the resulting endocardial surface deformation is extracted to obtain the synthetic input data set.

Unless stated otherwise, the parameters of the reference case were applied, as described in the following.

Reference case In the reference case, the parameters of the forward and inverse simulations were the same, except that in the inverse simulation, no active tension model was provided. Instead, the active tension curve was reconstructed. In particular, for the geometry elli15, the reference fiber direction was $(90°, -90°)$ and for the image-based left ventricular geometry geo20LV $(80°, -70°)$. A sine and a Hill pressure curve were applied to the endocardial surface of geo20LV (respectively, Case 11 and Case 12 in Table 8.1). The Hill

curve has the same morphology as the DH active tension curve, described in Chapter 3.3. The cycle length was $T_{CL} = 800\,\text{ms}$ and the time step size $\Delta t = 10\,\text{ms}$. The target surfaces were extracted from the endocardial deformation of the forward simulation every 20 ms. The passive material parameters were the same in the forward and inverse model.

Fiber variation The fiber direction was varied only in the forward simulation, which led to a different target surface deformation compared to the reference case. Three additional fiber combinations were investigated: $(80°, -90°)$, $(90°, -80°)$ and $(80°, -80°)$. In Table 8.1, they correspond to Case 1, Case 2 and Case 3, respectively. For the model used in the inverse solver, $(90°, -90°)$ was used. In these cases, an infarct area was not present in the forward simulation. The fiber variation study was conducted only for the ellipsoid geometry elli15.

Target surface variation The endocardial surfaces were extracted from the forward simulation and the position of a target node was varied in the direction of the node normal. The node normal was calculated as the mean of the normals of the adjacent triangles, which all point towards the barycenter of the geometry. Only the nodes which were not fixed due to the boundary conditions were varied.

In total, nine experiments were defined in which the surface node coordinates were varied with different percentages of wall thickness. The first three experiments were executed with elli15: Case 4, Case 5 and Case 6 in Table 8.1. In Case 4, 20 % of the wall thickness was added to the node coordinates in the positive normal direction, i.e., towards the center. In Case 5, 20 % of the wall thickness was added to the node coordinates in the negative normal direction. In Case 6, also 20 % of the wall thickness was added to the node coordinates, but the normal direction was alternating between positive and negative each 20 ms.

The other six experiments were executed with geo20LV: Cases 13–18 in Table 8.1. In Case 13, Case 15 and Case 17, respectively, 10 %, 20 % and 30 % of the wall thickness was added to the node coordinates in positive normal direction, i.e., towards the center. In Case 14, Case 16 and Case 18, respectively, 10 %, 20 % and 30 % of the wall thickness was added to the node coordinates in negative normal direction. The variation was applied to the target surface over all time steps except the target surface at 0 ms. It was assumed that there is no active tension present at the simulation's initial state. Therefore, the distance vector is the zero vector as the target surface and the reconstructed surface match at 0 ms. In these cases, an infarct area was not present in the forward simulation.

Infarct size variation Simplified infarct areas were modeled as regions that developed no active tension in the ellipsoid geometry elli15 to see whether the proposed inverse method, which reconstructs the active tension, can detect these infarct areas. In order to explore the limits of the reconstructed infarct size, connected transmural infarct areas of different size were defined in the forward simulations: 1 %, 5 %, 10 % and 22 % of the number of volume elements. In those elements, the active tension was constantly set to zero in the forward simulation. The passive material parameters were the same in the healthy and the infarct cells. The presence of an infarct area led to a different target surface deformation compared

Table 8.1: Overview of the cases of the sensitivity analysis and the corresponding variations used to generate the synthetic data. Grey values were unaltered with respect to the reference simulation.

Cases	Geometry	Fiber	Surface	Infarct	Pressure
Case 1	elli15	(80°, -90°)	0 %	0 %	-
Case 2	elli15	(90°, -80°)	0 %	0 %	-
Case 3	elli15	(80°, -80°)	0 %	0 %	-
Case 4	elli15	(90°, -90°)	+ 20 %	0 %	-
Case 5	elli15	(90°, -90°)	− 20 %	0 %	-
Case 6	elli15	(90°, -90°)	± 20 %	0 %	-
Case 7	elli15	(90°, -90°)	0 %	1 %	-
Case 8	elli15	(90°, -90°)	0 %	5 %	-
Case 9	elli15	(90°, -90°)	0 %	10 %	-
Case 10	elli15	(90°, -90°)	0 %	22 %	-
Case 11	geo20LV	(80°, -70°)	0 %	0 %	Sine Curve
Case 12	geo20LV	(80°, -70°)	0 %	0 %	Hill Curve
Case 13	geo20LV	(80°, -70°)	+10 %	0 %	Hill Curve
Case 14	geo20LV	(80°, -70°)	-10 %	0 %	Hill Curve
Case 15	geo20LV	(80°, -70°)	+20 %	0 %	Hill Curve
Case 16	geo20LV	(80°, -70°)	-20 %	0 %	Hill Curve
Case 17	geo20LV	(80°, -70°)	+30 %	0 %	Hill Curve
Case 18	geo20LV	(80°, -70°)	-30 %	0 %	Hill Curve

to the reference case. In Table 8.1, the described variations correspond to Case 7, Case 8, Case 9 and Case 10, respectively.

8.1.4 Reconstruction with Clinical Data

While in the sensitivity analysis the geometry of geo20LV is created based on clinical images (Section 4.1.4), the deformation data used as input was extracted from a forward simulation of the mechanics. In the clinical case, also referred to as *Case CA*, both the geometry (geo-CardAtl, Section 4.1.4) and the target surfaces (the deformation of the endocardial surface) were extracted from a Cine MRI acquisition. The image data were provided in Sunnybrook Cardiac Data[1] (2009 Cardiac MR Left Ventricle Segmentation Challenge), published under Public Domain (CC0 1.0 Universal) License [118]. The data set SCD0003801 was used for the reconstruction. It was acquired from a healthy volunteer. The fiber orientation was created with 80° on the endocardium and -70° on the epicardium [30]. No pressure was applied and no pressure measurement was included in the data set.

Note on the data set The segmentation of the endocardial surfaces for 22 time points was included in the data set. Unfortunately, they had a data format, which is not commonly used and the tools provided to transform the data format into a more common one (.stl or .vtu/.vtk) did not work. Fortunately, Dr. Charlene Alice Mauger (Research Fellow in Auckland Bioengineering Institute) could provide the endocardial deformation data set

[1] `https://www.cardiacatlas.org/studies/sunnybrook-cardiac-data/`

already converted in .stl format. She confirmed that the provided surfaces were obtained from segmented short axis Cine slices, which were manually aligned by the analyst in case breath-misregistration was observed. All endocardial surfaces were remeshed to obtain better element quality, especially at the apex. They were used as target surfaces for the reconstruction of the active tension.

Temporal alignment of the surface The temporal alignment of the target surfaces was done manually. A forward simulation was run to obtain the deformation of the endocardial surfaces and these were compared to target surfaces. For target surface 1, 5, 7, 9, 13 and 19, the time point of the best match were chosen (0.11, 0.22, 0.34, 0.53, 0.65 s). The other surfaces were distributed equidistantly in-between these points. The time point for each target surface is provided in Appendix E.

8.1.5 Evaluation of the Inverse Reconstruction

Five criteria were defined to quantify the quality of the reconstructed active tension in the inverse simulation. They were applied only on the results of the sensitivity analysis and not on the reconstruction with clinical data since, in the latter case, no ground truth was available.

Peak tension time (PTT) PPT was denoted by t_p^l ($l = 1 \dots M$) and defined as the time step in which the maximum (over time) active tension of the l-th finite element is reached in the inverse reconstruction.

Peak tension error The peak tension error ε_a^l of the l-th finite element is the difference between the reconstructed active tension at PTT $s^l(t_p^l)$ and the ground truth active tension ${s^l}_{GT}(t_p^l)$ at PTT

$$\varepsilon_a^l = s^l(t_p^l) - {s^l}_{GT}(t_p^l). \tag{8.7}$$

Mean tension error (MTE) The MTE of the inverse reconstruction is defined as the mean over the absolute value of the peak tension error of all volume elements

$$\varepsilon_a = \frac{1}{|\mathscr{E}|} \sum_{l:e_l \in \mathscr{E}} |\varepsilon_a^l|. \tag{8.8}$$

Relative tension error The relative tension error ε_r^l of the l-th finite element is the peak tension error divided by the active tension at PTT ${s^l}_{GT}(t_p^l)$

$$\varepsilon_r^l = \varepsilon_a^l \left({s^l}_{GT}(t_p^l) \right)^{-1}. \tag{8.9}$$

Mean relative tension error (MRTE) The MRTE ε_r of the inverse reconstruction is the mean of relative tension errors of all elements

$$\varepsilon_r = \frac{1}{|\mathscr{E}|} \sum_{l:e_l \in \mathscr{E}} |\varepsilon_r^l|. \tag{8.10}$$

Root mean square error (RMSE) To capture the reconstruction error during the entire time course, the RMSE was calculated for every element ε_m^l. It is the second norm of the differences of the reconstructed active tension $s^l(t_i)$ and the ground truth active tension ${s^l}_{GT}(t_i)$ divided by the root of the number of time steps T

$$\varepsilon_m^l = \frac{1}{\sqrt{T}} \sqrt{\sum_{i=1\dots T} \left(s^l(t_i^l) - {s^l}_{GT}(t_i^l)\right)^2}. \tag{8.11}$$

Identification of infarct tissue To separate infarct tissue from healthy tissue, a relative threshold $\mathbb{T}$ for the reconstructed active tension was defined. Each element $e_l \in \mathscr{E}$ was classified as an infarct element in $\mathscr{E}_i$ or as a healthy element in $\mathscr{E}_h$. An element e_l was considered to be infarcted if the reconstructed peak tension was less than the percentage threshold of the maximum over all reconstructed active tension for all elements

$$\mathscr{E}_i = \left\{e_l \in \mathscr{E}, l = 1,\dots,M | s^l(t_p^l) < \mathbb{T} \max_{j=1\dots M} s^j(t_p^j)\right\}.$$

All other elements were considered healthy

$$\mathscr{E}_h = \left\{e_l \in \mathscr{E}, l = 1,\dots,M | s^l(t_p^l) \geq \mathbb{T} \max_{j=1\dots M} s^j(t_p^j)\right\},$$

where $\mathscr{E} = \mathscr{E}_i \cup \mathscr{E}_h$. Based on the forward simulation, the ground truth set of infarct elements $\mathscr{E}_i^{\text{corr}}$ and of healthy elements $\mathscr{E}_h^{\text{corr}}$ were defined

$$\mathscr{E}_i^{\text{corr}} = \{e_l \in \mathscr{E}, l = 1,\dots,M | s_{GT}^l(t_p) = 0\} \quad \text{and} \quad \mathscr{E}_h^{\text{corr}} = \{e_l \in \mathscr{E}, l = 1,\dots,M | s^l(t_p) > 0\}.$$

Choice of the threshold $\mathbb{T}$ The cardinalities of intersections of these four sets were used to calculate the sensitivity and specificity for each experiment. Since the elements in the sets are the IDs of the discrete finite elements of the geometry, the metrics inherently consider the locations of the healthy and unhealthy elements. The elements satisfying the true positive condition are the ones defined as infarct elements in the forward simulation as well as reconstructed as infarct elements in the inverse result ($\mathscr{E}_i^{\text{corr}} \cap \mathscr{E}_i$). Thus, the sensitivity is calculated only for the experiments with defined infarct areas in the forward settings. Based on those cases, an overall receiver operating characteristic (ROC) curve is calculated to determine one optimal threshold $\mathbb{T}$ for all cases with different infarct sizes. To determine the overall ROC curve, for each threshold value, the mean over the corresponding values of all ROC curves (for each infarct case separately determined) was calculated.

For the cases of infarct size variation, MTE was calculated for both sets $\mathscr{E}_i^{\text{corr}}$ and $\mathscr{E}_h^{\text{corr}}$. MRTE was calculated only for healthy elements since the active tension for infarct elements was set to be zero in the forward simulation. The infarct classification was also applied if, in the forward simulation, no infarct area was defined.

8.2 Results

8.2.1 Results with Ellipsoid Geometry

Reference case In the reference case, the reconstructed active tension was matching the ground truth active tension with an MRTE of 0.7 % and a maximal peak tension error < 0.5 kPa (Figure 8.2(a)). All elements were correctly identified as non-scar elements. This result was obtained with spatial regularization $\lambda_2 = 10^{-14}$. Applying stronger spatial regularization (e.g. $\lambda_2 = 10^{-12}$ and $\lambda_2 = 10^{-10}$) slightly improved the result as the MRTE decreased to 0.6 %. Less spatial regularization led to higher MRTE, for $\lambda_2 = 10^{-16}$ it was 2 %. The peak tension errors for all elements for different spatial regularization parameters $\lambda_2 = 10^{-22}, 10^{-20}, \ldots, 10^{-10}$ are visualized in Figure 8.3. The following results were obtained with spatial regularization $\lambda_2 = 10^{-14}$, except stated otherwise. No temporal regularization was imposed ($\lambda_1 = 0$), except stated otherwise.

Fiber variation Next, the fiber direction in the forward model was varied. In the inverse model, the fibers of the reference case were used. For the cases of the endocardial or epicardial angles varied by 10° (Case1, $(80^\circ, -90^\circ)$ and Case 2, $(90^\circ, -80^\circ)$) in the forward simulation, the reconstructed active tension had an MRTE of about 26 %. Furthermore, a large spread of the active tension at the PTT was observed (Figure 8.2(b) and (c)), ranging from 15 kPa to 55 kPa, whereas the maximum of the forward tension was 40 kPa for all elements. In both cases, the tension in the apex region was underestimated and led to an incorrect detection of an infarct region (specificity 0.92 for threshold $\mathbb{T} = 0.52$). Nevertheless, the shape of the time course of the reconstructed active tension curve resembled the shape of the Hill curve used in the forward model as visualized in Figure 8.2(b) and (c).

The variation of both endocardial and epicardial angles by 10° (Case 3, $(80^\circ, -80^\circ)$) in the forward simulation led to an MRTE of 68 % for the reconstructed active tension. The spread of the tension ranged from 0.7 kPa to 76 kPa (Figure 8.2(d)) and thus, led to a misclassification of elements with specificity 0.85.

Target surface variation Here, the endocardial surfaces extracted from the forward simulation were varied and provided as input target surfaces for the inverse solver. In Case 4 in Table 8.1, the nodes were shifted towards the inside of the ellipsoid by 20 % of the initial wall thickness. This led to a severe overestimation of the active tension, ranging from 66 kPa to 140 kPa at the PTT, as visualized in Figure 8.4(a). Thus, a misclassification of some elements was observed with a specificity of 0.95 ($\mathbb{T} = 0.52$).

In Case 5 in Table 8.1, the nodes were shifted towards the outside of the ellipsoid by 20 % of the initial wall thickness. In contrast to the case described before, an underestimation of the active tension was observed (Figure 8.4(b)). The reconstructed tension ranged from 3.5 kPa to 30 kPa, also leading to a misclassification of elements (specificity 0.42).

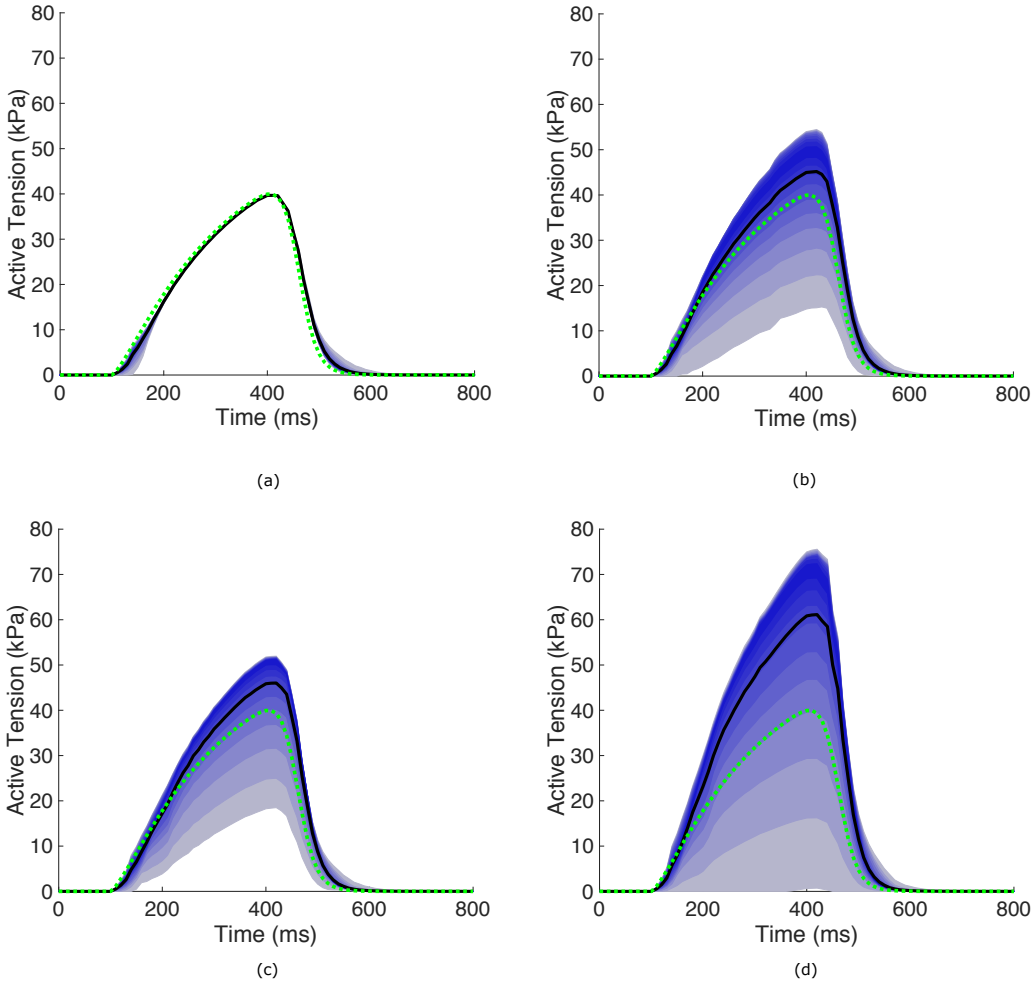

Figure 8.2: (a) Reconstruction of the active tension in the reference case; (b) reconstruction for fiber variation $(80°, -90°)$, Case 1; (c) for $(90°, -80°)$, Case 2; (d) for $(80°, -80°)$, Case 3. The reconstructed mean active tension time course is the black line and the time-varying distribution percentiles (from $5\,\%$ to $95\,\%$) are shown as blue bands ($5\,\%$) around the median (not shown) of the reconstructed active tension time course for all volume elements. For every time step, each blue band represents the active tension range in 5 % of the finite elements. The green dotted line is the ground truth active tension. Adapted from [123], published under the Creative Commons Attribution 4.0 International (CC BY 4.0) License.

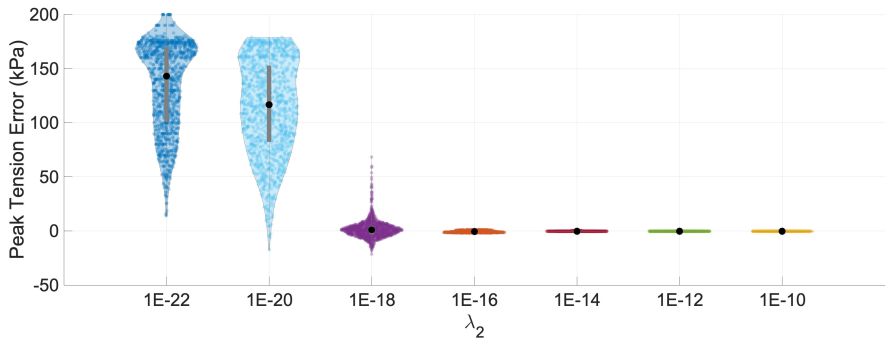

Figure 8.3: The peak tension error of all volume elements and their distribution for different values of the spatial regularization parameter λ_2. The black dot represents the median of the peak tension error and the gray bar represents the error between the first and third quartile. Adapted from [123], published under the Creative Commons Attribution 4.0 International (CC BY 4.0) License.

These two experiments explored the maximal variation of the target surface regarding the potential uncertainty in the segmentation of clinical data. In Case 6 in Table 8.1, variation of the target surface was added in alternating directions, changing between positive and negative displacement every 20 ms. The reconstruction of the active tension had an MRTE of 95 % and values at the PTT ranging from 46 kPa to 86 kPa (Figure 8.4(c)). All elements were classified correctly (specificity 1.0).

In a further experiment for Case 6, additional to the spatial regularization, temporal regularization was imposed. For temporal regularization $\lambda_1 = 10^{-20}$, the MRTE decreased to 12 % and the active tension values at the PTT were between 40 kPa and 48 kPa (Figure 8.4(d)). Less temporal regularization $\lambda_1 < 10^{-20}$ did not improve the reconstruction compared to the result with no temporal regularization. More temporal regularization $\lambda_1 = 10^{-18}$ led to an MRTE over 200 % as the PTT for all elements was higher than 600 ms with a range for the reconstructed active tension between 62 kPa and 100 kPa.

Infarct size variation In order to estimate the infarct size based on the inverse solution, all finite volume elements were classified as healthy, or infarct elements by a relative threshold applied on the reconstructed active tension. The optimal threshold value was $\mathbb{T} = 0.52$ as determined by the overall ROC curve (Figure 8.5). The area under the curve (AUC) was 0.968. The calculated threshold value is close to the optimal threshold for the case with 1 % infarct area, which is 0.53 (AUC 0.999) and further away from the optimal threshold for the case with 22 % infarct area, which is 0.28 (AUC 0.975).

For an infarct with a size of 1 % (Case 7 in Table 8.1) of the whole left ventricular wall volume in the forward simulation (Figure 8.7(a)), the sensitivity was 0.95 and the specificity was 0.99. For cases of infarct sizes of 5 % and 10 % (Case 8 and 9 in Table 8.1, respectively), the sensitivity was 1.0 and the specificity was 0.89. For the infarct size of 22 % (Case 10 in Table 8.1), the sensitivity was 0.98 and the specificity was 0.71. The threshold value 0.52 was applied for all experiments in this work to calculate the specificity of the classification.

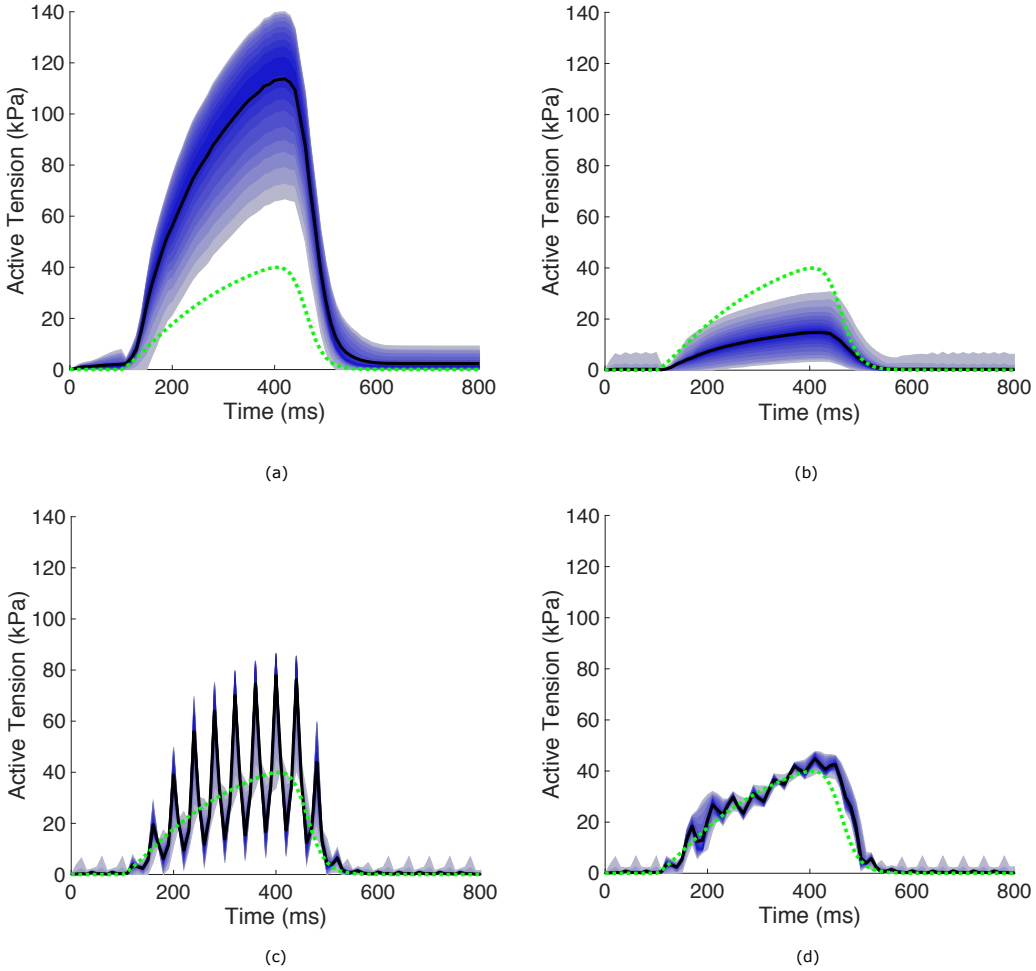

Figure 8.4: (a) Reconstruction of active tension for $+20\,\%$ constant shift of the target surface, Case 4; (b) $-20\,\%$ constant shift, Case 5; (c) target surface variation in altering direction $\pm 20\,\%$, Case 6; (d) Case 6 with additionally imposed temporal regularization with $\lambda_1 = 10^{-20}$. The reconstructed mean active tension time course is the black line and the time-varying distribution percentiles (from $5\,\%$ to $95\,\%$) are shown as blue bands ($5\,\%$) around the median (not shown) of the reconstructed active tension time course for all volume elements. For every time step, each blue band represents the active tension range in 5 % of the finite elements. The green dotted line is the ground truth active tension. Adapted from [123], published under the Creative Commons Attribution 4.0 International (CC BY 4.0) License.

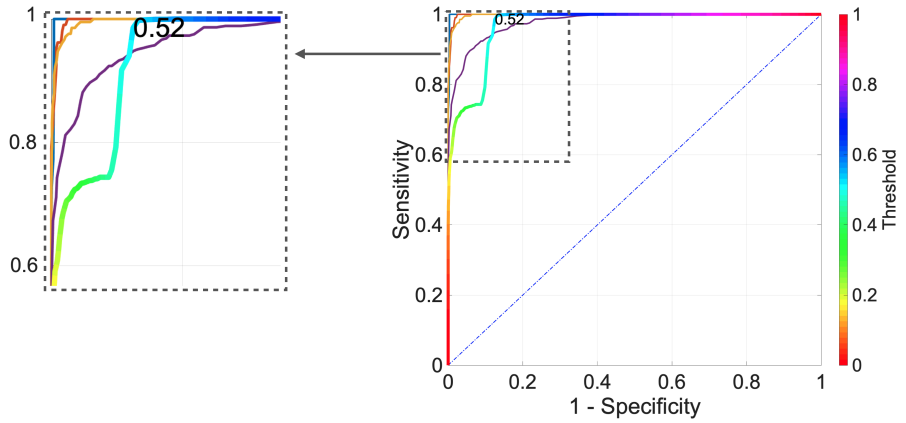

Figure 8.5: The overall ROC curve is the multi-colour line. The single-colour curves are the ROC curves calculated for each experiment with an infarct scar of specific size: 1 % (blue line), 5 % (orange), 10 % (yellow) and 22 % (purple). Modified from [123], published under the Creative Commons Attribution 4.0 International (CC BY 4.0) License.

In the forward simulation, the elements of the infarct area experienced some deformation due to the surrounding healthy elements. For all infarct cases, the mean reconstructed active tension of the infarct elements varied up to 22 kPa (Figure 8.6(a)–(d)), which is an overestimation compared to the zero tension in the forward simulation. On the other hand, as the inactive (only passive) behavior of the infarct elements restricts the overall contraction, the mean reconstructed active tension of the healthy elements was slightly underestimated and varied between 34 kPa and 40 kPa (Figure 8.6(a)-(d)). Additionally, this effect was amplified by the spatial regularization ($\lambda_2 = 10^{-14}$), which led to blurring of the active tension distribution across the elements. In particular, in the border zone of the detected infarct, the active tension gradually rose from the inside of the infarct area in the direction of the surrounding tissue (Figure 8.7(a)–(d)).

In general, the reconstruction of the infarct size was improved by applying less spatial regularization ($\lambda_2 < 10^{-14}$). For example, for the 5 % infarct case, the specificity rose to 0.96 and the MRTE decreased from 14 % to 11 % for $\lambda_2 = 10^{-16}$. When more spatial regularization was applied, the peak tension error of the reconstructed active tension for elements in the scar region rose compared to the case with $\lambda_2 = 10^{-14}$. The distribution of the peak tension error for all infarcted elements for different values of the spatial regularization parameter is visualised in Figure 8.8.

8.2.2 Results with Image-Based Geometry

Reference case The reference case of the image-based left ventricular geometry (geo20LV) did not consider pressure in the forward and the inverse simulation. The reconstructed active tension was matching the ground truth active tension with an MRTE of 0.1 % and a maximal peak tension error < 0.05 kPa for $\lambda_2 = 10^{-12}$. Applying stronger spatial regularization (e.g.

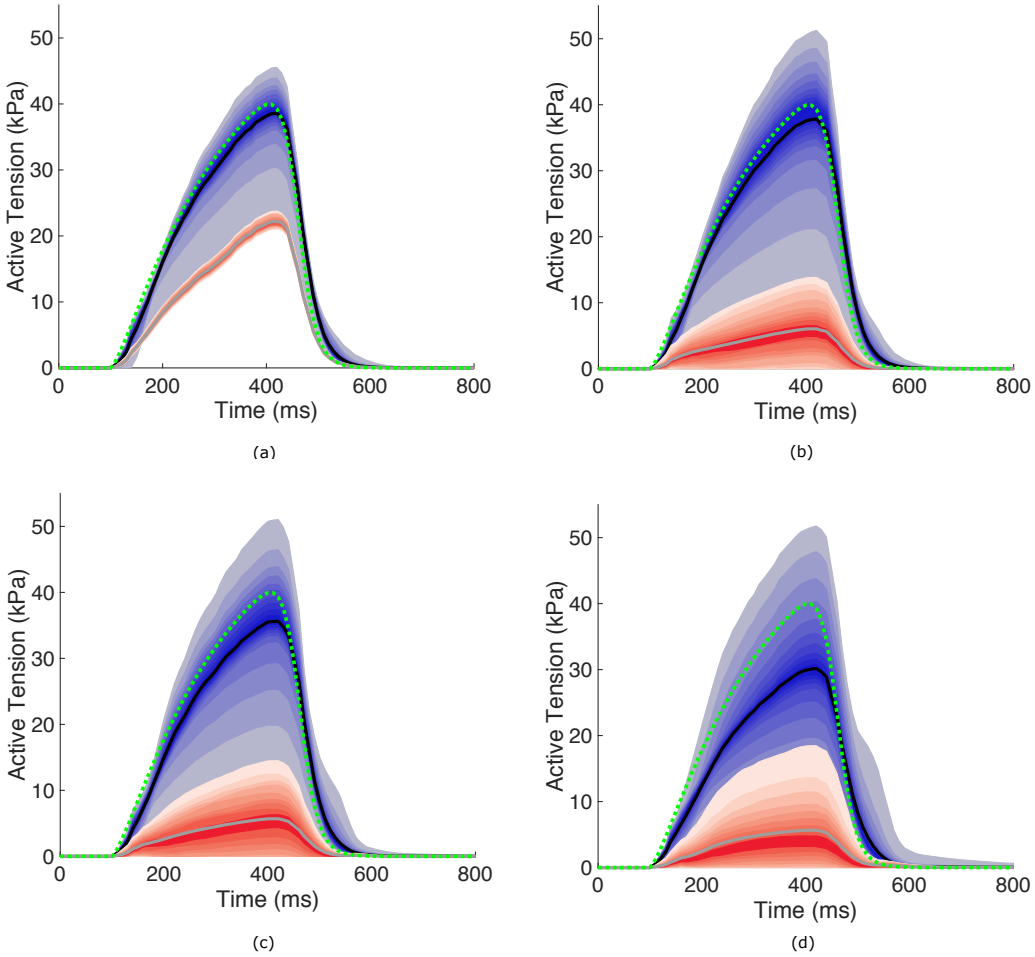

Figure 8.6: (a) Reconstruction of active tension for infarct size $1\,\%$, Case 7; (b) for $5\,\%$, Case 8; (c) for $10\,\%$, Case 9; (d) for $22\,\%$, Case 10. The reconstructed mean active tension time course of healthy and infarct elements is visualized by the black and gray line, respectively. The time-varying distribution percentiles (from $5\,\%$ to $95\,\%$) are shown as shaded bands ($5\,\%$) around the median (not shown) of the reconstructed active tension time course for all volume elements. For every time step, each band represents the active tension range in 5 % of the finite elements. The blue bands represent the healthy elements and the red ones the infarct elements (as defined in the forward simulation). The green dotted line is the ground truth active tension of the healthy elements. Adapted from [123], published under the Creative Commons Attribution 4.0 International (CC BY 4.0) License.

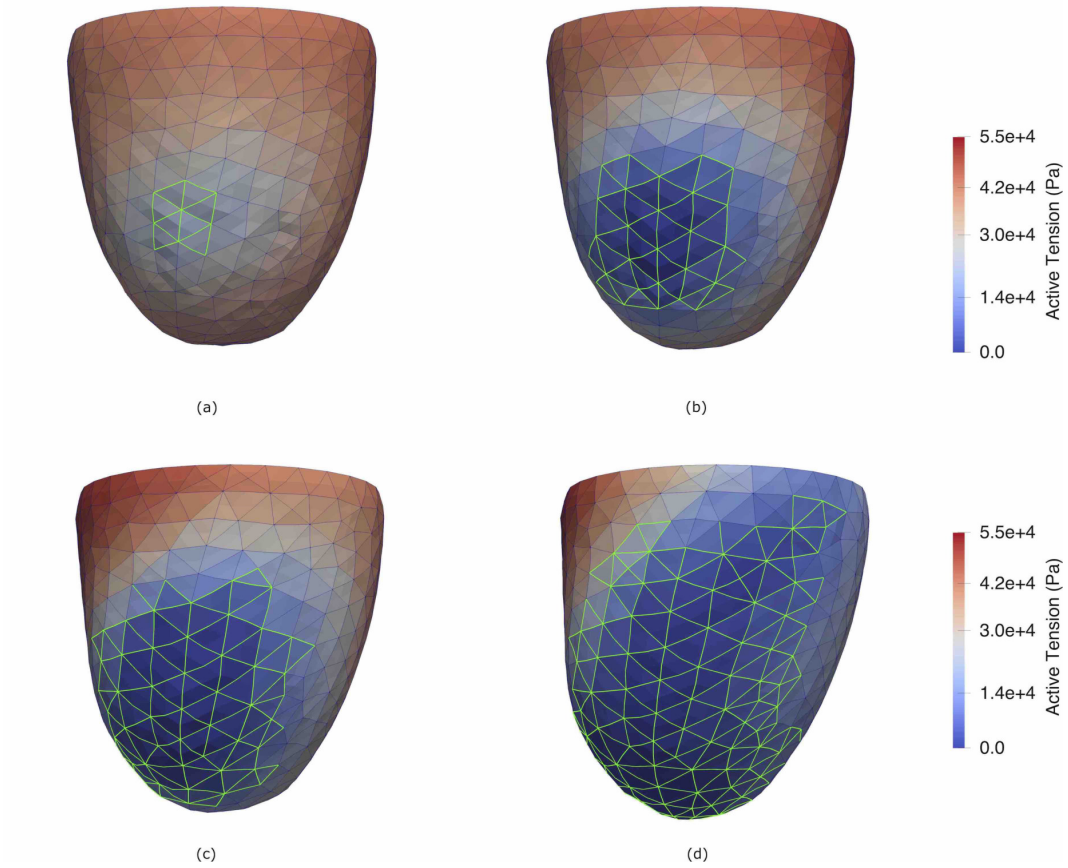

Figure 8.7: The reconstructed active tension at 400 ms is colour coded on the geometry for the different infarct sizes: (a) for 1 %, Case 7; (b) for 5 %, Case 8; (c) for 10 %, Case 9; (d) for 22 %, Case 10. The infarct area as defined in the forward simulation is indicated by green wireframe. Adapted from [123], published under the Creative Commons Attribution 4.0 International (CC BY 4.0) License.

$\lambda_2 = 10^{-10}$ and $\lambda_2 = 10^{-8}$) slightly improved the result as the MRTE decreased to 0.06 %. Less spatial regularization led to higher MRTE: 3.8 % for $\lambda_2 = 10^{-16}$. The peak tension errors for all elements for different spatial regularization parameters $\lambda_2 = 10^{-16}, \ldots, 10^{-6}$ are visualized in Figure 8.9. The results with applied pressure and varied target surfaces were obtained with spatial regularization $\lambda_2 = 10^{-12}$. This was the smallest value of λ_2 to lead to a small MRTE ($< 1\,\%$) for the reference case. No temporal regularization was imposed.

Furthermore, an a priori method to determine the regularization parameter λ_2 for the geo20LV was calculated, based on the L-curve. The parameter, which yields the minimal regularization norm combined with the minimal residual norm, is chosen (the *corner* of the L-curve, in which the highest curvature is available). The L-curve was calculated for a predefined time point, at 110 *ms*, which is the first time step after the active tension has started rising (Figure 8.10). In this way, an equality between the current change in tension($\tau_{i,n}$) and the accumulated active tension $s_{i,n} + \tau_{i,n}$ is obtained. One time point was chosen since

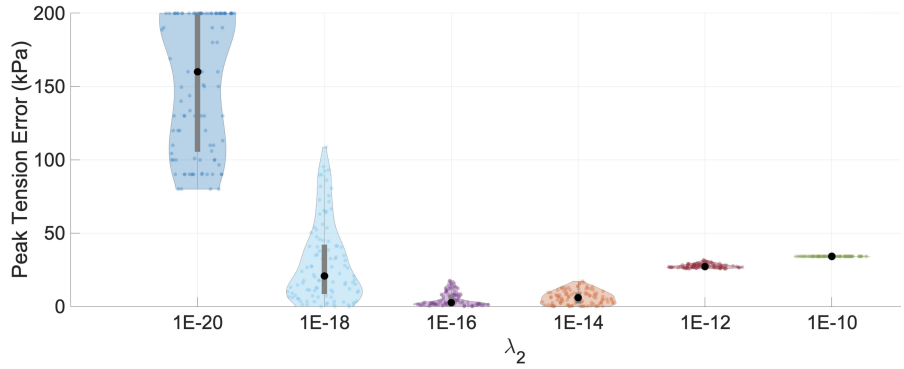

Figure 8.8: The peak tension error and its distribution for all infarcted elements $e^l \in \mathscr{E}_i^{\text{corr}}$ of the ellipsoid geometry for different values of the spatial regularization parameter λ_2. The black dot represents the median of the peak tension error and the gray bar represents the error between the first and third quartile. Adapted from [123], published under the Creative Commons Attribution 4.0 International (CC BY 4.0) License.

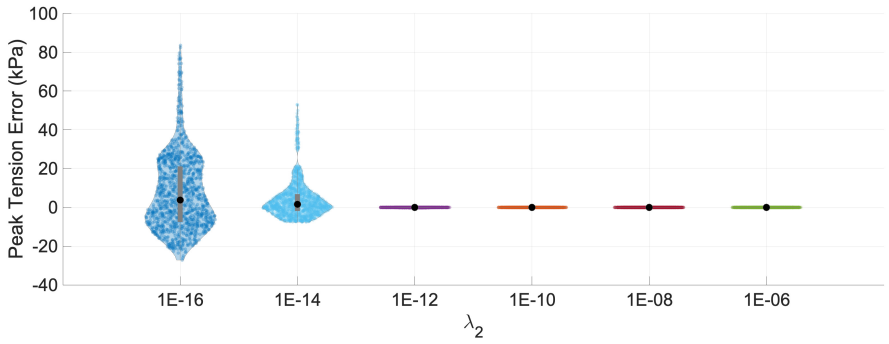

Figure 8.9: The peak tension error of all volume elements of the image-based left ventricle and their distribution for different values of the spatial regularization parameter λ_2. The black dot represents the median of the peak tension error and the gray bar represents the error between the first and third quartile. Adapted from [123], published under the Creative Commons Attribution 4.0 International (CC BY 4.0) License.

the matrix A changes each time step and leads to different L-curves. The L-curve shown in Figure 8.10 has an optimal value between 10^{-12} and 10^{-11}.

Pressure application For Cases 11–18, pressure on the endocardial surface in the forward and inverse simulation was applied. Two pressure curves were considered: a sine curve (Case 11 in Table 8.1) and a Hill curve (Case 12 in Table 8.1). In both cases, the reconstructed active tension matched the ground truth active tension with an MRTE of 0.2 % and a maximal peak tension error < 0.05 kPa. Figure 8.11 visualizes the time course of the corresponding volume change. The volume change of the ventricular cavity with the Hill curve was only 2 ml between 320 ms and 420 ms. At 400 ms, which lies inside this quasi-isovolumetric time

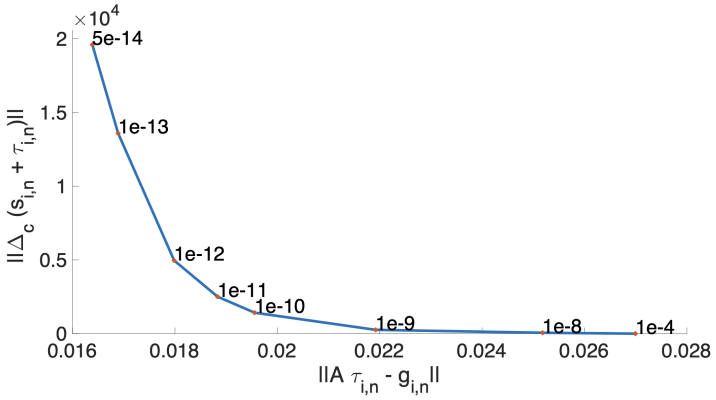

Figure 8.10: The L-curve for a reconstruction with the image-based left ventricular geometry.

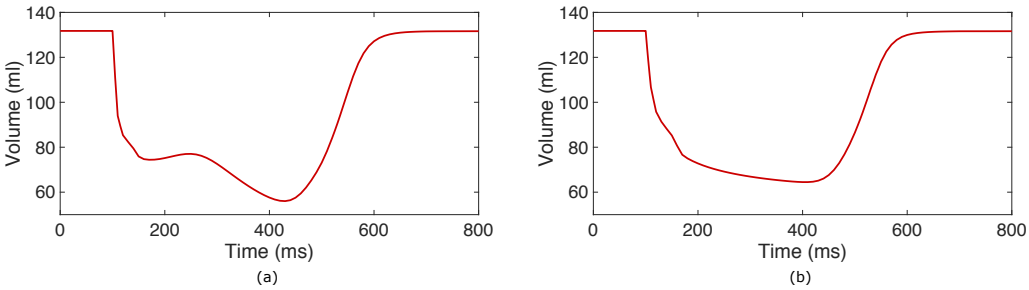

Figure 8.11: Volume curves obtained with pressure on the endocardial surface: (a) with a sine pressure curve (b) with the Hill pressure curve. Adapted from [123], published under the Creative Commons Attribution 4.0 International (CC BY 4.0) License.

interval, the maximal tension is applied in the forward simulation and correctly reconstructed in the inverse reconstruction.

For Case 11 and Case 12, the Newton solver reached the maximum number of iterations ($\bar{N}_{max} = 5$) for 77 % of the time steps of the whole simulation (800 ms) and for more than 90 % of time steps for which the ground truth active tension was > 0 kPa. In both cases, the median of the mean gap was 0.004 mm (gray horizontal line in Figure 8.12), the maximal value of the mean gap was 0.03 mm and the minimum was 0.0005 mm. The mean gap is the mean of the distances between the nodes on the target and the nodes on the reconstructed surface. The median of the mean gap is the median over all time steps for which the Newton solver reached the maximum number of iterations.

Target surface variation In the image-based left ventricular geometry, endocardial surfaces extracted from the forward simulation were systematically altered to study the influence of imaging and segmentation uncertainty. In both forward and inverse simulations, the Hill pressure curve was applied.

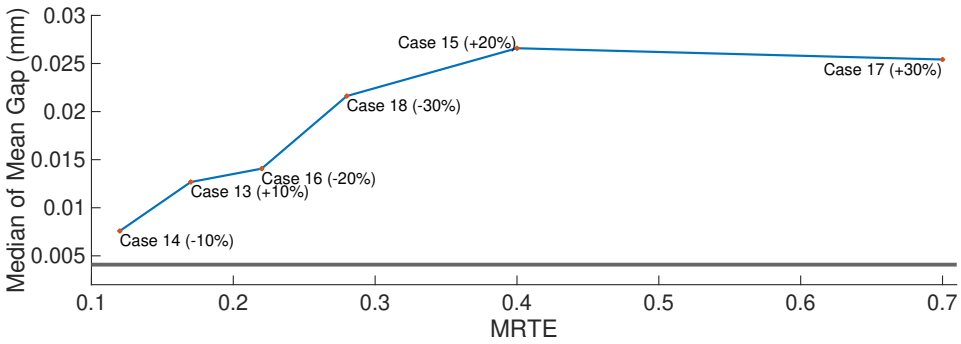

Figure 8.12: Relation between the mean relative tension error (MRTE) and the median of the mean gap distance for Cases 13–18 in Table 8.1. The gray line is the median of the mean distance for Case 12 (no variation of the target surface). Adapted from [123], published under the Creative Commons Attribution 4.0 International (CC BY 4.0) License.

In Case 13 (Table 8.1), the nodes were shifted towards the inside of the ventricle by 10 % of the initial wall thickness. This led to an overestimation of the active tension, ranging from 209 kPa to 211 kPa at the PTT, as visualized in Figure 8.13 (a). The median of the mean distance between the target and the reconstructed surface was 0.01 mm as visualized in Figure 8.12. For Case 15 and Case 17, the nodes were shifted by 20 % and 30 %, respectively, towards the inside of the ventricle. This led to an overestimation with a mean value of 251 kPa at the PTT for Case 15 and 306 kPa at the PTT for Case 17, as visualized in Figure 8.13 (c) and (e). For both cases, the median of the mean gap was above 0,02 mm (Figure 8.12).

In Case 14 (Table 8.1), the nodes were shifted towards the outside of the ellipsoid by 10 %. The mean of the active tension over all elements (156 kPa) was slightly underestimated compared to the ground truth, visualized by the green dotted line in Figure 8.13 (b). The median of the mean gap was 0.007 mm, which is the closest to the one of Case 12 (gray horizontal line in Figure 8.12). In Case 16 and Case 18, the nodes were shifted towards the outside of the ellipsoid by 20 % and 30 %, respectively. Here, an underestimation of the active tension was observed (Figure 8.13 (d), (f)), ranging from 138 kPa to 142 kPa for Case 16 and from 126 kPa to 131 kPa for Case 18. For Case 16, the median of the mean distance between the target and the reconstructed surface was above 0.014 mm and for Case 18 – 0.026 mm (Figure 8.12).

All elements were classified correctly (specificity 1.0) for all cases of target surface variation with the image-based left ventricular geometry.

Figure 8.12 shows the relation between the MRTE and the median of the mean gap for all cases with a varied target surface. The median was calculated only for the time steps when the Newton solver met the maximal number of iterations ($\bar{N}_{max} = 5$). In these cases, the Newton solver could not provide an active tension field which leads to distances between the target and the reconstructed surface below the absolute tolerance $\varepsilon_a = 10^{-5}$ mm. The gray line in Figure 8.12 is the median of the mean gap for Case 12 and it is below the median of the mean gap of all cases with varied target surfaces. As the MRTE rises, the median of the mean gap also increases.

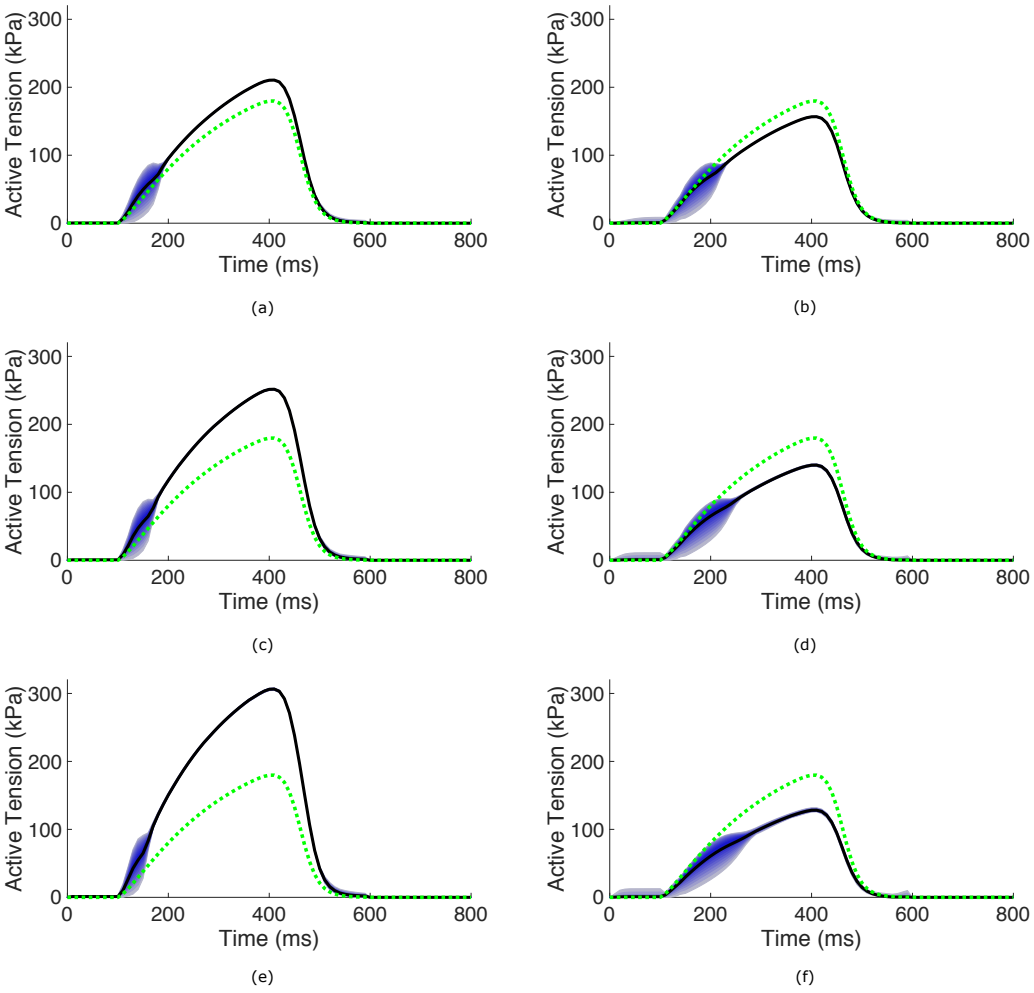

Figure 8.13: Reconstruction of active tension for (a) $+10\,\%$, Case 13; (b) $-10\,\%$, Case 14; (c) $+20\,\%$, Case 15; (d) $-20\,\%$, Case 16; (e) $+30\,\%$, Case 17; (f) $-30\,\%$, Case 18 constant shift of the target surface. The reconstructed mean active tension time course is the black line and the time-varying distribution percentiles (from $5\,\%$ to $95\,\%$) are shown as blue bands ($5\,\%$) around the median (not shown) of the reconstructed active tension time course for all volume elements. For every time step, each blue band represents the active tension range in 5 % of the finite elements. The green dotted line is the ground truth active tension. Adapted from [123], published under the Creative Commons Attribution 4.0 International (CC BY 4.0) License.

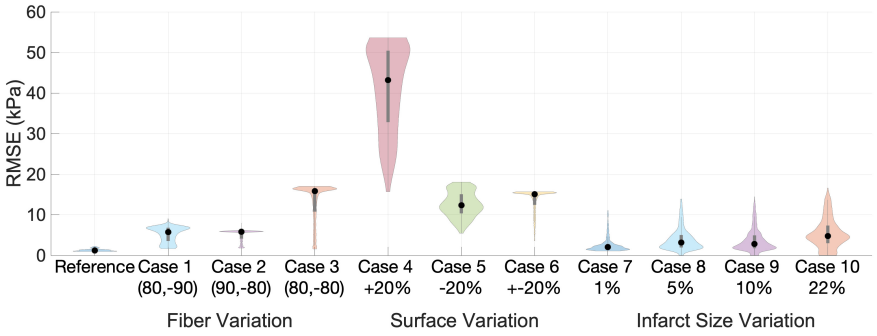

Figure 8.14: The root mean square error and its distribution for all elements of the ellipsoid geometry for the reference case and Cases 1–10 as described in Table 8.1. The black dot represents the median of the peak tension error and the gray bar represents the error between the first and third quartile. Adapted from [123], published under the Creative Commons Attribution 4.0 International (CC BY 4.0) License.

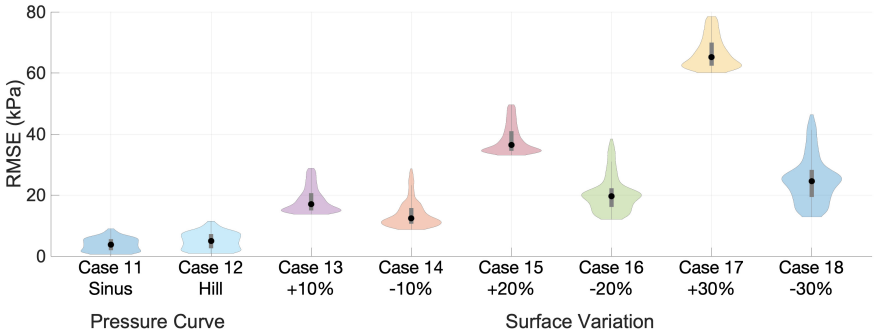

Figure 8.15: The root mean square error and its distribution for all elements of the image-based left ventricular geometry for the reference case and Cases 11–18 as described in Table 8.1. The black dot represents the median of the peak tension error and the gray bar represents the error between the first and third quartile. Adapted from [123], published under the Creative Commons Attribution 4.0 International (CC BY 4.0) License.

8.2.3 Overview of the Results of the Sensitivity Analysis

For the ellipsoid geometry, the RMSE for all elements and its distribution is visualized in Figure 8.14 for the reference case and Cases 1–10 as described in Table 8.1. For these experiments, spatial regularization with $\lambda_2 = 10^{-14}$ was applied. The errors correspond to the courses of the reconstructed active tension for all visualized cases. For example, the highest RMSE was calculated for Case 4, where the reconstructed tension was overestimated (Figure 8.4 (a)). The lowest RMSE (median of 1.2 kPa) was obtained for the reference case.

For the image-based left ventricular geometry, the RMSE for all elements and its distribution is visualized in Figure 8.15 for the reference case and Cases 11–18 as described in Table 8.1. For those experiments, spatial regularization with $\lambda_2 = 10^{-12}$ was applied. Again,

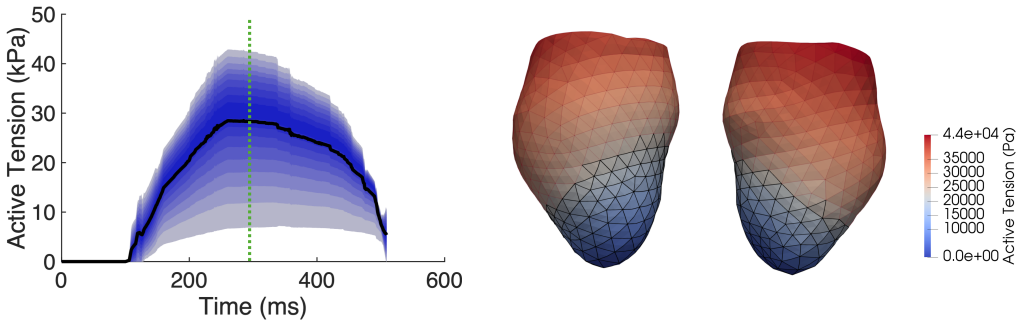

Figure 8.16: Left: Reconstruction of active tension for Case CA. The reconstructed mean active tension time course is the black line and the time-varying distribution percentiles (from 5 % to 95 %) are shown as blue bands (5 %) around the median (black line) of the reconstructed active tension time course for all volume elements. For every time step, each blue band represents the active tension range in 5 % of the finite elements. Right: The distribution of the reconstructed tension at 300 ms is colour-coded (in anterior and posterior view) and the black wireframe indicates elements in an infarct region.

the errors correspond to the courses of the reconstructed active tension for all visualized cases. The highest RMSE was calculated for Case 17, where the tension was overestimated (Figure 8.13 (e)). All cases with target surface variation towards the inside of the ventricle (Case 13, 15 and 17) lead to higher RMSE compared to the cases with the same amount of target surface variation (Case 14, 15 and 18, respectively), but pointing in the opposite direction (towards the outside of the ventricle). Low RMSE were obtained for Case 11 and 12 (median of 3.7 kPa and 4.9 kPa, respectively), where no variations of the input models were included. Furthermore, the RMSE obtained for the cases of surface variations ($+20\,\%$ and $-20\,\%$) for both geometries (Case 4, 15 and Case 5, 16, respectively) are in a similar range (around 40 kPa and 20 kPa, respectively), despite the difference in the maximal tension value of the ground truth (40 kPa for the ellipsoid and 180 kPa for the image-based geometry).

8.2.4 Results with Clinical Data

For Case CA, the target surfaces were obtained from Cine MRI images. The reconstructed active tension course is visualized in Figure 8.16, left. Spatial regularization $\lambda_2 = 10^{-10}$ was applied and no temporal regularization was imposed. The threshold ($\mathbb{T} = 0.52$), which was determined in the sensitivity analysis with infarct size variation with synthetic cases, was applied on the reconstructed tension with clinical data. This led to a false identification of an infarct region, which is superimposed with a black wireframe in the right part of Figure 8.16. The tissue around the apex was identified as an infarct region, which included 675 elements.

The distance between the target and reconstructed surface was increasing during the systole (Figure 8.17). The median of the mean gap was 0.25 mm, which is about ten times more than the largest median of the gap calculated for the synthetic cases (Figure 8.12). Again, the median was calculated for the time steps when the Newton solver met the maximal

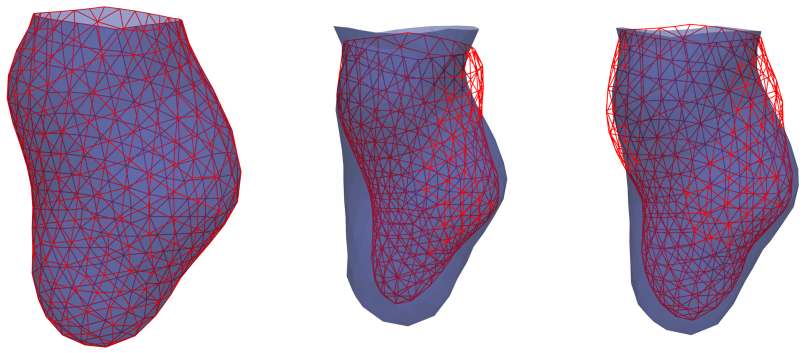

Figure 8.17: The target surface is shown in red wireframe and the reconstructed surface is shown in semi-transparent blue colour. From left to right: at 100 ms, 300 ms and 500 ms.

number of iterations ($\bar{N}_{max} = 5$). The MRTE and RMSE were not calculated since no ground truth was available.

8.3 Discussion

A numerical method was described for solving an inverse problem of cardiac biomechanics – a reconstruction of the dynamic active tension field. It delivers the estimated active tension for every time step, resolved on the scale of the individual finite element. The algorithm was already available as described in [4]. It was adapted to be usable in the current state of the framework CardioMechanics. A sensitivity analysis with synthetic data was conducted and the results of the first application of this method with clinical data was presented.

Input deformation data The deformation data used in the sensitivity analysis and in the clinical case capture shape changes during the cardiac cycle. However, those shape changes are not based on material displacements, so they are not true measures of deformation. In contrast to data extracted from 3D tagged MRI data and echocardiographic speckle tracking, the data used in this work contained no information about the twist and the rotation of the tissue.

For the inverse method, the deformation of the endocardial wall is required as input data, whereas other methods use three-dimensional displacement data [98], [81], [87] or strain and volume data [80], [85]. In the presented results, the deformation of the epicardial surface aligned very well with the expected deformation of the forward simulation, probably due to the combination of an incompressibility term added to the material law and the transmural resolution of one element. This advantage can be especially valuable for the reconstruction of the active tension of the right ventricle since, in MRI data, the right ventricular epicardial surface is hardly visible.

Regularization parameter choice Already in the control case with elli15, spatial regularization was necessary and applied to all other cases. λ_2 was set to 10^{-14}, striking a reasonable trade-off between the reconstruction in presence of infarct regions (Figure 8.8) and the reconstruction accuracy for entirely healthy tissue (Figure 8.3). Furthermore, temporal regularization improved the result if the added variation to the displacement field of the target surface was changing over time.

For the reference case with the image-based geometry, λ_2 was set to 10^{-12}. As mentioned in Chapter 8.1.1, the regularization parameter depends on the squared value of the residual norm. The matrix involved in the residual norm depends on the volume of each finite element, which was approximated by the third power of the mean surface edge length. For the used geometries (elli15 and geo20LV), the third power of the ratio between the mean edge length of the image-based left ventricle and the ellipsoid is $(4.38/1.9)^3 = 12.25$. This leads to a factor of about 12^2 between the regularization parameters for the image-based and ellipsoid geometries. In the sensitivity study, the regularization parameters were determined with the knowledge of the ground truth. Furthermore, the chosen spatial regularization parameter fulfils the L-curve criterion for the image-based geometry since the value is in the corner of the L-curve (Figure 8.10).

For the clinical case Case CA, no ground truth exists and λ_2 was chosen to be 10^{-10}. The mean edge length of geoCardAtl was 6.7 mm, which suggests an increase in regularization parameter λ_2 by a factor of about $2 \cdot 10^3$ compared to the one applied for the ellipsoid geometry.

Fiber variation In the case of fiber variation, an infarct area of varying size was always falsely detected (specificity was below 1.0). As the limits of the fiber variation lay just at the level of accuracy with which fiber orientation can be measured by diffusion tensor MRI [157], the reconstruction result is not satisfying. Furthermore, the generation of the fiber orientation using a rule-based model differs from the real fiber orientation and thus, introduces further fiber variation [158].

Target surface variation In the case of target surface variation, the results were as expected. In Case 4, Case 13, Case 15 and Case 17 in Table 8.1, an overestimation of the active tension was expected, as a stronger deformation towards the inside can be achieved by higher tension. In Case 5, Case 14, Case 16 and Case 18 in Table 8.1, again, the obtained result was expected, as lower tension leads to less deformation. Case 6 in Table 8.1 provided very promising results by adding temporal regularization. The ellipsoid and image-based left ventricular geometry results show the same tendency of the method to overestimate (Case 4 and Case 15) or underestimate (Case 5 and Case 16) the tension when the input deformation is noisy. For both geometries, the root mean square error is in the same range, although the absolute values differ due to the different maximal tension values assumed in the forward models. In the image-based geometry, pressure was applied, which counteracts the active tension. Therefore, the maximum of the active tension (180 kPa) is higher compared to the idealized geometry (40 kPa), where no blood pressure was considered. Additionally, the

initial wall thickness differs between the two geometries used in the sensitivity study. Thus, 20 % of the relative thickness change results in different absolute displacements of target surfaces.

Case 6 is expected to occur also using clinical data due to the intra-observer variability during the segmentation of MRI data [154]. In the reconstruction with the image-based geometry, the overestimation was severe, while the underestimation was rather minor. This suggests that the method is robust against an overly thin segmentation of the ventricular wall.

Identification of infarct tissue For all four experiments with an infarct present in the forward simulation (Case 7–10 in Table 8.1), the size and the location of the infarct were reconstructed well. Additionally, the active tension distribution inside and around the infarct area might provide valuable diagnostic information. Nevertheless, the correct identification of an infarct area strongly depends on the choice of the regularization parameters. Too much spatial smoothness imposed on the solution will blur the boundary of the infarct area and will lead to misclassification of the infarct area. Furthermore, in the presented sensitivity analysis, it was not investigated how noisy input data influence the reconstruction of the size and location of an infarct area.

Material properties The material properties were assumed to be homogeneous in the entire geometry, although they are expected to vary in the infarct region compared to healthy tissue [95]. The ventricle wall thickness and fiber orientation can also be significantly affected after an ischemic injury.

Pressure application In case pressure was included in the model (Case 11 and Case 12 in Table 8.1), the reconstruction of the tension matched the ground truth very well. The Hill pressure curve was applied to obtain quasi-isovolumetric phases around the peak tension. This suggests that the presented method will be able to reconstruct the active tension correctly also during isovolumetric phases. In Case 11, the sine pressure curve was applied since it is more similar to the shape of the measured pressure curve compared to the Hill curve (Case 12).

Quality measures In the sensitivity analysis, all quality measures are defined based on a comparison with the ground truth, which is not available for applications with clinical data. Therefore, further quality assessment methods should be investigated. It was observed that higher tension error occurs together with an increased median of the mean gap for the cases with varied displacement data (Figure 8.12). Thus, the distance between the target and reconstructed surface can potentially be a useful indicator for the quality of the solution.

Comparison to literature In the work of Balaban et al. [80] and Finsberg et al. [85], a sequential quadratic programming algorithm was used to minimize the misfit between model and measurement data. To further constrain the optimization, they introduced a first-order Tikhonov regularization, which smooths the amount of muscle shortening. In contrast, spatial

and temporal second-order Tikhonov regularization was implemented to smooth the change of active tension among the neighbouring elements and in the time course of the active tension.

In the case of fiber variation, Otani et al. [87] stated that their inverse model performed reasonably successfully. This is in contrast to the presented results. However, they perturbed the fiber direction with a random error from a distribution of zero mean and a standard deviation of 10°. In this work, a constant shift in fiber directions was chosen of 10° on the epicardial or endocardial surface or on both surfaces, which resulted in a 20° deviation. Also, Asner et al. [81] performed the reconstruction of active tension with different fiber angle ranges that deviated by 5° on both the endocardial and epicardial surface and concluded that the result is thereby not significantly affected. The reconstruction method of Asner et al. [81] used tagged MRI data as input data, where information about the rotation and twist of the tissue is available. In contrast, as stated previously, such information is not provided by the surface deformation used as input for the inverse method. In conclusion, uncertainty in fiber orientation impairs the accuracy of the estimated tension field if only endocardial surfaces are used as input.

The presented results are in line with the work of Asner et al. [81], where the displacement noise in the synthetic data was set to 10% – 20% of the maximal displacement. The reconstruction of the global active tension parameter resulted, thereby, in a minimal increase in error. Also, in the work of Otani et al. [87], the method performed reasonably well when white noise of relative amplitude of 10% was added to the displacement data.

Reconstruction with clinical data The reconstruction with clinical data did not provide a plausible result since an infarct was detected, although the image data were from a healthy volunteer. Furthermore, the simulation broke after 510 ms due to oscillations in the deformation at the base. It might be that the boundary condition (fixation of the free end of the tissue connected to the apex (see Chapter 4)) was not sufficient to provide a unique solution of the system. However, this boundary condition was necessary to ensure the motion of the base towards the apex, as seen in the motion data. The maximal values of the reconstructed active tension were comparable with the one of the reference cases (around 40 kPa), which was also executed without pressure application. An increase and decrease of the active tension was also available during contraction and relaxation, respectively.

This first result indicates that an improvement in the simulation set-up and reconstruction method is necessary before further reconstructions with clinical data can be executed (e.g., using the other data sets from the Cardiac Atlas).

Possible applications of the method One of the possible applications of the proposed inverse method is to locate and detect the size of infarct scars and to identify the elastomechanical consequences. Furthermore, a reconstruction of the temporal and spatial distribution of the active tension field might be useful for diagnostic and therapeutic assessment. For example, wall stress is a sensitive marker of hypertrophic cardiomyopathy [159]. In addition, the presented inverse method can be adapted to provide the temporal and spatial distribution

of the material properties of the myocardium as they also influence the tension field in the tissue.

Future works In future, the sensitivity analysis can be extended to investigate the variation of the material properties, the wall thickness and the fiber orientation in infarct regions. The presented method can be adapted to estimate the parameters of the material law for each finite element based on the deformation information in the relaxation phase. In comparison, the active tension can be estimated in the systolic phase, as it dominates the overall tension in this phase.

To overcome the difficulties due to the approximation of fiber direction, the inverse solver can be extended to first estimate the direction of the fibers and then estimate the active tension. For the estimation of the fiber orientation, additional input data might be used, e.g., including rotational information. Also, a cross-fiber active tension can be implemented to alleviate the difficulty arising from uncertain fiber orientation.

The rule-based assumption of cardiac fiber orientation could in the future be personalized by diffusion tensor MRI [160] or quantified by echocardiography [161, 162].

Conclusion

In this chapter, a method including second-order Tikhonov regularization for solving an inverse problem of cardiac biomechanics was used to perform a sensitivity analysis with synthetic data and applied on one example using clinical data. By imposing spatial regularization in the reference case, the active tension can be reconstructed well (maximal peak tension error $< 0.5\,\mathrm{kPa}$). To obtain a maximal RMSE $< 20\,\%$ with the inverse method, it was necessary to provide the fiber orientation with an accuracy of 10° in the experiments. If temporal variation up to $\pm 20\%$ of wall thickness was present in the input deformation data, the imposing temporal regularization in the inverse method could decrease the MRTE to 12% (from 95% without temporal regularization). Despite the reconstruction errors in the active tension, different sized infarct areas could be accurately identified in the inverse solution (sensitivity > 0.95). The morphology of the reconstructed active tension curve matched the ground truth's curve in all cases, whereas the amplitude of the reconstructed tension differed compared to the ground truth. Using clinical data, the method reconstructed a reasonable active tension course, which is promising, but further effort is needed to apply the method on motion data from clinical images. Furthermore, the performance of the reconstruction with uncertain fiber orientation needs to be improved.

Chapter 9

Outlook and Conclusions

In this work, methods were presented to estimate elastomechanical properties of the human heart based on a numerical model.

A computational model of the human heart was generated by a workflow presented in Chapter 4. The geometry was personalized based on static magnetic resonance imaging (MRI) data. The tissue surrounding the heart was represented by pericardial tissue and a pressure-free configuration was estimated. As a result, an error in the geometrical model was introduced compared to the segmented surfaces: the mean error was below 3 mm, which is in the range of errors obtained for whole heart segmentation methods found in the literature. In future, these errors might be avoided by excluding the adipose tissue from the heart model and by improving the method, which calculates the pressure-free configuration. The workflow was demonstrated on one geometry with a coarse computational mesh, which led to a deviation in the angles of the fiber orientation in the model from the angles used as input. In future, this can be improved by estimating the input angles depending on the coarseness of the geometry. Furthermore, the solver can be adapted to handle heart models with higher number of elements (> 150000). This will allow to run a convergence analysis on whole heart models. For this work, the element quality was evaluated and for the coarse heart geometry, the quality criteria at end-diastole (ED) were fulfilled. Therefore, the geometry was valid and used to evaluate the deformation during the heart beat.

A framework was developed, which allows evaluating the deformation of a virtual heart via measures commonly used in clinical practice (wall thickening, strain, strain rate and deformation velocities). The deformation obtained in the simulation with the numerical solver *CardioMechanics* was validated against clinically measured MRI data and general value ranges provided in the literature for healthy hearts. The morphology of the left ventricle (LV) volume matched the one obtained from clinical data very well. The strain in all directions was in the range found in the literature. However, the values found in the literature were in a broad range. Furthermore, differences were already present between measures extracted from the different acquisition sequences on the same heart (static whole heart vs. Cine MRI). In future, it is necessary to obtain a larger data set of clinical data and to extract more information from these data. The data set can be separated to 1) generate the heart model 2) calibrate the model and its parameters and 3) validate the model.

In this work, a sensitivity study was performed to quantify the influence of the elastomechanical properties on the deformation measures. Furthermore, the geometrical heart model and the cardiac cell orientations were modified to create pathologies described for hypertrophic cardiomyopathy (HCM). Causes of altered mechanics in virtual HCM hearts were identified. The study showed which pathological mechanisms are required to be present in the LV to obtain altered mechanics and how they affect the deformation measures. An increased wall thickness led to deformation alteration during the systole, while the ES values are comparable to the control case. Stiffer tissue equalized the strains at end-systole (ES), while reduced active force development reduced the deformation of LV. Disarrayed fiber orientation in the mid wall did not significantly influence the deformation of the LV. In future, the sensitivity study can be extended to include stronger variations in the elastomechanical properties. The geometrical models of the HCM hearts can be derived from imaging data to ensure the simulated cases are also seen in clinical routine. Further clinical data can be included to validate the deformation of the virtual HCM heart.

Optimization frameworks were presented which can identify parameters for the constitutive law describing the heart's biomechanics. A commonly used normalized ED pressure volume relation derived from experiments was adapted to yield a better fit to the experimental data. An objective function based solely on this relation could not deliver a unique parameter set and was therefore extended to include an additional term involving an absolute volume ratio. Furthermore, the starting state of the geometry (initial state or unloaded) was shown to have only minor influence on the optimal parameters. Avoiding the calculation of the unloaded state simplifies the procedure and saves calculation time. However, further investigation is needed, since the same unloaded state was employed for the simulations with different passive parameter sets. In future, the frameworks could be extended to include clinical measurements in the objective function to yield a patient specific tuning of the passive properties.

A further optimization method was adapted (initially proposed and developed by Thomas Fritz [4]) which reconstructs a dynamic active force field from motion data of the LV. The method included second order Tikhonov regularization for solving this inverse problem and was used to perform a sensitivity analysis with synthetic data and applied on one example using clinical data. By imposing spatial regularization in the reference case, the active tension can be reconstructed well (maximal peak tension error $< 0.5\,\mathrm{kPa}$). To obtain a maximal root mean square error (RMSE) $< 20\,\%$ with the inverse method, it was necessary to provide the fiber orientation with an accuracy of 10° in the experiments. If temporal variation up to $\pm 20\%$ of wall thickness was present in the input deformation data, the imposing temporal regularization in the inverse method could decrease the mean relative tension error (MRTE) to 12% (from 95% without temporal regularization). Despite the reconstruction errors in the active tension, different sized infarct areas could be identified accurately in the inverse solution (sensitivity > 0.95). The morphology of the reconstructed active tension curve matched the ground truth's curve in all cases, whereas the amplitude of the reconstructed tension differed compared to the ground truth. In future, the performance of the reconstruction with uncertain fiber orientation needs to be improved. It could be

considered to first estimate the orientation of the fibers and subsequently, reconstruct the tension field. For this purpose, more data can be included in the estimation process, e.g., tagged MRI, which reveals the rotation of the ventricle. Using endocardial motion data derived from clinically measured imaging data, the method reconstructed a realistic active tension course, which is promising, but further effort is needed to apply the method directly on clinical data. Here again, more data might be needed to achieve a reasonable result. Furthermore, the influence of the boundary conditions should be considered for further reconstructions. In future, the inverse solver can be challenged by a four chamber model of the heart including the pericardial tissue.

Appendix A

Seed points for Creation of Atrial Fiber Orientation of geo20

In Table A.1 the input seed points used in the tool *SetAtrialFiberOrientation* are provided. The tool was called as follows:

```
SetAtrialFiberOrientation Input/atriaFine.vtu Output/AtriaFiber.vtu
   Input/Seedpoints.txt -intermediateResultPrefix debug
   -noUpperPosteriorBridge  -noCoronarySinusBridge
   -noMiddlePosteriorBridge -noBachmannBundle
   -noWideBachmann -growPathOffestLeft 1.5
   -writeViewFiberOrientation -debug
   -noEndCleanup -growPectToRAppendage
```

Table A.1: Seed points for generation of the atrial fiber orientation.

SCV1 G	-18.1926	4.2939	73.3178
SCV2 G	-10.7091	-4.9605	81.4646
SCV3 G	-19.1292	-3.6435	83.3798
SCV4 G	-19.8686	-0.0335	30.2515
SCV5 G	-4.1522	6.3354	32.5476
SCV6 G	4.6485	-32.1293	92.0851
SCV7 G	-1.2245	-33.9575	48.2598
SCV8 G	-4.7848	-23.7689	21.9555
SCV9 G	11.0468	-13.5936	28.6832
LV1 G	43.1704	20.7773	46.2609
LV2 G	28.6735	12.9032	33.5593
LV3 G	30.8701	2.4442	52.7844
LV4 G	-12.1415	11.5769	75.5968
LV5 G	19.0284	20.1488	88.8843
LV6 G	-16.3701	23.5526	69.0514
LV7 G	24.1973	33.2162	79.1526
LV8 G	-16.1647	24.4435	51.7459
LV9 G	23.3558	36.4674	65.6333
LV10 G	26.1908	11.7099	80.8437
LV11 G	40.5791	19.3751	80.0721
LV12 G	32.3921	27.7259	76.9322
LV13 G	-18.9335	13.6608	61.9249

Appendix **B**

Settings for the Simulation with geo20

The input setting for the simulation evaluated in Chapter 5 is provided in the following.

```
<settings> geo20 with quadratic elements</settings>
<General>
<LogFile>Baseline_T10.log</LogFile>
</General>

<Mesh>
<Type>T10</Type>
<Format>Tetgen</Format>
<Sorting>None</Sorting>
<Tetgen>
<Unit>1e-3</Unit>
<Nodes>../geometry/tetgen/Inflated_periAdjusted.node</Nodes>
<Elements>../geometry/tetgen/heartT10.ele</Elements>
<Surfaces>../geometry/tetgen/heartT10.sur</Surfaces>
<Bases>../geometry/tetgen/heartT10.bases</Bases>
<DetermineNeighbors>true</DetermineNeighbors>
<EnforceOrthonormalBases>true</EnforceOrthonormalBases>
</Tetgen>
<Surfaces>
<!-- epicardium -->
<Surface_159>
<Type>CAVITY</Type>
</Surface_159>
<!-- pericardium -->
<Surface_160>
<Type>CONTACT_MASTER</Type>
</Surface_160>
<Surface_161>
<Type>CONTACT_SLAVE</Type>
</Surface_161>
</Surfaces>
<Transform>
<T4toT10>false</T4toT10>
<T3toT6>false</T3toT6>
</Transform>
</Mesh>

<Materials>
<Global>
<Damping>
<Rayleigh>
<Alpha>500</Alpha>
<Beta>0.005</Beta>
</Rayleigh>
```

```
</Damping>
</Global>

<Mat_30> <!-- RV -->
<IgnoreCorruptElements>false</IgnoreCorruptElements>
<Type>Guccione</Type>
<Density>1082</Density>
<Guccione>
<C>156.5</C>
<b1>17.8</b1>
<b2>7.1</b2>
<b3>12.4</b3>
<K>1e6</K>
</Guccione>
<TensionMax>160000</TensionMax>
<TensionModel>FromFunction</TensionModel>
<FromFunction>
<Type>DoubleHill</Type>
<StartTime>0.0</StartTime>
<StopTime>30.0</StopTime>
<DoubleHill>
<Period>          0.8  </Period>
<ContrTimeOffset> 0.215</ContrTimeOffset>
<RelaxTimeOffset> 0.362</RelaxTimeOffset>
<ContrRateConst>  1.32 </ContrRateConst>
<RelaxRateConst> 21.9  </RelaxRateConst>
<OnsetTime>       0.15 </OnsetTime>
</DoubleHill>
</FromFunction>
</Mat_30>

<Mat_31> <!-- LV -->
<IgnoreCorruptElements>false</IgnoreCorruptElements>
<Type>Guccione</Type>
<Density>1082</Density>
<Guccione>
<C>156.5</C>
<b1>17.8</b1>
<b2>7.1</b2>
<b3>12.4</b3>
<K>1e6</K>
</Guccione>
<TensionMax>160000</TensionMax>
<TensionModel>FromFunction</TensionModel>
<FromFunction>
<Type>DoubleHill</Type>
<StartTime>0.0</StartTime>
<StopTime>30.0</StopTime>
<DoubleHill>
<Period>          0.8  </Period>
<ContrTimeOffset> 0.215</ContrTimeOffset>
<RelaxTimeOffset> 0.362</RelaxTimeOffset>
<ContrRateConst>  1.32 </ContrRateConst>
<RelaxRateConst> 21.9  </RelaxRateConst>
<OnsetTime>       0.15 </OnsetTime>
</DoubleHill>
</FromFunction>
</Mat_31>

<Mat_32> <!-- RA -->
<IgnoreCorruptElements>false</IgnoreCorruptElements>
<Type>Guccione</Type>
<Density>1082</Density>
<Guccione>
<C>156.5</C>
<b1>17.8</b1>
<b2>7.1</b2>
<b3>12.4</b3>
<K>1e6</K>
</Guccione>
<TensionMax>40000</TensionMax>
<TensionModel>FromFunction</TensionModel>
```

```
<FromFunction>
<Type>DoubleHill</Type>
<StartTime>0.0</StartTime>
<StopTime>30.0</StopTime>
<DoubleHill>
<Period>          0.8  </Period>
<ContrTimeOffset> 0.042</ContrTimeOffset>
<RelaxTimeOffset> 0.138</RelaxTimeOffset>
<ContrRateConst>  1.99 </ContrRateConst>
<RelaxRateConst> 11.2  </RelaxRateConst>
<OnsetTime>       0.0 </OnsetTime>
</DoubleHill>
</FromFunction>
</Mat_32>

<Mat_33> <!-- LA -->
<IgnoreCorruptElements>false</IgnoreCorruptElements>
<Type>Guccione</Type>
<Density>1082</Density>
<Guccione>
<C>156.5</C>
<b1>17.8</b1>
<b2>7.1</b2>
<b3>12.4</b3>
<K>1e6</K>
</Guccione>
<TensionMax>40000</TensionMax>
<TensionModel>FromFunction</TensionModel>
<FromFunction>
<Type>DoubleHill</Type>
<StartTime>0.0</StartTime>
<StopTime>30.0</StopTime>
<DoubleHill>
<Period>          0.8  </Period>
<ContrTimeOffset> 0.042</ContrTimeOffset>
<RelaxTimeOffset> 0.138</RelaxTimeOffset>
<ContrRateConst>  1.99 </ContrRateConst>
<RelaxRateConst> 11.2  </RelaxRateConst>
<OnsetTime>       0.0 </OnsetTime>
</DoubleHill>
</FromFunction>
</Mat_33>

<Mat_34> <!-- RAV ring -->
<IgnoreCorruptElements>false</IgnoreCorruptElements>
<Type>Guccione</Type>
<Density>1082</Density>
<Guccione>
<C>156.5</C>
<b1>17.8</b1>
<b2>7.1</b2>
<b3>12.4</b3>
<K>1e6</K>
</Guccione>
<TensionMax>160000</TensionMax>
<TensionModel>FromFunction</TensionModel>
<FromFunction>
<Type>DoubleHill</Type>
<StartTime>0.0</StartTime>
<StopTime>30.0</StopTime>
<DoubleHill>
<Period>          0.8  </Period>
<ContrTimeOffset> 0.215</ContrTimeOffset>
<RelaxTimeOffset> 0.362</RelaxTimeOffset>
<ContrRateConst>  1.32 </ContrRateConst>
<RelaxRateConst> 21.9  </RelaxRateConst>
<OnsetTime>       0.15 </OnsetTime>
</DoubleHill>
</FromFunction>
</Mat_34>

<Mat_35> <!-- LAV ring -->
```

```
<IgnoreCorruptElements>false</IgnoreCorruptElements>
<Type>Guccione</Type>
<Density>1082</Density>
<Guccione>
<C>156.5</C>
<b1>17.8</b1>
<b2>7.1</b2>
<b3>12.4</b3>
<K>1e6</K>
</Guccione>
<TensionMax>160000</TensionMax>
<TensionModel>FromFunction</TensionModel>
<FromFunction>
<Type>DoubleHill</Type>
<StartTime>0.0</StartTime>
<StopTime>30.0</StopTime>
<DoubleHill>
<Period>          0.8  </Period>
<ContrTimeOffset> 0.215</ContrTimeOffset>
<RelaxTimeOffset> 0.362</RelaxTimeOffset>
<ContrRateConst>  1.32 </ContrRateConst>
<RelaxRateConst> 21.9  </RelaxRateConst>
<OnsetTime>       0.15 </OnsetTime>
</DoubleHill>
</FromFunction>
</Mat_35>

<Mat_36> <!-- RAV plane -->
<IgnoreCorruptElements>false</IgnoreCorruptElements>
<Type>MooneyRivlin</Type>
<TensionMax>0</TensionMax>
<Density>1082</Density>
<MooneyRivlin>
<C1>100000</C1>
<C2>0</C2>
<B>2e5</B>
</MooneyRivlin>
</Mat_36>

<Mat_37> <!-- LAV plane -->
<IgnoreCorruptElements>false</IgnoreCorruptElements>
<Type>MooneyRivlin</Type>
<TensionMax>0</TensionMax>
<Density>1082</Density>
<MooneyRivlin>
<C1>100000</C1>
<C2>0</C2>
<B>2e5</B>
</MooneyRivlin>
</Mat_37>

<Mat_38> <!-- inner trunks -->
<IgnoreCorruptElements>false</IgnoreCorruptElements>
<Type>MooneyRivlin</Type>
<TensionMax>0</TensionMax>
<Density>1082</Density>
<MooneyRivlin>
<C1>14900</C1>
<C2>0</C2>
<B>2e5</B>
</MooneyRivlin>
</Mat_38>

<Mat_39> <!-- outer trunks -->
<IgnoreCorruptElements>false</IgnoreCorruptElements>
<Type>MooneyRivlin</Type>
<TensionMax>0</TensionMax>
<Density>1082</Density>
<MooneyRivlin>
<C1>14900</C1>
<C2>0</C2>
<B>2e5</B>
```

```
</MooneyRivlin>
</Mat_39>

<Mat_40> <!-- fat -->
<IgnoreCorruptElements>false</IgnoreCorruptElements>
<TensionMax>0</TensionMax>
<Type>Guccione</Type>
<Density>1082</Density>
<Guccione>
<C>1200.0</C>
<b1>10.0</b1>
<b2>10.0</b2>
<b3>10.0</b3>
<K>1e3</K>
</Guccione>
</Mat_40>

<Mat_60> <!-- surrounding tissue -->
<IgnoreCorruptElements>false</IgnoreCorruptElements>
<TensionMax>0</TensionMax>
<Type>Guccione</Type>
<Density>1082</Density>
<Guccione>
<C>1200.0</C>
<b1>10.0</b1>
<b2>10.0</b2>
<b3>10.0</b3>
<K>1e3</K>
</Guccione>
</Mat_60>
</Materials>

<Export>
<Format>VTK</Format>
<Prefix>./Baseline_T10</Prefix>
<TimeStep>1e-2</TimeStep>
<Options>
<Material>true</Material>
<Fixation>true</Fixation>
<Jacobian>true</Jacobian>
<FiberAllQuadraturePoints>true</FiberAllQuadraturePoints>
<SurfaceElementID>false</SurfaceElementID>
<SurfaceID>false</SurfaceID>
<SurfaceNormal>false</SurfaceNormal>
<ActiveStress>true</ActiveStress>
<TetgenBases>true</TetgenBases>
<Deformation>true</Deformation>
<Lambda>true</Lambda>
<Cauchy>false</Cauchy>
<LocalActivationTime>false</LocalActivationTime>
<Fiber>true</Fiber>
<Sheet>true</Sheet>
<SheetNormal>true</SheetNormal>
<AbsDisplacement>true</AbsDisplacement>
<Displacement>true</Displacement>
<Velocity>true</Velocity>
<Acceleration>true</Acceleration>
<NodalForces>true</NodalForces>
</Options>
</Export>

<Solver>
<NonZeros>2000</NonZeros>
<DomainDecomposition>false</DomainDecomposition>
<Precision>1e-9</Precision>
<Verbose>true</Verbose>
<LU>true</LU>
<Type>NewmarkBeta</Type>
<NewmarkBeta>
<!-- Dissipation of higher frequencies for Gamma >= 0.5 -->
<!-- Unconditional stability for 2*Beta >= Gamma >= 0.5 -->
<Beta>0.3</Beta>
```

```
<Gamma>0.6</Gamma>
<ConsistentMassMatrix>true</ConsistentMassMatrix>
</NewmarkBeta>
<Formulation>TotalLagrangian</Formulation>
<StartTime>0</StartTime>
<StopTime>10</StopTime>
<TimeStep>5e-3</TimeStep>
<MinTimeStep>5e-6</MinTimeStep>

<SNES>
<Export>
<Filename>./Baseline_T10/SNES.dat</Filename>
</Export>
</SNES>

<Plugins>
<Circulation>true</Circulation>
<ContactHandling>true</ContactHandling>
<LoadUnloadedState>true</LoadUnloadedState>
<DetermineCavityVolume>true</DetermineCavityVolume>
</Plugins>
</Solver>

<Plugins>

<LoadUnloadedState>
<unloadedNodes>../geometry/tetgen/UnloadedState_Cycle1.node</unloadedNodes>
<inflatedNodes>../geometry/tetgen/Inflated_periAdjusted.node</inflatedNodes>
<SettleDown>true</SettleDown>
</LoadUnloadedState>

<DetermineCavityVolume>
<ExportFile>./Baseline_T10/Cavity_1.dat</ExportFile>
<VolumeUnit>ml</VolumeUnit>
</DetermineCavityVolume>

<ContactHandling>
<Export>./Baseline_T10/ContactHandling.dat</Export>
<MaxDistance>0.05</MaxDistance>
<TransitionDistance>1e-4</TransitionDistance>
<MaxAngle>90</MaxAngle>
<Alpha>1e7</Alpha>
<Beta>1</Beta>
<InitType>Linear</InitType>
<Steps>5</Steps>
<FlipSlaveNormals>false</FlipSlaveNormals>
<SurfaceNormalDirection>bidirectional</SurfaceNormalDirection>
</ContactHandling>

<Circulation>
<Tolerance>1e-7</Tolerance>
<MaxIterations>250</MaxIterations>
<Perturbation>false</Perturbation>
<SecantIterations>0</SecantIterations>
<IterationsFile>./Baseline_T10/CircIter.dat</IterationsFile>

<PreloadingTime1>0.0</PreloadingTime1>
<PreloadingTime2>0.0</PreloadingTime2>

<PressureUnit>mmHg</PressureUnit>
<VolumeUnit>ml</VolumeUnit>

<CouplingDamping>
<InitialFactor> 0.5 </InitialFactor>
<DeclineFactor> 0.9 </DeclineFactor>
</CouplingDamping>

<Circs>

<Circ_1>
<Active>true</Active>
<Type>CircWholeHeartValvesDynamic</Type>
```

```
<ExportFile>./Baseline_T10/Circ_1.dat</ExportFile>
<MaxIntegrationTimeStep>1e-4</MaxIntegrationTimeStep>

<SteadyStateCheck>
<Active>true</Active>
<Mode>StrokeVolumeDifference</Mode>
<StartTime>0.8</StartTime>
<Period>0.8</Period>
<Threshold>0.5</Threshold>
</SteadyStateCheck>

<CircParameters>
<BloodDensity>7.95e-4</BloodDensity>

<SysArtValveMax> 0.95 </SysArtValveMax>
<SysArtValveMin> 0.001 </SysArtValveMin>
<SysArtValveAreaRef> 7.0 </SysArtValveAreaRef>
<SysArtValveRateOpening> 10.0 </SysArtValveRateOpening>
<SysArtValveRateClosing> 6.0 </SysArtValveRateClosing>

<SysArtResist>0.07</SysArtResist>
<SysArtCompli>2.0</SysArtCompli>
<SysArtVolumeUnstr>800.0</SysArtVolumeUnstr>

<SysPerResist>0.9</SysPerResist>

<SysVenResist>0.03</SysVenResist>
<SysVenCompli>100.0</SysVenCompli>
<SysVenVolumeUnstr>2850.0</SysVenVolumeUnstr>

<RavValveMax> 0.7 </RavValveMax>
<RavValveMin> 0.001 </RavValveMin>
<RavValveAreaRef> 15.0 </RavValveAreaRef>
<RavValveRateOpening> 20.0 </RavValveRateOpening>
<RavValveRateClosing> 6.0 </RavValveRateClosing>

<PulArtValveMax> 0.98 </PulArtValveMax>
<PulArtValveMin> 0.001 </PulArtValveMin>
<PulArtValveAreaRef> 7.0 </PulArtValveAreaRef>
<PulArtValveRateOpening> 20.0 </PulArtValveRateOpening>
<PulArtValveRateClosing> 10.0 </PulArtValveRateClosing>

<PulArtResist>0.02</PulArtResist>
<PulArtCompli>10.0</PulArtCompli>
<PulArtVolumeUnstr>150.0</PulArtVolumeUnstr>

<PulPerResist>0.07</PulPerResist>

<PulVenResist>0.03</PulVenResist>
<PulVenCompli>15.0</PulVenCompli>
<PulVenVolumeUnstr>200.0</PulVenVolumeUnstr>

<LavValveMax> 0.7 </LavValveMax>
<LavValveMin> 0.001 </LavValveMin>
<LavValveAreaRef> 15.0 </LavValveAreaRef>
<LavValveRateOpening> 20.0 </LavValveRateOpening>
<LavValveRateClosing> 6.0 </LavValveRateClosing>
</CircParameters>

<InitialConditions>
<TotalVolume>5500.0</TotalVolume>
<SysArtVolume>969.453</SysArtVolume>
<PulArtVolume>261.202</PulArtVolume>
<PulVenVolume>281.373</PulVenVolume>
<RvPressure>4.0</RvPressure>
<LvPressure>7.5</LvPressure>
<RaPressure>4.0</RaPressure>
<LaPressure>7.5</LaPressure>
</InitialConditions>

<Cavities>
<RvSurface>130</RvSurface>
```

```
<LvSurface>131</LvSurface>
<RaSurface>132</RaSurface>
<LaSurface>133</LaSurface>

<RvPreloading>0.0</RvPreloading>
<LvPreloading>0.0</LvPreloading>
<RaPreloading>0.0</RaPreloading>
<LaPreloading>0.0</LaPreloading>
</Cavities>
</Circ_1>
</Circs>
</Circulation>

</Plugins>
```

Appendix C

Difference between Cases Defined in the Sensitivity Analysis

Figure C.1 and Figure C.2 provide root mean squared deviation (RMSD) matrices for pair-wise comparison of cases (row vs. column, Table 1 in the main document) for each evaluation metric. In each matrix, the systolic difference is above the diagonal and the diastolic difference is below the diagonal—e.g. the RMSD of the longitudinal strain rate (top right in Figure C.1) between Case 1 and Case 13 during the systole is the last entry in the first row (11.7) and the RMSD between these cases during the diastole is the last entry in the first column (12.4) of the corresponding matrix.

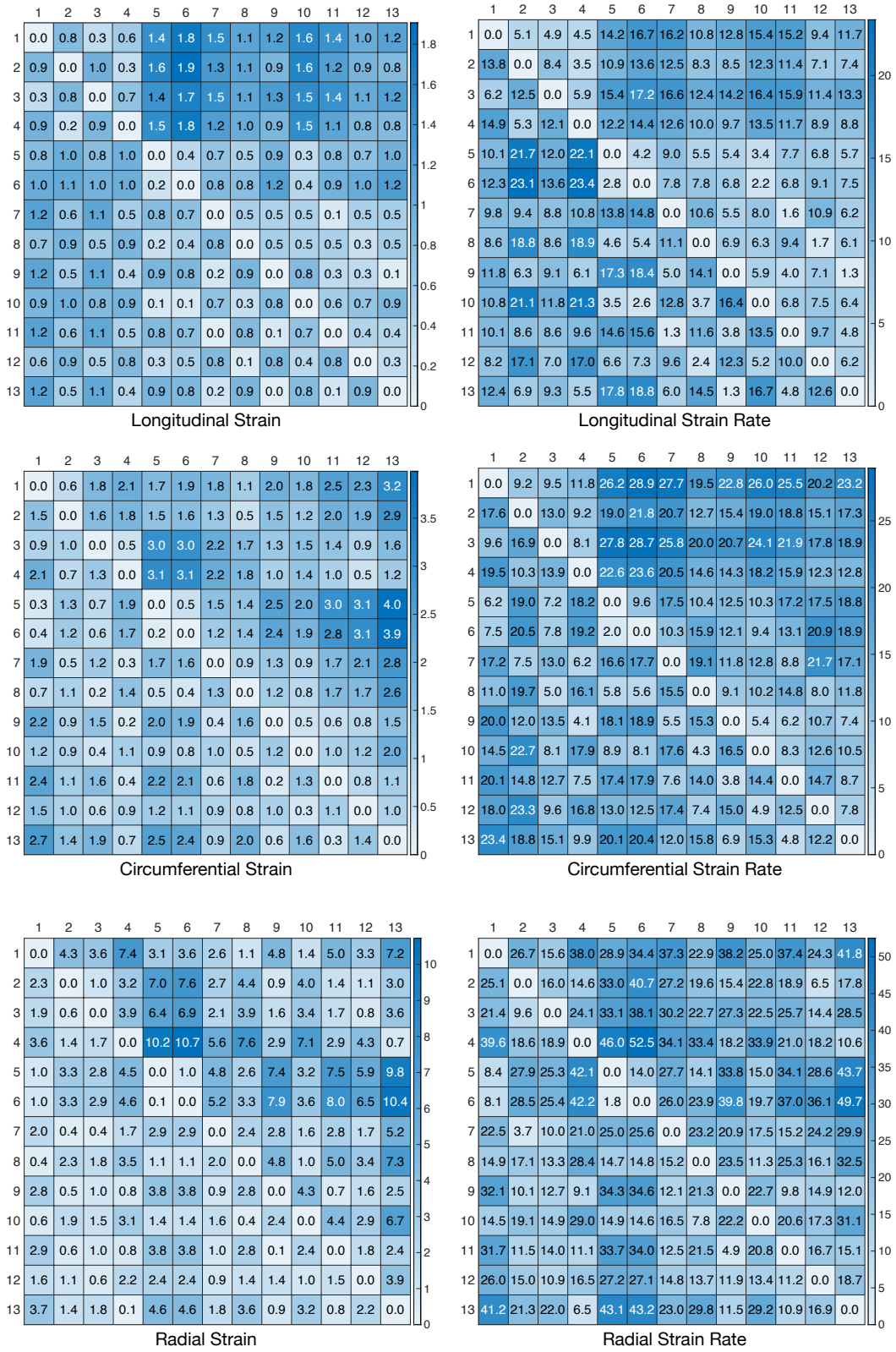

Figure C.1: RMSD matrices for the strains(%) and strain rates (%/s) in the local directions. Adapted from [117], published under the Creative Commons Attribution 4.0 International (CC BY 4.0) License.

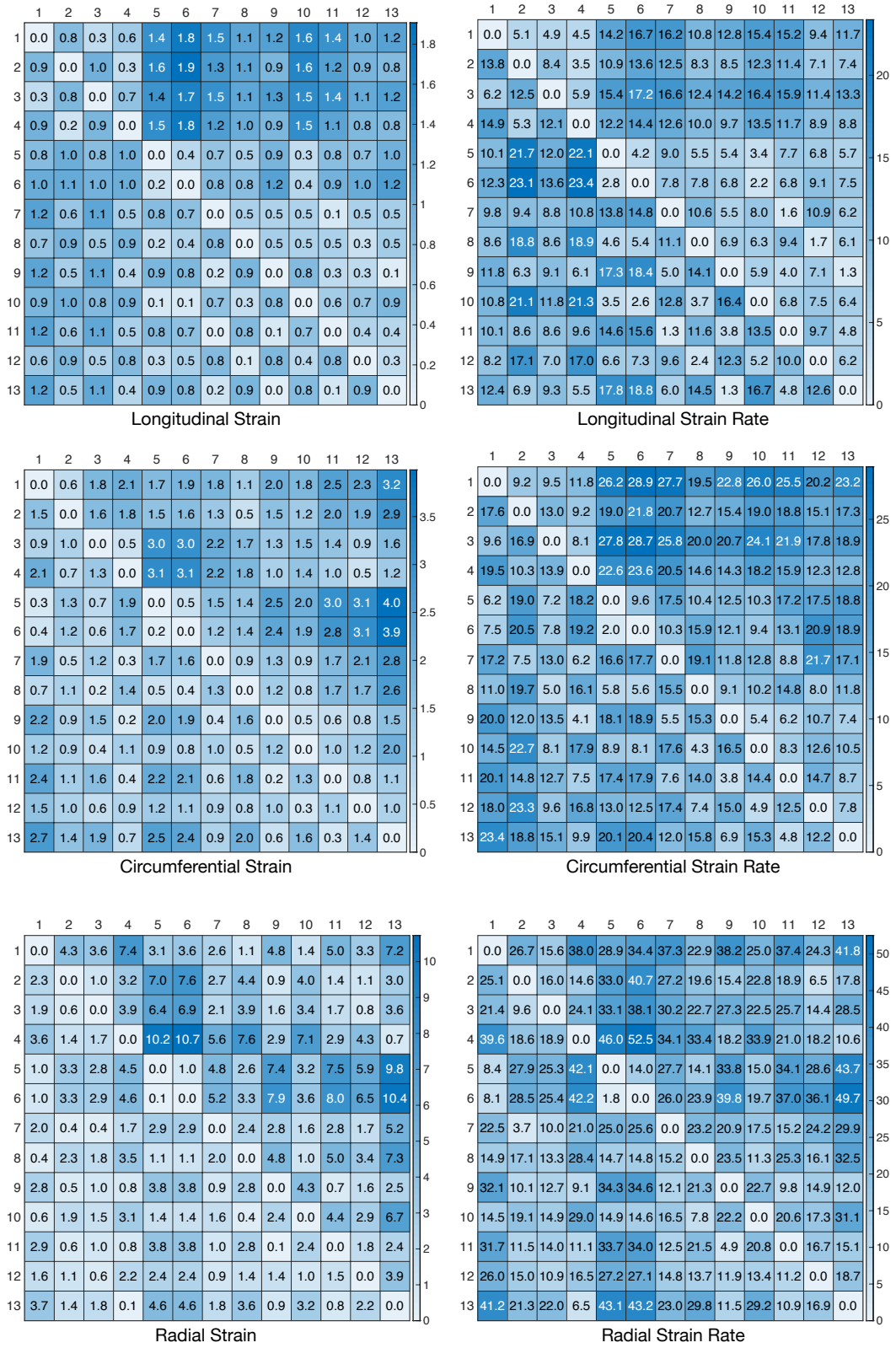

Figure C.2: RMSD matrices for the velocities (mm/s) in the local directions, LA strain (%) and wall thickening (%). Adapted from [117], published under the Creative Commons Attribution 4.0 International (CC BY 4.0) License.

Appendix **D**

Strain for the Cases Defined in the Sensitivity Analysis

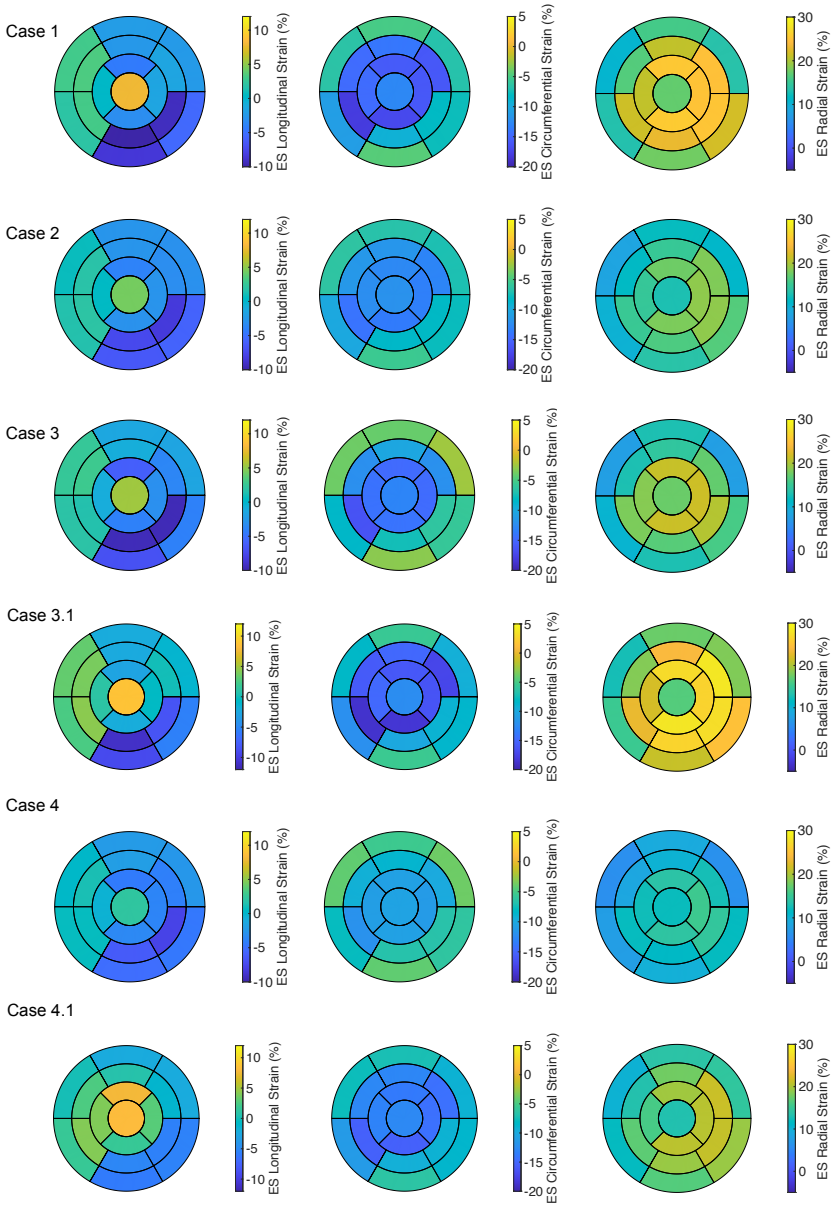

Figure D.1: Bull's-eye displays for Case 1, 2, 3, 3.1, 4, 4.1 showing the longitudinal, circumferential and radial strain at ES (first, second and third column, respectively). Each row corresponds to one case. Case 1: control case; Case 2: increased stiffness; Case 3: decreased active force; Case 3.1: increased active force; Case 4: increased stiffness + decreased active force; Case 4.1: increased stiffness + increased active force; Adapted from [117], published under the Creative Commons Attribution 4.0 International (CC BY 4.0) License.

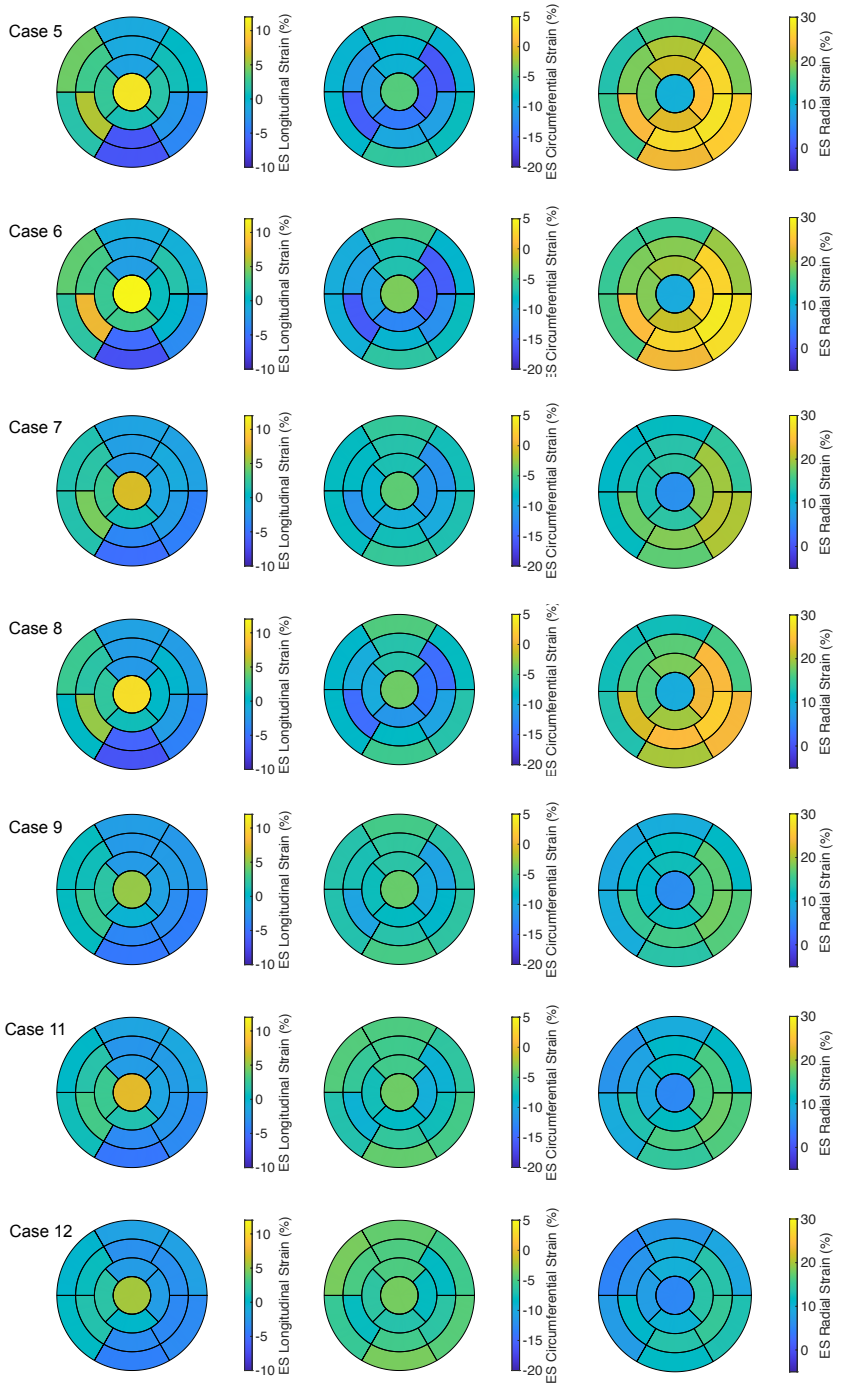

Figure D.2: Bull's-eye displays for Case 5, 6, 7, 8, 9,11 and 12 showing the longitudinal, circumferential and radial strain at ES (first, second and third column, respectively). Each row corresponds to one case. Case 5 hypertrophic geometry (15 mm); Case 6: hypertrophic geometry (17 mm); Case 7: hypertrophic geometry (17 mm), increased stiffness; Case 8: hypertrophic geometry (17 mm), decreased active force; Case 9: hypertrophic geometry (17 mm), increased stiffness + decreased active force; Case 10: hypertrophic geometry, fiber disarray; Case 11: hypertrophic geometry, increased stiffness, fiber disarray; Case 12: hypertrophic geometry, decreased active force, fiber disarray;. Adapted from [117], published under the Creative Commons Attribution 4.0 International (CC BY 4.0) License.

Appendix **E**

Temporal Alignment of the Target Surface

```
.0  TargetSurfaces/forward.0.vtu.dat
.1   TargetSurfaces/forward.0.vtu.dat
.11 TargetSurfaces/forward.1.vtu.dat
.12 TargetSurfaces/forward.2.vtu.dat
.13 TargetSurfaces/forward.3.vtu.dat
.16 TargetSurfaces/forward.4.vtu.dat
.22 TargetSurfaces/forward.5.vtu.dat
.26 TargetSurfaces/forward.6.vtu.dat
.34 TargetSurfaces/forward.7.vtu.dat
.44 TargetSurfaces/forward.8.vtu.dat
.49 TargetSurfaces/forward.9.vtu.dat
.50 TargetSurfaces/forward.10.vtu.dat
.51 TargetSurfaces/forward.11.vtu.dat
.52 TargetSurfaces/forward.12.vtu.dat
.53 TargetSurfaces/forward.13.vtu.dat
.55 TargetSurfaces/forward.14.vtu.dat
.57 TargetSurfaces/forward.15.vtu.dat
.59 TargetSurfaces/forward.16.vtu.dat
.61 TargetSurfaces/forward.17.vtu.dat
.64 TargetSurfaces/forward.18.vtu.dat
.65 TargetSurfaces/forward.19.vtu.dat
.70 TargetSurfaces/forward.0.vtu.dat
.80 TargetSurfaces/forward.0.vtu.dat
```

References

[1] S. A. Niederer, J. Lumens, and N. A. Trayanova, "Computational models in cardiology." *Nature reviews. Cardiology*, 2018.

[2] C. Constantinides, *Protocols and methodologies in basic science and clinical cardiac MRI*, C. Constantinides, Ed. Springer International Publishing AG 2018, 2018.

[3] V. Gulani, F. Calamante, F. G. Shellock, et al., "Gadolinium deposition in the brain: summary of evidence and recommendations," *The Lancet Neurology*, vol. 16, no. 7, pp. 564–570, 2017.

[4] T. Fritz, "Biomechanical modeling of the human heart - modeling of the ventricles, the atria and the pericardium and the inverse problem of cardiac mechanics," PhD thesis, Karlsruhe, 2015.

[5] S. Land, V. Gurev, S. Arens, et al., "Verification of cardiac mechanics software: benchmark problems and solutions for testing active and passive material behaviour," *Proceedings. Mathematical, Physical, and Engineering Sciences / the Royal Society*, vol. 471, no. 2184, p. 2015.0641, 2015.

[6] A. A. Young and A. F. Frangi, "Computational cardiac atlases: from patient to population and back," *Experimental Physiology*, vol. 94, no. 5, pp. 578–596, 2009.

[7] S. Ordas, E. Oubel, R. Leta, et al., "A statistical shape model of the heart and its application to model-based segmentation," *Medical Imaging 2007: Physiology*, vol. 6511, p. 65111K, 2007.

[8] C. G. Fonseca, M. Backhaus, D. A. Bluemke, et al., "The cardiac atlas project an imaging database for computational modeling and statistical atlases of the heart," *Bioinformatics*, vol. 27, no. 16, pp. 2288–2295, 2011.

[9] W. Bai, W. Shi, A. de Marvao, et al., "A bi-ventricular cardiac atlas built from 1000+ high resolution MR images of healthy subjects and an analysis of shape and motion." *Medical image analysis*, vol. 26, no. 1, pp. 133–45, 2015.

[10] C. Nagel, S. Schuler, O. Dössel, et al., "A bi-atrial statistical shape model for large-scale in silico studies of human atria: model development and application to ECG simulations," 2021.

[11] A. J. Prassl, F. Kickinger, H. Ahammer, et al., "Automatically generated, anatomically accurate meshes for cardiac electrophysiology problems." *IEEE transactions on bio-medical engineering*, vol. 56, no. 5, pp. 1318–30, 2009.

[12] A. Crozier, C. M. Augustin, A. Neic, et al., "Image-based personalization of cardiac anatomy for coupled electromechanical modeling," *Annals of Biomedical Engineering*, 2015.

[13] C. M. Augustin, A. Neic, M. Liebmann, et al., "Anatomically accurate high resolution modeling of human whole heart electromechanics: A strongly scalable algebraic multigrid solver method for nonlinear deformation." *Journal of computational physics*, vol. 305, pp. 622–646, 2016.

[14] M. R. Pfaller, M. C. Varona, J. Lang, et al., "Parametric model order reduction and its application to inverse analysis of large nonlinear coupled cardiac problems," 2018.

[15] M. Strocchi, C. M. Augustin, M. A. F. Gsell, et al., "A publicly available virtual cohort of four-chamber heart meshes for cardiac electro-mechanics simulations." *PloS one*, 2020.

[16] A. Neic, M. A. Gsell, E. Karabelas, et al., "Automating image-based mesh generation and manipulation tasks in cardiac modeling workflows using meshtool," *SoftwareX*, vol. 11, p. 100454, 2020.

[17] M. Fedele and A. Quarteroni, "Polygonal surface processing and mesh generation tools for the numerical simulation of the cardiac function." *International journal for numerical methods in biomedical engineering*, p. e3435, 2021.

[18] S. A. Niederer, Y. Aboelkassem, C. D. Cantwell, et al., "Creation and application of virtual patient cohorts of heart models," *Philosophical Transactions of the Royal Society A: Mathematical, Physical and Engineering Sciences*, vol. 378, no. 2173, p. 20190558, 2020.

[19] A. Jafari, E. Pszczolkowski, and A. Krishnamurthy, "A framework for biomechanics simulations using four-chamber cardiac models." *Journal of biomechanics*, vol. 91, pp. 92–101, 2019.

[20] K. C. L. Wong, L. Wang, H. Zhang, et al., "Meshfree implementation of individualized active cardiac dynamics," *Computerized Medical Imaging and Graphics : the Official Journal of the Computerized Medical Imaging Society*, vol. 34, no. 1, pp. 91–103, 2010.

[21] E. Lluch, O. Camara, R. Doste, et al., "Calibration of a fully coupled electromechanical meshless computational model of the heart with experimental data," *Computer Methods in Applied Mechanics and Engineering*, vol. 364, p. 112869, 2020.

[22] T. Eriksson, A. Prassl, G. Plank, et al., "Influence of myocardial fiber/sheet orientations on left ventricular mechanical contraction," *Mathematics and Mechanics of Solids*, vol. 18, no. 6, pp. 592–606, 2013.

[23] S. Niederer, K. Rhode, R. Razavi, et al., "The importance of model parameters and boundary conditions in whole organ models of cardiac contraction," vol. 5528, pp. 348–356, 2009.

[24] L. Baron, T. Fritz, G. Seemann, et al., "Sensitivity study of fiber orientation on stroke volume in the human left ventricle," in *Computing in Cardiology*, vol. 41, 2014, pp. 681–684.

[25] L. Geerts, P. Bovendeerd, K. Nicolay, et al., "Characterization of the normal cardiac myofiber field in goat measured with MR-diffusion tensor imaging," *Am J Physiol Heart Circ Physiol*, vol. 283, p. 139, 2002.

[26] P. A. Helm, H.-J. Tseng, L. Younes, et al., "Ex vivo 3d diffusion tensor imaging and quantification of cardiac laminar structure." *Magnetic resonance in medicine*, vol. 54, no. 4, pp. 850–9, 2005.

[27] S. Nielles-Vallespin, Z. Khalique, P. F. Ferreira, et al., "Assessment of myocardial microstructural dynamics by in vivo diffusion tensor cardiac magnetic resonance." *Journal of the American College of Cardiology*, vol. 69, no. 6, pp. 661–676, 2017.

[28] J. D. Bayer, R. C. Blake, G. Plank, et al., "A novel rule-based algorithm for assigning myocardial fiber orientation to computational heart models," *Annals of Biomedical Engineering*, vol. 40, no. 10, pp. 2243–2254, 2012.

[29] R. Doste, D. Soto-Iglesias, G. Bernardino, et al., "A rule-based method to model myocardial fiber orientation in cardiac biventricular geometries with outflow tracts." *International journal for numerical methods in biomedical engineering*, vol. 35, no. 4, p. e3185, 2019.

[30] J. Wong and E. Kuhl, "Generating fibre orientation maps in human heart models using poisson interpolation." *Computer methods in biomechanics and biomedical engineering*, vol. 17, no. 11, pp. 1217–26, 2014.

[31] M. W. Krueger, W. H. W. Schulze, K. Rhode, et al., "Towards personalized clinical in-silico modeling of atrial anatomy and electrophysiology," *Medical & Biological Engineering & Computing*, vol. 51, no. 11, pp. 1251–1260, 2013.

[32] A. Wachter, A. Loewe, M. W. Krueger, et al., "Mesh structure-independent modeling of patient-specific atrial fiber orientation," vol. 1, no. 1. De Gruyter, 2015, pp. 409–412.

[33] R. Piersanti, P. C. Africa, M. Fedele, et al., "Modeling cardiac muscle fibers in ventricular and atrial electrophysiology simulations," *Computer Methods in Applied Mechanics and Engineering*, vol. 373, p. 113468, 2021.

[34] A. Nagler, C. Bertoglio, M. Gee, et al., "Personalization of cardiac fiber orientations from image data using the unscented kalman filter," vol. 7945, pp. 132–140, 2013.

[35] A. Nagler, C. Bertoglio, C. T. Stoeck, et al., "Cardiac fibers estimation from arbitrarily spaced diffusion weighted MRI," vol. 9126, pp. 198–206, 2015.

[36] T. Grandits, S. Pezzuto, F. S. Costabal, et al., "Learning atrial fiber orientations and conductivity tensors from intracardiac maps using physics-informed neural networks," 2021.

[37] T. E. Fastl, C. Tobon-Gomez, A. Crozier, et al., "Personalized computational modeling of left atrial geometry and transmural myofiber architecture." *Medical image analysis*, vol. 47, pp. 180–190, 2018.

[38] D. D. Streeter, H. M. Spotnitz, D. P. Patel, et al., "Fiber orientation in the canine left ventricle during diastole and systole," *Circ. Res.*, vol. 24, no. 3, pp. 339–347, 1969.

[39] T. Fritz, C. Wieners, G. Seemann, et al., "Simulation of the contraction of the ventricles in a human heart model including atria and pericardium : Finite element analysis of a frictionless contact problem," *Biomechanics and Modeling in Mechanobiology*, vol. 13, no. 3, pp. 627–641, 2014.

[40] M. R. Pfaller, J. M. Hörmann, M. Weigl, et al., "The importance of the pericardium for cardiac biomechanics: from physiology to computational modeling." *Biomechanics and modeling in mechanobiology*, 2018.

[41] A. Santiago, M. Zavala-Aké, J. Aguado-Sierra, et al., "Fully coupled fluid-electro-mechanical model of the human heart for supercomputers." *International journal for numerical methods in biomedical engineering*, 2018.

[42] A. V. S. Ponnaluri, I. A. Verzhbinsky, J. D. Eldredge, et al., "Model of left ventricular contraction: Validation criteria and boundary conditions." *Functional imaging and modeling of the heart : FIMH proceedings*, vol. 11504, pp. 294–303, 2019.

[43] M. Strocchi, M. A. Gsell, C. M. Augustin, et al., "Simulating ventricular systolic motion in a four-chamber heart model with spatially varying robin boundary conditions to model the effect of the pericardium," *Journal of Biomechanics*, p. 109645, 2020.

[44] R. C. P. Kerckhoffs, M. L. Neal, Q. Gu, et al., "Coupling of a 3d finite element model of cardiac ventricular mechanics to lumped systems models of the systemic and pulmonic circulation," *Annals of Biomedical Engineering*, vol. 35, no. 1, pp. 1–18, 2007.

[45] J. Lumens, T. Delhaas, B. Kirn, et al., "Three-wall segment (triseg) model describing mechanics and hemodynamics of ventricular interaction." *Annals of biomedical engineering*, vol. 37, no. 11, pp. 2234–55, 2009.

[46] S. Schuler, L. Baron, A. Loewe, et al., "Developing and coupling a lumped element model of the closed loop human vascular system to a model of cardiac mechanics," in *BMTMedPhys 2017*, vol. 62, no. S1. Dresden, September 10 13: de Gruyter, 2017, p. S69.

[47] A. Quarteroni, T. Lassila, S. Rossi, et al., "Integrated heart—coupling multiscale and multiphysics models for the simulation of the cardiac function," *Computer Methods in Applied Mechanics and Engineering*, vol. 314, pp. 345–407, 2017.

[48] M. R. Pfaller, M. Cruz Varona, J. Lang, et al., "Using parametric model order reduction for inverse analysis of large nonlinear cardiac simulations." *International journal for numerical methods in biomedical engineering*, 2020.

[49] C. M. Augustin, M. A. F. Gsell, E. Karabelas, et al., "Physiologically valid 3d-0d closed loop model of the heart and circulation – modeling the acute response to altered loading and contractility," 2020.

[50] L. Marx, M. A. F. Gsell, A. Rund, et al., "Personalization of electro-mechanical models of the pressure-overloaded left ventricle: fitting of windkessel-type afterload models." *Philosophical transactions. Series A, Mathematical, physical, and engineering sciences*, vol. 378, no. 2173, p. 20190342, 2020.

[51] F. Regazzoni, M. Salvador, P. C. Africa, et al., "A cardiac electromechanics model coupled with a lumped parameters model for closed-loop blood circulation. part i: model derivation," 2020.

[52] F. Regazzoni, M. Salvador, P. C. Africa, et al., "A cardiac electromechanics model coupled with a lumped parameters model for closed-loop blood circulation. part II: numerical approximation," *Numerical Analysis (math.NA)*, 2020.

[53] M. Peirlinck, K. L. Sack, P. De Backer, et al., "Kinematic boundary conditions substantially impact in silico ventricular function." *International journal for numerical methods in biomedical engineering*, vol. 35, no. 1, p. e3151, 2019.

[54] V. Rajagopal, J.-H. Chung, D. Bullivant, et al., "Determining the finite elasticity reference state from a loaded configuration," *International Journal for Numerical Methods in Engineering*, vol. 72, pp. 1434–1451, 2007.

[55] M. Sellier, "An iterative method for the inverse elasto-static problem," *Journal of Fluids and Structures*, vol. 27, pp. 1461–1470, 2011.

[56] J. Bols, J. Degroote, B. Trachet, et al., "A computational method to assess the in vivo stresses and unloaded configuration of patient-specific blood vessels," *Journal of Computational and Applied Mathematics*, vol. 246, pp. 10–17, 2013.

[57] L. Marx, J. A. Niestrawska, M. A. F. Gsell, et al., "Efficient identification of myocardial material parameters and the stress-free reference configuration for patient-specific human heart models," *Elsevier*, 2021.

[58] M. Genet, L. C. Lee, R. Nguyen, et al., "Distribution of normal human left ventricular myofiber stress at end diastole and end systole: a target for in silico design of heart failure treatments," *Journal of Applied Physiology*, vol. 117, no. 2, pp. 142–152, 2014.

[59] S. Kallhovd, J. Sundnes, and S. T. Wall, "Sensitivity of stress and strain calculations to passive material parameters in cardiac mechanical models using unloaded geometries." *Computer methods in biomechanics and biomedical engineering*, vol. 22, no. 6, pp. 664–675, 2019.

[60] A. Nasopoulou, A. Shetty, J. Lee, et al., "Improved identifiability of myocardial material parameters by an energy-based cost function." *Biomechanics and modeling in mechanobiology*, vol. 16, no. 3, pp. 971–988, 2017.

[61] J. Corral-Acero, F. Margara, M. Marciniak, et al., "The 'digital twin' to enable the vision of precision cardiology." *European heart journal*, 2020.

[62] S. Pagani, L. Dede', A. Manzoni, et al., "Data integration for the numerical simulation of cardiac electrophysiology." *Pacing and clinical electrophysiology : PACE*, 2021.

[63] C. M. Augustin, A. Crozier, A. Neic, et al., "Patient-specific modeling of left ventricular electromechanics as a driver for haemodynamic analysis." *Europace : European pacing, arrhythmias, and cardiac electrophysiology : journal of the working groups on cardiac pacing, arrhythmias, and cardiac cellular electrophysiology of the European Society of Cardiology*, vol. 18, no. suppl 4, pp. iv121–iv129, 2016.

[64] B. Baillargeon, N. Rebelo, D. D. Fox, et al., "The living heart project: A robust and integrative simulator for human heart function." *European journal of mechanics. A, Solids*, vol. 48, pp. 38–47, 2014.

[65] J. O. Campos, J. Sundnes, R. W. Dos Santos, et al., "Effects of left ventricle wall thickness uncertainties on cardiac mechanics." *Biomechanics and modeling in mechanobiology*, vol. 18, no. 5, pp. 1415–1427, 2019.

[66] M. D. Cerqueira, N. J. Weissman, V. Dilsizian, et al., "Standardized myocardial segmentation and nomenclature for tomographic imaging of the heart," *Circulation*, vol. 105, no. 4, pp. 539–542, 2002.

[67] J. O. Campos, J. Sundnes, R. W. Dos Santos, et al., "Uncertainty quantification and sensitivity analysis of left ventricular function during the full cardiac cycle." *Philosophical transactions. Series A, Mathematical, physical, and engineering sciences*, vol. 378, no. 2173, p. 20190381, 2020.

[68] H. Osnes and J. Sundnes, "Uncertainty analysis of ventricular mechanics using the probabilistic collocation method." *IEEE transactions on bio-medical engineering*, vol. 59, no. 8, pp. 2171–9, 2012.

[69] C. M. Augustin, T. E. Fastl, A. Neic, et al., "The impact of wall thickness and curvature on wall stress in patient-specific electromechanical models of the left atrium," *Biomechanics and Modeling in Mechanobiology*, 2019.

[70] N. Hensley, J. Dietrich, D. Nyhan, et al., "Hypertrophic cardiomyopathy: a review." *Anesthesia and analgesia*, vol. 120, no. 3, pp. 554–69, 2015.

[71] J. A. Urbano-Moral, E. J. Rowin, M. S. Maron, et al., "Investigation of global and regional myocardial mechanics with 3-dimensional speckle tracking echocardiography and relations to hypertrophy and fibrosis in hypertrophic cardiomyopathy." *Circulation. Cardiovascular imaging*, vol. 7, no. 1, pp. 11–9, 2014.

[72] D. C. L. d. Oliveira, F. B. Assunção, A. A. S. M. D. D. Santos, et al., "Cardiac magnetic resonance and computed tomography in hypertrophic cardiomyopathy: an update." *Arquivos brasileiros de cardiologia*, vol. 107, no. 2, pp. 163–72, 2016.

[73] A. Li, A. Ruh, H. Berhane, et al., "Altered regional myocardial velocities by tissue phase mapping and feature tracking in pediatric patients with hypertrophic cardiomyopathy." *Pediatric Radiology*, vol. 50, no. 2, pp. 168–179, 2020.

[74] R. Ariga, E. M. Tunnicliffe, S. G. Manohar, et al., "Identification of myocardial disarray in patients with hypertrophic cardiomyopathy and ventricular arrhythmias." *Journal of the American College of Cardiology*, vol. 73, no. 20, pp. 2493–2502, 2019.

[75] O. Villemain, M. Correia, D. Khraiche, et al., "Myocardial stiffness assessment using shear wave imaging in pediatric hypertrophic cardiomyopathy." *JACC. Cardiovascular imaging*, vol. 11, no. 5, pp. 779–781, 2018.

[76] A. C. Hoskins, A. Jacques, S. C. Bardswell, et al., "Normal passive viscoelasticity but abnormal myofibrillar force generation in human hypertrophic cardiomyopathy." *Journal of Molecular and Cellular Cardiology*, vol. 49, no. 5, pp. 737–45, 2010.

[77] T. Ito and M. Suwa, "Echocardiographic tissue imaging evaluation of myocardial characteristics and function in cardiomyopathies." *Heart failure reviews*, 2020.

[78] M. F. A. Aly, W. P. Brouwer, S. A. Kleijn, et al., "Three-dimensional speckle tracking echocardiography for the preclinical diagnosis of hypertrophic cardiomyopathy." *The international journal of cardiovascular imaging*, vol. 30, no. 3, pp. 523–33, 2014.

[79] T. P. Usyk, J. H. Omens, and A. D. McCulloch, "Regional septal dysfunction in a three-dimensional computational model of focal myofiber disarray." *American journal of physiology. Heart and circulatory physiology*, vol. 281, no. 2, pp. H506–14, 2001.

[80] G. Balaban, H. Finsberg, H. H. Odland, et al., "High-resolution data assimilation of cardiac mechanics applied to a dyssynchronous ventricle." *International journal for numerical methods in biomedical engineering*, vol. 33, no. 11, 2017.

[81] L. Asner, M. Hadjicharalambous, R. Chabiniok, et al., "Estimation of passive and active properties in the human heart using 3d tagged MRI." *Biomechanics and modeling in mechanobiology*, vol. 15, no. 5, pp. 1121–39, 2016.

[82] H. Gao, W. G. Li, L. Cai, et al., "Parameter estimation in a holzapfel-ogden law for healthy myocardium." *Journal of engineering mathematics*, vol. 95, no. 1, pp. 231–248, 2015.

[83] V. Y. Wang, H. I. Lam, D. B. Ennis, et al., "Modelling passive diastolic mechanics with quantitative MRI of cardiac structure and function." *Medical image analysis*, vol. 13, no. 5, pp. 773–84, 2009.

[84] J. Guccione, K. D. Costa, and A. D. McCulloch, "Finite element stress analysis of left ventricular mechanics in the beating dog heart," *Journal of Biomechanics*, vol. 28, no. 10, pp. 1167–1177, 1995.

[85] H. Finsberg, G. Balaban, S. Ross, et al., "Estimating cardiac contraction through high resolution data assimilation of a personalized mechanical model," *Journal of Computational Science*, vol. 24, pp. 85–90, 2018.

[86] Y. Dabiri, K. Sack, N. Rebelo, et al., "Method for calibration of left ventricle material properties using 3d echocardiography endocardial strains," *Journal of Biomechanical Engineering*, 2019.

[87] N. F. Otani, S. Luther, R. Singh, et al., "Transmural ultrasound-based visualization of patterns of action potential wave propagation in cardiac tissue," *Annals of Biomedical Engineering*, vol. 38, no. 10, pp. 3112–23, 2010.

[88] C. A. Linte, M. Wierzbicki, T. M. Peters, et al., "Towards a biomechanics-based technique for assessing myocardial contractility: an inverse problem approach." *Computer methods in biomechanics and biomedical engineering*, vol. 11, no. 3, pp. 243–55, 2008.

[89] J. D. Humphrey, R. K. Strumpf, and F. C. Yin, "Determination of a constitutive relation for passive myocardium: I. a new functional form." *Journal of biomechanical engineering*, vol. 112, no. 3, pp. 333–9, 1990.

[90] J. D. Humphrey, R. K. Strumpf, and F. C. Yin, "Determination of a constitutive relation for passive myocardium: II. parameter estimation." *Journal of biomechanical engineering*, vol. 112, no. 3, pp. 340–6, 1990.

[91] P. M. F. Nielsen, D. T. K. Malcolm, P. J. Hunter, et al., "Instrumentation and procedures for estimating the constitutive parameters of inhomogeneous elastic membranes." *Biomechanics and modeling in mechanobiology*, vol. 1, no. 3, pp. 211–8, 2002.

[92] D. Martonova, M. Alkassar, J. Seufert, et al., "Passive mechanical properties in healthy and infarcted rat left ventricle characterised via a mixture model," *Journal of the Mechanical Behavior of Biomedical Materials*, p. 104430, 2021.

[93] K. F. Augenstein, B. R. Cowan, I. J. LeGrice, et al., "Method and apparatus for soft tissue material parameter estimation using tissue tagged magnetic resonance imaging." *Journal of biomechanical engineering*, vol. 127, no. 1, pp. 148–57, 2005.

[94] J. C. Walker, M. B. Ratcliffe, P. Zhang, et al., "Magnetic resonance imaging-based finite element stress analysis after linear repair of left ventricular aneurysm." *The Journal of thoracic and cardiovascular surgery*, vol. 135, no. 5, pp. 1094–102, 1102.e1–2, 2008.

[95] G. Balaban, H. Finsberg, S. Funke, et al., "In vivo estimation of elastic heterogeneity in an infarcted human heart." *Biomechanics and modeling in mechanobiology*, vol. 17, no. 5, pp. 1317–1329, 2018.

[96] H. Finsberg, G. Balaban, J. Sundnes, et al., "Personalized cardiac mechanical model using a high resolution contraction field," in *Virtual Physiological Human*, 2016.

[97] H. Finsberg, C. Xi, J. L. Tan, et al., "Efficient estimation of personalized biventricular mechanical function employing gradient-based optimization." *International journal for numerical methods in biomedical engineering*, vol. 34, no. 7, p. e2982, 2018.

[98] Z. Hu, D. Metaxas, and L. Axel, "In vivo strain and stress estimation of the heart left and right ventricles from MRI images," *Medical Image Analysis*, vol. 7, no. 4, pp. 435–444, 2003.

[99] M. Hadjicharalambous, R. Chabiniok, L. Asner, et al., "Analysis of passive cardiac constitutive laws for parameter estimation using 3d tagged MRI." *Biomechanics and modeling in mechanobiology*, vol. 14, no. 4, pp. 807–28, 2015.

[100] S. Klotz, I. Hay, M. L. Dickstein, et al., "Single-beat estimation of end-diastolic pressure-volume relationship: a novel method with potential for noninvasive application." *American journal of physiology. Heart and circulatory physiology*, vol. 291, no. 1, pp. H403–12, 2006.

[101] A. Palit, S. K. Bhudia, T. N. Arvanitis, et al., "In vivo estimation of passive biomechanical properties of human myocardium." *Medical & biological engineering & computing*, vol. 56, no. 9, pp. 1615–1631, 2018.

[102] J. E. Hall, *Guyton and hall textbook of medical physiology - pageburst e-book on vitalsource (retail access card)*, Guyton Physiology. Elsevier Health Sciences, 2010.

[103] J. G. Betts and K. A. Young, *Anatomy and physiology*. OpenStax, 2013.

[104] T. Belytschko, W. Kam Liu, and B. Moran, *Nonlinear finite elements for continua and structures*. Wiley, 2000.

[105] J. M. Guccione, A. D. McCulloch, and L. K. Waldman, "Passive material properties of intact ventricular myocardium determined from a cylindrical model," *J. Biomechanical Engineering*, vol. 113, no. 1, pp. 42–55, 1991.

[106] B. Kim, S. B. Lee, J. Lee, et al., "A comparison among neo-hookean model, mooney-rivlin model, and ogden model for chloroprene rubber," *International Journal of Precision Engineering and Manufacturing*, vol. 13, no. 5, pp. 759–764, 2012.

[107] N. Stergiopulos, J. J. Meister, and N. Westerhof, "Determinants of stroke volume and systolic and diastolic aortic pressure." *The American journal of physiology*, vol. 270, no. 6 Pt 2, pp. H2050–9, 1996.

[108] S. Schuler, "Developing and coupling a lumped parameter model of the closed loop human vascular system to a model of cardiac mechanics," Master's thesis, 2016.

[109] L. Baron, A. Loewe, and O. Dössel, "From clinics to the virtual beating heart a general modeling workflow for patient-specific electromechanical heart simulations," in *BMTMedPhys 2017*, vol. 62, no. S1. Dresden, September 10 13: de Gruyter, 2017, p. S70.

[110] W. Jakob, M. Tarini, D. Panozzo, et al., "Instant field-aligned meshes," *ACM Transactions on Graphics*, vol. 34, no. 6, pp. 1–15, 2015.

[111] A. C. Daub, "Numerical haemodynamics in the human heart," 2018.

[112] R. Karim, R. J. Housden, M. Balasubramaniam, et al., "Evaluation of current algorithms for segmentation of scar tissue from late gadolinium enhancement cardiovascular magnetic resonance of the left atrium: an open-access grand challenge." *Journal of cardiovascular magnetic resonance : official journal of the Society for Cardiovascular Magnetic Resonance*, vol. 15, p. 105, 2013.

[113] S. Apostolakis and S. Konstantinides, "The right ventricle in health and disease: insights into physiology, pathophysiology and diagnostic management." *Cardiology*, vol. 121, no. 4, pp. 263–73, 2012.

[114] C. Geuzaine and J.-F. Remacle, "Gmsh: A 3-d finite element mesh generator with built-in pre- and post-processing facilities," *International Journal for Numerical Methods in Engineering*, vol. 79, no. 11, pp. 1309–1331, 2009.

[115] T. A. Burkhart, D. M. Andrews, and C. E. Dunning, "Finite element modeling mesh quality, energy balance and validation methods: a review with recommendations associated with the modeling of bone tissue." *Journal of biomechanics*, vol. 46, no. 9, pp. 1477–88, 2013.

[116] U. Ayachit, *The paraview guide: A parallel visualization application*. Kitware, 2015.

[117] E. Kovacheva, T. Gerach, S. Schuler, et al., "Causes of altered ventricular mechanics in hypertrophic cardiomyopathy—an in-silico study," *Preprint*, 2021.

[118] P. Radau, Y. Lu, K. Connelly, et al., "Evaluation framework for algorithms segmenting short axis cardiac MRI." 2009.

[119] I. Santana-Perez and M. S. Pérez-Hernández, "Towards reproducibility in scientific workflows: An infrastructure-based approach," *Scientific Programming*, vol. 2015, pp. 1–11, 2015.

[120] A. Prabhu and P. Fox, "Reproducible workflow."

[121] R. Zhou, Z. Liao, T. Pan, et al., "Cardiac atlas development and validation for automatic segmentation of cardiac substructures." *Radiotherapy and oncology : journal of the European Society for Therapeutic Radiology and Oncology*, vol. 122, no. 1, pp. 66–71, 2017.

[122] X. Zhuang, L. Li, C. Payer, et al., "Evaluation of algorithms for multi-modality whole heart segmentation: An open-access grand challenge." *Medical image analysis*, vol. 58, p. 101537, 2019.

[123] E. Kovacheva, L. Thämer, T. Fritz, et al., "Estimating cardiac active tension from wall motion - an inverse problem of cardiac biomechanics," *International journal for numerical methods in biomedical engineering*, 2021.

[124] J. M. Guccione, A. D. McCulloch, and L. K. Waldman, "Passive material properties of intact ventricular myocardium determined from a cylindrical model." *Journal of biomechanical engineering*, vol. 113, no. 1, pp. 42–55, 1991.

[125] J. D'hooge, A. Heimdal, F. Jamal, et al., "Regional strain and strain rate measurements by cardiac ultrasound: principles, implementation and limitations." *European journal of echocardiography : the journal of the Working Group on Echocardiography of the European Society of Cardiology*, vol. 1, no. 3, pp. 154–70, 2000.

[126] A. Scatteia, A. Baritussio, and C. Bucciarelli-Ducci, "Strain imaging using cardiac magnetic resonance." *Heart failure reviews*, vol. 22, no. 4, pp. 465–476, 2017.

[127] A. J. Yezzi and J. L. Prince, "An eulerian PDE approach for computing tissue thickness." *IEEE transactions on medical imaging*, vol. 22, no. 10, pp. 1332–9, 2003.

[128] E. Heiberg, J. Sjögren, M. Ugander, et al., "Design and validation of segment-freely available software for cardiovascular image analysis," *BMC medical imaging*, vol. 10, no. 1, pp. 1–13, 2010.

[129] G. Korosoglou, S. Giusca, N. P. Hofmann, et al., "Strain-encoded magnetic resonance: a method for the assessment of myocardial deformation." *ESC heart failure*, vol. 6, no. 4, pp. 584–602, 2019.

[130] Y. Nabeshima, Y. Seo, and M. Takeuchi, "A review of current trends in three-dimensional analysis of left ventricular myocardial strain." *Cardiovascular ultrasound*, vol. 18, no. 1, p. 23, 2020.

[131] D. Augustine, A. J. Lewandowski, M. Lazdam, et al., "Global and regional left ventricular myocardial deformation measures by magnetic resonance feature tracking in healthy volunteers: comparison with tagging and relevance of gender." *Journal of cardiovascular magnetic resonance : official journal of the Society for Cardiovascular Magnetic Resonance*, vol. 15, p. 8, 2013.

[132] K. Lin, L. Meng, J. D. Collins, et al., "Heart deformation analysis: the distribution of regional myocardial motion patterns at left ventricle." *The international journal of cardiovascular imaging*, vol. 33, no. 3, pp. 351–359, 2017.

[133] A. Nemes, A. Kormanyos, P. Domsik, et al., "Normal reference values of three-dimensional speckle-tracking echocardiography-derived left atrial strain parameters (results from the MAGYAR-healthy study)." *The international journal of cardiovascular imaging*, vol. 35, no. 6, pp. 991–998, 2019.

[134] V. T. Truong, H. T. Phan, K. N. P. Pham, et al., "Normal ranges of left ventricular strain by three-dimensional speckle-tracking echocardiography in adults: A systematic review and meta-analysis." *Journal of the American Society of Echocardiography : official publication of the American Society of Echocardiography*, vol. 32, no. 12, pp. 1586–1597.e5, 2019.

[135] J.-U. Voigt and M. Cvijic, "2- and 3-dimensional myocardial strain in cardiac health and disease." *JACC. Cardiovascular imaging*, vol. 12, no. 9, pp. 1849–1863, 2019.

[136] S. Schuler, N. Pilia, D. Potyagaylo, et al., "Cobiveco: Consistent biventricular coordinates for precise and intuitive description of position in the heart – with matlab implementation," 2021.

[137] P. Song, X. Bi, D. C. Mellema, et al., "Quantitative assessment of left ventricular diastolic stiffness using cardiac shear wave elastography," *Journal of Ultrasound in Medicine*, vol. 35, no. 7, pp. 1419–1427, 2016.

[138] C. Mekkaoui, T. G. Reese, M. P. Jackowski, et al., "Diffusion MRI in the heart." *NMR in biomedicine*, vol. 30, no. 3, 2017.

[139] P. Mukherjee, J. I. Berman, S. W. Chung, et al., "Diffusion tensor MR imaging and fiber tractography: theoretic underpinnings." *AJNR. American journal of neuroradiology*, vol. 29, no. 4, pp. 632–41, 2008.

[140] I. Pozios, A. Pinheiro, C. Corona-Villalobos, et al., "Rest and stress longitudinal systolic left ventricular mechanics in hypertrophic cardiomyopathy: Implications for prognostication." *Journal of the American Society of Echocardiography : official publication of the American Society of Echocardiography*, vol. 31, no. 5, pp. 578–586, 2018.

[141] A. Satriano, B. Heydari, N. Guron, et al., "3-dimensional regional and global strain abnormalities in hypertrophic cardiomyopathy." *The international journal of cardiovascular imaging*, vol. 35, no. 10, pp. 1913–1924, 2019.

[142] T. Kato, N. Ohte, K. Wakami, et al., "Myocardial fiber shortening in the circumferential direction produces left ventricular wall thickening during contraction." *The Tohoku journal of experimental medicine*, vol. 222, no. 3, pp. 175–81, 2010.

[143] H. M. Hurlburt, G. P. Aurigemma, J. C. Hill, et al., "Direct ultrasound measurement of longitudinal, circumferential, and radial strain using 2-dimensional strain imaging in normal adults." *Echocardiography (Mount Kisco, N.Y.)*, vol. 24, no. 7, pp. 723–31, 2007.

[144] S. S. Bhupathi, S. Chalasani, and R. Rokey, "Stiff heart syndrome." *Clinical medicine & research*, vol. 9, no. 2, pp. 92–9, 2011.

[145] D. Phelan, P. Collier, P. Thavendiranathan, et al., "Relative apical sparing of longitudinal strain using two-dimensional speckle-tracking echocardiography is both sensitive and specific for the diagnosis of cardiac amyloidosis." *Heart (British Cardiac Society)*, vol. 98, no. 19, pp. 1442–8, 2012.

[146] K. Lin, J. D. Collins, V. Chowdhary, et al., "Heart deformation analysis: measuring regional myocardial velocity with MR imaging." *The international journal of cardiovascular imaging*, vol. 32, no. 7, pp. 1103–11, 2016.

[147] M. S. Maurer, D. Burkhoff, L. P. Fried, et al., "Ventricular structure and function in hypertensive participants with heart failure and a normal ejection fraction: the cardiovascular health study." *Journal of the American College of Cardiology*, vol. 49, no. 9, pp. 972–81, 2007.

[148] S. Land, S.-J. Park-Holohan, N. P. Smith, et al., "A model of cardiac contraction based on novel measurements of tension development in human cardiomyocytes," *Journal of Molecular and Cellular Cardiology*, vol. 106, pp. 68–83, 2017.

[149] K. Werys, L. Blaszczyk, A. Kubik, et al., "Displacement field calculation from CINE MRI using non-rigid image registration," pp. 672–675, 2015.

[150] E. Kovacheva, L. Baron, S. Schuler, et al., "Optimization framework to identify constitutive law parameters of the human heart," in *Current Directions in Biomedical Engineering*, vol. 6, no. 3. Leipzig; online Conference: De Gruyter, 2020, pp. 95–98.

[151] F. Gao and L. Han, "Implementing the nelder-mead simplex algorithm with adaptive parameters," *Computational Optimization and Applications*, vol. 51, no. 1, pp. 259–277, 2010.

[152] E. Jones, T. Oliphant, P. Peterson, et al., "Scipy: Open source scientific tools for python," 2001.

[153] L. Geerts, R. Kerckhoffs, P. Bovendeerd, et al., *Towards patient specific models of cardiac mechanics: A sensitivity study*, Lecture Notes in Computer Science, vol. 2674, 2003.

[154] Y. Tsadok, Y. Petrank, S. Sarvari, et al., "Automatic segmentation of cardiac MRI cines validated for long axis views," *Computerized Medical Imaging and Graphics : the Official Journal of the Computerized Medical Imaging Society*, vol. 37, no. 7-8, pp. 500–511, 2013.

[155] R. J. Feezor, J. Caridi, I. Hawkins, et al., "Angiography," *Endovascular Surgery*, pp. 209–225, 2011.

[156] T. Fritz, E. Kovacheva, G. Seemann, et al., "The inverse problem of cardiac mechanics - estimation of cardiac active stress from endocardial motion tracking," in *Computational & Mathematical Biomedical Engineering Proceedings*, N. Perumal, O. Makoto, and M. O. Marie, Eds., vol. 1. Cardiff, UK: Zeta Computational Resources, 2019, pp. 91–95.

[157] D. F. Scollan, A. Holmes, R. Winslow, et al., "Histological validation of myocardial microstructure obtained from diffusion tensor magnetic resonance imaging," *The American Journal of Physiology*, vol. 275, no. 6, pp. H2308–18, 1998.

[158] D. Gil, A. Borras, R. Aris, et al., "What a difference in biomechanics cardiac fiber makes," in *STACOM 2012, LNCS 7746*. Springer-Verlag Berlin Heidelberg, 2013, pp. 253–260.

[159] X. Zhao, R.-S. Tan, H.-C. Tang, et al., "Left ventricular wall stress is sensitive marker of hypertrophic cardiomyopathy with preserved ejection fraction," *Frontiers in Physiology*, vol. 9, p. 250, 2018.

[160] S. Nielles-Vallespin, A. Scott, P. Ferreira, et al., "Cardiac diffusion: Technique and practical applications," *Journal of Magnetic Resonance Imaging : JMRI*, 2019.

[161] M. L. Milne, B. M. Schick, T. Alkhazal, et al., "Myocardial fiber mapping of rat hearts, using apparent backscatter, with histologic validation." *Ultrasound in medicine & biology*, vol. 45, no. 8, pp. 2075–2085, 2019.

[162] W.-N. Lee, M. Pernot, M. Couade, et al., "Mapping myocardial fiber orientation using echocardiography-based shear wave imaging." *IEEE transactions on medical imaging*, vol. 31, no. 3, pp. 554–62, 2012.

List of Publications and Supervised Theses

Journal Articles

- **E. Kovacheva**, L. Thämer, T. Fritz, G. Seemann, M. Ochs, O. Dössel, and A. Loewe, *Estimating Cardiac Active Tension from Wall Motion – An Inverse Problem of Cardiac Biomechanics*, International Journal for Numerical Methods in Biomedical Engineering, 2021
- **E. Kovacheva**, T. Gerach, S. Schuler, M. Ochs, O. Dössel, and A. Loewe, *Causes of Altered Ventricular Mechanics in Hypertrophic Cardiomyopathy – an In-Silico Study*, BioMedical Engineering OnLine (in review), 2021
- T. Gerach, S. Schuler, J. Fröhlich, L. Lindner, **E. Kovacheva**, R. Moss, E. Wülfers, G. Seemann, C. Wieners and A. Loewe, *Electro-mechanical Whole-Heart Digital Twins: a Fully Coupled Multi-Physics Approach*, Mathematics, MDPI, 2021

Refereed Conference Articles

- **E. Kovacheva**, L. Baron, S. Schuler, T. Gerach, O. Dössel, and A. Loewe, *Optimization Framework to Identify Constitutive Law Parameters of the Human Heart*, Current Directions in Biomedical Engineering, vol. 6(3), pp. 95–98, 2020
- **E. Kovacheva**, L. Baron, O. Dössel, and A. Loewe, *Electro-Mechanical Delay in the Human Heart: A Study on a Simple Geometry*, Computing in Cardiology Conference (CinC), vol. 45, 2018
- J. Brenneisen, S. Schuler, **E. Kovacheva**, T. Gerach, O. Dössel, and A. Loewe, *Influence of Geometrical Properties for the Calculation of a Pressure-Free Whole Heart Geometry*, 14th WCCM-ECCOMAS Congress, 2020
- T. Gerach, S. Schuler, **E. Kovacheva**, O. Dössel, and A. Loewe, *Consequences of Using an Orthotropic Stress Tensor for Left Ventricular Systole*, Computing in Cardiology Conference (CinC), 2020

- A. Müller, **E. Kovacheva**, M. Fritz, O. Dössel, and A. Loewe, *Validating a Numerical Simulation of Human Heart Motion Using Clinical Data*, Current Directions in Biomedical Engineering, vol. 6(3), pp. 547–550, 2020
- T. Fritz, **E. Kovacheva**, G. Seemann, O. Dössel, and A. Loewe, *The inverse problem of cardiac mechanics - estimation of cardiac active stress from endocardial motion tracking*, Computational and Mathematical Biomedical Engineering Proceedings, vol. 1, pp. 91–95, 2019
- A. Müller, **E. Kovacheva**, S. Schuler, O. Dössel, and L. Baron, *Effects of local activation times on the tension development of human cardiomyocytes in a computational model*, Current Directions in Biomedical Engineering, vol. 4(1), pp. 247–250, 2018

Refereed Conference Abstracts

- **E. Kovacheva**, T. Gerach, O. Dössel, and A. Loewe, *In-Silico Study on Hypertrophic Cardiomyopathy – Causes of Altered Myocardial Velocities*, iHeart Workshop, 2020
- **E. Kovacheva**, S. Schuler, T. Gerach, O. Dössel, and A. Loewe, *A Method for Pressure-Volume-Based Parameter Identification for a Passive Constitutive Model of Myocardium*, RISM Congress: iHEART – Modelling the Cardiac Function, 2019
- **E. Kovacheva** and T. Gerach, L. Hütter, O. Dössel, A. Loewe, *A Bidirectionally Coupled Model of Electrophysiology and Elastomechanics of the Human Heart*, Towards an integrated numerical heart model, 2019
- **E. Kovacheva**,T. Fritz, G. Seeman, O. Dössel, A. Loewe, *Estimating Cardiac Active Tension from Wall Motion – The Inverse Problem of Cardiac Mechanics*, GACM, 2019
- **E. Kovacheva**, L. Baron, O. Dössel, A. Loewe, *Distribution of the Electromechanical Delay in the Heart Muscle: a Study on a Simple Geometry*, BMT, 2018
- J. Brenneisen, **E. Kovacheva**, T. Gerach, A. Daub, L. Hütter, B. Frohnapfel, O. Dössel, A. Loewe, *Characterization of the Fluid Dynamic Pressure Field in the Human Heart as a Basis for Coupled Fluid-Structure Simulations*, BMT, 2020
- J. Brenneisen, A. Daub, **E. Kovacheva**, T. Gerach, L. Hütter, B. Frohnapfel, O. Dössel, A. Loewe, *A Sequential Coupling Approach for Fluid-Structure Interaction in a Patient Specific Whole Heart Geometry*, Frontiers in Cardiovascular Medicine, 2021 and iHeart Congress, 2021 (submitted)

Conference Presentations

- *Optimization Framework to Identify Constitutive Law Parameters of the Human Heart*, BMT, 2020, online conference

- *In-Silico Study on Hypertrophic Cardiomyopathy – Causes of Altered Myocardial Velocities*, iHeart, 2020, online workshop
- *Estimating Cardiac Active Tension from Wall Motion – The Inverse Problem of Cardiac Mechanics*, GACM, 2019, Kassel
- *A Bidirectionally Coupled Model of Electrophysiology and Elastomechanics of the Human Heart*, Towards an integrated numerical heart model, 2019, Bad Herrenalb

Reports

- Final report of the HeiKa project *Improved Phenotyping of Cardiomyopathy Patients by Means of Imaging-Driven Computational Modeling of Cardiac Biomechanics*, 2018
- corresponding parts of the intermediate and final reports of the BMBF joint project *Ein integriertes Herz-Modell – Kopplung von Elektrophysiologie, Elastomechanik, Fluss und Kreislauf*, 2016–2019

Supervised Student Works

- Larissa Hütter, *An Integrated Heart Model: Aspects of Coupling Fluid Dynamics, Elastomechanics and Electrophysiology*, supervision with Tobias Gerach and Anna Daub, Master Thesis, Institute of Biomedical Engineering, Karlsruhe Institute of Technology (KIT), 2019
- Armin Müller, *Validation of a Numerical Simulation of Elastomechanics of the Human Heart and Parameter Estimation Using Clinical Data*, Master Thesis, Institute of Biomedical Engineering, Karlsruhe Institute of Technology (KIT), 2019
- Laura Thämer, *The Inverse Problem of the Heart Mechanics – Reconstruction of the Active Tension*, Master Thesis, Institute of Biomedical Engineering, Karlsruhe Institute of Technology (KIT), 2019
- Armin Müller, *Optimierung der Parameter für die Simulation eines Herzschlags*, Student Assistant, 2018–2019
- Marc Alexander Fritz, *Segmentieren von MRI Cine Daten und Geometrie Erstellung*,Student Assistant, 2019–2021

Awards

- Bill and Gary Sanders Poster Award, Conference "Computing in Cardiology" 2018 in Maastricht (the Netherlands) Ekaterina Kovacheva, Lukas Baron, Olaf Dössel, Axel Loewe: *Electro-Mechanical Delay in the Human Heart: A Study on a Simple Geometry*
- Semi-Finalist at Rosanna Degani Young Investigators Award, Conference „Computing in Cardiology“ 2020 in Rimini (Italy) Tobias Gerach, Steffen Schuler, Ekaterina Kovacheva, Olaf Dössel, Axel Loewe *Consequences of Using an Orthotropic Stress Tensor for Left Ventricular Systole*
- 5th place in student competition, German Society for Biomedical Engineering (DGBMT) annual conference 2020, Online Armin Müller, Ekaterina Kovacheva, Axel Loewe *Validating a Numerical Simulation of Human Heart Motion Using Clinical Data*

DFG Grant Application

- *Unravelling the Hypertrophic Cardiac Phenotype: Biomechanical Twin Modelling to Distinguish Hypertensive Heart Disease, Athletes' Heart and Hypertrophic Cardiomyopathy*, submitted in May 2021